# Coopérativité photo-induite dans des matériaux bistables avec changement de volume

Alix Volte

UNIVERSITÉ DE RENNES 1

# THESE DE DOCTORAT DE

L'UNIVERSITE DE RENNES 1

ECOLE DOCTORALE N° 596
*Matière, Molécules, Matériaux*
Spécialité : *Physique*

Par
**Alix VOLTE**

## Photo-induced cooperativity in bistable volume-changing materials

**Thèse présentée et soutenue à Rennes, le 10 novembre 2020**
**Unité de recherche : Institut de Physique de Rennes UMR 6251**

**Rapporteurs avant soutenance** :

| | |
|---|---|
| Pascale Foury-Leylekian | Professeure, Université Paris-Saclay |
| Matias Bargheer | Professeur, University of Potsdam |

**Composition du Jury :**

| | | |
|---|---|---|
| Président : | Sergio Di Matteo | Professeur, Université de Rennes 1 |
| Examinateurs : | Felisa Berenguer | Scientifique de ligne, Université Paris-Saclay |
| | Sergio Di Matteo | Professeur, Université de Rennes 1 |
| | Guillaume Chastanet | Chargé de Recherche, Université de Bordeaux |
| Dir. de thèse : | Maciej Lorenc | Directeur de recherche, Université de Rennes 1 |
| Co-dir. de thèse : | Benoît Corraze | Maître de conférence, Université de Nantes |

# Acknowledgements

This PhD manuscript is the product of a joint scientific effort, which involved several members of the scientific community over three years.
Of course, this work would not have been possible without my supervisors Maciej Lorenc and Benoît Corraze, who welcomed me in the ELASTICA project and guided me from the beginning to the end. Their optimism, teaching skills and constant support were real cornerstones of this work.
I also deeply thank Céline Mariette, for her availability and patience, and for having introduced me to x-ray diffraction principles and analysis. Her support was of great help throughout these three years.
For his dynamism and great knowledge of ultrafast x-ray science, I would like to thank Marco Cammarata, who also welcomed me in Rennes with a walk in the Mont saint Michel bay. Such a nice way to discover a new place! I also thank Roman Bertoni, who really helped with discussions about photo-induced processes in spin-crossover compounds, and Elzbieta Trzop for her kindness and for having introduced me to single-crystal diffraction. Gluing these tiny pieces on cactus thorns is definitely not a piece of cake!
I would like to thank Hervé Cailleau for the endless yet deeply interesting discussions about solid state physics and for his great help grasping at theoretical aspects underlying this work. Behind the surly manners, hides a really nice and passionate man. I also thank Bertrand Toudic, for discussions about phonons, phase transitions and past and future of the scientific community, in no particular order.
And more generally, I thank all members of the Materials and Light team, for having welcomed me during these three years.
This work would have been very little without strong collaborations with high-level scientists: I deeply thank Cristian Enachescu and Laurentiu Stoleriu, who developed and shared their knowledge about Monte-Carlo molecular dynamics model. Romanian culinary specialties and fog-pinned down plane also make good memories!
From the Physics of Materials and Nanostructures team in Nantes, I thank Etienne Janod for enthralling discussions about reflectivity models and Laurent Cario for his help on x-ray diffraction analysis on $V_2O_3$ thin films.
I also thank Marie-Laure Boillot, who provided spin-crossover samples, along with insightful discussions about these materials.
Even if we tend to look down on it, administrative work represents an important facet of any project. Therefore, I want to thank Valérie Ferri for her listening, availability and reactivity. Things would have certainly gone way less smoothly without her support.
I also thank my companions in arms Danylo Babich (the guy who never stops working, even almost fainting on his keyboard) and Giovanni Azzolina (the most taciturn Italian guy I ever met, and yet such a nice and subtle person). My thoughts also go to Vibe Jakobsen, for the endless discussions and mutual support along the PhD journey.
I was really lucky to be surrounded by such nice and skillful people.

Lastly, I would like to thank my parents, for having etched into my mind that curiosity is the utmost value. And Matthieu, for his unfailing love and support.
This is just a milestone on the way!

“Present is infinity in motion.”
O. Kakuzo, *The Book of Tea*

# Introduction

The field of ultrafast structural dynamics is based on remarkable developments of available pulse sources, from THz to x-rays. Currently, pump-probe techniques operate on the femtosecond (1 fs = $10^{-15}$ s) time scales, i.e. faster than atomic motions. Typically, a laser pump pulse drives a system onto an electronically excited state, while the structural dynamics temporal evolution is tracked with a delayed probe pulse. Moreover, laser light sources can generate intense pulses with a number of photons approaching the number of potentially photo-excited species. Such pulses can induce highly excited states, involving a macroscopic number of atoms or molecules and driving the system far from equilibrium [Cailleau2010, Hamm2017]. These precursor effects may be followed by the establishment of a new electronic and structural order and thus may bring about a phase transition of the excited system [Lantz2017]. This represents a new approach to direct materials functionalities: timely acting on an atomic or molecular excited state, rather than switching from an equilibrium state to another by tuning a static control parameter (such as pressure, temperature, electric/magnetic field, etc.). Moreover, atomic displacements may occur in a collective coherent motion, in a fundamentally different way from incoherent thermal excitation. The possibility to drive the transformation process coherently makes it non-thermal and particularly efficient, as well as very selective since it involves controlling the system via few degrees of freedom.

The collective oscillation of atoms in a crystalline solid is called a phonon mode. Since atoms in a crystal are coupled through interatomic interactions, their displacements around their equilibrium position manifest by the generation of oscillating waves in the crystalline medium. The quantum energy of an oscillating mode is proportional to the phonon frequency , more precisely $\hbar$ . The name phonon was chosen by analogy with a photon for light, to qualify the quasi-particle associated to an oscillating structural mode. Different types of atomic motions define the different phonon modes. In the long wavelength limit, two types can be distinguished:

- optical phonons corresponding to in-phase oscillation modes associated to relative motions of atoms within the unit cell. The adjective “optical” refers to the possibility to excite these phonons with infrared light or via Raman scattering.
- acoustic phonons are associated to the propagation of acoustic strain waves. The sound velocity varies from one type of material to another: it is typically in the order of 7000 m.s$^{-1}$ in metal oxides [Mariette2020, Word1981] and around 4000 m.s$^{-1}$ in molecular materials [Parpiiev2017], for instance.

The internal interactions between the different particles constituting a solid, make the medium in which they are imbedded act on itself through positive feedback. This emerging cooperativity between different degrees of freedom, for instance electronic photo-excited state and crystalline lattice deformations, underlies the resulting non-linear responses and threshold phenomena [Bertoni2016]. The dynamical picture of a photo-induced phase transition, involving only a small number of selected degrees of freedom, strays from the mechanism of phase transitions at thermal equilibrium. Indeed, the latter is governed by critical fluctuations, involving a macroscopic number of interplaying degrees of freedom.

Richard Feynman defines equilibrium at the stage “when all fast things have happened, but the slow things have not” [Feynman1972]. Considering ultrafast photo-induced phase transitions, following the initial electronic excitation, the material is put out-of-equilibrium and transforms in a complex evolution. Several degrees of freedom are at play, acting on different time and length

scales and thus leading to successive partial equilibriums. During the first step taking place in the fs regime, photo-excited electrons reorganize while the positions of atoms, which are significantly heavier, remain frozen. This new electronic distribution, for instance the photo-induced change of electron bands population, defines a new potential driving atomic motions and their subsequent displacements from their original position. Many studies have focused so far on optical coherent phonon oscillations around new atomic positions [Lindenberg2017, Basov2017]. This previously described process drives intracell atomic displacements that preserve the crystal shape and volume. Additional stabilization of a new macroscopic structural order requires the establishment of long-range crystal deformations along a coherent dynamical pathway involving propagating acoustic waves.

At early stage, when pump energy is just absorbed, the photo-excited electron distribution in an insulating or semiconducting phase generates internal stresses, which can be either compressive or tensile, depending on the sign of the electron-acoustic phonon deformation potential [Ruello2009]. Around the 100 fs time scale, the electrons and holes had the time to thermalize in their respective bands, and an electronic (hole) temperature can be defined, which is generally very high (reaching 1000 K). In addition, intra-band energy transfer operates from electrons (holes) to phonons. This results in the fast local increase in phonon population, which induces an ultrafast heating of the lattice, the latter leading to a so-called thermoelastic stress.

Both electronic and thermoelastic processes gives rise to spatial inhomogeneity of the photo-induced stresses in the material, originating from the exponential depth profile of the pump laser and from the existence of surfaces and/or interfaces. The resulting stress gradient generates a force, which accelerates atoms and launches an acoustic strain wave from the surface, to recover mechanical equilibrium. The propagation of this collective strain wave allows establishing crystal deformations over long distances, thereby occurring at the acoustic time scale. This time is defined by the ratio between the relevant length depending of the investigated material (penetration depth, size), and the speed of sound in the material. Depending on the system, these acoustic motions will thus take place on a time scale ranging from picosecond (ps) for nano-sized samples, to nanosecond (ns) for molecular single crystals for instance.

In contrast with the numerous experiments investigating coherent optical phonons, the role of acoustic phonons and photo-induced strain driving cell deformations, albeit looked upon, is rather uncommonly studied and lacks thorough description. The coupling between the strain wave and the order parameter field of the transition raises the question whether such coupling can induce self-amplification of the phase transition, the elastic interaction acting as a positive feedback. This approach strays from the usual picture of nucleation and growth, inspired from kinetic processes at thermal equilibrium.

The emitted hypothesis underpinning the approach of this PhD is that, in volume-changing materials, these elastic processes are essential to establish a true phase transition at macroscopic scale and represent the key to stabilize the excited states over a long lifetime, overcoming the relaxation to equilibrium with the environment. If verified, this assumption would suggest that light-driven expansion is not, as generally considered, a secondary phenomenon in photo-induced phase transitions and allows dynamically acting on materials. Technological applications suffer indeed from the difficulty to maintain excited states due to their transient nature, which often do not survive the fast relaxation of electrons and optical phonons. It is thus of paramount interest, both on a fundamental and applicative point of view, to explore how photo-excited phases can become persistent.

In this context, the main work of my PhD is dedicated to improving methods of quantitative analysis of experimental data from pump-probe measurements and to deepening the theoretical

concepts associated with photo-induced elastic cooperativity. The second aspect is to go further in the study of the universality of the phenomenon, by testing several types of phase transitions and different sample morphologies, thus shining a different light on the physical picture of photo-induced phase transitions through the strain wave pathway concept. This project stands between the field of photo-induced phase transitions, the physics of photo-acoustics and non-linear wave phenomena, as well as the study of the elastic field effects in correlated electrons materials.
We expect this photo-induced elastic cooperative process to be particularly efficient in bistable materials showing significant volume change at the transition, as those investigated here. It is the case of spin crossover materials, where cooperativity is governed by long-range elastic field arising from the swelling of molecules between the two spin states [Bertoni2016]. Other promising candidate materials to explore the universality of photo-induced elastic cooperativity are Mott insulators exhibiting resistive switching [Janod2015], and metal oxide nano-crystals with a bistable regime at room temperature [Ohkoshi2010].

In this manuscript, we will first present state-of-the-art knowledge about the role of volume as a parameter in phase transitions dynamics (chapter I). Experimental methods used to access structural information in real time will be described in chapter II. Finally, chapter III and IV will be dedicated to the presentation of the study of photo-induced phase transition in two bistable systems undergoing volume change: a spin-crossover material (chapter III) and a Mott insulator (chapter IV).

# Chapter I: Introduction to thermal and photo-induced phase transitions and the role of volume

Phase transitions correspond to qualitative and quantitative spectacular changes of the macroscopic state and properties (electronic, magnetic and/or structural) of a material, as a response of the system to the variation of external conditions.
This chapter begins with the description of thermal phase transitions, both thermodynamically and under symmetry considerations. Then, we introduce the ultrafast phase transitions induced by a light pulse. In both cases, we highlight the key role of volume in the phase transition process.

## I.1. Description of phase transitions at thermal equilibrium

### I.1.a. Thermodynamical description

#### *I.1.a.i. Thermodynamical potential*

In a thermodynamical description of a macroscopic system, it is essential to distinguish between thermodynamical control parameters which are external macroscopic constraints, such as temperature T, pressure P, external electric E or magnetic B field, … and internal macroscopic variables able to fluctuate, such as volume V, polarization P or magnetization M, … at which a statistical distribution is associated. For instance, choosing T and P as external parameters as it will be the case for all experimental studies presented in this manuscript, it is well known that the convenient thermodynamic function, called thermodynamic potential, used to describe the equilibrium states is the Gibbs free energy ( , ). Defining a potential energy landscape is the simplest appropriate way to describe the stability, instability and metastability of a system (mechanical, dynamical, thermodynamical, …). This description can also be done in statistical thermodynamics by the use of a so-called ”incomplete” [Strukov1998] or “partial” [Diu1989] thermodynamical potential Φ( ), associated to the probability distribution ( ) for the internal macroscopic variable *X*:

$$( ) \propto \ xp\,(-\frac{\Phi( )}{\quad}).$$

To calculate ( ) and Φ( ), it is necessary to perform an integration over all microscopic states of internal degrees of freedom, for each value of the macroscopic variable . The maximum of ( )corresponds to the minimum of Φ( ) and defines the equilibrium state . There is an analogy between the thermodynamical potential Φ( ) and the potential energy in mechanics.
At the thermodynamic limit, and for a homogeneous phase, the probability distribution ( ) becomes sharply peaked and the difference between complete and incomplete thermodynamical potential fades away. However, when two (or more) wells emerge in the potential landscape, associated to stable or metastable macroscopic states, incomplete thermodynamical potential becomes a useful conceptual tool to describe a phase transition, the latter corresponding to the system passing from one of these states to another. In particular, incomplete thermodynamical potential is essential to write the Landau expansion, introduced in part I.1.b.

#### *I.1.a.ii. Phase diagram*

A phase transition is a transformation between two different macroscopic states, driven by the variation of an external control parameter. Phase transitions are of various nature (electronic, magnetic and/or structural). The macroscopic states may differ by their symmetry, as can be seen in the ferromagnetic to paramagnetic transition in iron, or quantitatively, as in the case of liquid-gas transition in water. Even if the zoo of phase transitions is quite broad, it is possible to describe them with a common approach, especially thanks to the universality of thermodynamical description.
A phase diagram is a topographic description in the external parameters space, of the areas where the different phases are thermodynamically stable (Figure 1). Phase transition lines mark the borders of these areas and the presence of specific points, such as triple point or critical point (Figure 1).

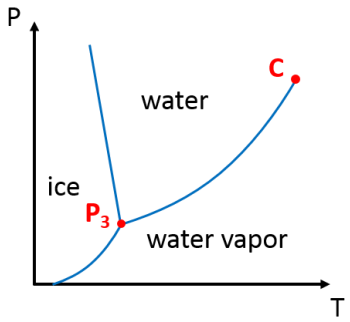


*Figure 1: Phase diagram of water, as a function of the external variables P (pressure) and T (temperature). $P_3$ is the triple point, whereby the three phases coexist. C represents the critical point, above which a crossover hypercritical regime takes place.*

### *I.1.a.iii. First- and second-order phase transitions*

A phase transition is characterized by the occurrence of a thermodynamical singularity, which can be either a discontinuity or a divergence of some physical quantities. It is defined as a first-order phase transition, if at least one of the physical quantities associated to a first-order derivative of the thermodynamical potential (as for instance the volume V, the entropy S or the magnetization M) presents some discontinuity when crossing the transition line. At finite temperature, the entropy discontinuity ΔS implies the occurrence of a latent heat: the system absorbs (or emits) a fixed amount of energy during the phase transition.
Another characteristic of first-order phase transitions, is that two different separate phases can coexist at the transition point, i.e. the system becomes heterogeneous at macroscopic scale and may exhibit a (more or less wide) metastable regime, with the occurrence of a hysteresis. The presence of two phases at equilibrium directly depends on the incomplete thermodynamical potential landscape. Each phase corresponds to a minimum of this potential. Depending on the concavity (second derivative) of the latter, the phase will be described either as locally stable or unstable and the relative depth of the states will determine their stable or metastable character. The domain of equilibrium between two phases corresponds to an equality of potential between both states, and defines the transition line in the phase diagram. This is shown in Figure 2a, for the liquid-gas transition.

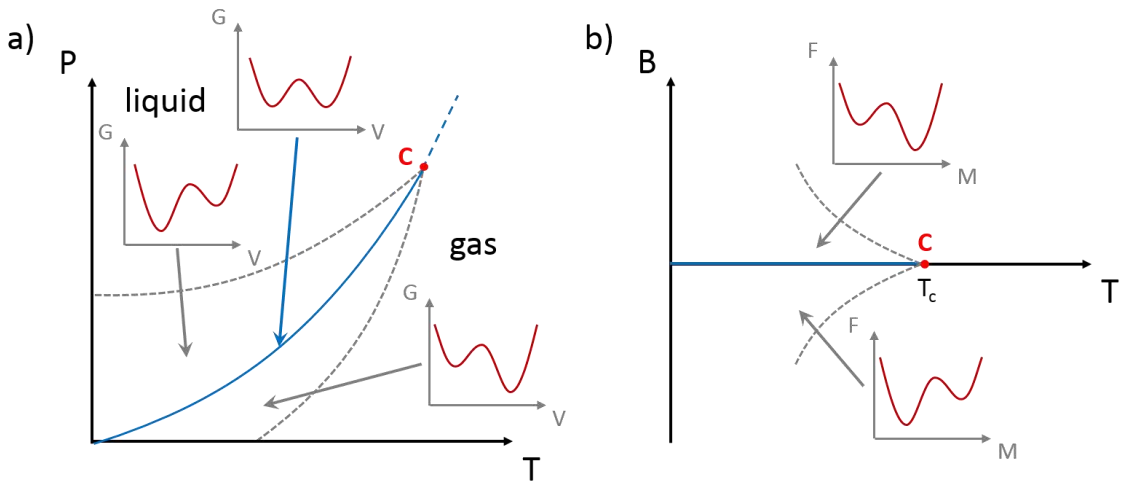


*Figure 2: a) Scheme of the phase diagram for the liquid-gas transition, with representation of the thermodynamical potential (Gibbs free energy G) versus volume V as an internal parameter, for the different regions of the diagram. b) Scheme of the ferromagnetic-to-paramagnetic transition, with representation of the thermodynamical potential (Helmholtz energy F) versus magnetization M as an internal parameter, for the different regions of the diagram.*

Second-order phase transitions present a continuous evolution of these physical quantities associated to first-order derivatives. Thus, in contrast with first-order phase transitions, they do not involve any latent heat. Second-order phase transitions exhibit singularity, discontinuity and more generally divergence, in the behavior of physical quantities associated to second derivatives, such as heat capacity or magnetic susceptibility. An example of second-order phase transition is the ferromagnetic to paramagnetic phase transition at zero field in iron. However, the vertical crossing of the blue transition line below (Figure 2b) by varying the magnetic field (from negative to positive) is a first-order phase transition (magnetization jump and hysteresis) .

#### *I.1.a.iv. Notion of cooperativity*

The microscopic origin of a phase transition results from cooperative interactions between the microscopic components (electrons, spins, normal modes, …) building the macroscopic crystalline system. The description of the system can thus not be realized considering independent particles, and the Hamiltonian of the system differs from the sum over all individual Hamiltonians of the particles making the system up.
Taking the interactions between particles into account is in general very challenging and, in most cases, the obtained model cannot be solved analytically, even in the case of the famous Ising model (in 3 dimensions). Hence, the common approach consists in defining a mean field approximation, to describe the effect of the average environment of each particle, considered in its average state. Thus, the hypothesis of molecular field introduced by Pierre Weiss to explain the main features of the para-ferromagnetic phase [Weiss1907] is based on the idea of cooperative positive feedback from the medium, to reinforce the magnetization, spontaneously or under the effect of a magnetic field. In the same way, the van der Waals model of a fluid constitutes a mean field approach of the gas-liquid phase transition.

### I.1.b. Symmetry considerations

### *I.1.b.i. The order parameter*

In 1937, Lev Landau proposed a universal approach of phase transitions, based on symmetry change, more precisely in the case where group-subgroup relationship exists between the two phases, as observed in numerous (anti)ferromagnetic, ferroelectric, ferroelastic and other types of materials [Landau1937]. A symmetry "breaks" when the structure loses some of its symmetry elements and converts into a structure with a smaller set of its symmetry elements [Levanyuk2020]. Landau's significant contribution was to define the concept of order parameter, to describe the loss of symmetry elements between the two phases. The order parameter is associated with the relevant irreducible representation of the high symmetry group, which describes the observed symmetry lowering. This symmetry change corresponds to a spontaneous symmetry breaking, in the sense that it occurs without any external field , but only by the effect of symmetry-preserving control parameters, such as temperature and pressure. Different equally low-symmetry macroscopic states, for instance for a ferromagnetic material the two magnetization states + and −, are equally stable. Actually, a high energy barrier separates these two macroscopic states, and the system is not able to explore the totality of the configuration space within the observation time scale. It therefore stabilizes in only one of these two states. This is a key characteristic of symmetry breaking. In other words, on the contrary to what happens in the high-symmetry state, the symmetry of the observed macroscopic state is lower than the allowed symmetry of the Hamiltonian. However, in most cases a micro-structuration in domains at long-range scale (+ and − ) is observed.

The order parameter represents a measure of the degree of symmetry breaking in the low-symmetry phase, while it becomes zero in the high-symmetry phase. Actually, the term "symmetry-breaking parameter" would be more suited, since the high-symmetry phase is not necessarily the one of higher entropy (more disordered), and may be also applied for quantum phase transition at zero temperature ($\Delta = 0$). Typical evolution of the order parameter is shown in Figure 3, in the simplest case where the symmetry breaking occurs between two spontaneous states corresponding to + and −. It is the case in many ferromagnetic or ferroelectric systems, for instance. Generally, at zero field the low-symmetry state is structured in domains, respectively associated to these two energetically equivalent spontaneous states.

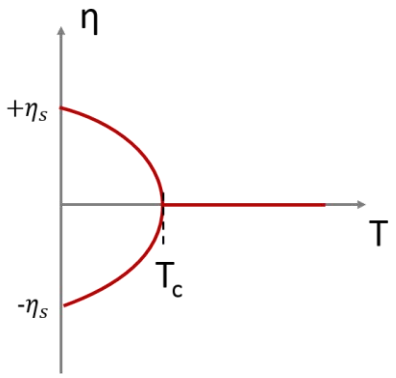


*Figure 3: Symmetry breaking observed on the order parameter η, showing discontinuity at the critical temperature $T_c$.*

Another Landau contribution was to propose an analytical expansion of the incomplete thermodynamical potential in power of , to determine the evolution of measurable physical properties around the transition temperature $T_C$. In the simplest situation as above, the potential must reproduce the symmetry between + and −, *i.e.* $\Phi(\ ) = \Phi(-\ )$. Therefore, all odd terms of the development cancel, such that:

$$\Phi(\ ) = \Phi(0) - H\eta + \frac{1}{2}\ ^2 + \frac{1}{4}\ ^4 + \frac{1}{6}\ ^6 + \cdots$$

The term is the symmetry breaking field conjugated to . As stated above, spontaneous symmetry breaking takes place for $= 0$. The coefficient is chosen such that $= (\ -\ )$ and $> 0$, so that the state $= 0$ becomes unstable below (critical temperature). Other coefficients are constant. The development may be stopped when it is possible to obtain minima in the potential landscape of $\Phi(\ )$, which requires a positive higher power term:

- $> 0$: the development is limited to the power 4
- $< 0$ and $> 0$: the development stops at power 6.

The above Landau description considers that the system is homogeneous in space. Its extension to the so-called Ginzburg-Landau theory allows taking into account the non-uniformity of the order parameter [Levanyuk2020]. It is characterized by a function $(\vec{\ })$, which is supposed to vary on a length scale larger than the microscopic scale (coarse graining). This approach is not only famous for this application to superconducting properties, but it allows treating different inhomogeneities, such as the effect of pre-transitional spatial fluctuations near the critical point (critical phenomena). Indeed, correlated regions develop on approaching the transition, defining a correlation length. This Ginzburg-Landau approach may also describe other inhomogeneities such as domain wall, which is the transition zone between two domains, associated to $+$ and $-$ respectively.

### *I.1.b.ii. First- and second-order phase transitions regarding symmetry breaking*

The temperature evolution of the order parameter presented in Figure 3 is continuous on approaching the critical temperature . This situation corresponds to a second order phase transition. From the expansion of the Landau potential, it is easy to show that the first order derivative of $\Phi$ at equilibrium does not present any discontinuity at , but a singularity in the heat capacity can be reproduced, as well as a divergence of the susceptibility associated to the order parameter.

Within Landau's description frame, it is also possible to describe the situations presenting, at the temperature of transition, a discontinuity of the order parameter (jumping from zero to finite value). In this case, entropy and volume may also present a discontinuity and the phase transition is first-order. Both phases of low and high symmetries coexist around the temperature of transition, in a bistable regime. This bistable region spans a certain temperature range, leading to a thermal hysteresis in the order parameter evolution (Figure 4) [Agarwal1981]. This situation of first-order transition occurs when the coefficient discussed above is negative, which requires pushing the Landau development up to sixth order. In this case, the transition temperature is characterized by equal stability between the high-symmetry phase ( $= 0$) and the two low symmetry phases ($+$ and $-$ ). Another situation is linked to the occurrence of a term at power 3 in the Landau development for more complex symmetry breaking, as we will discuss later for the ferroelastic transition in $V_2O_3$ (Chapter IV).

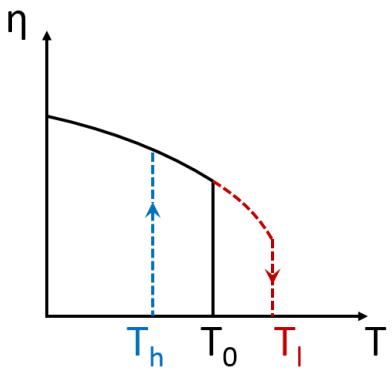


*Figure 4: Evolution of the order parameter versus temperature, in the case of a transition showing hysteresis. $T_h$ is the limit temperature determining the existence of high-symmetry phase; $T_l$ is the limit temperature for the low-symmetry phase and $T_0$ the temperature of transition.*

### I.1.c. Isostructural phase transitions: when no symmetry breaking occurs

In the solid state, some phase transitions exist, which are not accompanied by any change of symmetry, similarly with the liquid-gas phase transition. These transitions are called isostructural. Actually, the term "isostructural" is quite misleading, since it suggests that no structural change occurs at the transition, whereas it is rarely the case. The word "isosymmetric" would have been more appropriate, but we will stick to the historical designation in the following. This situation has to be distinguished from reconstructive phase transitions, characterized by a change in symmetry, but without group-subgroup relationship, and requiring a reconstruction of the crystalline structure, as in the graphite-diamond transition.

These previously introduced isostructural phase transition are first-order, with a jump of entropy and volume (or density) when crossing the transition line in the (P,T) phase diagram. This transition line ends to a critical point (Figure 1), beyond which the system enters a "crossover" regime (supercritical). In this crossover region, no phase transition but continuous evolution of internal variables with some inflexion along the extension of transition line (Widom line) takes place [Luo2014]. Typical examples of isostructural phase transitions in the solid state are the spin transition in spin-crossover materials [Tissot2011, Ridier2017] or the Mott transition [McWhan1970, Kagawa2004], which show significant volume jumps.

Currently, the physical aspects of isostructural phase transitions are not very well known and understood, compared with the description of symmetry breaking transitions. Isostructural transitions are therefore generally absent of textbooks. Actually, since no symmetry breaking occurs in these systems, the Landau's theory cannot be applied strictly speaking and every macroscopic internal variable concerned by the transition is by nature fully symmetric. However, comparing the phase diagrams of the liquid-gas transition and of the magnetic transition (Figure 2b), one can notice deep analogies in their thermodynamical behavior [Stanley1971]. The crossing of the first-order transition line in the (P,T) plane is indeed equivalent to the crossing of the horizontal first-order transition line ( $= 0$) separating the two energetically equivalent macroscopic states, with a jump between both opposite spontaneous magnetization $+$ and $-$ . In the same way, inducing the ferromagnetic-to-paramagnetic phase transition by the increase of temperature above the critical temperature amounts to follow the liquid-gas system along the transition line, then Widom line above the critical point. The major difference between these systems comes from the intrinsic symmetry in the magnetic case, absent in the isostructural liquid-gas one.

It is worth noticing that pressure and temperature are symmetry-conserving control parameter, while the magnetic field breaks the symmetry. To describe the isostructural transitions, it may be useful to introduce a new coordinate system (A', H'), where A' corresponds to the inverse of the susceptibility and is tangent to the transition line and H' perpendicular (Figure 5a). Both of them are functions of pressure P and temperature T. In this configuration, a generalized totally symmetrical order parameter can be defined, measuring the difference with the state observed at the critical point, for instance using density ( − ) for the liquid-gas transition. This parameter follows the evolution of every relevant fully symmetric internal variable around the critical point, in particular when crossing the transition line, in an analogy with magnetic transitions. The Landau expansion in power series for the Gibbs free energy may be written:

$$= {}_0 - {}' + \frac{1}{2} {}'^2 + \frac{1}{4} {}^4 + \cdots$$

It might be surprising at first that no term of power 3 appears. Actually, it has been shown that such terms can be eliminated by convenient substitution [Yu2003, Chernyshov2004]. In other words, on the transition line, close to the critical point, the evolution is almost symmetrical between + and − (Figure 5b).

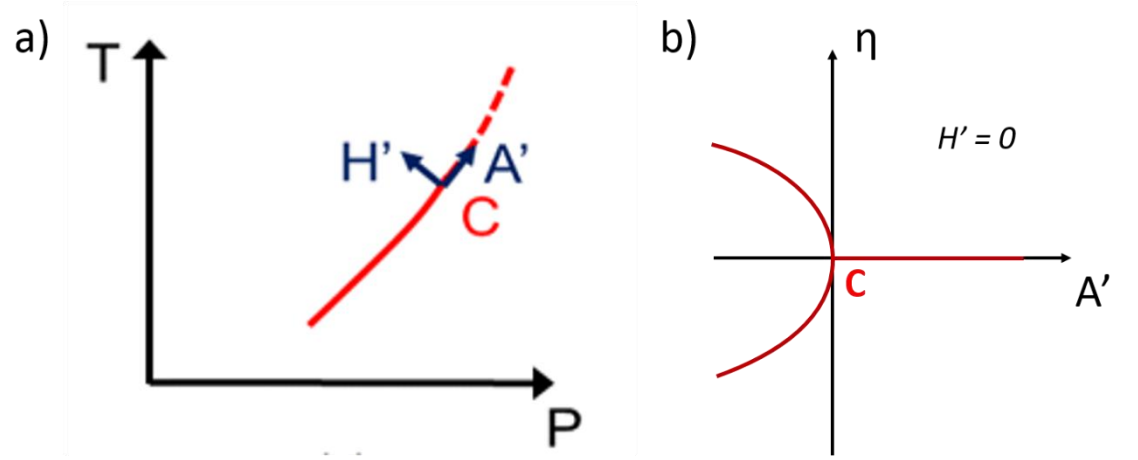


*Figure 5: a) Phase diagram showing the new set of coordinates (A',H'), derived from (T,P). C indicates the critical point. b) Symmetry breaking observed on the order parameter η, showing discontinuity at the critical point. In the vicinity of C, the distribution of is practically symmetric for ' = 0.*

## I.2. Photo-induced phase transitions

Beyond phase transitions of a material at thermal equilibrium, performed by varying macroscopic external static control parameters (temperature, pressure, electric or magnetic fields, …), the field of light-driven phase transitions emerges, bringing the system far away from equilibrium.

### I.2.a. Photo-steady phase transitions

Using light, phase transitions can be performed under continuous irradiation. This phenomenon can be encountered in spin-crossover [Bousseksou2011], cyano-bridged metal [Azzolina2019], metal oxide [Ohkoshi2010] and even biochemical [Sollogoub2008] systems. These materials can exhibit light-driven bistability between two macroscopic steady states. In the case of continuous laser irradiation, the energy from the photon flux competes with energy dissipation in the thermal bath. Multistability originates from positive feedback mechanisms due to cooperative interactions in the system between photo-excited species [Desaix1998]. This type of switching also occurs in the case of current-induced resistance switching phenomena [Janod2015]. The description of

these phenomena is based on nonlinear dynamics approach and bifurcation theory [Strogatz2014]. It presents similarities with the Landau analysis, showing a deep analogy with phase transitions at thermal equilibrium.

### I.2.b. Out-of-equilibrium phase transitions induced by ultrashort light pulses

Over the last century, technologic and instrumental developments unlocked the access to observation and control of matter at relevant time and length scales [Fleming2008]. Ultrafast photo-induced transformations may therefore be triggered by intense, ultrashort light pulses. This emerging field stands at the intersection between diverse domains, such as out-of-equilibrium phenomena, coherence and quantum control, complex correlations and nonlinear responsiveness, as well as interconversion of energy and information. For instance, femtochemistry which was granted with the Nobel prize in 1999 [Zewail1994], consists in promoting a molecule in an excited state by ultrashort laser irradiation. This induces a change in the interatomic potential and determines the motion of the atomic wavepacket prepared by the laser pulse. These changes may drive significant effects, such as the breaking of bonds and the subsequent transformation from transient states, illustrating the new ability to decide the outcome of a chemical reaction, through the control of transformation pathway. Since then, more developments broadened the field of phase transitions induced by a light pulse, so-called photo-induced phase transitions, towards a new electronic and/or structural order. This is associated with drastic switching of the material properties, for instance driving the transition between nonmagnetic and magnetic states in spin-crossover materials, or from insulator to metal in $V_2O_3$. The field has been rapidly emerging and developing, supported by the elaboration of new theoretical concepts [Nasu2004, Yonemitsu2008], elaborated pump-probe experiments and the advent of new experimental tools, such as time-resolved x-ray and electron diffractions, or time- and angle-resolved photoelectron spectroscopy.

Ultrafast photo-induced phase transitions represent a new way for triggering material functionalities, by acting through highly excited electronic states upon quasi-simultaneous absorption of many photons, rather than by modifying the ground state through the change of external static control parameters. The description of these phenomena requires building new conceptual tools, going beyond the concept of thermodynamic equilibrium. The explored systems are diverse and there exists a wide variety of experimental results, which often present contradictory physical pictures. Hence, the universality of the description of photo-induced phenomena is probably less developed than for phase transitions at equilibrium. The multiscale nature, inherent to photo-induced phase transitions, and this new kind of non-linear and non-equilibrium physics adds a degree of complexity. It is therefore needed to extend existing approach to this new regime and to reconsider concepts.

### I.2.c. From excitation to relaxation, different time scales to describe multi-step processes

In the case of photo-irradiation by an ultrashort laser pulse, the photo-induced processes are fundamentally different from a continuous photo-excitation. Since the laser pulse may contain a macroscopic number of photons, i.e. a significant number with respect to the number of potentially photo-excited species, the irradiated system is initially prepared in a highly electronically excited state, far away from equilibrium. Following this ultrashort photo-excitation, macroscopic internal variables, such as magnetization, polarization, ferroelastic deformation and volume, will evolve. The external control parameters, such as pressure and temperature, remain fixed, but the material is not at equilibrium with its environment, neither mechanically, nor

thermally. Another major difference compared with experimental observation of thermodynamic state, is that the evolution of microscopic internal variables, related to degrees of freedom of various nature, may be monitored in unprecedented way by pump-probe measurements. Additionally, some coherent dynamics may emerge in the dynamics of internal variables, which is fundamentally different from thermal processes. A typical well-known example is the generation of coherent optical phonons, where atoms oscillate in-phase around a new displaced position [Hase1996, Lindenberg2000].

During dynamical evolution following the strong laser pulse impact, the photo-excited system can then transform through multistep non-thermal or thermal processes towards another macroscopic electronic and/or structural state. Indeed, the description of the different degrees of freedom of a material requires to consider different subsystems of different nature, playing their part on significantly different time and length scales, from fast electrons to slower atoms or molecules, and finally propagative and diffusive processes at longer length scale. Intrinsically to this multiscale nature, during the motion of fast degrees of freedom, slower ones can be considered as frozen, while they will further act by their quantum or statistical average on the motion of slower ones. Therefore, no unique dynamical description and potential energy picture are valid at every time scale. This multi-step character can lead to a decoupling in time of the processes related to different degrees of freedom, and the possibility of bottlenecks during the evolution of the system, with a sequence of partial equilibriums.

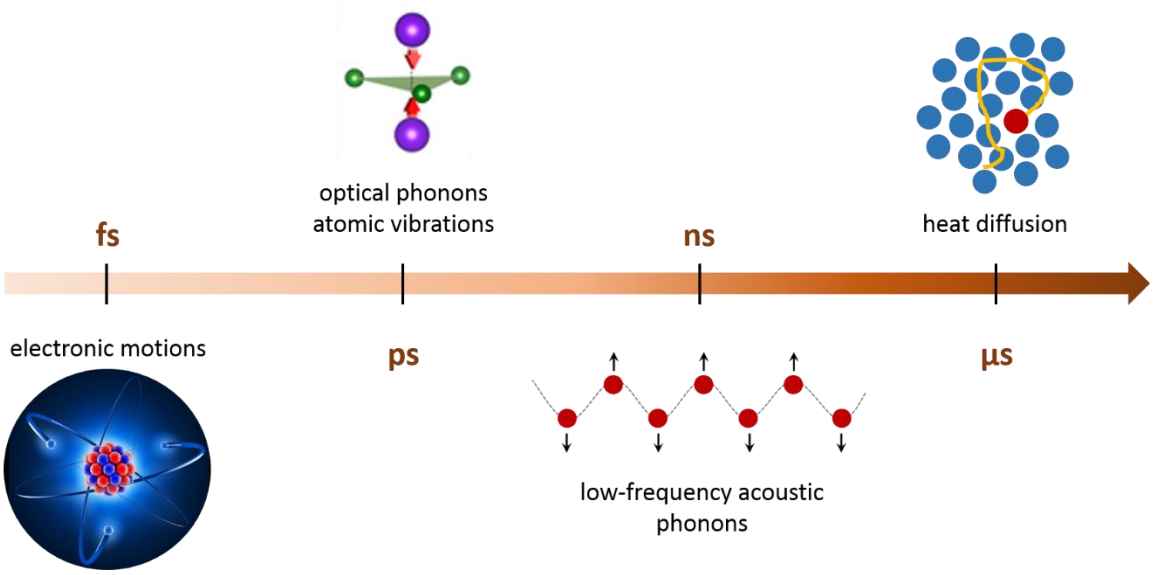


*Figure 6: Different time scales correspond to different elements constitutive of a material. The arrow points towards long time scale.*

Thus, several time scales have to be distinguished, reflecting the different degrees of freedom inherent to the solid state. Main features can be summarized as in the following:

- Electrons are light particles. Consequently, the distribution of photo-excited electrons-holes in a semiconductor or insulator is reorganized on an ultrafast time scale. Thus, electrons can thermalize quickly through electron-electron collisions in their respective conduction and valence energy bands, reaching proper intra-band thermal equilibrium in less than 100 femtoseconds (fs) (Figure 6) and defining electronic and hole temperatures, which may reach few 1000 K. However, this electronic thermalization remains local and the distribution of electronic temperature is therefore inhomogeneous regarding a finite penetration depth of light in the material. On the other hand, localized electron excitation, for instance self-trapped in

a molecule [Hauser2004], is rather different and no thermalization between the electronic states of different molecules occurs on this ultra-short time scale, thus preventing from defining an electronic temperature.

- Atoms, significantly heavier than electrons, show slower motion. For low-frequency coherent optical phonons, the time scale is determined by the period of atomic oscillations, of the order of hundreds of fs. After a few oscillations, atoms stabilize in the new displaced positions (Figure 6). Additionally, during the intra-band electronic relaxation, incoherent emission of phonons may take place, yielding to the heating of the initially cold lattice. However, reaching complete thermalization between the different acoustic and optical phonons requires phonon-phonon interactions, leading to the establishment of a local lattice thermalization on a typical time scale about 10 of picoseconds (ps). Further complete thermalization between electronic and lattice degrees of freedom implies electron-hole recombination and takes place over longer time scale.
- On a larger length and time scales, the expansion (or contraction) of the volume of the material occurs, witnessing the establishment of mechanical equilibrium with the environment. Indeed, the inhomogeneous distribution of photo-excited electrons leads to inhomogeneous distribution of internal stresses in disequilibrium with external pressure, even after electronic and lattice thermalization took place. Due to the long-range nature of elastic interactions, volume expansion requires a concerted deformation of unit cells, through the generation of tensile strain waves. This collective phenomenon is driven by acoustic phonons and its propagation is governed by the speed of sound. Considering a propagation over 100 nm to a few micrometer (µm) (from oxide to molecular materials), the acoustic time scale $\tau_{ac}$ lies from a 10 ps to the nanosecond (ns) (Figure 6). Similar situation occurs for the generation of shear strain wave in ferroelastic materials, however on smaller time scale due to the smaller length scale introduced by domain size.
- In the situation where the transition occurs between two molecular configurations, such as in spin-crossover materials, the internal dynamical evolution at molecular scale is governed by an activation energy , which value directly relates to the transition rate [Hauser1986]. Typical values are of the order of several , thermal equilibrium with the lattice is usually reached from 10 ns to the microsecond (µs) time scale or even later.
- Depending on the material morphology, longer time scales come at play. Actually, the finite effect of laser penetration depth induces a temperature (volume strain) gradient inside the material. Thermal (and volume) homogeneity is governed by thermal diffusivity, the latter being of the order of $10^{-6}$ $m^2.s^{-1}$ (Figure 6). For samples reaching a size of several µm, this leads to dynamics reaching 100 µs.
- Finally, the recovery of the initial state by relaxation towards equilibrium with the environment is dictated by both heat capacity of the sample and its heat exchange coefficient at the surface. The relaxation time of micron-sized sample lies in the microsecond-millisecond (ms) range.

The different steps described above are not exhaustive. More diversity is observed, depending on the nature and morphology of the studied material.

In summary, processes for ultrafast photo-induced phase transformations in materials take place far away from equilibrium. They are multiscale by nature and mainly non-thermal. This multiscale character raises several challenges, both in experimental and theoretical research, about the control of the transformation pathway from atomic to macroscopic scale. A particular case is the

non-linearity, intrinsic to every cooperative feedback, at the origin of phase transition at macroscopic scale. Within the work presented in this manuscript, we would like to focus on the role of volume effects to shed new light on this field.

## I.3. Volume effects in the phase transition processes

Among the different parameters coming at play in phase transitions dynamics, volume change is by nature a fully symmetric (non-symmetry breaking) parameter. Indeed, volume is a macroscopic quantity, which fulfills all symmetry elements of the point group of the high-symmetry phase (identity representation). Actually, a pure volume deformation occurring in a crystalline system does not modify the symmetry of the latter. Thermal dilation or compression under hydrostatic isotropic pressure for instance, preserve the crystalline class and consequently the form of the deformation tensor. However, crystalline symmetry can break under application of a distortion, for example in the case of ferroelastic transitions. In this situation, the deformation tensor can be split in two parts: one describing the purely symmetric volume change and the second one related to ferroelastic distortion inducing symmetry breaking. It must be underlined that volume symmetry differs from the one of order parameter describing a symmetry breaking. This is not the case in isostructural phase transitions, where the order parameter is totally symmetric.
Volume is the internal variable conjugated to pressure, the latter being in general an external control parameter. Volume can fluctuate freely and evolve if external conditions are changed or if the system is prepared in a non-equilibrium state.
A key effect of volume change in phase transitions, is to induce a better stabilization of the new formed phase. This is true for both phase transitions at thermal equilibrium and ultrafast photo-induced phase transitions. This volume effect is particularly significant in the case of large volume changing materials.

### I.3.a. Volume effect at thermal equilibrium

For a first-order phase transition, the slope of the transition line (coexistence line) is directly determined by the volume jump Δ and the entropy jump Δ (latent heat), through the well-known Clapeyron relation dT/dP = ΔV/ΔS. This is a first general expression of volume effect, only originating from thermodynamics.

#### *I.3.a.i. General case: when symmetry breaking occurs*

The relevant thermodynamic potential to describe the phase transition is the Gibbs free energy ( , ), where the volume is an internal variable. An additional external parameter is the field conjugated to the order parameter , but its value is zero for a spontaneous symmetry breaking. Since every term in the Landau expansion has to be symmetric (cf part I.1.b.i of this chapter), in the simplest situation of a scalar order parameter, the coupling term Δ between the volume strain = Δ / , fully symmetric, and the order parameter , which describes the loss of symmetry, is linear-quadratic ( symmetric x $^2$ symmetric) at the lowest order. Adding the cost in elastic energy Δ $_{el} = \frac{1}{2}$ $^2$, one gets:

$$= {}_0 + \frac{1}{2}\,{}^2 + \frac{1}{4}\,{}^4 + \alpha\varepsilon\,{}^2 + \frac{1}{2}\,{}^2$$

With a constant coefficient. The condition to determine the equilibrium state generates two coupled equations:

$$\partial G/\partial\eta = A\eta + {}^3 + \alpha\varepsilon\eta = 0$$

$$\partial G/\partial \varepsilon = \frac{1}{2}\ ^2 + K\varepsilon = 0$$

which leads to $= -\ ^2$. Therefore, a spontaneous strain appears only in the low-symmetry phase, proportional to the square of the order parameter. At equilibrium, the sum of the coupling energy and elastic energy is necessarily negative:

$$\Delta\ + \Delta_{el} = -\ ^2\ ^2 + \frac{1}{2}\ ^2\ ^2 = -\frac{1}{2}\ ^2\ ^2 < 0$$

Therefore, the effect of volume strain induces an energy gain (Figure 7), leading to better stabilization of the system.

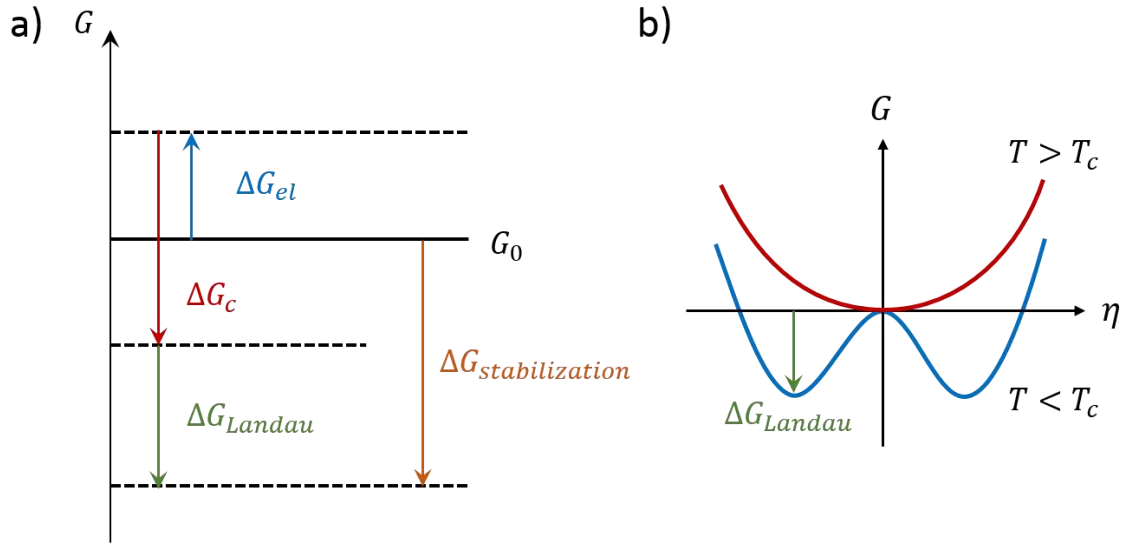


*Figure 7: a) Schematic energy diagram showing the contribution of each term of the Gibbs energy. b) Δ $_{nd}$ $= \frac{1}{2}\ ^2 + \frac{1}{4}\ ^4$ is the energy gain in the low symmetry phase, when the system stabilizes in one of the two equivalent states $+$ or $-$. a) The combined effect of $\Delta G_{el}$ and $\Delta G$ leads to an additional energy gain, increasing the total energy gain $\Delta G_{sta\ iliz\ io}$.*

In the first equation, replacing by $-\ ^2$ allows introducing $^* = -\frac{1}{2}\ ^2/$ in the equilibrium equation. If the coupling is strong enough to induce $^* < 0$, the solution becomes negative. In this case, the correct description of the system requires adding a sixth degree term to recover a stable solution, leading to the renormalized form of the Landau expansion:

$$= {}_0 + \frac{1}{2}\ ^2 + \frac{1}{4}\ ^* {}^4 + \frac{1}{6}\ ^6$$

As discussed in part I.1.b.i., this drives the transition first-order type, with the possibility of thermal hysteresis.

### *I.3.a.ii. Isostructural phase transitions*

In the case of an isostructural phase transition, both the generalized order parameter and the volume strain $= \Delta\ /$ are fully symmetric. Therefore, all terms in the power series development in are allowed, and the $-$ coupling of lowest order becomes bi-linear:

$$= {}_0 - \ ' + \frac{1}{2}\ '\ ^2 + \frac{1}{4}\ ^4 + \alpha\varepsilon\eta + \frac{1}{2}\ ^2$$

The equilibrium condition for leads to a linear relation between the two internal variables $= -\alpha\eta/$. Similar stabilization energy gain as for a symmetry-breaking transition is obtained, with an absolute value of Δ equal to half of the elastic energy cost Δ $_{el}$. However, it is now to the quadratic term to be renormalized $^* = \ ' - \ ^2/$ :

$$= {}_0 - \ ' + \frac{1}{2}\ ^*\ ^2 + \frac{1}{4}\ ^4$$

$^*$ value is decreased compared to $'$, which subsequently changes the position of the critical point.

### *I.3.a.iii. Non-linear elasticity*

It is well known that the response to an external magnetic field ( ) for a ferromagnetic system is strongly non-linear when crossing the first order line below the critical temperature (magnetic hysteresis), but also above, close to the critical point. In the simplest approach, this system can be described in terms of the "molecular field" of Weiss, which introduces cooperative feedback.
This approach applies to first order phase transitions, where the symmetry group is the same on each side of the coexistence line. Hence, this situation is similar to the case of an isostructural phase transition. This analogy is nicely illustrated by the experimental results presented by Gati et al. for a Mott transition in an organic conductor [Gati2016]. In this compound (κ-(BEDT-TTF)$_2$Cu[N(CN)$_2$]Cl), they show the breakdown of the Hooke's law, i.e. in the volume response versus pressure becomes non-linear, as the external temperature is varied around the critical point (Figure 8). In this context, we may speak about non-linear elasticity.

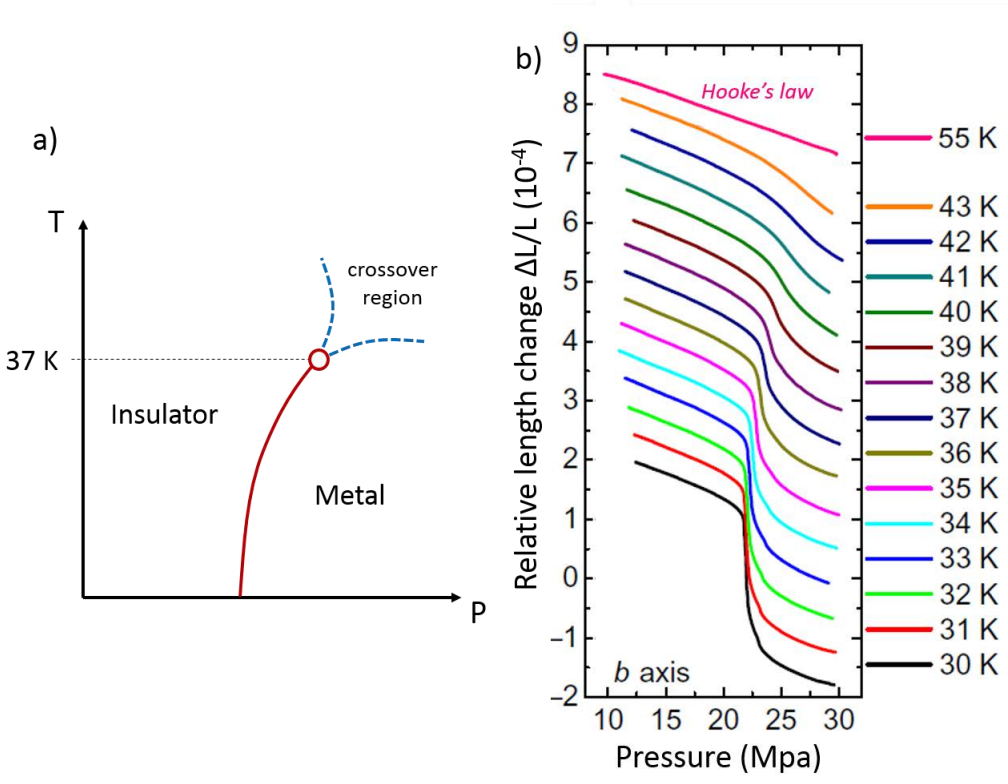


*Figure 8: Adapted from [Gati2016]. a) Generic phase diagram of organic Mott insulator system κ-(BEDT-TTF)$_2$Cu[N(CN)$_2$]Cl. Red solid line represents the 1$^{st}$-order transition line that ends in a critical point (open red circle). Blue dotted lines represent the predicted crossover lines. b) Strain along the crystalline b axis versus pressure, measured for different temperatures across the transition line shown in (a). Below the critical point, Hooke's law breaks down and volume versus pressure becomes non-linear.*

In chapter III of this manuscript, we will present the study of photo-induced transformation in spin crossover molecular crystals, which show similar phase diagram (Figure 9) as κ-(BEDT-TTF)$_2$Cu[N(CN)$_2$]Cl. In this type of compounds, low spin-low volume molecules undergo an isostructural transition to high spin-high volume molecules. Volume expansion triggered by the spin state switching acts as a negative chemical pressure to pull on the low-spin molecules. This tensile force favors their switching to the high-spin state. A simple picture to describe cooperative

elastic feedback effect occurring after photo-excitation in this compound would be that "the more high spin molecules, the higher volume, the more high spin molecules, …". However, this description remains intuitive, and it is still a long way to roam to a quantitative description…

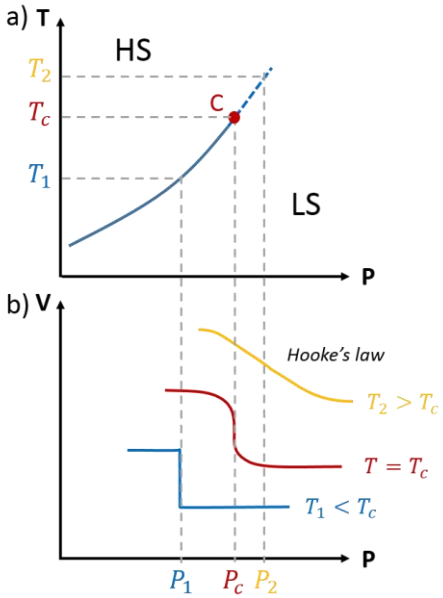


*Figure 9: a) Schematic phase diagram of a spin-crossover molecular crystal. b) Schematic strain along the crystalline b axis versus pressure, measured for different temperatures across the transition line shown in (a). Below the critical point, Hooke's law breaks down and volume versus pressure becomes non-linear.*

## I.3.b. Role of volume in ultrafast photo-induced phase transitions

In the case of ultrafast photo-induced phase transitions, an ultrashort light pulse prepares the system in a far-from-equilibrium state, where many electrons have been photo-excited. Following photo-excitation, the driving forces governing the evolution from the initial strongly excited electronic state naturally lead the system towards more stable states. By nature, this stabilization proceeds through several steps. First, in-phase coherent atomic oscillations of relevant optical modes are generated around more stable intra-cell atomic positions. These coherent phonon precursor processes have been extensively reported in many materials [Hase2003, Singer2018, Borroni2020]. These precursor effects represent the counterpart of pre-transitional phenomena occurring in static phase transitions. Often neglected, the role of volume change, to stabilize the macroscopic photo-induced state, is central. Indeed, the excited electronic state needs to be stabilized in a different volume, eventually reaching the one of the new phase. This process is slower than precursor atomic reorganization, and develops on acoustic time scale.

"*The (elastic) force is the only interaction known which is truly infinitely range … and necessarily attractive*" J. Friedel (1954). Long-range nature of elastic interactions justifies the mean-field approach at thermal equilibrium and thus the use of Landau's theory. For a light pulse-driven process, the mean-field picture implies that cell deformations do not process independently from cell to cell, but rather proceed through coherent propagation of strain waves. Long-wavelength acoustic phonon modes manage the recovery of mechanical equilibrium with the environment. This is well established in the case of thermal expansion induced by the ultrafast drop of thermal energy by a light pulse [Thomsen1986].

## I.3.c. Light-induced strain wave propagation

### *I.3.c.i. Origins of photo-induced stress*

As discussed in part 2.c. of this chapter, consequently to the pump laser hitting the sample, photo-excited electrons generate internal stresses through different structural and/or electronic mechanisms [Thomsen1986, Wright 1994, Ruello2015, Reid2018].
The most discussed mechanism so far is the thermo-elastic one, in which thermal stresses come out for the lattice heating by incoherent energy transfer between photo-excited electrons and phonons, modifying the phonon populations ($\vec{n}$). This process is involved in the laser-induced thermal expansion of metals, where generally this lattice heating takes place at ultrashort time scale, compared with acoustic time.
In semiconductors and insulators, the electron-hole recombination occurs on much longer time scale. Therefore, once the laser pulse impacts the sample, a non-equilibrium electronic (hole) distribution is established, associated with the change in electronic populations ($\vec{n}$) and characterized by a high electronic (hole) temperature. This non-equilibrium distribution may subsist until acoustic time scale. This yields so-called electronic stresses, which may be tensile or compressive. In other words, the excited electronic distribution may finally lead to a volume expansion or contraction. This mechanism may be expected to be particularly efficient in the situation of an insulating-to-metal phase transition with large volume change, as in the case of $V_2O_3$ (Chapter IV) and $Ti_3O_5$ (Annex). Finally, we can mention the case of cooperative molecular switching in spin-crossover materials (chapter III). In this type of molecular materials, the photo-induced change from low-spin to high-spin state takes place at the molecular level and leads to a large intramolecular metal-ligand bond length expansion. The consequent swelling of the photo-excited molecule generates local stresses in its immediate surrounding [Spiering1982, Spiering2004]. The description of elastic stress in spin-crossover materials goes beyond the currently explored mechanisms, focused on metals and conventional semiconductors.

### *I.3.c.ii. Elastic model to describe strain wave propagation*

Stabilization of the photo-irradiated material in the volume required by the new thermal state and/or electronic distribution requires mechanical equilibrium with external pressure to be established. This equilibrium recovery proceeds through the coherent dynamics of strain waves, more precisely through the propagation of an acoustic pulse, as a superposition of longitudinal plane waves. At time zero, the photo-irradiated free surface exhibits a large stress gradient with external pressure, inducing the strain wave propagation from this surface into the material. Due to a finite penetration depth of light in the sample, the established stress distribution follows an exponential law along the propagation direction . The strain wave travels on a distance , within the acoustic time scale $_{ac} = \ / \ ,$ being the sound velocity.
A one-dimensional model is currently used to describe the propagation of this photo-induced strain wave in a semi-infinite elastically isotropic continuous medium [Thomsen1986, Matsuda2015]. The semi-infinite character is defined by the sample thickness $\gg$ (Figure 10a). This model was further extended by Schick et al. to thin film samples of thickness $<$ , for which acoustic time scale becomes reduced [Schick2014] (Figure 10b).

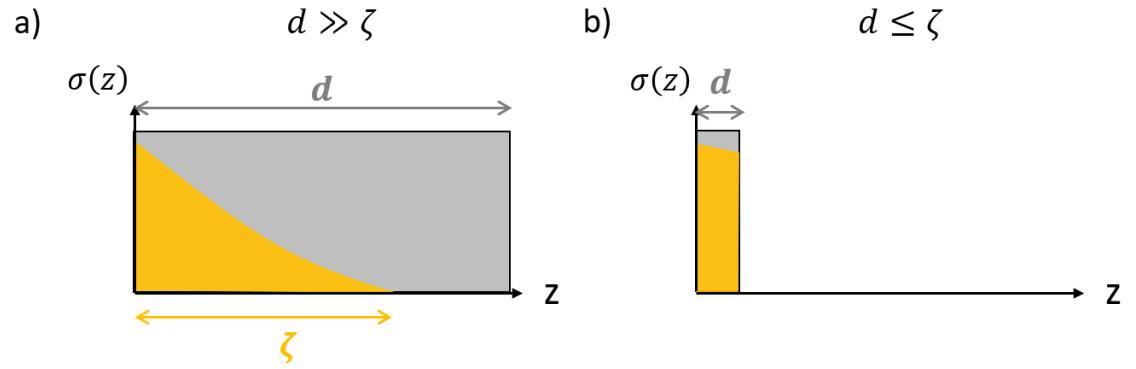


*Figure 10: Schematic propagation of laser light and therefore distribution of stress, for both semi-infinite sample ≫ (a) and thin film ≤ (b).*

This 1D description is based on the fact that, along the propagation direction ( > 0), only the tensor component of the longitudinal strain $_{zz}$ plays a significant role. Indeed, the laser spot size (≈ 100 µm) is much larger than the penetration depth or the thickness of thin film, which induces clamping for lateral expansion or contraction [Matsuda2015, VonReppert2018]. Therefore, the relation between the stress and strain at depth is given by:

$$( , ) = 3\frac{1-}{1+}B\eta( , ) + ( ,0)$$

where is the bulk modulus, the Poisson ratio and $( ,0) = (0,0)^{-/}$.
Elastic wave equations may be expressed in terms of the displacement in the direction ( , ) and the density of the material:

$$\frac{^2( , )}{\partial ^2} = \frac{\partial\sigma( , )}{\partial z}$$
$$( , ) = \frac{\partial u( , )}{\partial z}$$

Initial conditions set initial strain to be zero:

$$( ,0) = 0$$

and boundary conditions force the stress to be zero at the surface:

$$(0, ) = 0$$

After the propagation of the strain wave ( >> $_{ac}$), mechanical equilibrium is recovered:

$$( , ) = 0$$

The strain distribution in the mechanically stabilized state is such that:

$$3\frac{1-}{1+}B\eta( , ) = - ( ,0).$$

Figure 11 (from [Schick2014]) shows simulated time evolution of strain ( , ) for two very different values of the shape factor = /. We can observe the propagation of the stain wave and the mechanically stabilized strain remaining after the passage of the wave, for the two limit cases of a thin film ≪ 1 (Figure 11a) and semi-infinite medium ≫ 1 (Figure 11b).

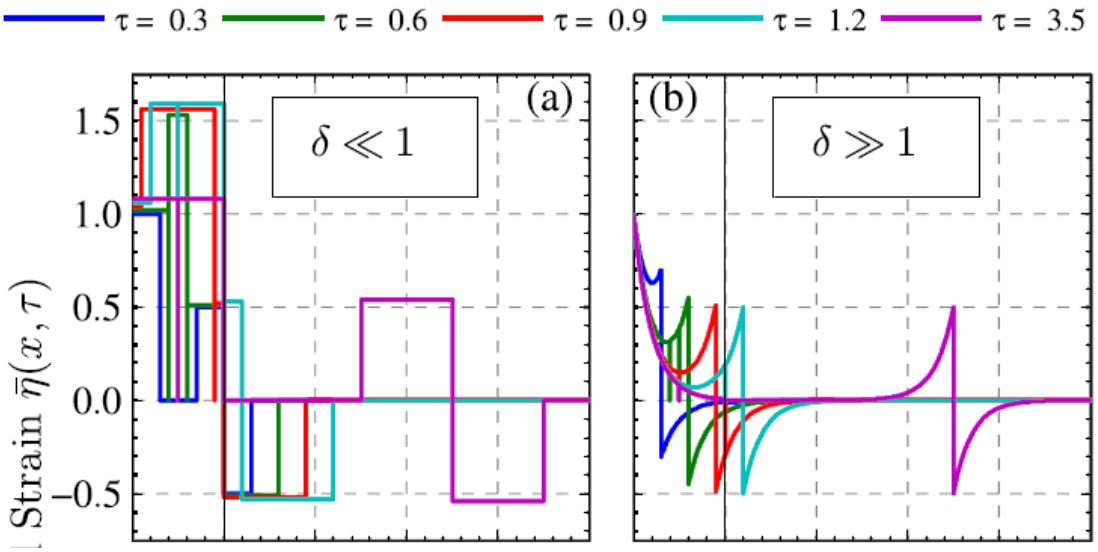


*Figure 11: from [Schick2014]. Simulated strain distribution at different delays after laser excitation, for an utra-thin film ≪ 1 (a) and a semi-infinite sample ≫ 1 (b). = / and = / are the normalized spatial and time coordinate, respectively.*

The 1D model introduced above will be used to rationalize experimental results presented in the following chapters, using several approximations to describe experimental conditions.

First, we consider instantaneous generation process of electronic or phononic internal stresses. This assumption seems reasonable for electronic stresses in semiconductor or insulator, and regarding structural reorganization at molecular scale for spin-crossover systems. However, lattice heating, for instance during intraband relaxation, may spread out over time. This effect is yet complicated to estimate (unsolved yet, to our knowledge), but can nonetheless be reduced choosing a pumping energy around the gap energy, therefore reducing the excess energy brought to the sample. It is also assumed in the model, that internal stress remains until the passage of strain wave, i.e. on the acoustic time scale. In $V_2O_3$ or $Ti_3O_5$ in particular, it is reasonable to consider even longer electron-hole recombination time.

Secondly, the lateral in-plane clamping for a continuous medium may be relaxed in case of a granular film ($V_2O_3$) or a pellet of nanocrystals ($Ti_3O_5$), opening the possibility of unconstrained volume change, which is a key factor for the establishment of a phase transition at macroscopic scale.

Finally, we remind that this model is only based on linear elasticity. Therefore, the study of the possibility to drive a phase transition at macroscopic scale, by coherent motions following a strain wave pathway (cf. I.3.a.iii), goes beyond the capacity of this model and remains a real challenge. Moreover, the situation might be very different depending on the stress origin. Actually, if this photo-induced phase transition involves only small atomic displacements (as it is the case for $V_2O_3$ and $Ti_3O_5$), it can be assumed to be completed at the same time as the propagation of the strain wave front. On the other hand, if the transition involves a relatively slow process, requiring significant activation energy (as in spin-crossover materials), this assumption is no more valid.

To date, few studies dug into elastic effects in phase transitions. The study of photo-induced phase transitions has mainly focused on one hand on the coherent optical phonon dynamics (displacive picture), often at the origin of precursor phenomena before a phase transition at macroscopic scale. On the other hand, studies were also performed on the role of coherent acoustic generation on thermo-elastic expansion and picosecond ultrasonics.

In the work presented in this manuscript, we investigated the role of long-range structural deformations associated with the ultrafast photo-induced phase transition, by performing time-resolved x-ray diffraction studies, allowing to monitor structural deformations and transformations occurring in volume-changing materials in real time. The experimental and analysis methods implemented for these experiments will be described in the next chapter (Chapter II). Chapter III reports the time-resolved structural investigation of a set of spin crossover microcrystals to explore size effects, while Chapter IV focuses on the photo-induced insulating-to-metal phase transition in a granular thin film of $V_2O_3$, a completely different type of material. A preprint of a publication on a pellet of $Ti_3O_5$ nanocrystals is also given in Annex.

# Chapter II. Experimental methods to access structural information in real time

From basic physics to material science, from chemistry to biology, x-ray techniques find applications in a wide range of scientific disciplines, allowing to access structural properties of materials. In this chapter, we describe the time-resolved powder x-ray diffraction technique and the related methods of analysis.
Time-resolved x-ray diffraction represents the dedicated tool to study transient structural changes occurring in a system undergoing a photo-induced phase transition. We used these techniques to perform studies on photo-excited volume-changing materials, described in the experimental chapters.

## II.1. Introduction: time-resolved x-ray diffraction as a tool to access structural information

### II.1.a. Principle of x-ray diffraction

X-ray diffraction is a powerful structural probe, therefore sensitive to any structural change occurring in a crystal.
In the following, we will detail the basic expression of x-ray diffraction. The latter connects Bragg peak intensities and positions on one hand, to unit cell parameters and atomic positions on the other hand.

Elastic scattering by crystals can usually be successfully addressed in the kinematical approximation, provided crystals are thin enough so that diffracted amplitude is much weaker than incident amplitude [Baruchel1993]. The assumption underpinning kinematical approximation, is that magnitude of the incident wave is the same at all points in the irradiated sample. Only the phase changes from point to point. This requires scattered amplitude to be small enough that it is negligible compared with incident wave amplitude, discarding energy conservation.
The diffracted amplitude is proportional to the Fourier transform $_0(\vec{\ })$ of the electronic density $(\vec{\ })$. The distribution of diffracted intensity in reciprocal space follows from the structure of $_0(\vec{\ })$ in the periodic arrangement of the crystal. The calculation is rather straightforward in a one-dimensional space, where the periodicity of the crystalline lattice can be described by the convolution of the pattern function by the Poisson distribution:

$$_{at\ ce}(\ ) = _{pa}\ \ (\ ) \times\ \ (\ )$$

with $(\ ) = \sum\ \ (\ - na)$ and the period of the lattice ( being an integer) and $_{pat}\ \ (\ )$ the electronic distribution within one unit cell. The Fourier transform of the Poisson distribution is also a Poisson distribution, of period $1/\ \ = \ ^*$:

$$FT[\ \ (\ )] = \tilde{}\ \ (\ ) = \ \ .\sum\ \ \ (\ - h\ ^*)$$

with $h$ an integer. Therefore, the Fourier transform of $_{at\ ce}(\ )$ is a set of Dirac distribution, with amplitude distribution defined by $FT[\ _{pa}\ \ (\ )]$.
In the three-dimensional space, one needs three basis vectors $\vec{\ }$, $\vec{\ }$, and $\vec{\ }$ to define the unit cell. From this description, one can define the basis vectors of the reciprocal lattice

$$\vec{a}^* = \frac{\vec{b}\times\vec{c}}{V}, \quad \vec{b}^* = \frac{\vec{c}\times\vec{a}}{V}, \quad \vec{c}^* = \frac{\vec{a}\times\vec{b}}{V}$$

with $V = \vec{a}.(\vec{b}\times\vec{c})$ the volume of the unit cell. These vectors verify the equations: $\vec{a}.\vec{a}^* = \vec{b}.\vec{b}^* = \vec{c}.\vec{c}^* = 2$ and $\vec{a}.\vec{b}^* = \vec{a}.\vec{c}^* = \vec{b}.\vec{a}^* = \vec{b}.\vec{c}^* = \vec{c}.\vec{a}^* = \vec{c}.\vec{b}^* = 0$.

$\vec{a}$, $\vec{b}$, and $\vec{c}$ are defined by their length a, b and c, which represent the unit cell parameters, and angles α, β, γ, which are the angles between $(\vec{b}, \vec{c})$, $(\vec{a}, \vec{c})$, $(\vec{a}, \vec{b})$ respectively.

Any reciprocal lattice vector can be written in the form $\vec{h} = h\vec{a}^* + k\vec{b}^* + l\vec{c}^*$. $\vec{h}$ is normal to the lattice planes with Miller indices $(hkl)$ of the direct space and the modulus $|\vec{h}| = 1/d_{hkl}$, $d_{hkl}$ being the distance between successive $(hkl)$ planes. Thus, the condition to observe non-zero scattered intensity from a periodic distribution of potential in space is $\vec{q} = \vec{q}_0 - \vec{q}_0 = \vec{h}$, known as the Laue's condition, with $\vec{q}_0$ and $\vec{q}$ the incident and outcoming wave vectors, respectively. Hence, the position of the nodes of the reciprocal lattice gives information about the periodicity of the electronic density $\rho(\vec{r})$, and thus of the crystal, but does not inform about what the unit cell contains.

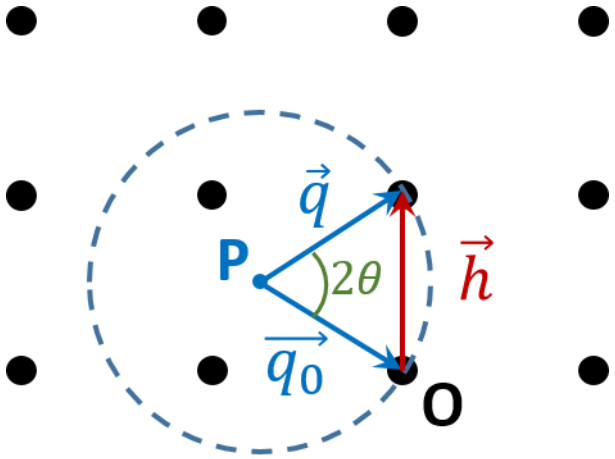


*Figure 12: 2D projection in the plane of the construction of the Ewald's sphere. $\vec{q}_0$ and $\vec{q}$ are the incident and outcoming wave vectors, respectively and $\vec{h}$ a reciprocal lattice vector.*

The assumption of elastic scattering means that no change in the wave vector amplitude is observed: $q = 2\sin\theta/\lambda = q_0$. This condition can be expressed geometrically with the Ewald's sphere construction (Figure 12):

- pick one node of the reciprocal lattice, which will be further designated as the origin O
- chose another point P, as the center of a sphere of radius $q_0$, going through O
- the diffracted wave vector must have its origin in P, its end on the sphere to satisfy $q = q_0$ and must fulfill the diffraction condition $\vec{q} = \vec{q}_0 + \vec{h}$. This means that the end of $\vec{q}$ must be on a node of the reciprocal lattice. $\vec{q}$ and $\vec{q}_0$ form an angle $2\theta$.

Therefore, diffracted intensity is observed only if the Ewald's sphere goes through both the origin O and another node: one says that the incident beam is Bragg-reflected by the lattice planes $(hkl)$. Bragg diffraction corresponds to coherent elastic scattering by a crystal, and the Bragg's law is defined such that:

$$2\pi q \sin 2\theta/2 = h \text{ or } 2d_{hkl}\sin 2\theta/2 = n\lambda.$$

If more than one node lies on the Ewald's sphere, multiple diffraction occurs, that we will not discuss further. Since crystal or not infinite but rather show a finite size, the Fourier transform of the potential is not composed of Dirac peaks, but can be described with a $inc()$ function, which gets broader as the crystal size decreases.

We stated above that, if the position of nodes in the reciprocal lattice informs about the periodicity of the crystal, it does not give more details about the content of the unit cell. However, x-rays are sensitive to electron density. In a crystal, this electronic density is periodic too and one can define a so-called structure factor $_h = \underset{cell}{FT}[\ _{at}\ \ (\ )]$:

$$_h = \sum_{=1} \ \ (\vec{h}).\ \ xp(2i\pi\vec{h}.\vec{\ \ })$$

With $(\vec{h})$ the atomic form factor for atom  at position $\vec{\ \ }$ in the unit cell, tabulated in the International Tables of Crystallography. Structure factor is a number, defined as the ratio of amplitude diffracted by one unit cell to that diffracted by one free electron placed at the origin. To take into account the incoherent atomic motions around equilibrium position (thermal phonon population), a correction is applied, in the form of the Debye-Waller factor $xp(-\ \ )$, with $= 8\ ^2\frac{\sin\ ^2}{\ ^2}\langle\ ^2\rangle$ and $\langle\ ^2\rangle$ the mean square displacement of atoms. $\langle\ ^2\rangle$ will increase with temperature and tends to be more important for light atoms. The Debye-Waller effect is proportional to $\sin\ ^2$ and consequently more significant for high diffraction angles (high-indices Bragg reflections). Finally, diffracted intensity writes:

$$_h = \ \ ^2\ _h|\ _h|^2\ \ xp(-2\ \ \ )$$

With

$h$: Miller indices of the diffracting atomic plane

 : Global scale factor depending on experimental conditions (incoming flux, absorption, polarization…)

 : Number of unit cells in the sample

$_h$: multiplicity for reflection $h$, corresponding to the number of symmetry-equivalent reflections contributing to the single observed peak

$_h$: structure factor for the reflection $h$

The information about the distribution of atoms within the unit cell is embedded in the structure factor, associated with the nodes of the reciprocal lattice, which govern the relative peaks intensities.

### II.1.b. Time-resolved x-ray diffraction

Time-resolved x-ray diffraction consists in measuring x-ray diffraction in real time, from a photo-excited crystalline sample. It makes use of the pump-probe measurement technique: an ultrashort laser pump pulse (fs-ps duration) excites the material under study, while a synchronized x-ray probe pulse is diffracted by the excited crystal and therefore shows the transient structural state. By varying the delay between the pump and probe pulses, in a stroboscopic way, one can reconstruct the overall structural dynamics [Cammarata2009]. In such technics, the time resolution cannot be better than the duration of the probe. Achieving resolutions in the range of ps or less requires the use of pulsed sources [Cammarata2009].

Since the end of the last century, the advent of intense pulsed x-ray sources allowed the development of ultrafast diffraction techniques. These large-scale facilities include synchrotron and more recent x-ray free electron laser (XFEL). Both of these types of sources can generate ps to fs x-ray pulses and offer experimental set-ups dedicated to time-resolved x-ray diffraction. For the synchrotron part, ESRF (France), SOLEIL (France), APS (US) and KEK (Japan) generate pulses of around 100 ps duration with a brilliance (photon flux per solid angle and per area) lying around $10^{21}$ photons/d/mm²/mrad²/0.1%bandwidth (even reaching $10^{23}$ for the new generation, ESRF for instance). On the other hand, XFELs like LCLS (US), SACLA (Japan), SwissFEL (Switzerland) and

EuXFEL (Germany) deliver pulses of 10-100 fs duration with brilliance reaching $10^{25}$ photons/d/mm²/mrad²/0.1%bandwidth. The pertinence of choosing one source or another depends on experimental requirements.
In the following, we will describe the x-ray sources we used to perform time-resolved x-ray diffraction on photo-excited volume changing materials, including ps diffraction at ESRF, ID9 beamline and fs diffraction at SwissFEL, Bernina beamline.

## II.2. Synchrotrons and Free Electron Lasers for time-resolved x-ray diffraction

### II.2.a. Picosecond x-ray diffraction at ESRF, ID09 beamline

#### *II.2.a.i. Synchrotron radiation*

Synchrotron radiation corresponds to the electromagnetic field radiated by relativistic accelerated charged particles and was first observed in 1947 [Elder1947]. Let us consider a particle of energy $= \gamma m \ ^2$ and velocity $= \sqrt{1 - 1/\ ^2}$ with the speed of light, the rest mass of the particle and $\gg 1$. The easiest way to accelerate a charge is to use a static magnetic field $\vec{\vec{}}$, which will generate a Lorentz force:

$$\vec{} = \ \vec{} \times \vec{\vec{}}$$

To make particles run on a circular path, $\vec{\vec{}}$ must be perpendicular to the plane of the circle. To get a large acceleration, one needs to consider particles of small rest mass. Electrons and positrons are thus good candidates. Synchrotron radiation sources make use of electron acceleration. The radius of curvature of the instrument is given by the equation:

$$\sim \frac{m\gamma}{eB}$$

As an example, the European Synchrotron Radiation Facility (ESRF) in Grenoble shows a radius of about 130 meters of its storage ring, where electrons circulate.
Importantly, these relativistic electrons have a sharp radiation profile, peaked in the direction of motion of the radiating charge. This makes synchrotron radiation a highly collimated source, with extremely large brightness. Typical values for the beam aperture stand around the tens of µrad.
Since the electrons run on a circular trajectory, the synchrotron radiation is emitted tangentially to this circle. Because of the natural collimation of synchrotron radiation, a stationary observer O located away from the particle will receive the radiation produced as the particle goes along an arc of angle $\sim 2/$ . The observed short pulse radiation will thus be of duration , corresponding to the difference between the time it takes for the electron to travel along the arc and the time for light to cross the associated chord (Figure 13). Frequency components within the pulse go up to the critical frequency $\sim \ ^{-1}$ and therefore synchrotron radiation corresponds to a broad white beam, with a spectrum ranging from infrared (low frequency) to tenths of angstrom (x-rays, critical frequency).

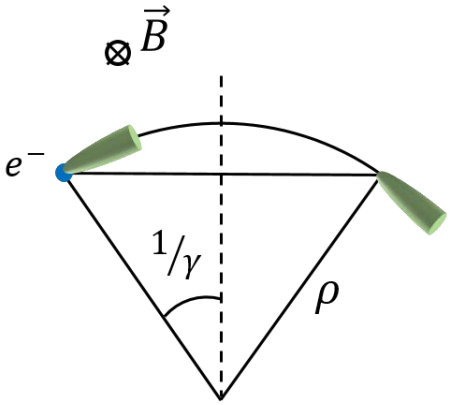


*Figure 13: Scheme of the electron trajectory on a circular way. An observer in the far-field will see the radiation (in green) produced by the electron along an arc of angle ~ 2/ .*

Several parameters allow for the characterization of the beam properties and are thus of interest when designing an experiment. Hence the critical wavelength, which is simply proportional to the inverse of the critical frequency: $= 2\pi c/$ . The power of the beam is described by the photon flux, representing the number of photons per second within a spectral bandwidth $\Delta$ / $= 10^{-3}$ emitted in a 1 mrad orbital fan (in experiments, only few mrad can be used, since the measurement is performed far from the x-ray source and thus a wide fan would result in a very large beam, namely a 20 cm wide beam for 10 mrad aperture and a distance of 20 m). Photon flux depends on particle energy and amount of current stored in the machine. The synchrotron radiation technology nowadays already reached a limit regarding these two quantities.

Actually, more important parameters are brightness and brilliance of the beam. Brightness is defined as the flux per solid angle, which can be tuned by focusing/defocusing optics. As for it, the brilliance corresponds to the brightness over the area of the optical source. Its value depends both on synchrotron radiation natural emittance (corresponding to a light beam radiated by a single electron) and on electron beam emittance. In the longitudinal dimension, the photon aperture often prevails, since the emittance angle $1/$ is significantly larger than the electron angular divergence. However, in the transverse direction synchrotron radiation emittance is diffraction-limited and electron beam emittance dominates, being determined by the electron bunch transverse size. Hence the brilliance of synchrotron radiation beam can be enhanced by tweaking the transverse size of the electron bunch. ESRF recently upgraded its instrument and reached a record in transverse emittance of few hundreds of picorad. Whereas the transverse size of the electron bunch determines the brilliance of the beam, the duration of the latter is defined by the length of the electron bunch, with typical values of $\sim 0.1\ ns$ corresponding to a 3 cm packet. Synchrotron radiation facilities are large scale instruments (the ESRF circumference reaches 844 m).

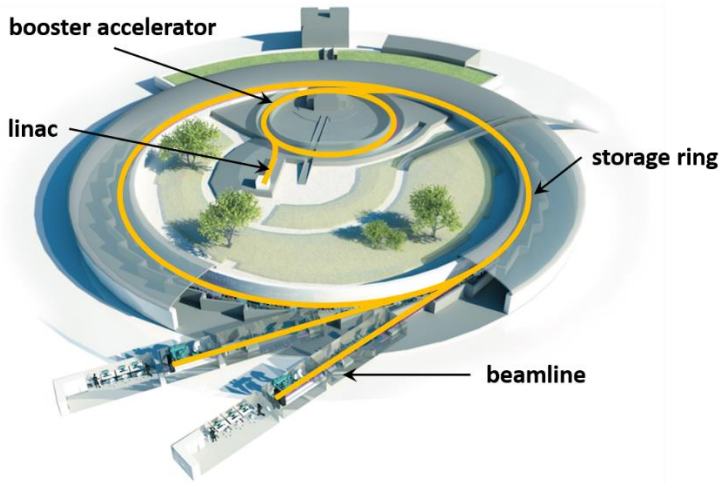


*Figure 14: Scheme of a synchrotron facility. Beam path is shown in orange.*

It is made of several components (Figure 14):

- once emitted from a gun, the electrons go the linac, for linear accelerator, which accelerates them to energies ranging from few MeV to almost the full energy of the storage ring (few GeV);
- the booster circular accelerator represents the second stage of acceleration, to reach the energy of the storage ring. The booster is not fundamentally necessary, but its role is to reduce the emittance of the electron beam coming from the linac and thus increase the efficiency of injection in the storage ring;
- the storage ring is the place where electrons circulate, and emit along beamlines;
- the beamlines are laboratories dispersed along the storage ring circumference. Each line is composed of an optical hutch, where optical instruments allow for the design of the beam for the desired experiment, an experimental hutch, which contains x-ray detectors and where the sample under study is placed, and a control hutch, allowing for the remote control of the experiment and data acquisition.

Experimental time at synchrotrons is granted to the scientific users following a competitive application procedure. Most of the time, experiments at synchrotrons run 24h for several days, making them a particularly intense and dynamic experience.

### *II.2.a.ii. Beamline experimental set-up*

The beamline is where the experiment happens. Whereas sharing the same electrons beams, each beamline has its own insertion devices (most often undulators nowadays) and x-ray optics, allowing to shape the x-ray beam to fit specific needs. The undulator determines the x-ray energy, while monochromators and mirrors determine energy resolution and spatial shape or the x-ray beam. The sample under study is then put in the experimental hutch, which environment is designed to control the experimental conditions (sample position, pressure, temperature, atmosphere, etc.). In the experimental cabin, detectors record the x-rays passing through or reflected from the sample. These detectors turn the x-ray photons into either visible-light photons (measured by scintillation detectors) or electrical signal (measured with semiconductor or charge-coupled detectors). Experiments usually produce a huge amount of data, which then have to be treated, analyzed and interpreted.

ID09 beamline at ESRF is designed for the study of ultrafast structural changes in condensed matter, induced by a light pulse. It benefits from the pulsed structure of synchrotron radiation,

which allows getting a time resolution of around 100 ps, the length of an electron bunch in the storage ring. The storage ring of a synchrotron radiation facility can operate in several conditions, which fit the diversity of experimental requirements. These operation modes differ in terms of filling conditions of the storage ring, described by the amount and distribution of electron bunches circulating in the ring. At ID09, a high-speed chopper is used as fast mechanical shutter to select the flash produced by a single bunch out of the high frequency train of flashes produced by the storage ring. Therefore, due to instrumental limitations, time-resolved x-ray diffraction at ID09 requires the use of filling modes presented isolated electron bunches. The "7/8$^{th}$ + 1" mode for instance, is composed of a train of 868 bunches (filling 7/8$^{th}$ of the storage ring), which both edges are filled with 1 mA single bunch. The remaining 1/8$^{th}$ gap is filled in its center with an isolated 2 mA-single bunch. As for them, the "4 bunch" and "16 bunch" modes both consist in equidistant bunches of 10 and 15 mA, respectively.
The beamline is composed of two sub-parts: the optics hutch and the experiments hutch. At the exit of the storage ring, x-ray pulses entering the optics hutch are shaped spatially (beam dimensions stand between [100.0 x 60.0] µm² and [250.0 x 100.0] µm²) and spectrally (spectral range spreads from 8.5 to 28 keV, with an energy resolution $\Delta \quad / \quad \sim 10^{-4}$). A set of fast shutters and rotative chopper also shape the temporal profile of x-ray pulses, to suit the time scale of the studied reaction [Cammarata2009].
In the experiments hutch, a femtosecond Ti:Sa laser system is synchronized with the x-ray bunch clock, in order to command synchronous emission of laser with x-rays. Timing electronics coupled with a fast timing diode allows setting fixed delays ranging from tens of ps to ms (limited by the repetition rate) between laser and x-ray pulses [Wulff2002], with a jitter significantly weaker than the x-ray pulse duration (< 5 ps). The laser beam is sent on the sample, whereas the x-ray beam probes the excited sample by diffraction. Experiments can be run at a repetition rate varying from 10 Hz up to 1 kHz. The pump-probe cycle is repeated several times for each delay and a two-dimensional MarCCD detector accumulates scattered signal from the sample for series of excitation events.
The experiments we present in chapter III and IV of this manuscript were performed at the ID09 beamline, with electrons circulating in the 7/8$^{th}$ + 1 filling mode of the synchrotron.

## II.2.b. Sub-picosecond x-ray diffraction at SwissFEL, Bernina beamline

Showing exceptionally high brightness and short pulse duration, Free Electron Lasers (FEL) will support progress towards the development of faster and smaller magnetic storage devices, providing bright x-ray pulses.

### *II.2.b.i. XFEL as an x-ray source*

The principle of Free Electron Lasers was first developed by Madey in 1971 [Madey1971] and demonstrated in his group 6 years later for an infrared FEL [Deacon1977]. Since then, considerable scientific and technologic developments have been performed to reach XFELs characteristics as they are nowadays. Actually, XFEL facilities currently deliver ultrashort x-ray pulses with fs duration, a million times shorter than synchrotron facilities and matching conventional optical lasers pulses duration. They represent a fully coherent light source, showing pulse intensity up to $10^6$ times higher than synchrotrons.
The principle of FELs is based on the interaction between a relativistic electron beam and the radiation the latter emits when passing through a periodic magnetic structure [Bostedt2016]. This

interaction is the product of a pump energy transferring from a wide bandwidth unphased reservoir (the electron beam) into one particular mode of an electromagnetic wave. In that sense, FEL are similar to conventional optical lasers and this is what they are named “Free Electron Lasers”. However, their properties do not rely on quantum effects, such as atomic energy levels and stimulated emission, as it is the case for optical lasers. As synchrotrons do, FELs operate in a wide wavelength range, from microwave to hard x-rays.

Free electron lasers make use of the self-amplified spontaneous emission (SASE) process: a small fraction of the kinetic energy of the relativistic electron beam is pumped into an intense electromagnetic radiation by resonant interaction between the electron bunch and the radiation of an undulator. Undulators, by having electrons oscillating perpendicularly to their direction of motion (Figure 15), allow increasing the efficiency of radiation. A radiation is emitted by each individual wiggle and thus the photon flux increases by a factor of 2N corresponding to the number of wiggles. Such oscillating trajectories are generated using magnetic fields of alternate signs perpendicular to the plane of electrons wiggles. Let us consider a planar magnetic undulator, with a sinusoidal magnetic field $_0$ and a spatial period .

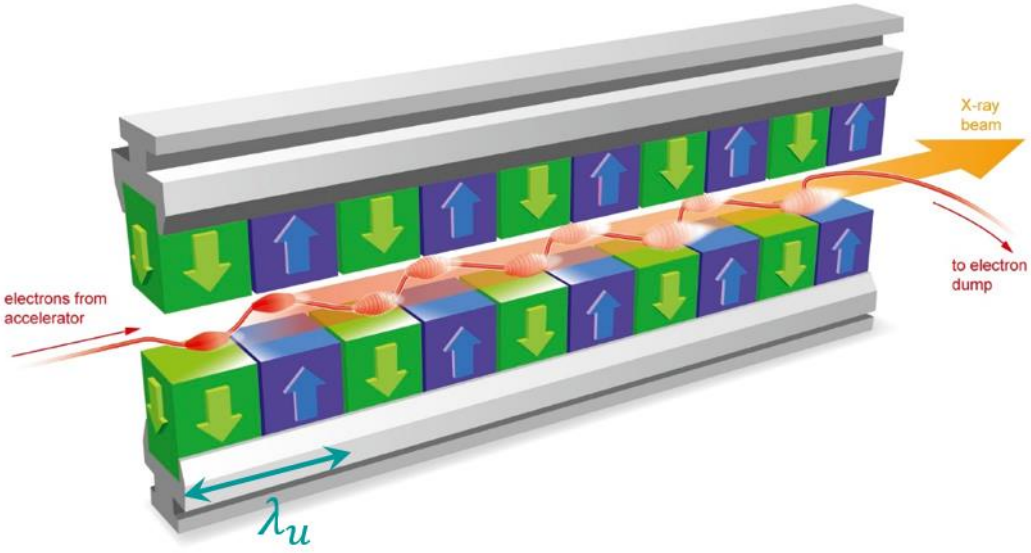


*Figure 15: Scheme of a planar undulator in an XFEL machine.*

Relativistic electrons of energy $\gamma m$ $^2$ follow a nearly sinusoidal trajectory when passing through the undulator (Figure 15) and emit a radiation at the fundamental undulator wavelength:

$$= \frac{}{2\ ^2}\left(1 + \frac{^2}{2}\right) = \frac{2\pi c}{}$$

with $=$ $_0$ $/2$ $mc$ the undulator strength parameter and its fundamental frequency. Higher harmonics are also produced, but with a reduced intensity. For a sufficiently bright beam and long undulator, the resonant interaction leads to the exponential growth of the fundamental radiation intensity along the undulator length. Actually, the beam-radiation interaction induces an energy modulation with periodicity in the initially monoenergetic electron beam: electrons losing energy travel on a sinusoidal trajectory of larger amplitude than the one of those gaining energy, allowing the latter to catch up the low-energy electrons and resulting in the formation of microbunches within the electron bunch. Electrons gathered in a microbunch radiate like a single particle wearing a high charge, corresponding to the sum of charges over the assembly, and therefore contribute to radiation growth. Growing radiation field enhances the microbunching further in a self-amplified process, and exponential growth continues until it eventually reaches the saturation of the radiation power.

Undulators can be planar or helical (for the sake of brevity, we only described the case of planar undulators here). To accommodate SASE saturation at angstrom wavelength required for power stability, the undulator is typically 100 m long (120 m for the Linac Coherent Light Source at Stanford). As is done in synchrotrons, focusing of the beam to ensure a small and nearly constant size is typically performed by quadrupole magnets. The focusing devices are inserted between undulator sections, along with beam position monitors and controllers, to correct beam position along the undulator length.
As high-gain process automatically selects the dominant fundamental mode, self-amplified stimulated emission (SASE) -FEL shows very good transverse coherence. However, due to the finite bandwidth of SASE and the shot noise start-up, the temporal coherence is limited and intensity shows shot-to-shot fluctuations, which must be measured and taken into account when performing an experiment.
Compared to incoherent synchrotron radiation sources, the amplification of coherent radiation in XFELs increases the number of photons by a factor of about one million. The pulse duration decreases from tens of ps to tens of fs, with excellent transverse coherence. All these factors combined lead to an increase of the brightness by several orders of magnitude compared to synchrotron facilities.

### *II.2.b.ii. Experimental set-up: the Bernina beamline at SwissFEL*

Unlike in a synchrotron, long complex and thus costly undulator arrays are needed to run an XFEL. Therefore, XFELs show much fewer beamlines than synchrotron facilities. A handful of XFEL facilities exist around the world, among which can be distinguished hard XFELs: LCLS (USA), SwissFEL (Switzerland), EuXFEL (Germany), PAL-XFEL (Korea), SACLA (Japan) and soft XFELs: FERMI (Italy), FLASH (Germany) and SACLA. The same procedure of application than for synchrotrons run for XFELs: scientists apply by sending a proposal of experiment. Since the number of beamlines is reduced, the procedure is even more competitive than for an experiment at synchrotron.
Ultrashort high-intensity pulses are of course of particular interest in the field of time-resolved experiments, allowing to reach time resolution and signal-to-noise ratio comparable to optical studies performed with conventional lasers as a probe, therefore providing complementary information about photo-induced phase transitions dynamics.
Bernina beamline at SwissFEL is dedicated to the study of ultrafast phenomena in condensed matter, by laser pump-x-ray probe experiments. It benefits from the ultrashort x-ray pulses ($\sim 20$ fs) generated by the XFEL, with photon energy ranging from 0.25 to 12 keV. The diffractometer platform allows tuning the x-ray incident angle on the studied sample.
A 20 mJ Ti:Sa laser system provides excitation beam ranging from THz to UV wavelength. Timing diagnostics manage delays between laser and x-ray pulses, with a repetition rate of 100 Hz.
A two-dimensional charge integrating Jungfrau detector collects diffracted x-ray photons from the sample [Mozzanica2018]. This new type of x-ray detector is specifically suited for high-flux x-ray beams generated at XFEL. Actually, it allows a shot-to-shot data acquisition, with low-noise, ultrafast x-ray detection and the possibility to detect several photons simultaneously.
I participated to the ultrafast x-ray diffraction experiment that my team performed at Bernina [Mariette2020]. Since the experiment was part of the commissioning for the facility, the beamline was operating under conditions, which did not reach the current SwissFEL performances, but still with very good temporal and q resolution. By the time, x-ray wavelength was limited to 2.2 keV. Actually, undulator did not reach its final length, allowing to accelerate electrons to the desired energy, and the beam trajectory stabilization did not reach the current precision, therefore maximum energy had not been reached yet. We worked with x-rays third harmonic: x-rays of 6.6 keV wavelength were sent on the sample at a grazing angle of around $= 0.5°$, resulting in

roughly 100 nm penetration depth of the x-ray beam. Excitation was performed with a 1.55 eV, 10 Hz, 500 fs duration laser pulse. The pump hit the sample at 10° angle, corresponding to approximately 65 nm penetration depth. This geometry was used to match the x-ray penetration depth at best. Overall time resolution was about 600 fs.
The method used to analyze the obtained data will be described at the end of this chapter.

## II.3. X-ray powder diffraction

### II.3.a. Powder morphology

A powder consists in a large number of small crystallites, randomly oriented with respect to each other, such that there are always several crystallites to satisfy the scattering condition, whatever the azimuthal angle of measurement . Therefore, whereas single crystal diffraction generates Bragg spots, powder diffraction will produce diffracted rings on the detector, designated as Debye-Scherrer rings (Figure 16).

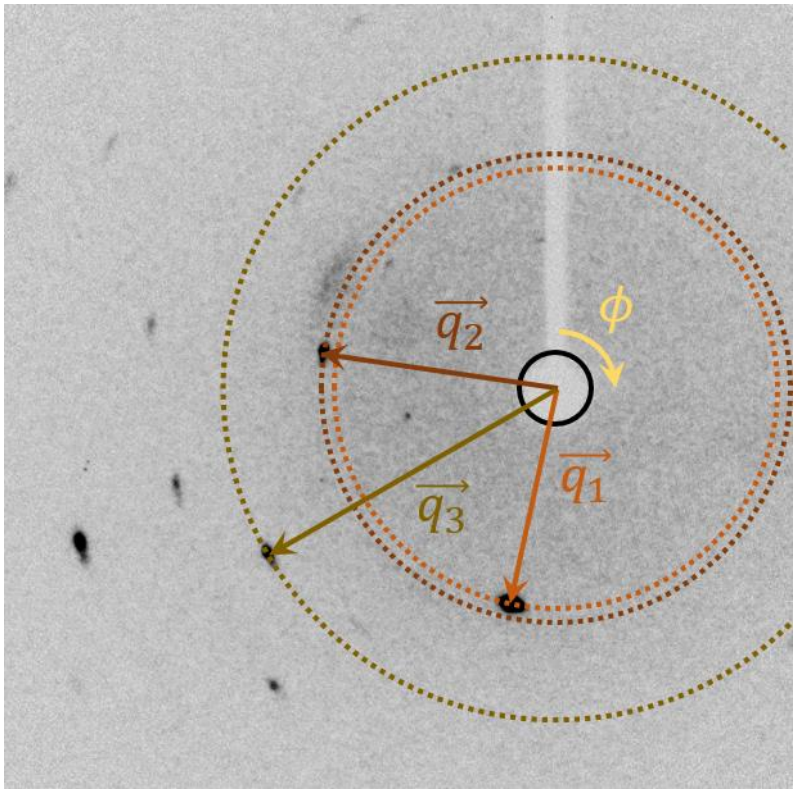


*Figure 16: Example of diffraction pattern from a single crystal, showing Bragg spots at diffraction condition for $\vec{q}_1$, $\vec{q}_2$, $\vec{q}_3$. In a polycrystalline crystal, these spots would transform into rings (represented as dotted lines), reflecting the randomness of crystal orientation in the powder.*

Several sample morphologies are included in the “powder” designation. In the work presented in this manuscript, we chose to use powder for different reasons depending on the studied material. We worked with three different morphologies of sample:

- spin-crossover molecular crystals (chapter III) were dispersed in a polymer thin film to facilitate manipulation and avoid oxidation of the metallic ion, and deposited on glassy substrate;
- $Ti_3O_5$ (presented at the end of this chapter) crystals show bistability in the nano-size only, synthetized under the form of flakes of agglomerated nanocrystals. Studied $Ti_3O_5$ samples consisted in pellets of flakes;

– $V_2O_3$ (chapter IV) was studied in polycrystalline thin films grown on $Al_2O_3$ substrate.

### II.3.b. Powder diffraction pattern

A powder diffraction pattern consists in a set of intensities associated with corresponding diffraction angles. In the diffraction experiments we will describe in the following chapters, data collection is performed on a fixed two-dimensional detector (Figure 17).

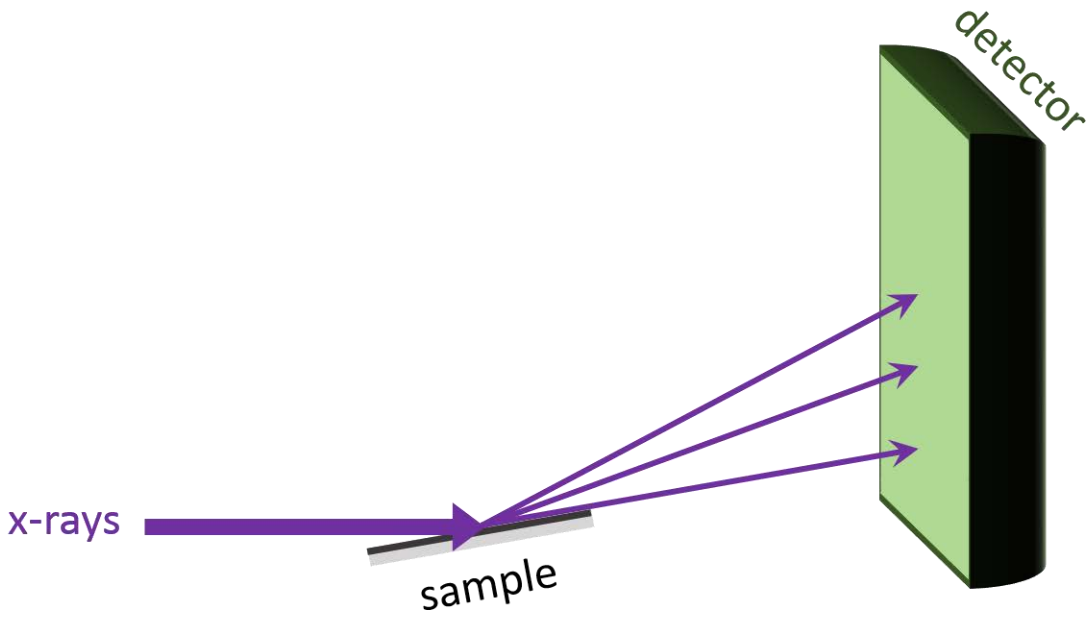


*Figure 17: Scheme of diffraction-detection set-up. The x-ray beam impacts the sample and gets diffracted on a 2D-detector.*

The distribution of diffracted intensity is described with the cylindrical coordinates in reciprocal space: radius q (distance from the center of the rings) and azimuthal angle (Figure 18). In the case of a perfectly randomly oriented polycrystalline sample, diffraction produces homogeneous rings. However, when crystallites show a preferred orientation in the sample, the distribution of diffracted intensity varies across .

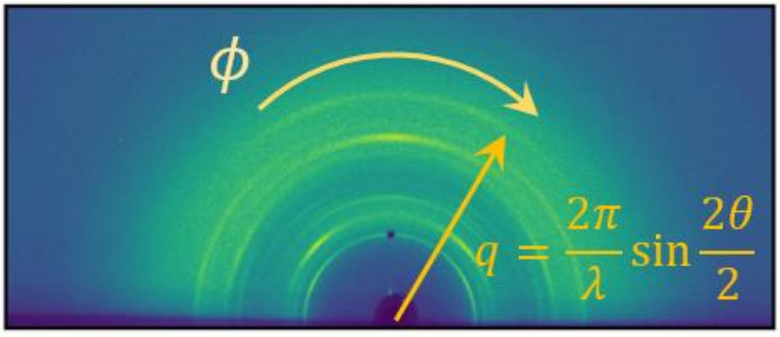


*Figure 18: Diffraction image from a polycrystalline sample. q is the reciprocal space coordinate and is the azimuthal angle.*

### II.3.c. Experimental geometry: grazing incidence diffraction

Tuning the x-ray beam incidence angle make x-ray penetrate in an oblique way with respect to the surface of the sample, therefore decreasing their effective penetration depth. Depending on the absorption characteristics of the sample, the effective penetration depth can be tweaked by several orders of magnitude by changing the x-ray incidence angle. Hence, working at grazing angle can be of interest to avoid parasitic diffraction from a substrate or, in the case of pump-probe experiments, to match x-ray and laser penetration depth, to effectively probe the excited region.
However, this geometry effectively widens the beam footprint of the sample, with the vertical dimension increasing from $h$ to $h' = h/\sin$ (Figure 19). This further broadens the diffraction peaks on the detector, inducing a loss in angular resolution. Therefore, performing grazing angle diffraction implies finding the best compromise between desired penetration depth and angular resolution.

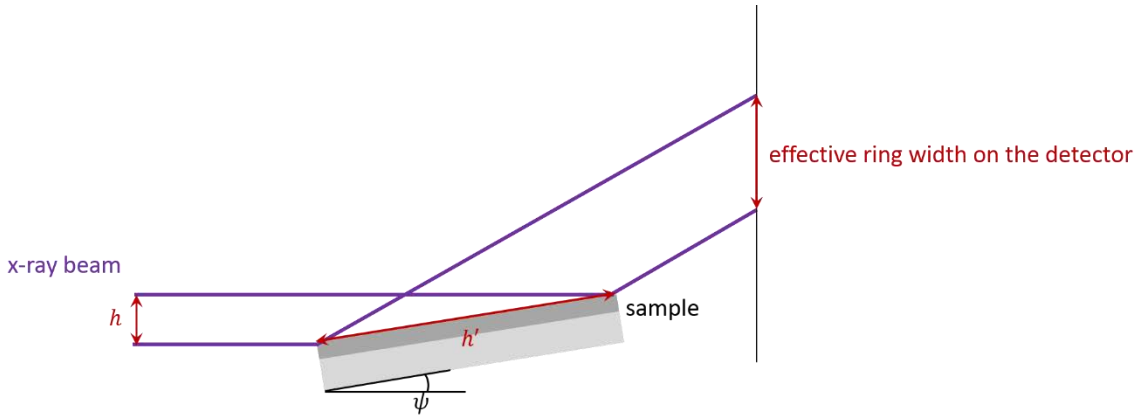


*Figure 19: Scheme of the broadening effect caused by grazing incidence diffraction geometry on the diffracted ring width.*

## II.3.d. One-dimensional diffraction pattern generation

Data processing then consists in several steps, to produce a one-dimensional (1D) diffraction pattern from the two-dimensional (2D) detector image (Figure 18). We use several Python libraries to perform data reduction.
pyFAI (standing for “Fast Azimuthal Integration using Python” [Ashiotis2015]) allows defining the region of interest of the image, then finding the center of the rings and “unfolding” the rings from this center, transforming the image with q in abscissa and as the ordinate (Figure 20a). Integration over is finally performed and leads to a 1D diffraction pattern, with $In \quad nsit =$ ( ) (Figure 20b).
Background removal is performed using the scikit-ued python library [Rene2017]. This library, originally designed for ultrafast electron diffraction, allows for advanced background detection and treatment [Galloway2009].

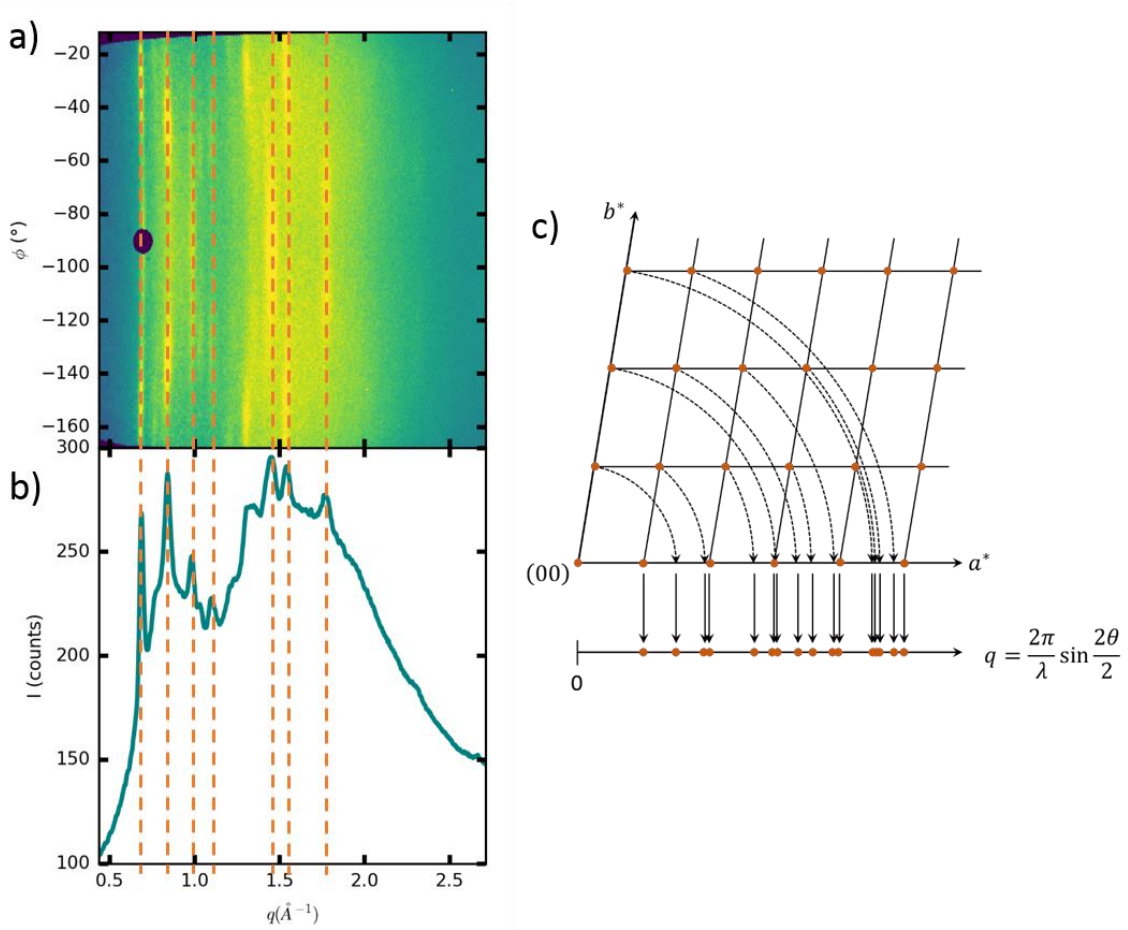


*Figure 20: a)" Unfolded" diffraction image from a powder sample. Rings become lines along the azimuthal angle. b) Diffraction pattern obtained after integration over . Diffraction lines evidenced by dashed orange lines give peaks in the one-dimensional pattern. c) Schematic representation of the relation between the diffraction pattern of a single crystal and the powder pattern. The latter is the projection of the crystal pattern (here 2D for the sake of clarity)onto a 1D line. Only the norm of the q vector is preserved – the information about the orientation is lost.*

In the case of time-resolved x-ray diffraction, this procedure is repeated for patterns taken at each delay between the pump laser and the x-ray probe.

## II.4. Time-resolved x-ray powder diffraction: methods of analysis

The diffraction patterns generated by pump-probe measurements contain the signature of photo-induced structural changes.

### II.4.a. Sequence of diffraction patterns measurement

Considering experiments at ESRF, each image corresponds to 1000 x-ray pulses. The different delays are usually recorded in random order, to avoid confusion between delay evolution and any experimental drift (Figure 21).

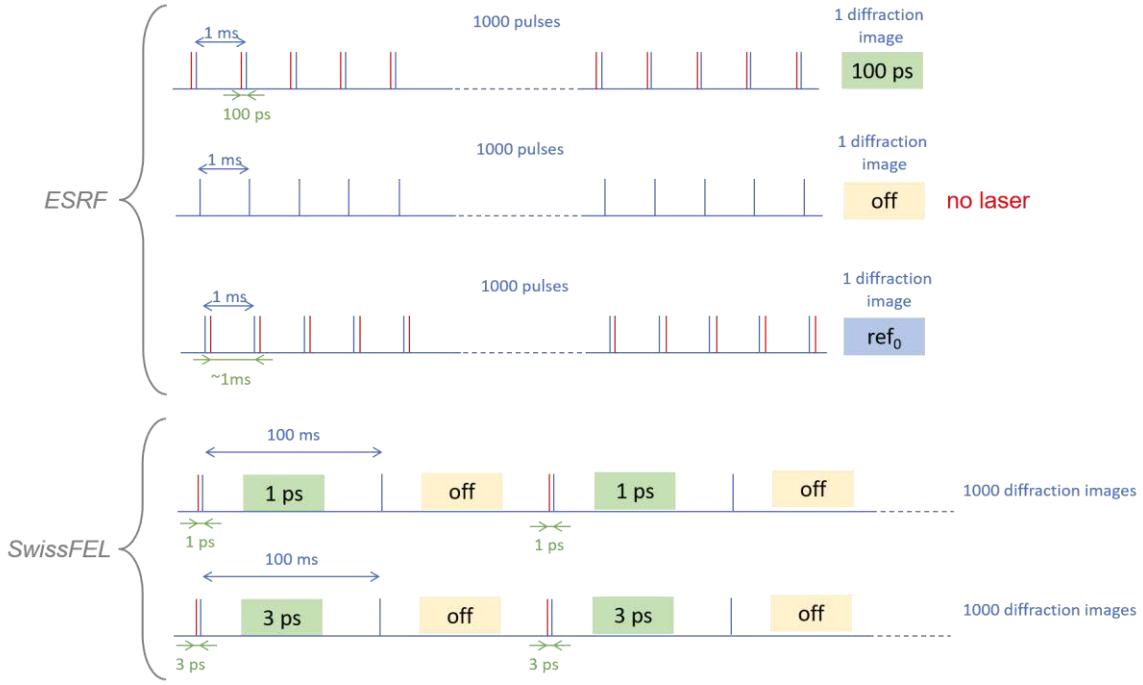


*Figure 21: Schematic pump (red) and probe (blue) distribution, for measurement at ESRF (up) and SwissFEL (down).*

In order to increase the statistics, the sequence is repeated several times (series in Figure 22). We recorded several reference patterns between measurements within one sequence. The reference corresponds to a measurement at – 5ns, i.e. 5 ns before the laser pulse hits the sample. For a 1 kHz experiment for instance, this delay also corresponds to + 999.995 µs (~1 ms). Hence, by building the differential signal, potential residual heating effects are taken into account and subtracted from the transient signal.

At SwissFEL, due to high photon flux, single-pulse images were recorded, alternating off patterns (no laser) and on patterns. Due to the low repetition rate of the experiment, no residual features were observed and thus no further reference was required (off patterns being taken as references).

## II.4.b. Differential signal

### *II.4.b.i. Calculation scheme*

At SwissFEL, the number of photon per pulse and sensitivity of the detector was good enough to analyze directly the absolute diffraction patterns. This is usually not the case in time-resolved experiments. The so-called differential signals are then used to extract the information about the photo-induced changes. The differential signal corresponds to the transient intensity change Δ in the diffraction pattern, for each delay. Differential signal at a certain delay is calculated by subtracting a reference pattern to the pattern measured at . At ESRF, an averaging strategy was developed to limit the fluctuations and get reliable differential signal. This procedure was applied to treat the data presented in chapter III and IV.

The procedure is schematized on Figure 22.

The average of the two references surrounding one given delay is subtracted from a given pattern (at delay t or “off”), producing the corresponding differential signal. This measurement cycle is performed for each delay between pump and probe, and repeated several times to average the signal and improve the signal-to-noise ratio of the measured patterns.

Finally, the overall average of the reference patterns is added to the average difference signal for each delay. This whole procedure is performed using a python library developed in our team by M. Cammarata to handle time-resolved x-ray diffraction patterns especially and called trx.

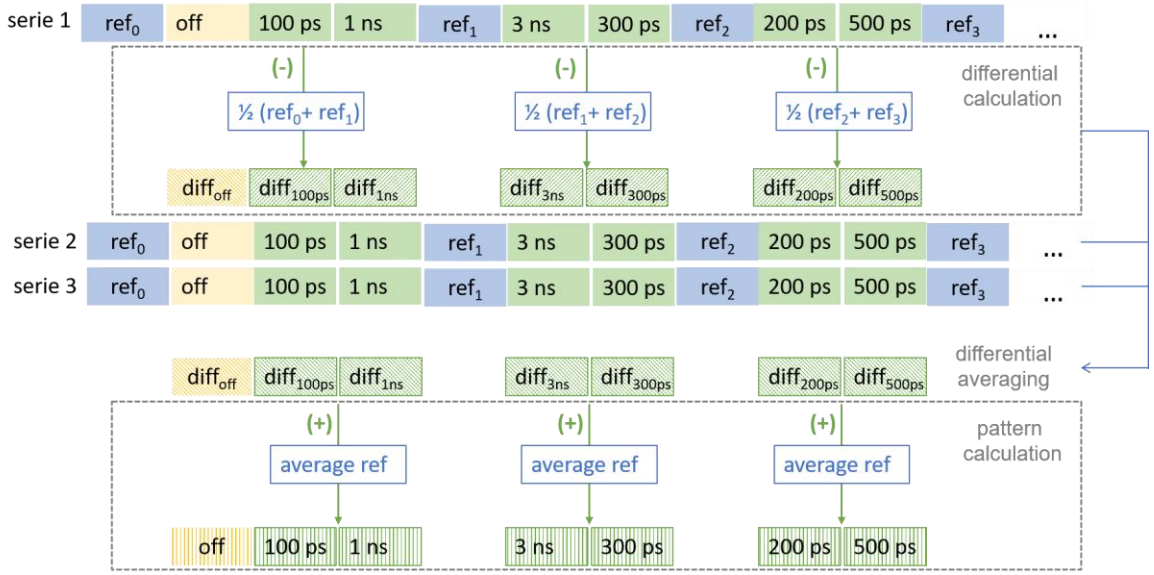


*Figure 22: Scheme of the differential and pattern calculation, for measurement sequence used at ESRF.*

### *II.4.b.ii. Interpretation of the differential signal*

Considering the diffraction pattern, the appearance, the disappearance or the shift of one or several peaks informs about the formation of a new crystalline phase or the deformation of unit cell of an already existing phase. Changes in relative peaks intensities, as for them, are the signature of changes of relative atomic positions within the unit cell. These transient modifications induce characteristic features in the differential signal:

- a peak shift towards high q (respectively low q), caused by unit cell volume contraction (respectively expansion), will translate into a bipolar feature in the differential signal: an intensity increase towards high q, $\Delta > 0$ (respectively low q, $\Delta < 0$) and a decrease towards low q, $\Delta < 0$ (respectively high q, $\Delta > 0$) (Figure 23);

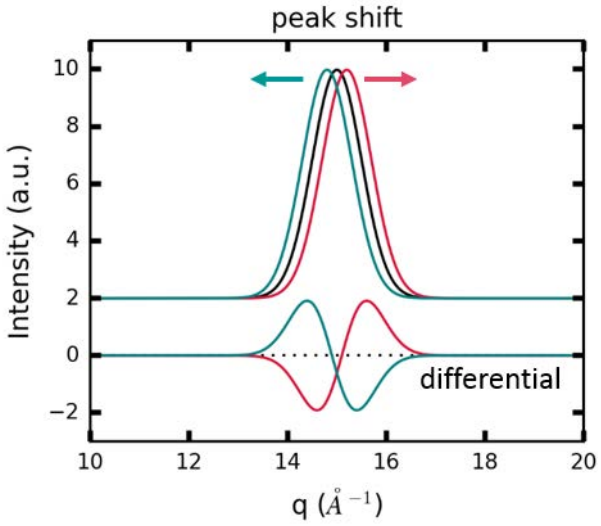


*Figure 23: Peak shift towards low q value (in green) and towards high q value (in red) give bipolar signal of opposite sign in the differential (bottom of the figure).*

- appearance (disappearance) of a peak is associated to a unipolar feature in the differential signal, with an increase (decrease) of intensity $\Delta > 0$ ($\Delta < 0$) (Figure 24a,b). This type of signature is also characteristic of relative peaks intensity changes (Figure 24c);

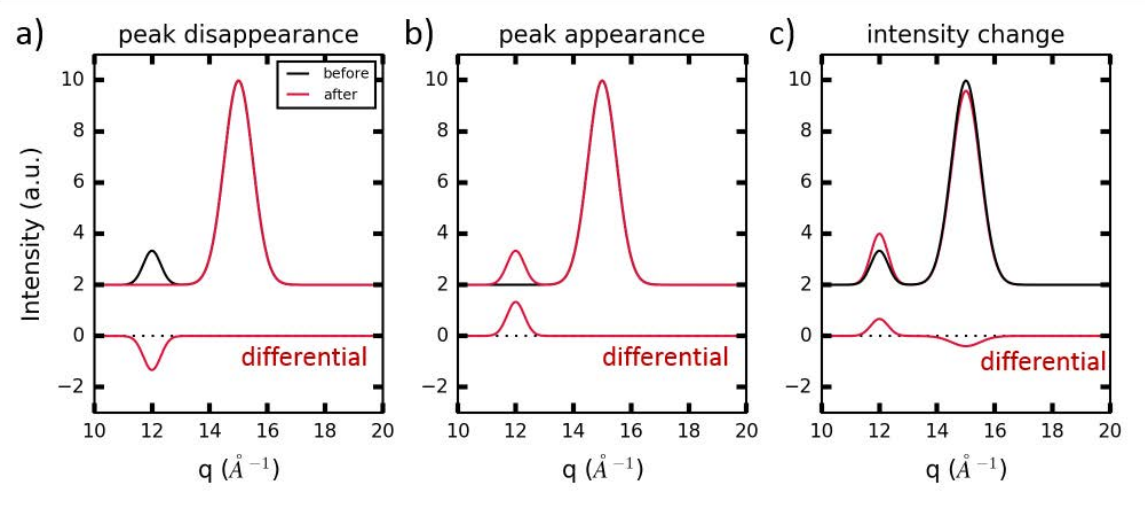


*Figure 24: The disappearance (a) or appearance (b) of a peak gives a unipolar signal in the differential. The same type of signal is observed when relative intensity of peaks changes (c).*

- peak splitting (merging) is often associated to symmetry change. The corresponding signature in the differential signal is a tripolar feature, showing intensity loss, $\Delta < 0$ (gain, $\Delta > 0$) in the center and intensity gain, $\Delta > 0$ (loss, $\Delta < 0$) in the aisles of the peak. This type of feature is actually characteristic of any peak broadening (narrowing) (Figure 25).

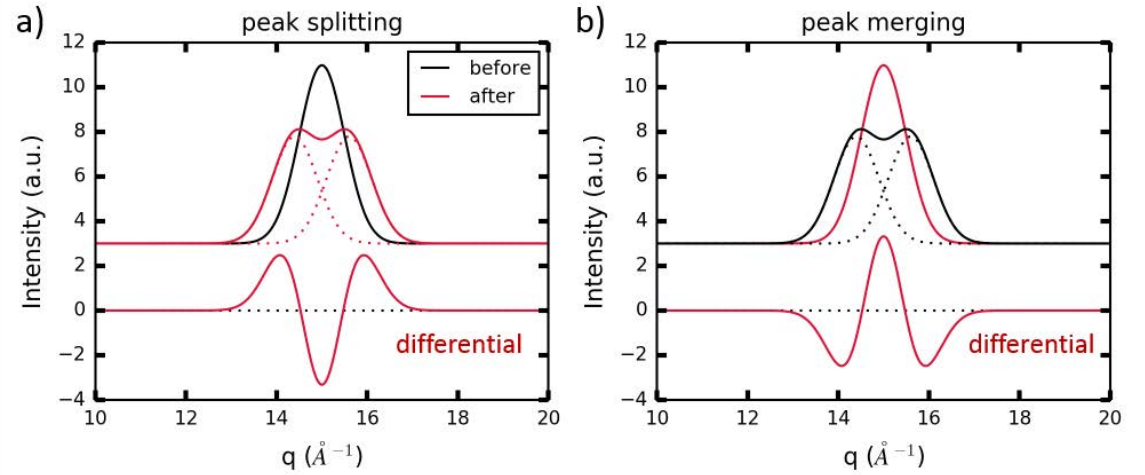


*Figure 25: Peak splitting/widening (a) and merging/narrowing (b) give tripolar signals of opposite signs in the differential (bottom of the figure).*

The observation of the differential signal thus allows for the qualitative analysis of the transient signal. Moreover, the overall amplitude of absolute differential signal informs about quantitative structural changes in the sample.
The pattern can then be analyzed, using a pattern refinement method.

### II.4.c. Pattern refinement

Pattern refinement consists in simulating a powder diffraction pattern, and trying to make this calculated pattern fit the experimental one. To describe the diffraction pattern, several parameters need to be considered: peaks positions, peaks profile, peaks relative intensities, background… Are all relevant parameters defining a diffraction pattern and including structural information about the studied sample. The work presented in this manuscript was conducted using the TOPAS software [Coelho2018], dedicated to powder diffraction pattern analysis.

### *II.4.c.i. Profile Shape Function (PSF)*

Ideally, an infinitely thick perfect sample would produce Dirac-type diffraction peaks. In practice, reflections are usually broadened by instrumental effects. Additional effects due to the sample itself can also impact the intensity distribution:

- particle-size broadening originates from the finite character of the size of coherently diffracting domains within the crystallites. For small particle, the assumption of infinite lattice no longer holds and the diffracted peaks are smeared out to an extent which is proportional to the average particle size.
- microstrain broadening results from local variations of the average d-spacing produced by non-uniform strain in the lattice.

These three effects (instrumental conditions, size broadening and strain broadening) can be present in the same material. In the experiments we describe in the chapters III and IV, performed at grazing incidence, the peak shape is mainly determined by large beam footprint effect (see paragraph II. 3c).

The usual function to describe the profile shape function (PSF) is a pseudo-Voigt function, which is a weighted sum of Lorentzian and Gaussian contributions. It has been shown that the widths and of the two components present variations of the form:

$$= \tan + /\cos$$

$$= ( \tan^2 + \tan + + /\cos^2 )^{1/2}$$

With $= 2 /2$ half of the scattering angle. The procedure is to refine the parameters , , , , , through a profile refinement technique. and correspond to strain broadening components, whereas and account for size broadening and and are related to instrumental conditions.

When the knowledge of experimental conditions is less precise, more simple functions can be used, such as Gaussian or Lorentzian models. A Gaussian fit was used to analyze time-resolved diffraction data presented in Chapter IV of this manuscript.

### *II.4.c.ii. Background*

In the thin films we studied, a strong background originated from the amorphous substrate. It was partially removed using the scikit-ued python library. Remaining part were added in the refinement procedure. This diffuse background was described by a polynomial function.

### *II.4.c.iii. Peaks position and intensity*

Peaks positions and relative intensities reflect the unit cell parameters and atomic positions within the unit cell. Depending on the quality of the diffraction data and on the a priori information about the sample, several refinement methods can be used.

Pattern refinement can be performed by considering the diffraction pattern as a whole. The so-called Pawley method performs a cell-constrained refinement, starting from approximate cell parameters but without structural model [Pawley1981]. In this technique, peaks positions are constrained by cell parameters and intensities are free variables, which are refined with the parameters describing the resolution function. The intensity at every step of the pattern is modeled by the calculated intensity:

$$_{ci} = _{bi} + \sum_{=1}^{2} \Omega_{ik}$$

$_{bi}$: background intensity

: integrated intensity of the k[th] peak contributing to the step

$\Omega_{ik}$: peak shape (PSF)

and fitted by a least-squares procedure. Quality of the fit is given by the $R_{wp}$ agreement factor. This method is convenient to extract the maximum information from patterns of sample with known cell parameters but unknown atomic arrangement, or from data with poor resolution. The output consists in refined cell parameters and peak intensities associated with reciprocal coordinate. This method was used to describe and analyze the time-resolved diffraction data presented in Chapter III of this manuscript.

The Rietveld method is another whole-pattern fitting type of analysis, which includes structural constraints from atomic positions (requiring a priori knowledge of the structure). Initially developed for neutron data in 1969 [Rietveld1969], the algorithm fits the diffraction patterns using instrumental characteristics, along with structural parameters of the sample (cell constants and atomic arrangement). It is more stable and computationally more efficient than the Pawley method, but requires high-resolution data (no peak overlap is allowed, since they cannot be separated in this case). The Rietveld refinement technique allows for structural analysis but requires a reasonable structural model to start with.

### *II.4.c.iv. An example of Rietveld refinement: time-resolved x-ray diffraction on $Ti_3O_5$ nanocrystals*

Previous section described state-of-the-art methods of diffraction pattern analysis. However, even used for long to extract information from patterns measured at equilibrium, these methods had never been applied to out-of-equilibrium patterns. During my PhD, we developed with my team a new approach of quantitative analysis of time-resolved x-ray diffraction patterns. This section presents an example of what can be extracted from such an analysis on good-quality diffraction data, with a q resolution allowing for precise Rietveld refinement.

As evoked above, we performed ultrafast x-ray diffraction experiment at the SwissFEL beamline Bernina [Mariette2020]. The goal of this experiment was to study structural effects in the photo-induced semiconductor-to-metal transition in $Ti_3O_5$ nanocrystals [Tokoro2015]. However being isostructural (i.e. showing no change in crystal symmetry), the transition is associated with strong volume change (+ 6.4%) and atomic reorganization within the unit cell. There is therefore a strong presumption that structural deformations have an impact on the out-of-equilibrium phase transition dynamics. Diffraction patterns were measured at delays ranging from -4.5 to 50 ps.

This measurement at Bernina followed a first experimental campaign performed on ID09 (Figure 26a). The diffraction patterns, even if qualitatively similar, show significantly better q resolution (narrow peaks) at XFEL (Figure 26b), thanks to smaller x-ray beam size (cf part 3.c of this chapter). Measurements at Bernina focused on ultrashort time scale (tens of ps), whereas ESRF data inform about the long-time scale dynamics (up to 1 ms) [Mariette2020].

These patterns were then analyzed with the Rietveld method, using the TOPAS software [Coelho2018]. This method is conventionally used on diffraction patterns measured at equilibrium. However, the good quality of the patterns we measured convinced us to apply it to our data, thus developing a new routine to extract quantitative information from time-resolved x-ray diffraction measurements. This method can be applied only to good-quality data and could not be used in the case presented in chapter IV, where preferred orientation prevented from descripting the diffraction peaks correctly.

Pawley refinements were also used and both methods gave consistent evolutions of the unit cell parameters and scale factors. The profiles were described using a beam energy of 6.5 keV ( $\lambda$ = 1.899 A) and a Gaussian emission profile with 1.3% FWHM. The peak width and sample displacement were described using the expressions from [Rowles2017], vertical width and incident angle of the beam being fixed as measured (4 µm and 0.5° respectively). The sample detector-distance was fixed to 61 mm, as refined in the azimuthal integration step. The absorption coefficient at 6.5 keV was calculated as 800 $cm^{-1}$ (for a packing density of 0.8, measured from x-ray transmission measurement). These parameters were fixed for the refinements against time-resolved patterns.

The refinements included two phases (semiconductor β- and metallic λ-, Figure 26). For each phase, the free parameters were the cell parameters (a, b, c, ϕ (monoclinic angle)), the atomic position in the (a, c) plane for the five independent atoms (position along b being symmetry-restricted) and the scale factor. An additional microstrain-type Gaussian convolution accounted for the strain distribution observed during the propagation of phase transition. The initial Bragg peak profile was well defined by the experimental resolution function defined as described above, as can be seen in Figure 26: the residual, which is the difference between experimental and calculated pattern, is rather low and flat (Figure 26). Thus, no extra size contribution was considered in the refinement of the reference patterns. The transformation being reversible and isostructural, no evolution of the crystallite size was expected and thus considered either. In any case and sticking to Occam's razor, which states that "entities should not be multiplied without necessity", the choice was made to retain the simplest convolution functions to ensure the robustness of the refinement. Hence no Lorentzian contribution, asymmetry or anisotropy was taken into account. The background was described as a third-order polynomial. The preferred orientation was described using Spherical Harmonics corrections, whose coefficients were refined on reference patterns and then kept constant for all delays.

Reference structures were taken from [Ohkoshi2010, Onoda1998] and atomic displacement parameters were fixed to the equilibrium room temperature value due to limited accessible q region.

Data analysis of the time-resolved x-ray diffraction of photo-excited $Ti_3O_5$ crystallites allowed monitoring the early intra-cell distortions around absorbing metallic atoms, but also long range crystalline deformations. Results of this analysis will be discussed in chapter IV, in regard with results obtained on another volume-changing metal oxide, $V_2O_3$.

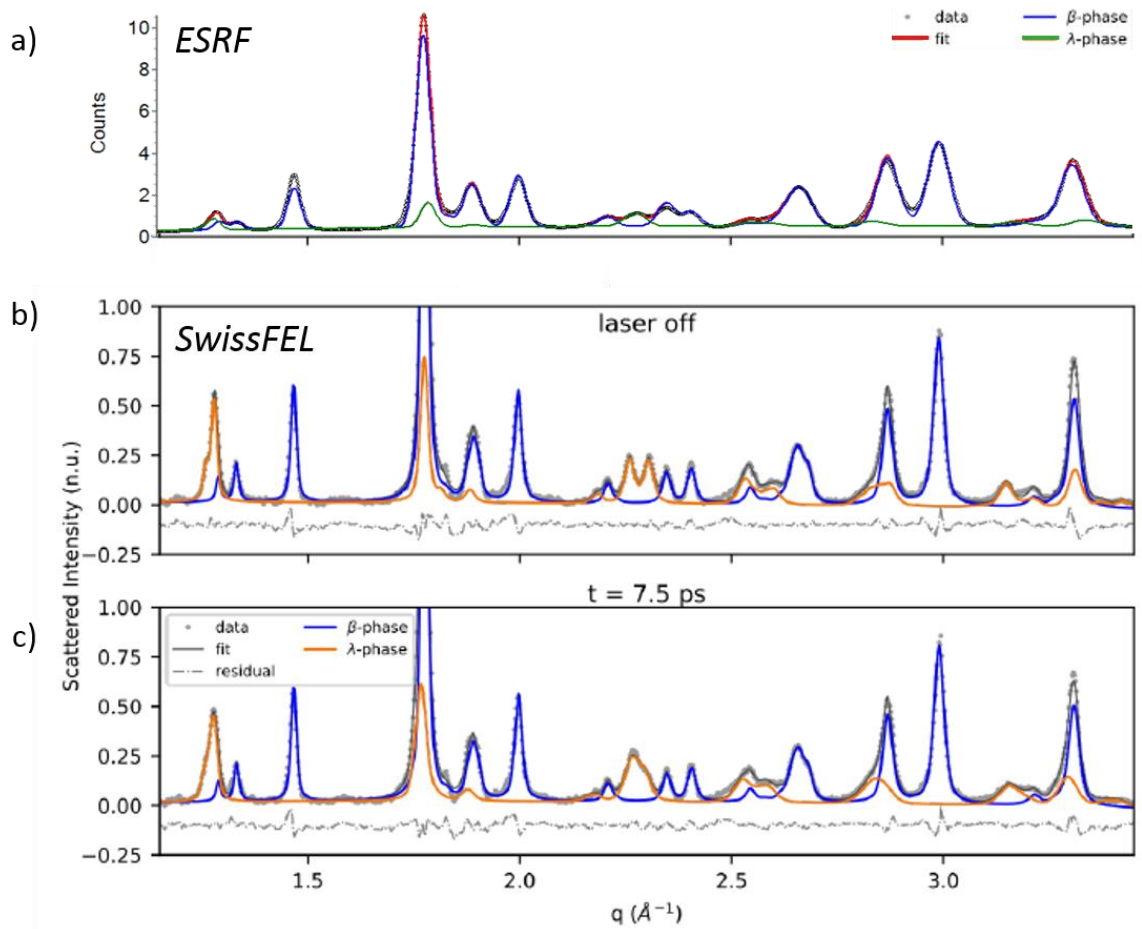


*Figure 26: a) Rietveld refinement of pattern at t = 10 ns, measured at ESRF on ID09 beamline. Plain circles are measured powder patterns and result of Rietveld refinement in red, plain line. Green and blue patterns are respective contributions to the refinement of the λ- and β-phases. b) and c) show Rietveld refinement of reference pattern (with no laser, b) and pattern at t = 7.5 ps (c), measured at SwissFEL on Bernina. Measured powder patterns are plotted in light gray, plain circles and result of Rietveld refinement in black, plain line. Orange and blue patterns are respective contributions to the refinement of the λ- and β-phases; the residual curve is shown in gray, dashed lines. b) and c) are adapted from [Mariette2020].*

Experimental and analytical methods presented in this chapter allow for qualitative and quantitative analysis of diffraction patterns measured out-of-equilibrium, therefore accessing transient structural changes in materials. We adapted these methods to the investigation of photo-induced phase transition in two different volume-changing materials. These studies will be detailed in the two following chapters.

# Chapter III: Photo-induced multistep spin transition in a molecular spin-crossover material

Materials are called bistable, if they show two electronic states, which coexist in the same values of external parameters. The application of an external perturbation leads to the commutation of the physical (optical, mechanic, magnetic …) properties of the compound. Among various types of bistable systems, the so-called spin-crossover materials are good candidates, as they show a thermally- or photo-induced bistability [Letard1997, Tissot2011, Azzolina2019].
This chapter focuses on an $Fe^{III}$ spin-crossover molecular compound, showing strong cooperativity associated with the electronic spin state. Despite strong volume change at the phase transition, spin-crossover materials were often discarded in strain propagation studies. However, since molecular spin state switching is at the origin of volume change, there is a strong supposition that strain propagation dynamics in this type of compounds might be different from commonly studied materials, such as metals and semi-conductors.
We performed a time-resolved structural study to investigate the role of both high-spin fraction and unit cell volume change, competing with activation energy to switch from low-spin to high spin state, in the photo-induced phase transition dynamics. This study led to the evidence of a decorrelation between volume and spin state switching out-of-equilibrium.

## III.1. Spin-Crossover Materials as switchable bistable systems

### III.1.a. Structure of spin-crossover molecular systems

In the solid state, spin-crossover molecular materials consist of crystalline compounds, built up by molecular units organized via relatively weak supramolecular interactions. In our case, the type of molecules under scrutiny are composed of a central metallic atom, surrounded by ligands and completed by a counter-ion (Figure 27).

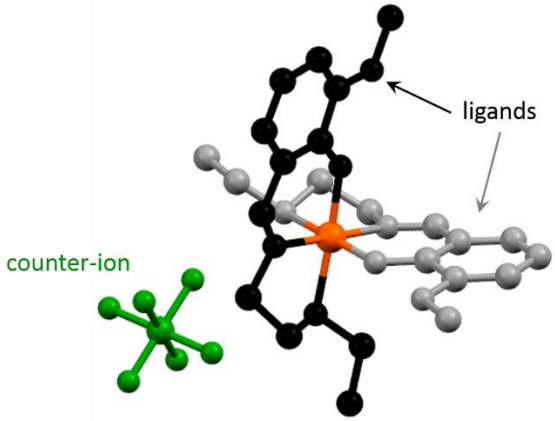


*Figure 27: Example of a spin-crossover molecular unit. The metallic ion (in orange) is surrounded by two identic ligands (in black and gray) and completed by a counter-ion (in green).*

The spin transition appears when the metallic ion at the center of the molecule can switch between two electronic states with different spin multiplicity but close energy. This phenomenon was first evidenced in the 30s by Cambi et al. [Cambi1934] on an $Fe^{III}$ compound in solution. However, we had to wait for the 60-70s to witness the establishment of conceptual basis of spin transition [Wajnflasz1970]. Since then, numerous complexes were discovered, the most studied

being $Fe^{II}$ compounds, but also $Fe^{III}$, $Co^{II}$ complexes and much more [Garcia2004, vanKoningsbruggen2004].

### III.1.b. Origin of spin transition

The spin transition phenomenon is described in the ligand field theory, by a partial degeneracy of d orbitals of the metallic ion. The surrounded ligands create a potential, which affects these five d orbitals. Supposing a perfectly octahedral ligand potential, the cubic symmetry of the ligand field lifts the degeneracy, splitting both orbitals $_2$ and $_2$ _ $_2$ from the three $_2$ orbitals $_{xy}$, $_{yz}$ and $_{xz}$. Two parameters play a major role in the lift of degeneracy of the d orbitals: the ligand field intensity Δ, which represents the energy difference between $_2$ and orbitals, and the pairing energy Π related to electronic repulsion within an orbital. If the ligand field is smaller than the pairing energy, the d electrons are distributed according to the Hund's rule, as they would be in an isolated atom (Figure 28). For an $Fe^{III}$ ion ($d^5$), the high spin (HS) multiplicity then becomes S = 5/2 and $e_g$ orbitals are populated, leading to a $t_{2g}^3e_g^2$ electronic configuration. Conversely, if Δ is higher than Π, only $t_{2g}$ orbitals are populated by the electrons, leading to $t_{2g}^5$ configuration and a low spin (LS) multiplicity value S = 1/2 [Hauser2004].

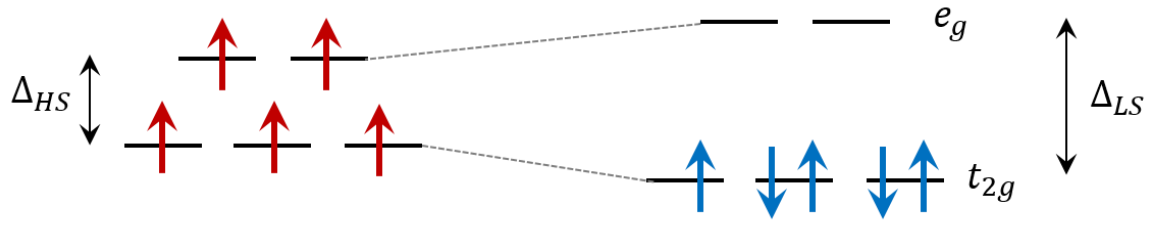


*Figure 28: Scheme of the lift of degeneracy of the d orbitals in octahedral symmetry and associated electronic population depending on the ligand field, illustrating the case of an $Fe^{III}$ system.*

It is important to notice that orbitals are anti-bonding compared to $_2$ orbitals. Both molecular configurations thus show significant structural variation at the level of the ligand-metal bond length. Typical changes in the metal–ligand donor atom bonds of $Fe^{III}$ complexes average from 0.12 to 0.15 Å, for a typical length of 2.0 Å, i.e. approximately 7.5% variation.
The spin transition can be seen in ions showing a configuration $3d^4$ or $3d^7$, with an octahedral or close-to-octahedral geometry. In $Fe^{III}$ complexes, the preferred coordination sphere is $FeN_4O_2$, with four nitrogen atoms and two oxygen atoms, which are brought by ligands.. When the energy difference between LS and HS states is small enough, the switching from one spin state to another can be potentially achieved applying an external perturbation (temperature, light, magnetic field …) [Lawthers1984, Bousseksou2004].

### III.1.c. Cooperativity in the solid state

The molecule can be characterized by potential energy curves showing two minima, associated with LS and HS state (Figure 29). The horizontal displacement of these two potential wells directly relates to the ligand-metal bond length difference between both spin states. The LS state shows a lower energy than the HS state. Moreover, since vibrational frequencies of the metal-ligand bond are higher in LS than in HS state, LS potential well is stiffer than the HS well [Gütlich2004].

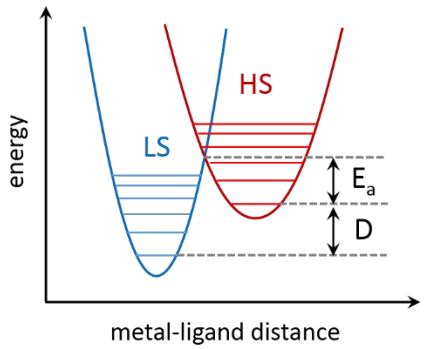


*Figure 29: Scheme of potential wells for both LS (blue) and HS (red) states in a spin-crossover material. Horizontal lines are the different levels lying within the wells. D is of the order of the thermal activation $k_BT$. $E_a$ represents the activation energy required for the molecule to cross the potential barrier when relaxing from HS to LS.*

Thermo-induced spin transitions proceeds through thermal population of the HS state. The transition can be described by Boltzmann statistics, with entropy variation standing as the driving force of the transition. However, if this approach describes well the behavior of isolated molecules in solution, it fails to reproduce the observations made in the solid state, such as abrupt transitions or the existence of a hysteresis. Actually, a proper description of phenomena in the solid state must involve molecular interactions, at the origin of such cooperative effects.

The spin transition of a molecular unit induces a discrepancy of volume, related to the size difference between LS and HS state. This molecule thus acts as a punctual defect and generates a displacement field in the crystal, interacting with other spin units throughout the elastic medium. Therefore, this description attributes the origin of cooperativity to the volume change at the transition (around 5%), which induces elastic constraints in the material, responsible for the observed effects in the solid state. In this approach, cooperativity will be all the more significant given that volume change associated to spin transition is important. This model settles in the frame of a mean field approach, describing cooperativity through long-range interactions.

Considering Fe complexes, structural reorganization is often weaker in $Fe^{III}$ systems, since volume change at the transition is smaller than in $Fe^{II}$ compounds (0.15 Å compared to 0.2 Å in average) and thus easier to accommodate by the crystalline lattice. However, several $Fe^{III}$ complexes such as $[Fe^{III}\text{-}(3\text{-MeO-SalEen})_2]PF_6$ show a weak hysteresis at the transition, witnessing cooperativity [Hayami2001, Tissot2011]. This characteristic of the $[Fe^{III}\text{-}(3\text{-MeO-SalEen})_2]PF_6$ compound makes it a designated candidate to study elastic cooperativity effects in photo-induced phase transitions.

### III.1.d. From microscopic to macroscopic properties

Spin switching at the molecular scale translates to macroscopic changes of the material properties, thus allowing to probe the spin transition using several techniques. Hence, magnetic susceptibility measurements characterize the variation of the magnetic state, which is directly induced by the spin switching [Tissot2011]. Other indirect probes allow for the monitoring of spin switching. As stated above, when going from LS to HS state, the population of antibonding $e_g$ orbitals induces an increase of the metal-ligand bond length. The electron transfer is coupled to a sizeable structural reorganization of the inner- and outer-sphere of coordination. These deformations are accompanied by a modification of vibrational properties, which can be probed by Raman or infrared spectroscopy [Moussa2007a, Moussa2007b]. At higher space scale, structural deformations are accompanied by a change of the unit cell volume. X-ray diffraction in the solid state allows characterizing this reorganization. The change in population of the d orbitals of the metal induces a modification of the optical properties of the sample. The spin transition is thus

often accompanied by a change in color, which can be used to monitor the phenomenon using optical reflectivity or transmission [Collet2012]. A change in resistivity is also visible, with the dielectric constant changing by up to 10%.

### III.1.e. Photo-induced spin transition by an ultrashort laser pulse

Not only are spin-crossover materials interesting for potential applications (e.g. as optical storage devices [Galle2013], or as actuators [Shepherd2013]), but their prototype bistable character make them good candidate for being case studies in the development of universal models describing phase transitions in volume-changing materials.
In the majority of compounds where bistability is shown due to a thermal spin transition, it is often possible to photo-induce the switching between the two states involved in the thermal transition. In that frame, the LIESST (Light-Induced Excited Spin-State Trapping) effect was evidenced in 1984 in the $[Fe^{II}(ptz)_6](BF_4)_2$ compound by Decurtins et al. [Decurtins1984]. At low T, laser irradiation of the LS state allows for the switching to a long-lived metastable HS state (Figure 30).

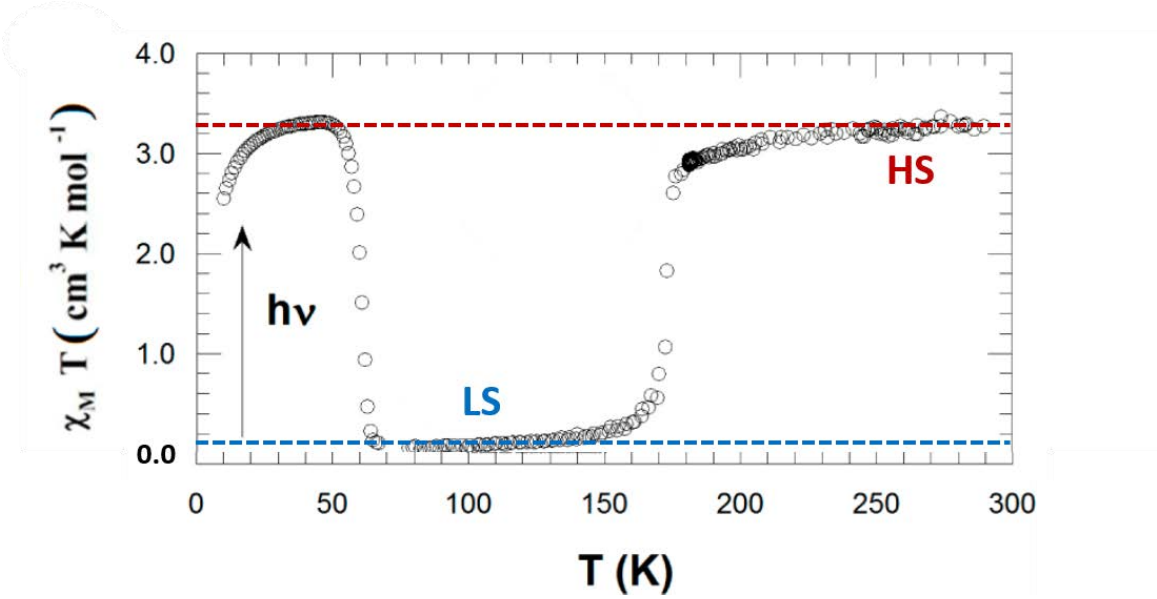


*Figure 30: adapted from [Bertoni2015a]. Thermal evolution of the magnetic susceptibility-temperature product of $[Fe^{II}(phen)_2(NCS)_2]$ single crystal, showing a thermal spin transition around $T_c$ = 180 K. The value above $T_c$ is typical of paramagnetic HS state (red dashed line)), whereas the value under 180 K is characteristic of the LS diamagnetic state (blue dashed line). Below 60 K, the HS state is reached by continuous light excitation of the LS state at 650 nm, represented by the hν -labelled vertical arrow.*

The mechanism proposed by Hauser [Hauser1991] states that light irradiation at 20 K of the LS complex induces the population of an excited triplet state, which undergoes a non-radiative decay (by intersystem conversion) towards another triplet state. The system then evolves either to LS or to HS state, where it remains trapped due to the significant difference in the metal-ligand bond length. This proposition leans on the fact that direct switching from singlet to quintet state is strictly forbidden. Therefore, intermediate triplet states seem necessary to explain the whole mechanism of LIESST effect. Since one photon switches one molecule in the LIESST effect, the phenomenon is linear with laser excitation density. The reverse LIESST process was also evidenced [Hauser1986], where the irradiation of the metastable HS state leads to an excited state, which then decays towards LS state.

## III.2. Numerical model to describe transition dynamics in spin-crossover crystalline materials

### III.2.a. Elastic interactions to describe cooperative effects

Several theoretical models have been elaborated in order to describe the behavior of spin-crossover systems. In the case of non-interacting complexes, the thermal transition and relaxation between the HS and LS states could be reproduced by simply considering the Boltzmann distribution between the vibronic levels of these two states. However, more complex phenomena such as abrupt thermal transitions accompanied by hysteresis, sigmoidal relaxation curves or in our case photoexcitation processes, required the introduction of the concept of cooperativity.
In 1971, Wajnflasz was the first to propose Ising-like models to describe spin-crossover complexes [Wajnflasz1971]. Doing so, he introduced intermolecular interactions through an Ising-like Hamiltonian and was the first to predict a first-order transition associated with spin change. This approach was the precursor of further elastic models, by stating that interactions between spin units are not of magnetic origin, but rather arise from strong bond length variation associated with spin switching. Following the pioneering work of Wajnflasz, Spiering et al. pointed out that interactions between spin-crossover units are not of magnetic origin, but rather result from the elastic interactions due to the large metal–ligand bond-length and molecular volume changes accompanying every spin change [Spiering1982]. They built a new theoretical description, based on elastic interactions arising from lattice distortions due to molecular size difference between LS and HS states. Unlike previous studies, this model incorporates the mechanism of global and inhomogeneous deformation of the system. Different volumes of the molecules in the two spin states are at the origin of the elastic stresses in the lattice, which leads to cooperative effects and thus variation of the switching probability with the HS fraction. The larger volume of HS molecules induces elastic stresses in its surroundings, thus changing the probability of other molecules to switch state. This new description replaced the ambiguous short- and long-range interactions with elastic interactions. This led to a new class of models, so-called “ball and spring models”, which consider the molecules as rigid and usually unfixed spheres, linked by springs. These springs can be compressed or elongated upon spin transition, resulting in an infinite number of possible interaction terms between molecules. Different ball and spring models have been independently proposed by a few groups of researchers working in the field of spin-crossover materials [Mikolasek2014, Enachescu2018]. Despite a common basis linking these models, formal differences can be noticed in the form of Hamiltonians used in the theoretical approaches, in the internal structure and shape of the samples, as well as in the methods used in the simulations.

### III.2.b. The mechanoelastic model

Among various models, the so-called mechanoelastic model makes use of molecular dynamics and Monte-Carlo methods [Enachescu2017]. In the following, we use this model to complete and rationalize our experimental study.
In the “ball and spring” concept, the spin units corresponding to molecules are represented as rigid spheres, interacting via connecting springs (Figure 31a,b). The latter can be either compressed or elongated relative to their equilibrium length, depending on the relative positions of the neighboring spheres (Figure 31c,d). The size of the spheres reflects the spin state of molecules: HS state is represented by a sphere showing a larger radius than LS state, with a ratio of radii corresponding to the ratio of <Fe-N> bond length in both states. The variation of volume due to spin switching produces instantaneous elastic force on its neighboring springs, which

consequently determines a shift of its closest neighbors (Figure 31) and subsequently propagates to all other molecules in the system. Therefore, the local positions of all molecules change with every single molecule switching from one state to another, and so do the volume and shape of the whole system. In such a configuration, the effect of one single switching process propagates through the entire system and its effects manifest themselves (although to lesser extent) at long-range distances, despite the short-range nature of elastic interactions. Effective interactions not only depend on spin state of interacting molecules and on HS fraction, but are also directly impacted by elastic distortions arising from volume change at spin transition. The elastic constant of springs acts as both a short- and a long-range parameter. Thus, a single parameter accounts for cooperativity in the system, rendering a larger effect on neighboring molecules on one hand and propagation throughout the whole sample on the other hand.

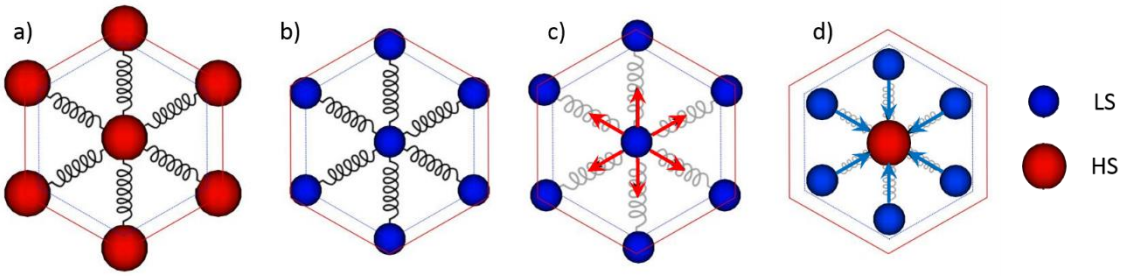


*Figure 31: Scheme of the unit cell as represented in the mechanoelastic model. a) HS unit cell, with no pressure acting on the central molecule. b) LS unit cell, with no pressure acting on the molecules. c) LS unit cell, but with displaced outer molecules, exerting a pulling force on the central molecule: the latter is more likely to switch to HS. d) displaced LS molecules exerting a pushing force on the neighboring HS molecule, tending to make it switch to LS. Many different configurations can occur, with neighboring molecules partially in LS and HS states.*

Spheres are distributed in a two-dimensional triangular lattice, in hexagonal, circular or rectangular shapes. This triangular structure - showing six nearest-neighbors - is more stable than a squared one – with four neighbors. For the rectangular lattices, an additional diagonal spring constant between the molecules situated at the opposite corners has to be introduced in order to ensure geometrical stability of the system. Consequently, the use of a triangular lattice keeps the number of parameters needed to describe the system at a minimum. The local pressure for a given molecule is calculated in a local mean-field approximation as the sum of forces per unit area applied to that molecule by all neighboring springs :

$$= \sum_{hbo \quad pr} - _{ij}$$

with the spring constant, divided by the molecular cross-sectional area . The spring elongation $_{ij}$ is taken positive for compressed springs, favoring LS state and negative for elongated ones, favoring HS state.

The temporal evolution of the system is simulated following a standard Monte Carlo (MC) algorithm. The procedure consists in checking every molecule in the system to verify whether it switches or not during a given time interval. To do so, we first calculate its state-dependent switching probability and then generate a random number $\in (0,1)$. If this number is smaller than the probability, then the molecule is allowed to change its state, otherwise it stays in the same state. A Monte Carlo step is concluded when all molecules in the system have been checked once.

The Hamiltonian of the system writes:

$$= \frac{1}{2}\sum \left( - Tln \right) + \frac{}{2}\sum \quad ^{2}_{,}$$

The first term corresponds to the Gibbs energy as in the Ising-like models, with being the zero-point energy difference corresponding to the enthalpy difference between the two spin states in the case of non-interacting molecules and $. ln(\ )$, where is the degeneracy ratio between LS and HS states, corresponds to the entropy difference. takes the value of +1 for HS and -1 for LS. The second term represents the elastic energy.

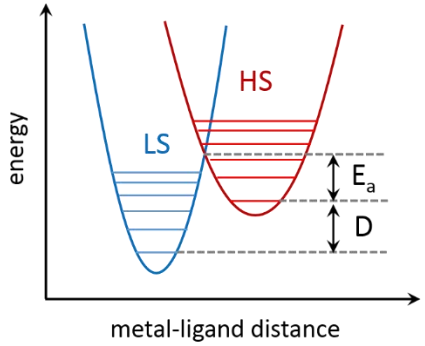


*Figure 32: Scheme of potential wells for both LS (blue) and HS (red) states in a spin-crossover material. D is of the order of the thermal activation $k_BT$. $E_a$ represents the activation energy required for the molecule to cross the potential barrier when relaxing from HS to LS.*

A wide portion of the field of chemical kinetics can be described by the Arrhenius equation:

$$\propto \ xp(- \ / \ )$$

which relates the rate constant (which has the dimension of the inverse of a time) of an elementary reaction to the absolute temperature and the parameter called the activation energy, corresponding to the energy barrier of the $HS \rightarrow LS$ relaxation relative to a global reference state where all molecules are HS (Figure 32). The Arrhenius equation is an empirical relationship, which usually describes kinetic data well. The aim of the Arrhenius equation is to describe the switching behavior of molecules in a system: if some molecules switch, why do not all molecules do the same? Why do some of them behave differently from others in a same assembly? Actually, all molecules are equal and thus have the same probability to switch. However, considering a given time, some of them switch and some do not. The Arrhenius approach states that one molecule must carry a threshold energy to react, and the fraction of molecules with such energy is given by the function $xp(- \ /KT)$. For a first order reaction:

$$LS \rightarrow HS$$

the corresponding differential rate equation writes:

$$-\frac{LS}{dt} = \ _{LS}$$

and thus:

$$_{LS}(\ ) = \ ^{0}_{LS} \ \ (-Kt)$$

In the mechanoelastic model, the probabilities to switch from low to high spin and vice versa are calculated considering an Arrhenius process:

$$_{HS\rightarrow LS} = \frac{1}{} \ xp\left(\frac{- \ \ lng}{2}\right) \ xp\left(-\frac{-}{}\right)$$

$$_{LS\rightarrow HS} = \frac{1}{} \ xp\left(-\frac{- \ \ Tln}{2}\right) \ xp\left(-\frac{+}{}\right)$$

is determined from experimental measurements. is a scaling constant, related to the inverse of high temperature relaxation rate. is a scaling factor between the local pressure and the activation energy of the individual molecule, with the local pressure acting on molecule and defined above. For molecules standing at the edges of the assembly, an external pressure is also taken into account to ensure the stability of the system.

The probability of transition of one molecule thus depends on pressure exerted by its neighbors. An elongation of the spring tends to make it switch to HS, whereas a shortening of the spring favors LS state. The coefficient represents the "cooperativity factor", used to modulate the weight of pressure compared to activation energy in the switching probability. Since represents both short- and long-range interactions in the system, the determination of its value is of paramount importance to simulate properly the experimental observations. An estimation of the elastic constant value is based on experimentally observed influence of both external pressure and cooperative effects on ligand-field strength, and therefore on energy difference between the two spin states [Enachescu2016]. The estimation of ligand-field strength effects and the measurement of the bulk modulus (considering that most of volume contraction is absorbed by the lattice, the compression of much harder <Fe-N> bonds being much smaller), gives a value of the elastic constant $\sim[5-10]$ . $^{-1}$.

When evaluating the switching probability of a molecule, three scenarios can be encountered. First, if all neighboring springs are at their normal length, the local pressure applied on the molecule is zero and neither state is favored. Second, if the springs near a LS molecule are elongated, then they will act towards increasing the molecular volume, so the probability that this molecule switches to the bigger volume HS state is higher (Figure 31c). This corresponds to a negative local pressure in the probability $_{LS\rightarrow HS}$. Reversely, if in the third case the springs near a LS molecule are compressed, the probability that the molecule switches to the HS state is lower.

The equilibrium configuration is then found by iteratively solving the following $(2*\ )$ system of coupled differential equations, (n being the number of molecules):

$$\frac{^2}{^2} = xi - \frac{}{dt}$$

$$\{\frac{^2}{^2} = yi - \frac{}{dt}\}$$

, is the sum of (elastic) forces acting on the particle in the direction ( , ) and is a damping constant.

The elastic model proved its robustness and reliability through several studies of spin-crossover complexes, at equilibrium or out-of-equilibrium [Konishi2008, Nishino2011, Enachescu2017].

## III.3. The $[Fe^{III}(3\text{-MeO-SalEen})_2]PF_6$ compound

### III.3.a. Compound structure

$[Fe^{III}(3\text{-MeO-SalEen})_2]PF_6$ complex (for the sake of brevity, the compound will be designated as FeSalEen in the following) belongs to a family of compounds, first studied by Hendrickson et al. [Haddad1981]. FeSalEen crystallizes in the triclinic $_{-1}$ space group.

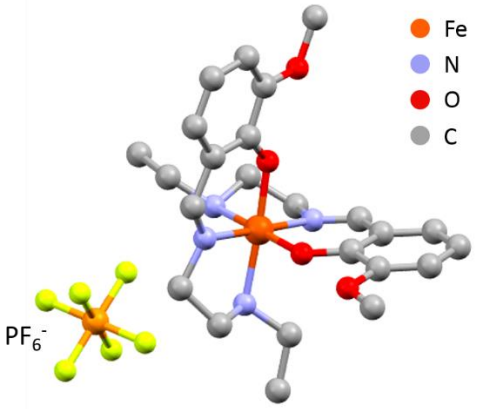


*Figure 33: FeSalEen molecular configuration at 120 K, in the LS state. Central Fe atom (in dark orange) is surrounded by two tridentate ligands, each of them forming 2 nitrogen and 1 oxygen bond with $Fe^{III}$. Hydrogen atoms are not shown for clarity. The neutrality of the assembly is ensured by the $_6^-$ counter-ion (in light orange and yellow).*

The $Fe^{III}$ metallic ion is placed in an $[FeN_4O_2]$ coordination sphere composed of two tridentate ligands (Figure 33) with H-3-MeO-SalEen being the condensation product of 3-methoxy-substituted salicylaldehyde and N-ethylethylenediamine. The <Fe-N> bond length increases by 0.0144 Å between the 120 K LS state and the 300 K HS state. The swelling of molecules at the spin transition leads to structural deformations and to an increase of the unit cell volume of around 2%, between LS volume (1381.4 $Å^3$) and HS volume (1403.8 $Å^3$). Except for the triclinic angle β, all cell parameters increase at the spin transition when increasing temperature.

The crystal packing of the material is made of cationic layers, separated by anionic $PF_6^-$ layers (Figure 34). Within the cationic planes, ferric complexes are arranged as dimers, via face-to-face $-$ interactions and C-H edge-to-face $\cdots$ contacts. The pairs of $PF_6^-$ anions interact with eight distinct ferric assemblies (Figure 34, 4 in the plane and 4 out-of-plane). The cohesion of the overall structure is achieved through intermolecular contacts or hydrogen bondings between the neighboring cations and anions [Tissot2011].

Upon decreasing temperature, the strength and number of contacts between ligands and $PF_6^-$ anions increases under the effect of cell contraction and $PF_6^-$ reorientation. Direct contacts between adjacent cations also appear, playing their part in the cooperative interactions between spin-transition centers. This extended three-dimensional network of interacting complexes mediated by dense and strong molecular contacts contribute to the cooperative transformation of the solid.

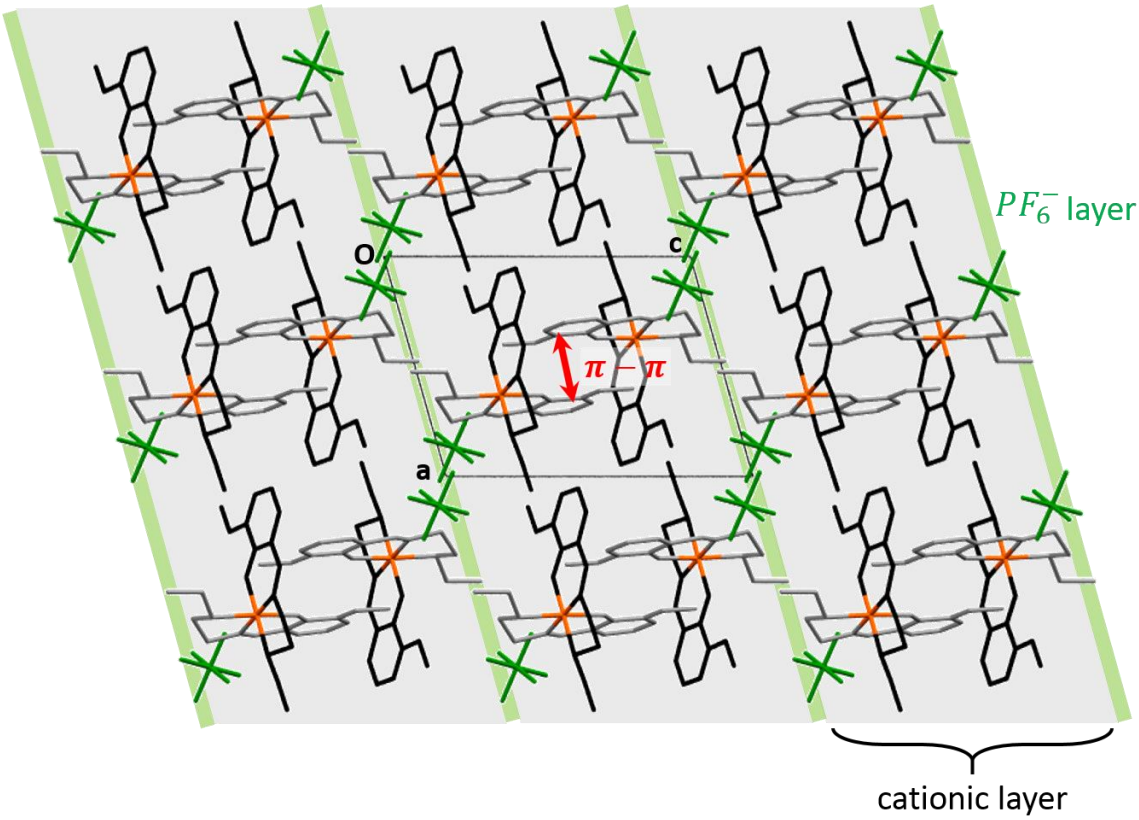


*Figure 34: View of crystal packing in the (a,c) plane. Black lines represent the unit cel. This view underlines π-π stacking interactions (in red) between aromatics cycles in the (a,c) plane. $PF_6^-$ pairs (in pale green) interact with 8 cationic centers (in orange): 4 in the plane and 4 out-of-plane. The methyl tail of the blue ligands also interacts with $PF_6^-$ unit, preventing strong rotation of the molecule within the unit cell.*

In the solid state, FeSalEen undergoes a thermal spin transition from LS (S = 1/2) to HS (S = 5/2). This is visible in Figure 35, showing magnetic susceptibility-temperature product versus temperature, directly related to spin state. Around T = 164 K, shows a sharp jump, witnessing spin state switching. The strongly first-order transition is accompanied by a small hysteresis, about 3 K wide, between the up-conversion temperature $_{\uparrow} = 165.5$ and down-conversion temperature $_{\downarrow} = 162.5$ [Tissot2011] (Figure 35). This witnesses an unusually significant cooperativity for an $Fe^{III}$ compound.

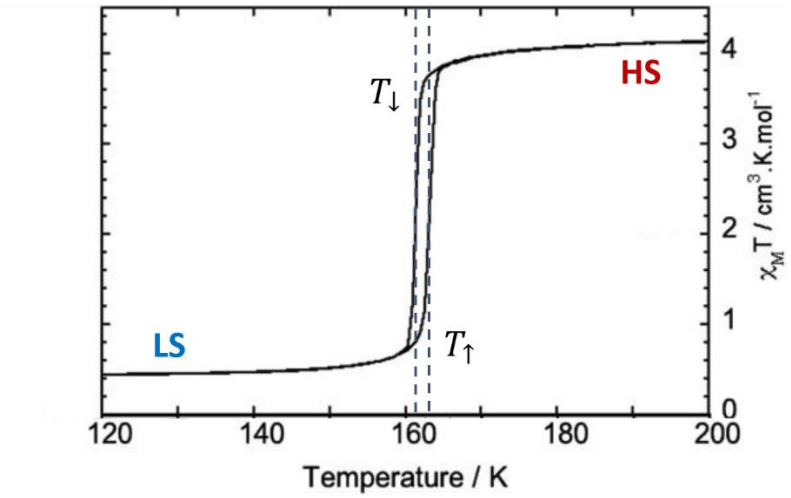


*Figure 35: adapted from [Tissot2011]. Magnetic susceptibility-temperature $X_MT$ product measured versus temperature in a bulk sample of 50 µm size. The $X_MT$ product is directly proportional to HS fraction and witnesses a small 3 K hysteresis loop around 164 K in FeSalEen bulk.*

Despite strong structural changes occurring at the molecular level, no symmetry breaking is observed at the transition, as it is often the case in spin-transition systems [Guionneau2004]. The spin transition in FeSalEen is therefore isostructural.

### III.3.d. Photo-induced spin transition in FeSalEen single crystal

In 2011, the first photo-switching of spin state by a femtosecond laser was evidenced in a single crystal by Tissot et al. [Tissot2011]. At 140 K, in the LS state, the sample was photo-excited at 880 nm wavelength with a 100 fs laser pulse. The compound showed weak but clear response to light excitation, monitored by transient optical transmission (Figure 36).

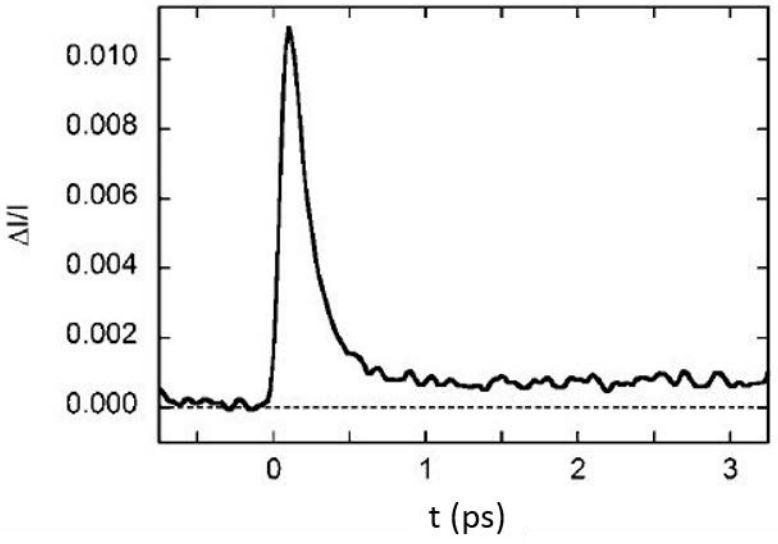


*Figure 36: from [Tissot2011]. Relative variation of the transmitted intensity ΔI/ , measured at 750 nm. The sample shows clear response at ps time scale.*

However, the attempt to increase the fraction of photo-switched molecules by increasing the laser energy density led to sample damage. A possible approach to overcome this limitation consists in reducing the size of crystals, hence optimizing laser penetration depth and subsequent spin conversion.

## III.4. Previous optical studies of photo-induced phase transition in FeSalEen crystals

The model describing spin-crossover molecular materials (part 2 of this chapter) points out the importance of volume change inducing elastic constraints at the spin transition. As was described in chapter I.2.b, this volume expansion requires the deformation of the unit cell, associated with long-range atomic motions. The propagation of this collective phenomenon is governed by the speed of sound . For the same material, the acoustic time scale – corresponding to the completion of these long-range atomic motions throughout the sample – will vary depending on the system size , as $_{ac} = /$ . Therefore, the down-sizing of crystals raises new challenging questions about the fundamental mechanism of photo-induced spin transition, asking whether and how the system size might influence the transition dynamics through cooperative effects.
The study presented hereinafter focuses on several samples of different sizes, described in the table below.

| Sample name | Size | Experiment |
|---|---|---|
| single crystal OR | [(300±50) x (200±50) x (15±5) µm$^3$] | time-resolved optical transmission |
| single crystal XRD | ≈ 100 µm in the long dimension | x-ray diffraction versus temperature |
| microcrystals OR | [(7.5±2.1) x (0.64±0.15) x (0.21±0.03) µm$^3$] | time-resolved optical transmission |
| microcrystals XRD | [(2.80±1.02) x (1.12±0.17) x (0.435±0.135) µm$^3$] | time-resolved x-ray diffraction |
| nanocrystals OR | [(950±150) x (270±40) x (35±7) nm$^3$] | time-resolved optical transmission |

To investigate the influence of the coupling between the deformation and the fraction of photo-switched molecules on the HS fraction dynamics, my team performed time-resolved optical spectroscopy on the photo-excited FeSalEen spin-crossover compound in a previous study [Bertoni2016]. Three different sizes of samples were studied: single crystal OR [(300±50) x (200±50) x (15±5) µm$^3$]; microcrystals OR [(7.5±2.1) x (0.64±0.15) x (0.21±0.03) µm$^3$] and nanocrystals OR [(950±150) x (270±40) x (35±7) nm$^3$].

### III.4.a. Synthesis of micro- and nano-crystals

Among the two major techniques employed for molecule-based inorganic solids synthesis, the chosen method to elaborate FeSalEen nano- and microcrystals was by precipitation of particles in an anti-solvent. Single crystal are first obtained by slow evaporation of a methanolic solution of the compound, then the synthesis of particles is performed from the powdered material, by sudden precipitation with an anti-solvent. External parameters such as temperature and anti-solvent composition are varied to design and control the shape and size of particles (Figure 37) [Tissot2012].

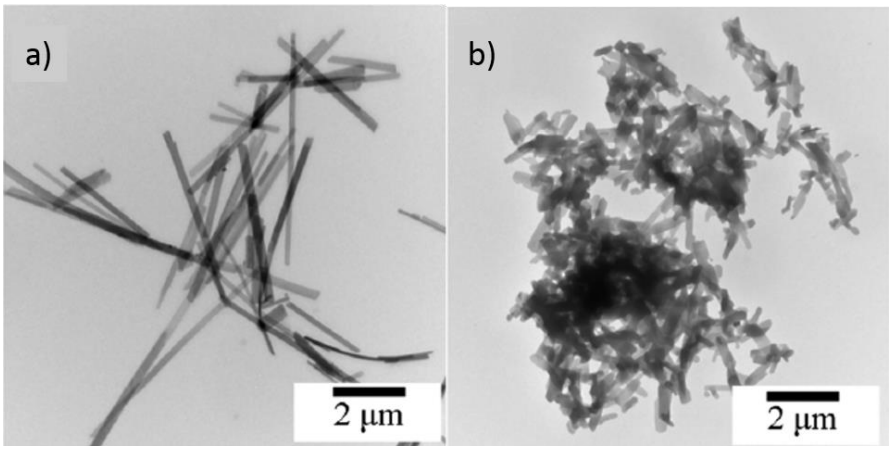


*Figure 37: adapted from [Tissot2012]. TEM images of micro- (a) and nano- (b) crystals.*

A magnetic susceptibility study performed on the obtained nano- and microcrystals [Tissot2012] shows a disappearance of the hysteresis loop for samples of lower sizes than the bulk crystal. Moreover, the transition temperature gets shifted towards low temperature, from 164 to 153 K. The transition is also more progressive in small samples: this asymmetry of the curve might be related to size distribution effects. These observations are consistent with the fact that for cooperative processes completed over a shorter distance, a relative decrease of interaction strength and transition temperature may be expected for smaller systems.
Although slightly affected, lattice and crystallinity, as well as thermal spin-state switching process, were preserved in the compound processed as nano- and microcrystals.
Microcrystals and nanocrystals are polydispersed in polyvynilpyrrolidone (PVP) thin films and deposited on a glass substrate. This morphology prevents oxidization of $Fe^{III}$ complexes and facilitates sample manipulation compared to a powdered compound.

### III.4.b. A multi-step process: nonlinear effects at nanosecond time scale

Nanocrystals OR were photo-excited at low temperature in the LS state, with a Ti:Sa laser delivering a femtosecond laser pulse at a wavelength of 800 nm. Once LIESST effect completed, optical transmission changes relate directly to photo-switched HS fraction $X_{HS}$. The monitoring of $X_{HS}$ after excitation over several temporal decades, from fs to ms, reveals a multi-step process (Figure 38). First, a fraction $X_{HS}^{hv}$ is photo-switched locally through ultrafast LIESST effect within hundreds of fs. During this step, the crystal does not have time to exchange energy with its environment. Then, a second increase occurs in the ns range. This rise of HS fraction happens well after the photo-switching, resulting from the establishment of mechanical equilibrium between the crystal and its environment.

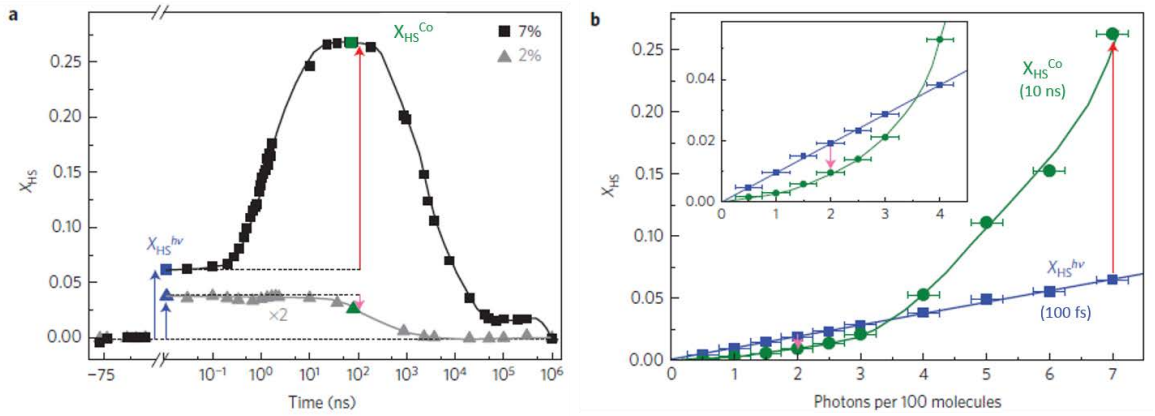


*Figure 38: adapted from [Bertoni2016]. a) Evolution of $_{HS}$ following femtosecond laser excitation (blue arrows) for 7% (black) and 2% (gray, scaled by a factor for clarity) of photoexcited molecules in the nanocrystals. Lines are guides for the eye. The difference between $^{h}_{HS}$ (dotted horizontal line) and $^{Co}_{HS}$ (green symbols) corresponds to relaxation (pink arrow) in the case of low excitation and amplification (red arrow) at high excitation. b) Linear evolution of $^{h}_{HS}$ (measured at 10 ps) and nonlinear evolution of $^{Co}_{HS}$ (measured at 100 ns) with laser excitation density scaled in photons per 100 molecules. The horizontal error bars represent the standard deviation of the mean excitation density. Insert: zoomed in section of the graph below threshold. Pink arrows and red arrow indicate relaxation and amplification, respectively.*

As expected from the linearity of LIESST effect, $X_{HS}^{h\nu}$ measured at ps time scale depends linearly on excitation density, reflecting the local and non-cooperative nature of the photo-switching process (Figure 38). As quantum efficiency of the LS to HS photo-excitation is close to 1 [Bertoni2015], laser excitation density was scaled in photons per 100 molecules. Considering the second step, two regimes are easily distinguishable. When the fraction of photo-switched molecules is low (< 3%), the LS ground state is recovered quickly, within 1 µs. However, at higher excitation density, $X_{HS}^{Co}$ increases by a factor of up to five during the second step. This spectacular amplification clearly witnesses a non-linear character leading to self-amplified response of the material at acoustic time scale. Such an effect observed above a threshold excitation, evidences the active role of the crystalline medium in the photo-induced transition dynamics and the cooperative nature of the process ($X_{HS}^{Co}$ stands for HS fraction at Cooperative step). Initial switching of molecules from LS to HS through ultrafast LIESST effect, induces the local swelling of these molecules. Neighboring LS molecules thus undergo a negative pressure exerted by the locally dilated lattice, tending to make them swell and switch to HS. The probability of spin transition for a given molecule is indeed modulated by local pressure changes, as described by the mechanoelastic model, presented in part 2.b:

$$_{LS\rightarrow HS} \propto \; xp\,(-\frac{+}{\qquad})$$

Following this equation, pulling on an LS molecule amounts to apply a negative pressure, which effectively lowers the activation barrier between LS and HS states and thus favors $\rightarrow HS$ switching. Therefore, the cooperative response $X_{HS}^{Co}$ resulting from simultaneous absorption of several photons far exceeds the sum over individual responses of single events.

### III.4.c. The acoustic hypothesis: role of volume deformation propagation

The aforementioned measurement was repeated for the three different sample sizes single crystal OR, microcrystals OR, and nanocrystals OR. The comparison of the dynamics depending on sample sizes shown in Figure 39 for an excitation of around 5% demonstrates a shift of the second step,

from tens of ns in the single crystal, to less than 1 ns in the microcrystals and nanocrystals. This observation tends to confirm the influence of system size and the acoustic propagation effect.

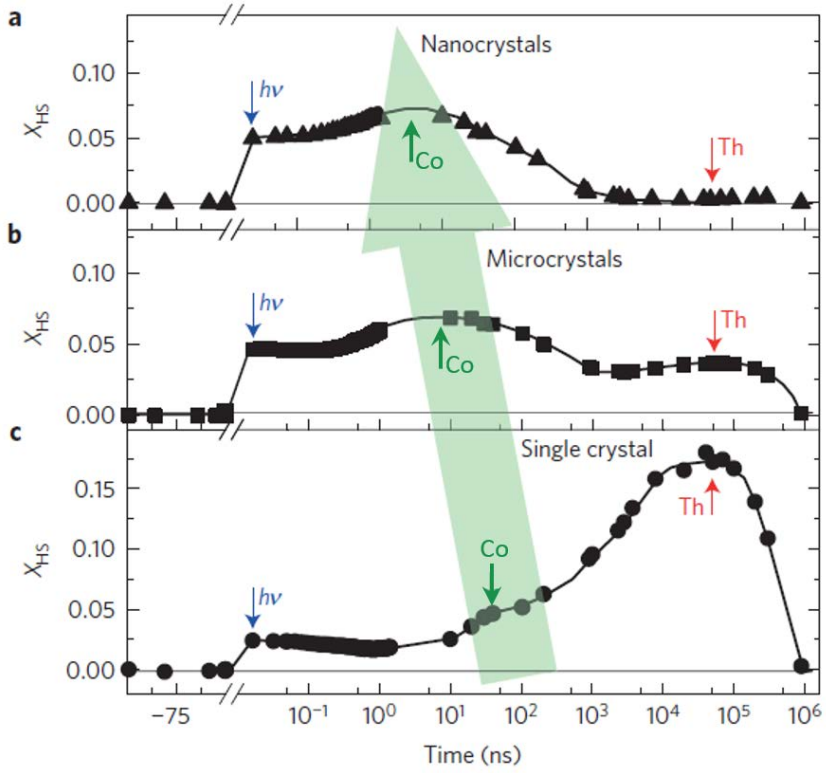


*Figure 39: adapted from [Bertoni2016]. Evolution of $X_{HS}$ following femtosecond laser excitation, for nano-crystals (a), micro-crystals (b) and single crystal (c). Black lines are guide for the eye. hν, Co and Th denote the photoinduced, cooperative and thermal step, respectively. Green arrow indicates the shift of cooperative step as the size of the system decreases.*

Energy redistribution at longer time scale leads to a global temperature increase of the system, leading to a third so-called thermal step. The thermal population of HS state is large for an isolated single crystal, but becomes smaller for micro- and nanocrystals dispersed in thin films. Actually, the surface/volume ratio in this configuration allows for efficient heat transfer with the polymer, which acts as heat sink preventing the rise of a thermal step. Therefore, crystal size might represent a critical parameter in the design and control of the photo-induced spin transition dynamics.

Optical measurements allow monitoring transient HS fraction from short (fs) to long (ms) time scales with a fine temporal resolution. However, information about the structural dynamics remains lacking. Associated to the rise of $X_{HS}^{Co}$, the crystal should indeed undergo a significant lattice expansion arising from an internal pressure. Two main effects should play their part in this expansion: the swelling of molecules switching to HS state in an LS lattice, and lattice heating due to laser energy dissipation into the phonon bath. The complete understanding of the photo-induced spin transition dynamics requires completing the picture given by transient optical transmission about spin state, by performing time-resolved x-ray diffraction of the photo-excited sample to access structural information.

## III.5. Structural study at equilibrium of spin transition in FeSalEen

Spin state switching of constitutive molecules of a spin-crossover molecular crystal leads to macroscopic changes of the material properties. Consequent to metal-ligand bond length variation at the transition, the lattice undergoes structural deformations at the long-range order. We measured static x-ray diffraction versus temperature from FeSalEen crystals to both qualify and quantify the structural changes occurring in this system. Measurements were first performed on a single crystal (single crystal XRD), then on micron-sized samples (microcrystals XRD).

## III.5.a. Static measurement versus temperature on a single crystal

### *III.5.a.i. Unit cell volume*

We measured x-ray diffraction from a single crystal (Figure 40) showing a long dimension of about 100 µm (single crystal XRD) on a Cu diffractometer at λ = 1.5406 Å. Data reduction was performed with the CrysalisPro software [CrysalisPro v. 1.171.38.46, Rigaku Oxford Diffraction (2018)].
The plot of unit cell volume versus temperature, extracted from data reduction, evidences the abrupt thermal transition occurring in FeSalEen, characteristic of a first-order transition (Figure 40). Datasets were measured with 5 K temperature step, reduced to 2 K around the phase transition, ramping down from 200 to 100 K (plain black circles), then increasing the temperature up to 250 K (hollow circles). The cycle in temperature reveals a narrow hysteresis (≈ 3 K) around the transition temperature $_{1/2} \sim 164.5$ , witnessing the cooperative character of the material (Figure 40b).

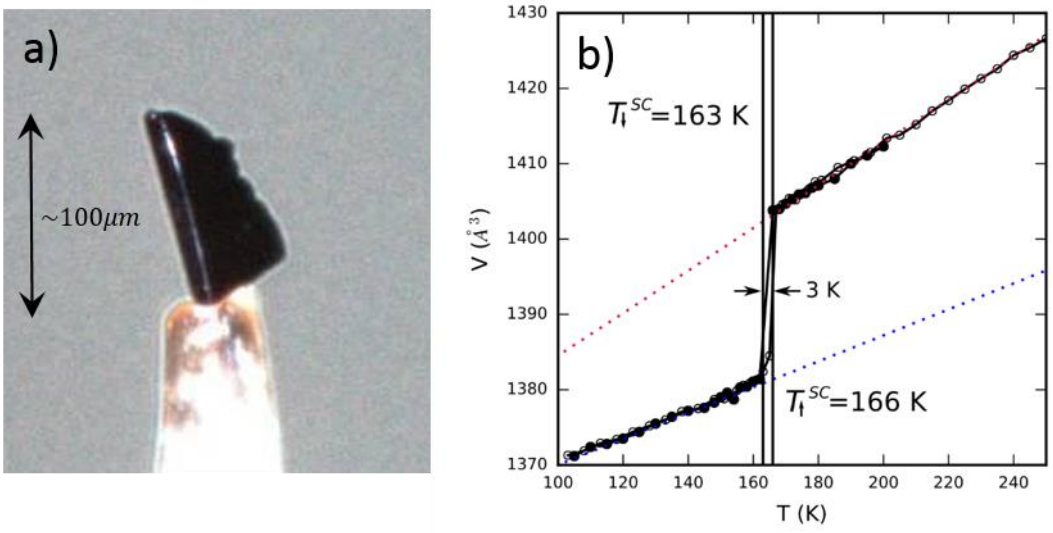


*Figure 40: a) Picture of the FeSalEen single crystal (in black) on a pin in the diffractometer. b) Temperature evolution of the unit cell volume of the single crystal. First order phase transition occurs around 163 K and 166 K upon decreasing and increasing temperature, respectively (black vertical lines). A narrow hysteresis is barely visible in the 2 K thermal resolution of the experiment. Plain and hollow circles represent data points measured while ramping temperature down and up, respectively. This measurement allowed extracting HS (red dotted line) and LS (blue dotted line) thermal expansions of the unit cell.*

Additionally to the abrupt volume expansion at the spin transition, volume change is characterized by a strong thermal dilation across the explored temperature range. This is in accordance with previous observations of unit cell contraction upon decreasing temperature [Tissot2011]. In both LS and HS state, temperature increase is accompanied by volume expansion, denoted by blue and red dotted lines on Figure 40b, respectively. From 250 to 170 K, the volume decreases by about

1.7%. This value is of the same order of magnitude as the volume jump due to spin transition (around 1.6%).

### *III.5.a.ii. Cell parameters evolution*

Unit cell parameters are also extracted from data reduction. Their variation shows thermal expansion (Figure 41), which can be fitted accurately by a linear expansion.

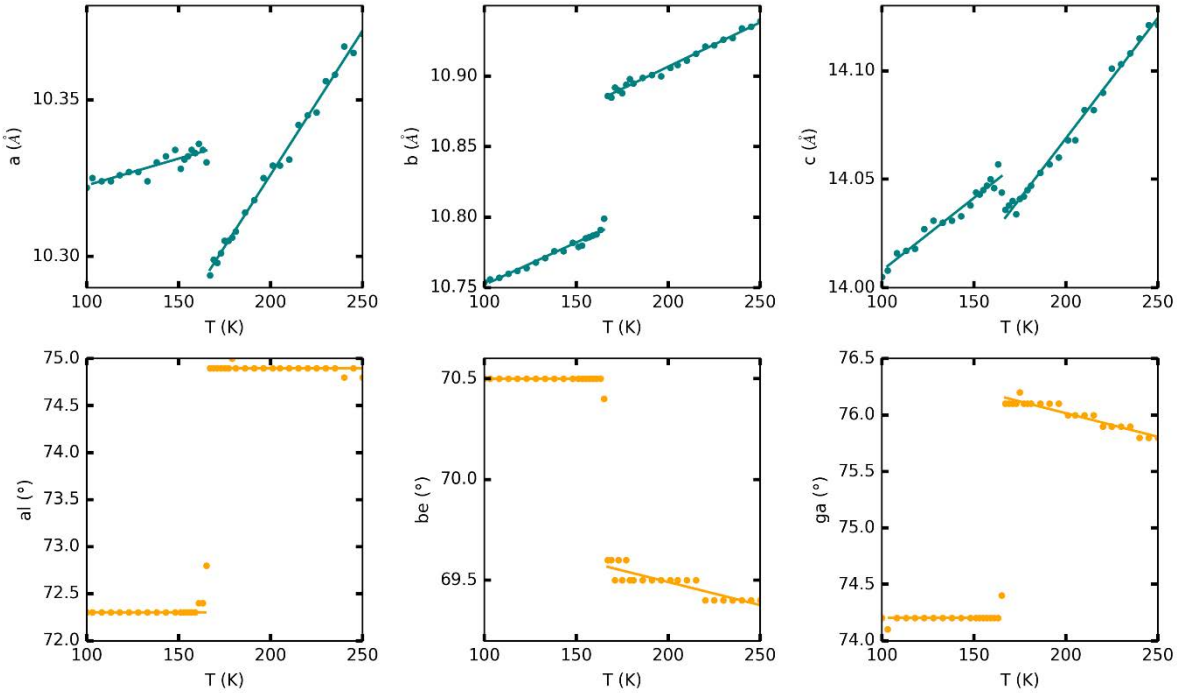


*Figure 41: FeSalEen unit cell parameter versus temperature, under 200-100-250 K cycle, in a single crystal. Dots represent measurement data, lines are linear fits in LS and HS states.*

Coefficients are listed in the tables below. Expansion coefficients of a, b, and c parameters are of the same order of magnitude (≈ $10^{-4}$ Å$^3$.K$^{-1}$), witnessing a rather isotropic thermal expansion of the unit cell. α, β, γ angles seem less likely to vary, which implies that unit cell does not deform significantly by thermal expansion. Angles were considered as constant in the LS phase and showing a weak variation in the HS phase (Figure 41). The overall thermal volume expansion in the LS state is characterized by a coefficient of $0.17\ \text{Å}^3.\ ^{-1}$, smaller than in the HS state, which shows a coefficient of $0.26\ \text{Å}^3.\ ^{-1}$. This originates from the greater softness of the compound in the HS state.

| | a (Å) | b (Å) | c (Å) |
|---|---|---|---|
| LS | 10.3056 + 1.71.10$^{-4}$.T | 10.6919 + 6.01.10$^{-4}$.T | 13.941 + 6.69.10$^{-4}$.T |
| HS | 10.1423 + 9.19.10$^{-4}$ T | 10.7814 + 6.27.10$^{-4}$ T | 13.8468 + 1.11.10$^{-3}$ T |

| | α (°) | β (°) | γ (°) |
|---|---|---|---|
| LS | 72.3 | 70.5 | 74.2 |
| HS | 74.9 | 69.95 - 2.29.10$^{-3}$ T | 76.85 - 4.18.10$^{-3}$ T |

With such a description of the unit cell, temperature can be used as a single parameter, conveniently allowing for the simultaneous description of all unit cell dimensions in both states. The transition being isostructural, i.e. it does not imply any symmetry breaking, unit cell volume is a relevant signature of the phase transition.

## III.5.b. Characterization of micro-crystals versus temperature

### *III.5.b.i. Grazing x-ray diffraction measurement*

To compare with single crystal behavior, we performed x-ray powder diffraction versus temperature, from 293 to 100 K. Control of temperature was managed under nitrogen flow, using an Oxford Cryostream cryostat. We worked with microcrystals of dimensions [(2.80±1.02) x (1.12±0.17) x (0.435±0.135) $\mu m^3$] (microcrystals XRD), of intermediate size compared to nano- and microcrystals in the previous optical study. Microcrystals were dispersed in PVP thin film of about 50 µm thickness and deposited on a glass substrate (Figure 42a), showing the same morphology as in the time-resolved optical experiment.
Since x-ray penetration depth far exceeds the film thickness, avoiding diffuse signal contribution from the glass substrate represents a big concern. By performing grazing incidence diffraction, the effective x-ray penetration depth is significantly reduced and allows getting rid of the major part of signal from the substrate. Two-dimensional diffraction images (Figure 42b) from the polycrystalline sample were recorded on a Rayonix detector and further treated with the method described in chapter II, leading to one-dimensional diffraction patterns.

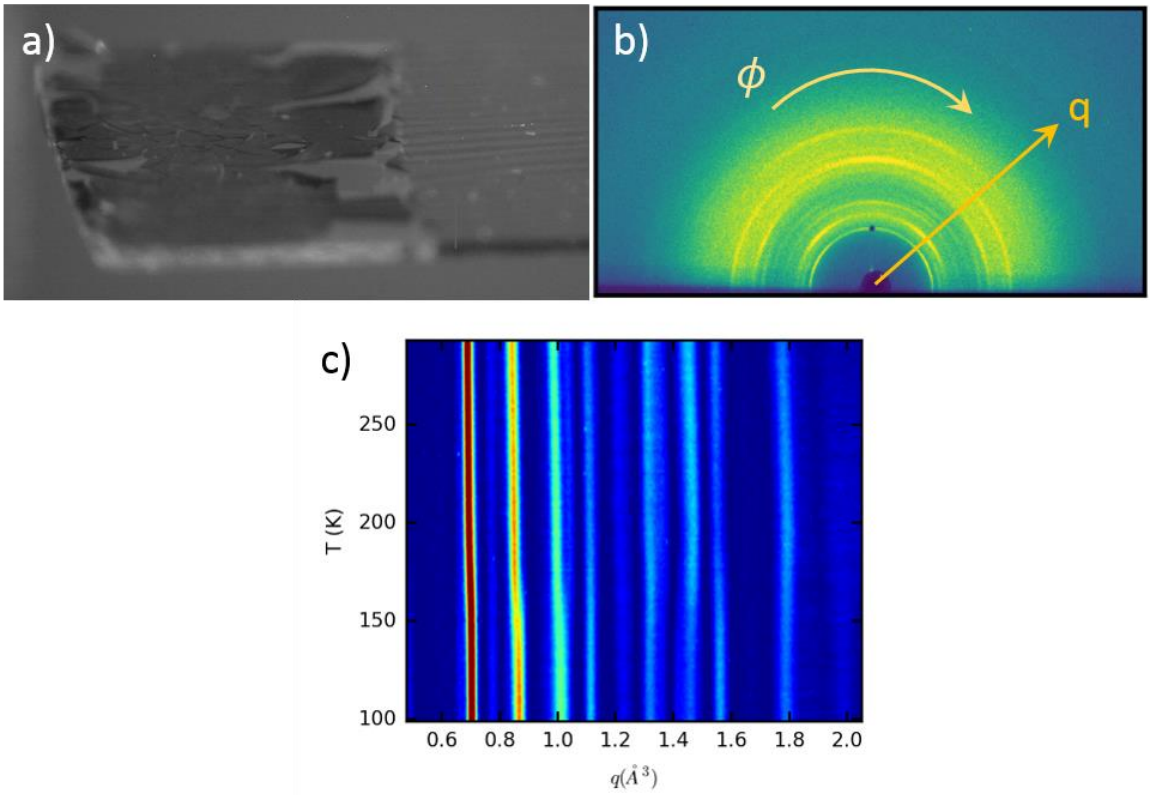


*Figure 42: a) Image of the PVP film on glass substrate, as used in x-ray diffraction experiment. b) 2D diffraction image from the sample. The rings inhomogeneity originates from preferred orientation of the pellet-shaped crystals. c) 1D diffraction patterns, plotted versus temperature. Color scale is blue for low and red for high intensity. Peak shift is clearly visible in the [160 – 130] K region, witnessing volume change.*

The two-dimensional plot of diffraction patterns versus decreasing temperature (Figure 42c) evidences a neat peak shift towards high q, in the region of expected transition temperature (160-130 K), witnessing clear volume change associated to the spin transition of the sample.

Although grazing incidence geometry represents a convenient way to reduce signal from the substrate, it comes with the pitfall of broadening the diffraction peaks significantly, compared to what would be obtained with fine q resolution (Figure 43). The peak profile is so wide that several peaks become buried under the same envelope. Moreover, since crystals are pellet-shaped, they tend to orient with their shortest dimension normal the film plane. Since polycrystalline orientation is therefore not perfectly random, the diffraction rings intensity shows inhomogeneities across the azimuthal angle. This effect of preferred orientation is clearly visible in the two-dimensional diffraction image (Figure 42b), which shows inhomogeneous diffraction rings. Moreover, the FeSalEen complex contains 82 atoms, which implies that 164 atoms are standing within a single unit cell. This situation constrained us to choose the Pawley method for data analysis, therefore not refining atomic positions, for which the resolution was not sufficient.

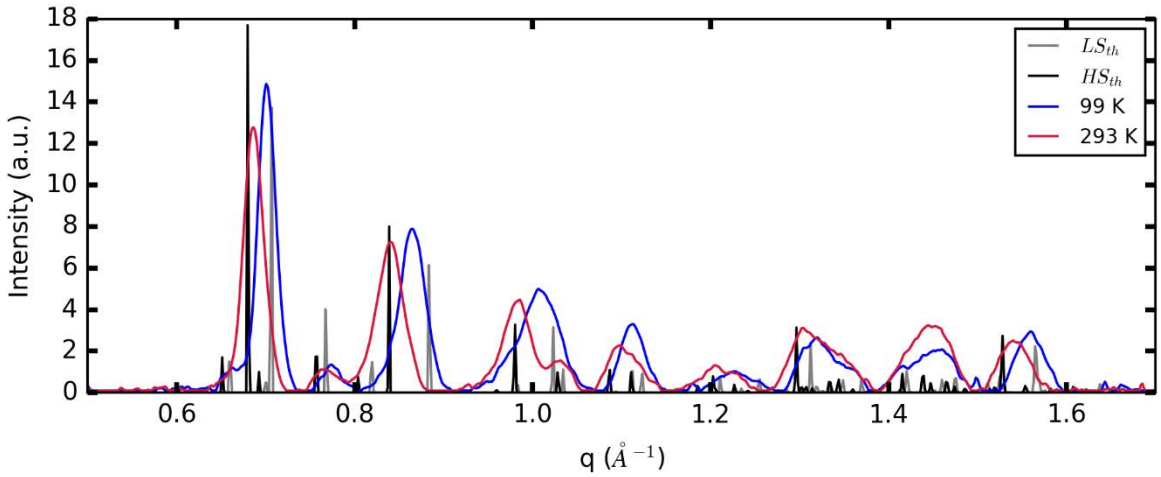


*Figure 43: Diffraction patterns measured at ESRF at low (blue) and high (red) temperature, compared to simulated diffraction patterns from theoretical LS and HS structures ($LS_{th}$ and $HS_{th}$) for fine q resolution. Experimental peak broadening due to large x-ray beam footprint does not allow to separate individual peaks. Absolute intensities of simulated patterns are in arbitrary units.*

### *III.5.b.ii. Pattern analysis*

The approach to describe the x-ray diffraction patterns is the following: using the TOPAS software [Coelho2018] two phases are considered, respectively in LS and HS states. Unit cell parameters of each of these phases are determined using thermal expansion coefficients extracted from single crystal measurement and considering the instruction temperature of the cryostat.
Since the spin transition is isostructral, no peak disappearance/appearance occurs. However, because of molecular reorganization within the unit cell, due to < Fe – N > bond length change, relative intensities of peaks in LS and HS state differ. At room temperature, the sample is fully in the HS state. Using the Pawley method with cell parameters calculated at 293 K, we extracted the peaks intensities corresponding to the HS phase. These intensities were then fixed, defining an effective fixed structure.
At 100 K, whereas single crystal measurement tend to prove that the sample is in the LS state, it was not possible to fit the pattern accurately considering LS phase only. Actually, it seems that there is a non-negligible residual HS fraction at this temperature. Therefore, we considered two phases to describe the low temperature pattern:

- an HS phase with already defined peaks intensities and which unit cell parameters at 100 K were calculated using linear thermal expansion;

- an LS phase, with unit cell parameters at 100 K calculated from thermal expansion extracted from the single crystal measurement. Peaks intensities corresponding to the LS phase were extracted with the Pawley method.

For intermediate temperatures, peaks intensities of both phases were fixed and the total diffraction pattern represents the sum of individual contributions from LS and HS phases, weighed by their respective fraction. The temperature was fixed to the instruction value of the cryostat. We thus refined the phase fractions, consisting in a multiplying factor for peaks intensities, as the only free parameters. This method of analysis allows extracting the evolution of both volume and HS fraction versus temperature in the thin film sample (Figure 44). The fraction of residual HS phase at 100 K was found to be around 30%.

An attempt to free the temperature parameter was also tested, but the difference in temperature and phase fractions in this case was small compared to the fixed-temperature scenario.

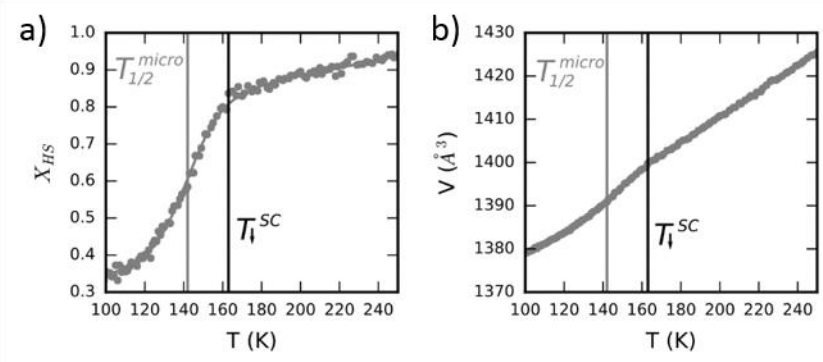


*Figure 44: a) HS fraction versus decreasing temperature, extracted from x-ray diffraction measurements at ERSF. b) Mean volume of the microcrystals versus temperature, as extracted from x-ray diffraction. Vertical gray line represents transition temperature as extracted from x-ray diffraction. The transition is clearly spread out compared to the single crystal case.*

The transition temperature in microcrystals was found to be $_{1/2} \sim 142$ , shifted from the single crystal value by roughly 22 K. Actually, a shift of the transition by around 10 K due to size-reduction effects was already observed in this compound under microparticle form [Tissot2012]. This effect most probably originates from polymer constraints and particle size distribution in polycrystalline sample [Tissot2011, Molnar2018]. Several HS molecules are subject to an effective pressure gradient and their temperature is thus shifted towards low temperature, spreading the transition curve compared to what is observed in a single crystal (Figure 44) [Tanasa2014]. Moreover, it may exist an uncertainty of several Kelvin degrees in the absolute temperature given by the cryostat, as was seen when freeing the temperature parameter in the diffraction patterns analysis. The addition of these effects may explain the observed discrepancy of the transition temperature values in bulk and thin film samples.

### *III.5.b.ii. Comparison with magnetic measurement*

Magnetization-temperature product ($MT$) is directly related to the spin state. The measurement of $MT$ with a SQUID apparatus (Superconducting Quantum Interference Device) shows a thermal evolution similar to the one extracted from x-ray diffraction analysis, but shifted by $\sim 14$ . Several factors may explain this discrepancy. As already stated, absolute value of temperature given by the cryostat might be off by few degrees. Moreover, a positive shift of the transition temperature is often observed in such magnetic measurement, when thermalization is not completed between two points of measurement in temperature [Tissot2012(SI)].

Discarding the temperature shift, the comparison of $MT$ data with HS fraction extracted from x-ray diffraction measurements shows a good agreement between both (Figure 45). This observation strengthens the validity of the method of analysis used to interpret the x-ray data measured on microcrystals.

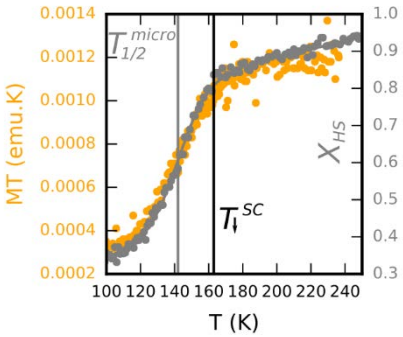


*Figure 45: HS fraction extracted from x-ray diffraction measurements at ERSF (in gray). MT measurement shifted by -14 K (orange) shows good agreement.Gray and black vertical lines represent temperature of transitions as extracted from x-ray diffraction on microcrystals and single crystal, respectively.*

## III.6. Time-resolved x-ray diffraction of the photo-induced transition in microcrystals

### III.6.a. X-ray diffraction measurement

Once having characterized thermal behavior of our sample and having developed a robust method of analysis to extract structural and spin state information from the x-ray diffraction data, we performed time-resolved x-ray diffraction of photo-excited spin transition in FeSalEen. This experiment was conducted at the ID09 beamline of the European Synchrotron Radiation Facility (ERSF) [Wulff2002], presented in chapter II.2.b.

Fast rotating choppers were used to isolate x-ray single pulses (each 100 ps long) at 1 kHz repetition rate. A fast shutter was used to lower the frequency to 40 Hz. The x-rays were partially monochromatized by using a multilayer monochromator, resulting in 1.5% bandwidth centered at 18 keV (λ = 0.6888 Å) and focused by a toroidal mirror to a size of [0.1 x 0.06] mm². In order to reduce the x-ray beam footprint on the sample, the last slits (≈ 0.6 m from the sample) were closed vertically to a 0.02 mm gap.

Laser beam size was (0.23 x 1.2) mm² with 11° incidence angle, leading to (0.23 x 6.3) mm² spot size on the sample, corresponding to an area of 1.44 mm². Laser wavelength was set to 800 nm, corresponding to the same photon energy as in the previous optical pump-probe experiment.

The pump-probe experiment was run with a repetition rate of 40 Hz. To ensure that laser energy dissipates within the 25 ms interval between two laser pulses, and thus that no residual signal builds up from shot to shot, we recorded a “reference pattern” at negative time delay $= -5\ ns$. This reference was then compared with an “off” pattern, recorded in the absence of laser, as was described in chapter II.3.a of this manuscript. Here, we ensured that amplitude of the signal difference between off and reference stands in the noise of the measurement.

XRD patterns were recorded under synchronized laser excitation at 100 K - where the system is in majority LS in the steady state - from hundred picoseconds to millisecond time scale.

Since ESRF delivers x-ray pulses of about $\sim 70\ ps$, diffraction patterns were recorded for time delays ranging from 50 ps to the ms.

### III.6.b. Pattern analysis

The major difference between LS and HS patterns (gray curve on Figure 46) consists in a shift of the Bragg peaks towards low q values when switching from LS to HS state, as is shown by vertical lines in Figure 46, corresponding to LS (blue) and HS (red) peaks positions. Moreover, increase of unit cell volume due to thermal expansion would also induce a peak shift towards low q. The time-resolved differential signal recorded under photo-excitation at 100 K (Figure 46) shows a bipolar shape, with intensity increasing towards low q values and decreasing towards high q. This is characteristics of a peak shift towards low q, witnessing an early volume expansion at t < 1 ns.

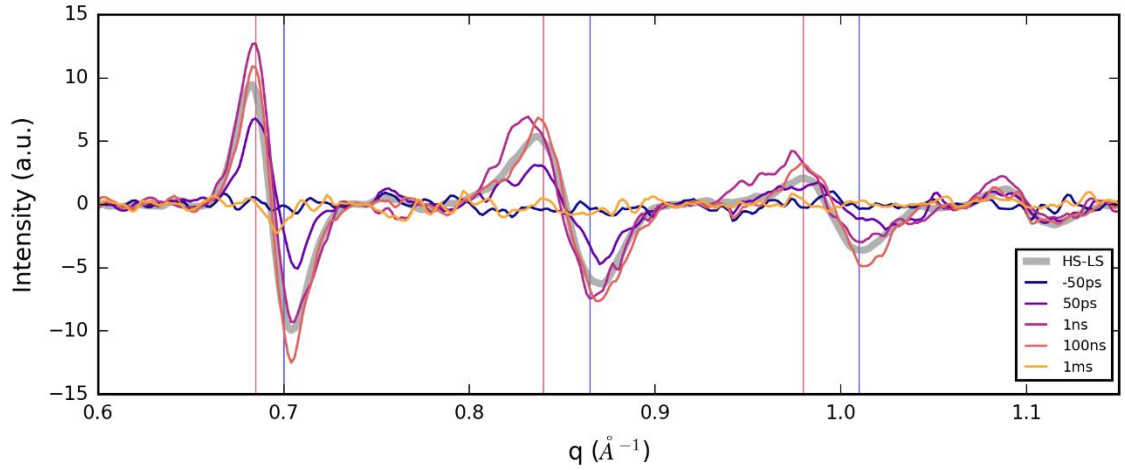


*Figure 46: Time-resolved difference signal for several delays. The difference between steady HS and LS patterns is shown in gray for comparison. Vertical red and blue lines show peaks center for high (HS) and low (LS) temperature patterns, respectively.*

We performed Pawley refinement of time-resolved diffraction patterns, considering a mixture of LS and HS phases. We used fixed peaks intensities determined from the temperature measurement and thermal expansion coefficients calculated from unit cell parameters of the single crystal.

Since the crystal structure is triclinic, all cell parameters change at the spin transition, as it was seen in the thermal evolution in part 5.a.ii. We thus allow the overall volume to change by freeing the temperature parameter. Hence, the two fitting parameters were:

1. an effective “temperature” parameter, directly related to volume change,
2. the HS phase fraction, extracted from relative intensities of peaks.

This refinement, repeated for patterns at each delay, allowed reconstructing volume and HS fraction $X_{HS}$ dynamics under photoexcitation (Figure 47).

### III.6.c. Comparison with time-resolved optical measurements

Propagation time of structural deformation at the long-range distance is ruled by both the sound velocity in the material and the distance over which the deformation has to propagate within the sample. In our case, typical sound velocities values in spin-crossover molecular materials stand around v ≈ $4.10^3$ $m.s^{-1}$ [Parpiiev2017]. These dimensions correspond to propagation time $_{ac} \sim [700\,;230\,;110]\,ps$ over the micro-crystals dimensions.

Volume dynamics observed in differential signal is confirmed by quantitative analysis of the diffraction patterns with the method described above. Volume expansion sets in around the 300

ps range (Figure 47), which corresponds to the time scale of sound wave propagation over the mean crystal dimension – $\sim 1.4\ \mu m/4000$ . $^{-1} \sim 350\ ps$. This observation corroborates the hypothesis of elastic propagation of the unit cell volume variation. At the molecular level, the relaxation from HS to LS state was found to occur later, after few ns [Bertoni2016]. This, compared with our x-ray diffraction results about volume expansion, has the following consequence: volume expansion propagation completes before relaxation does, which means that individual HS molecules do not relax to LS state before the onset of volume increase. We suspect that initially excited molecules are maintained in the HS state, with volume expansion prolonging their lifetime and that more LS molecules will switch towards HS state, favored by dilated volume.

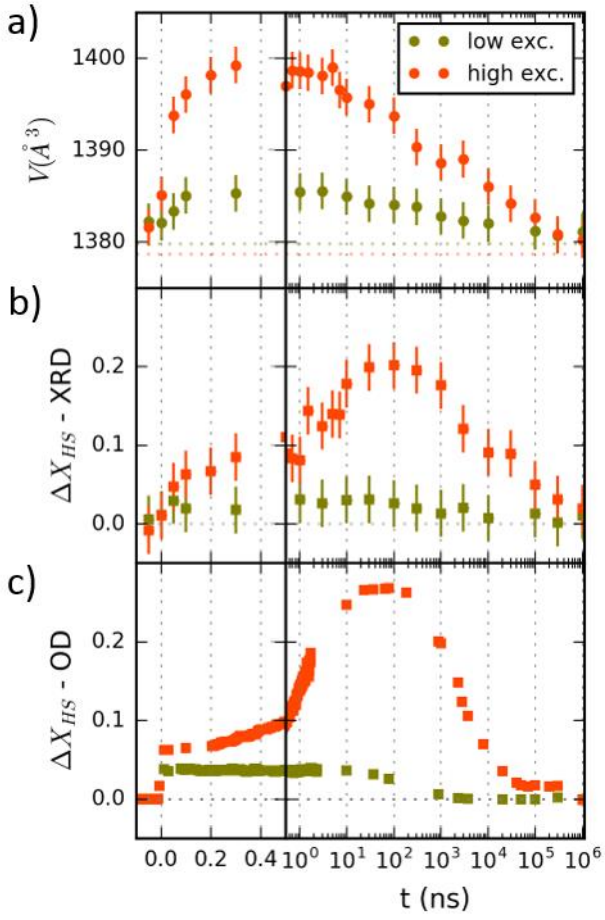


*Figure 47: Volume (a) and photoinduced HS fraction (b) extracted from Pawley refinement of x-ray diffraction data. Dotted horizontal lines represent off values. Photoinduced HS fraction from optical density (OD) measurement is shown in (c) for comparison. Green and orange points were recorded at low (60 µJ.mm$^{-2}$ for XRD and 100 µJ.mm$^{-2}$ for OD) and high (380 µJ.mm$^{-2}$ for XRD and 410 µJ.mm$^{-2}$ for OD) laser excitation density, respectively.*

The comparison between previous results obtained from time-resolved optical transmission [Bertoni2016] and $X_{HS}$ extracted from x-ray diffraction shows a good agreement, both arising at the same time scale (Figure 47). This long-lived excited state, stabilizing between 10 ns and 1 µs roughly, witnesses structural transition towards HS state and the presence of ordered diffracting domains.

Surprisingly, this analysis reveals a latency time, around two decades in time, between volume expansion at acoustic time scale and the amplification of the spin transformation (the "cooperative step").

## III.6.d. Rationalization of the experimental results

Transient volume increase in spin-crossover compounds can arise from the increase of bond length, induced by LIESST effect occurring below ps time scale [Lemke2017]. This molecular swelling induces chemical pressure, which tends to increase the volume of the unit cell. On the other hand, considering the great softness of the material regarding temperature (Figure 40b), the deposition of thermal energy into the lattice may also induce the increase of its volume [Lorenc2009].

### *III.6.d.i. Energy transfer to the lattice by vibrational cooling of the molecules in the crystal*

Time-resolved infrared (TRIR) spectroscopy measurements, the main theme of a recent PhD project carried out jointly between my group in Rennes and University of Poznan, investigated the dynamics of vibrational energy levels of photo-excited FeSalEen molecules in a crystal at ultrafast time scale.

When excited, large molecules embedded in a crystal exchange energy with their surroundings. Upon laser excitation, the molecule, newly switched to HS, stands in a vibrationally excited state. This excited molecule then steps through a ladder of vibrational levels, until it reaches the HS ground state (Figure 48a). Phonons are emitted during this process and heat up the surrounding lattice, as the molecule cools down. The rate of ground state population is equal to the rate of lattice heating. This energy transfer from vibrationally hot molecules to the lattice is called vibrational cooling [Dlott1990].

Since potential energy surfaces are anharmonic, the energy difference between adjacent vibrational levels is bigger for a transition towards lower vibrational level than it is for higher vibrational level. That is, the rungs of the ladder are not evenly spaced. Consequently, the vibrational frequency of a molecular bond in an excited HS molecule may show a redshift compared with that of HS molecule. Monitoring the vibrational frequency of a relevant bond after photoexcitation allows following the dynamics of vibrational cooling towards equilibrium of the HS molecule.

In crystalline FeSalEen, the C=C band is located within the [1580-1610] $cm^{-1}$ frequency interval. No other feature stands in this spectral range, making it a direct and convenient probe of vibrational cooling dynamics. TRIR spectroscopy performed on an FeSalEen photoexcited crystal [Dong2017] shows a shift of the C=C band frequency towards higher energy, typical of vibrational cooling of the molecules. This shift over time was fitted with an exponential curve of characteristic time $\sim 5.6\ ps$ (Figure 48b). This leads to a completion of the vibrational cooling process within 20 ps (crudely $3$ ) (Figure 48b), which corresponds to the time for molecular energy to be transferred to the lattice through phonons. Even though monitoring one vibration only is an approximation, it provides a good estimation of vibrational cooling duration [Wang2002].

This energy transfer induces the subsequent adiabatic heating of the system and rise of volume expansion under around 300 ps, according to our analysis of diffraction patterns (Figure 47a).

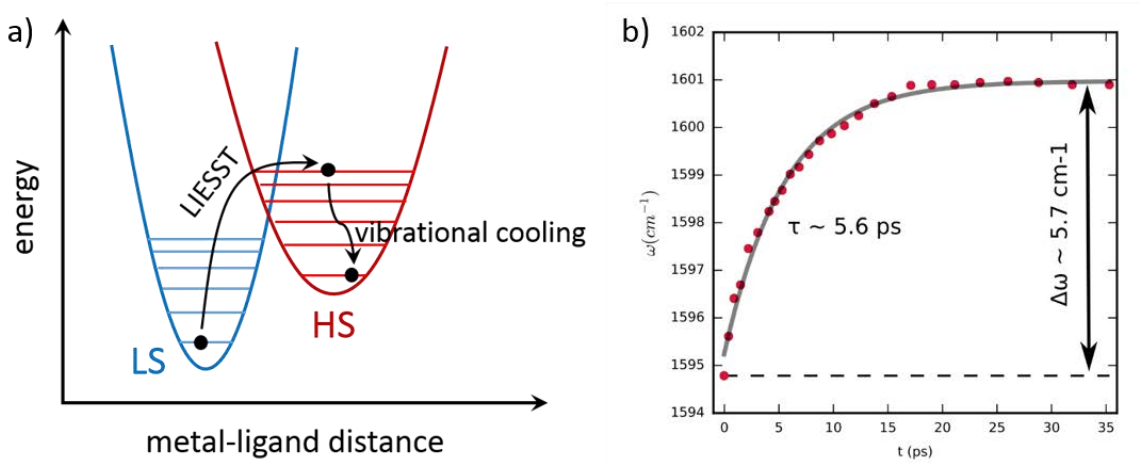


*Figure 48: a) Scheme of LS-to-excited HS photo-excitation process, followed by vibrational cooling of excited HS molecule towards HS ground state (black arrows). b) Frequency shift extracted for each TRIR delay (red dots) and fitted with an exponential curve (gray line) of characteristic time* $\sim 5.6\ ps$*. Vibrational cooling is completed within about 20 ps.*

Both spin switching at ultrashort time scale and thermal energy transfer through vibrational cooling certainly contribute to volume increase around 300 ps. However, $\Delta\ (300ps)$, corresponding to 10% high-spin conversion, is significantly higher than $\Delta\ (100ns)$, for 20% conversion. Therefore, there is a hint that thermal effect might dominate volume increase at 300 ps in this material.

A perspective to test this hypothesis, would be to perform pump-probe experiment choosing infrared light as a pump. In this configuration, using same excitation density but lower photon energy would result in lattice heating only, but no direct spin switching by photo-excitation. This would allow to better dissociate spin switching and thermal dilation impacts on volume dilation of the lattice.

Actually, the activation energy between low-spin and high-spin states requires promoting the molecule to the electronically excited states well above this barrier to effectively switch molecules to high spin state. This requirement might be a limitation to spin-crossover compounds photo-driven applications, making void the efforts lead on reducing the size of crystals over the last years. A new avenue for the design of spin-crossover systems for applications would be to chemically tune the barrier by carefully choosing appropriate ligands [Chastanet2018].

### *III.6.d.ii. Simulations with modified mechanoelastic model*

Despite sub-nanosecond energy transfer from molecules to the lattice, Arrhenius dynamics governing the spin transition as a statistical process implies that switching requires an incompressible time to occur [Ridier2019]. This time might be longer than propagation time of volume expansion, as we observe from x-ray diffraction data. The latency time of one-two decades in time between volume expansion and elastic step, evidenced in our experiment, points to a bottleneck in switching dynamics and hence redefines the ultimate timescale for switching of nanoscale objects in this class of solids.

In order to rationalize the experimental results, we used the mechanoelastic model, described in part 2.b of this chapter and successfully applied previously to simulate the elastic self-amplification [Enachescu2017, Bertoni2019].

Usually, to simulate the effect of simple photoexcitation in the framework of the mechanoelastic model, the following steps are performed:

- the system is considered at a temperature below the thermal transition temperature, at which most of the molecules are in the LS state. Several (at least 5000) MC steps are run to find equilibrium;
- then the homogenous laser photoexcitation is simulated by randomly choosing a number of LS molecule and switching them instantaneously to the HS state, thus increasing their radius by 0.02 Å, which corresponds to a 10% variation. Their temperatures is increased by a constant term (here, 100 K), simulating the laser power excitation;
- the system is let subsequently to evolve by solving alternately Monte-Carlo probabilities and differential equations of motion, while temperature is relaxed exponentially.

This procedure allows reconstructing the entire dynamics of a spin-crossover system, from laser excitation to relaxation. However, since the mechanoelastic model is two-dimensional, volume variation Δ is reduced to surface variation / $_0$.

In this model, the temperature parameter affects the switching probability only in the $k_BT$ denominator, but thermal expansion is not taken into account: the temperature parameter does not play any role in the surface variation / $_0$. Actually, the model as it was described above does not reproduce the latency time observed in x-ray diffraction experiments, between volume increase and cooperative step. This is visible in Figure 49, showing a concomitant increase of surface / $_0$ (Figure 49a) and of HS fraction Δ $_{HS}$ (Figure 49b).

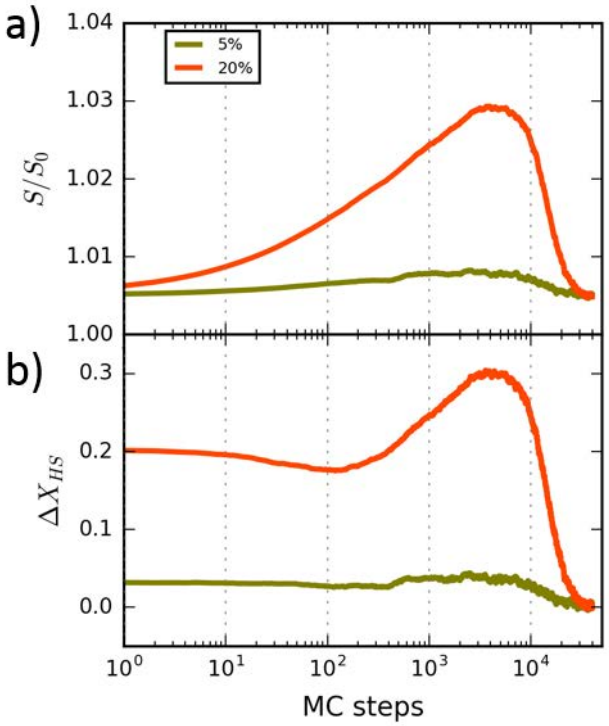


*Figure 49: Evolution of the system surface (a) and of the HS fraction (b) as extracted from Monte-Carlo simulations with the unmodified model. Green and orange curves represent low (5%) and high (20%) initial excitations, respectively. Unlike in the experiment, surface expansion and HS fraction increase concomitantly.*

In an attempt to reproduce the observed experimental situation, we worked with our collaborators from the University of Iasi (Romania) and adapted the MC model they developed. The model was modified to mimic the thermal increase of distance between spin crossover molecules with the temperature. This is an important aspect, as the heat released after the irradiation may raise the local temperature of the system by tens of degrees, thus significantly impacting unit cell volume of both phases, as was observed in x-ray diffraction data.

As stated previously, the energy deposited by the laser on photoexcited molecules is transferred to the surrounding lattice by dissipation through acoustic phonons, which results in an increase of

its local temperature. As an immediate consequence, the spring length should increase due to the thermal expansion. Hence we introduced an additional step right after photoexcitation, whereby we considered an increase of spring length by a constant term for all molecules ($\delta l = 15\%$) (Figure 50). This thermal increase is of the same order of magnitude (slightly higher) as volume increase due to spin transition ($\delta l = 10\%$), consistent with experimental observations.

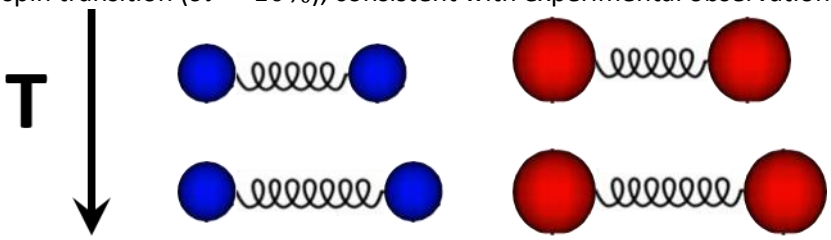


*Figure 50: Schematic representation of spring length increase $\delta l$ due to thermal dilation subsequent to laser excitation. Blue and red spheres stand for LS and HS molecules, respectively.*

After photoexcitation, alternative computing MC steps and differential equation systems solving were performed, while both temperature and spring length variation $\delta l$ exponentially decrease due to exchanges with the environmental thermal bath, as the system returns to equilibrium.
In that framework, we present the evolution of both HS fraction and surface (Figure 51), for low and high initial photoexcitation ratios. The cooperative step, corresponding to the rise of $\Delta_{HS}$ at long time scale (Figure 51b), reveals the nonlinear effect observed in both optical and x-ray diffraction experiments, as was already visible in the unmodified MC model.

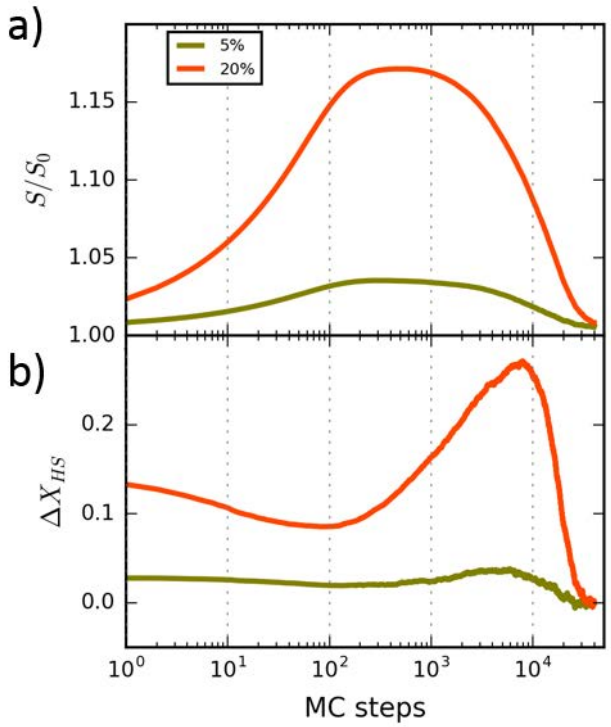


*Figure 51: Evolution of the system surface (a) and of the HS fraction (b) as extracted from Monte-Carlo simulations with the modified model. Green and orange curves correspond to 5 and 20% of initially excited molecules, respectively. Latency time is clearly observed between surface expansion and $\Delta_{HS}$ increase.*

The initial increase of spring length mimics thermal dilation hitherto lacking in the model. This change induces a strong volume dilation (Figure 51a), which arises two temporal decades before elastic increase of $\Delta_{HS}$. Hence, Monte-Carlo simulations using mechanoelastic model confirm the experimentally observed latency time between volume expansion and elastic step, observed in x-ray diffraction measurements.

A feature, which can be surprising at first, is that volume dynamics does not show any second jump when HS fraction reaches its maximum value, whereas one could expect a further increase of volume, consequently to significant $\rightarrow HS$ switching at the cooperative step. This situation is explained by the strong thermal expansion of the material. Indeed, thermal lattice expansion arising from an increase of temperature by few tens of K can easily overcome the spin switching effect in terms of volume. This is demonstrated in Figure 52a, which shows volume contribution from spin switching (horizontal gray lines) compared to volume change observed at 300 ps (horizontal black line), mainly originating from thermal expansion (dashed blue (LS), black (LS-HS mixture at 100 K) and dashed red (HS) curves). This predominance of thermal expansion prevents from seeing any second volume increase related to spin switching at the cooperative step, the latter being buried in thermal expansion effect.

To evaluate the effect of thermal volume increase value, we performed simulations using the adjusted mechanoelastic model for three different cases. Spring length variation due to thermal effect was considered either significantly lower than ($\delta l = 0.005$ Å), roughly equal to ($\delta l = 0.015$ Å) or bigger than ($\delta l = 0.03$ Å) the variation associated to spin switching effect ($\delta l = 0.02$ Å). The latter situation corresponds to what was chosen in previous simulations and reflects the strong thermal expansion in FeSalEen (Figure 52b). In all three cases, volume expansion arises two orders of magnitude in time earlier than the elastic step (Figure 52b,c), witnessing the same latency time as in experimental data. Normalized curves shown in Figure 52b,c demonstrate the same time scale for both volume and HS fraction. However, in the case of small volume expansion ($\delta l = 0.005$ Å), a second jump in volume increase is visible (Figure 52b), arising from the elastic step. This behavior could be expected for a material showing weaker thermoelastic expansion than FeSalEen does.

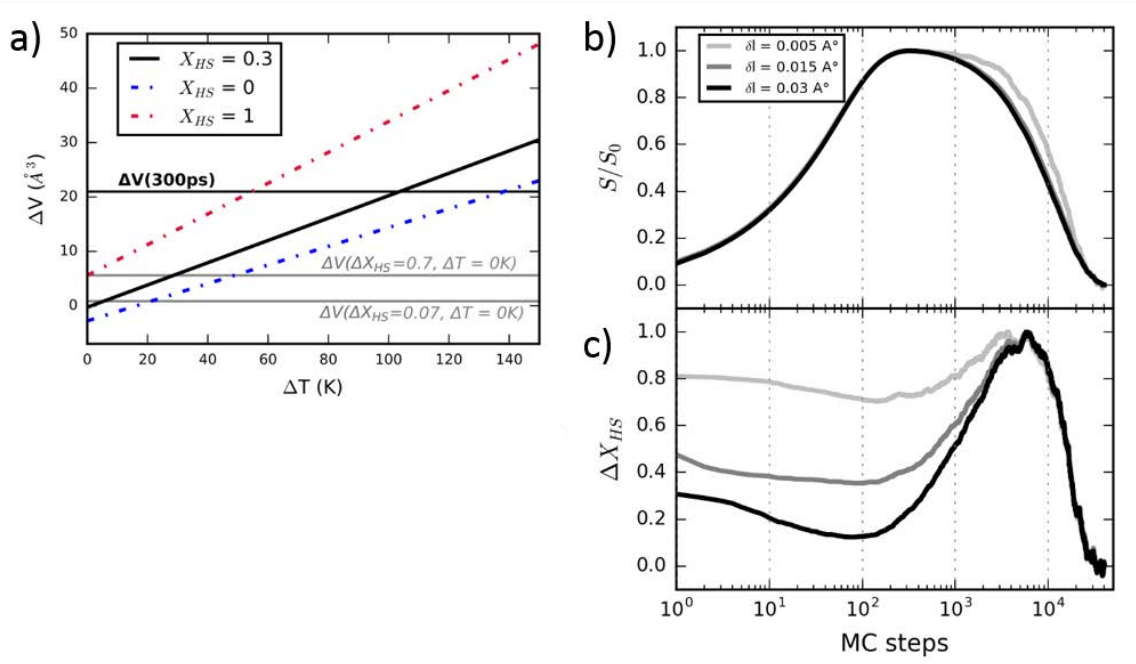


*Figure 52: a) Variation of unit cell volume with temperature, as extracted from XRD on single crystal. Black line corresponds to initial LS-HS proportions, as determined from x-ray diffraction versus temperature. Blue and red dashed lines represent pure LS and HS thermal expansions, respectively, for comparison. Volume increase observed on microcrystals at 300 ps ($\Delta X_{HS}$ = 0.7, ΔT = 85 K, as extracted from XRD analysis) is shown as black horizontal line. The comparison with volume change due to only spin switching fraction of all remaining LS molecules at 100 K ($\Delta X_{HS}$ = 0.7, ΔT = 0 K, gray horizontal line) shows that contribution of spin switching to volume expansion is much lower than thermal expansion effect at acoustic time scale. Contribution of spin switching to ΔV(300 ps) as refined from TR-XRD*

*measurement ($\Delta X_{HS}$ = 0.07, gray horizontal line) is also shown for comparison. It is clear that thermal variation of dozens of K induces a much higher volume dilation than spin switching, regardless of $\Delta X_{HS}$. b) and c) Monte-Carlo simulations: b) Normalized surface (equivalent to volume) dynamics for three different spring length increases. The second jump is only visible for small thermos-elastic expansion; c) Normalized photoinduced HS fraction for three different radius increases show the same time scale regarding the cooperative step.*

This study represents the first real-time observation of intertwined volume expansion and spin state switching in microscale materials, allowing relating structural to spin changes at the transition, by the refinement of time-resolved x-ray diffraction patterns. Based on direct experimental evidence and Molecular Dynamics Monte Carlo simulations, we conclude that energy activation barriers, albeit modified by crystalline volume expansion, are the non-vanishing limit for macroscopic spin transition in coordination metal compounds. This is a major result, as it strays from the intuitive steady state picture of correlated spin state and volume, and questions the relevance of further sample miniaturization.

### III.6.e. Study of the influence of excitation density

Transient optical transmission [Bertoni2016] revealed a nonlinear behavior of the cooperative step amplitude, depending on laser excitation density. With a laser excitation reaching 3 photons per 100 molecules (around 150 µJ.mm$^{-2}$), the transient HS fraction $_{HS}^{Co}$ versus photons per 100 molecules changed slope and overcame the initially photoinduced HS fraction $\mathrm{X}_{\mathrm{HS}}^{\mathrm{h\nu}}$ (Figure 53c). To investigate the structural dynamics of the system, we measured transient x-ray diffraction for several excitation densities.

As can be seen on Figure 53a, volume expansion Δ at 300 ps increases linearly with excitation density. This behavior is expected for volume expansion, as it is related to the amount of thermo-elastic energy released in the lattice. Actually, as was demonstrated by x-ray diffraction measurements at equilibrium with changing temperature (part 5.a of this chapter), thermal expansion in FeSalEen can be approximated to be linear, with coefficients $0.17$ Å$^{3}$. $^{-1}$ in the LS state and $0.26$ Å$^{3}$. $^{-1}$ in the HS state.
Amplification of transient HS fraction Δ $_{HS}$ at 10 ns, compared to short time scale (100 ps) value, is clearly visible at all laser excitation densities, except at the lowest one (≈ 60 µJ/mm²), where the excitation density lies below threshold (Figure 53b, circles). As opposed to optical measurements (Figure 53b, squares), the change in slope of Δ $_{HS}$ at elastic time scale is not visible in our x-ray diffraction experiment (Figure 53b). This discrepancy may be due to both uncertainty in Δ $_{HS}$ and a lack of data points in the x-ray diffraction experiment. Yet, the cooperative response, setting in between 100 ps (Figure 53b, blue) and 10 ns (Figure 53b, green), is rather clear: the higher the excitation the higher the gain of switched molecules on the “cooperative step”, compared to those laser-excited.

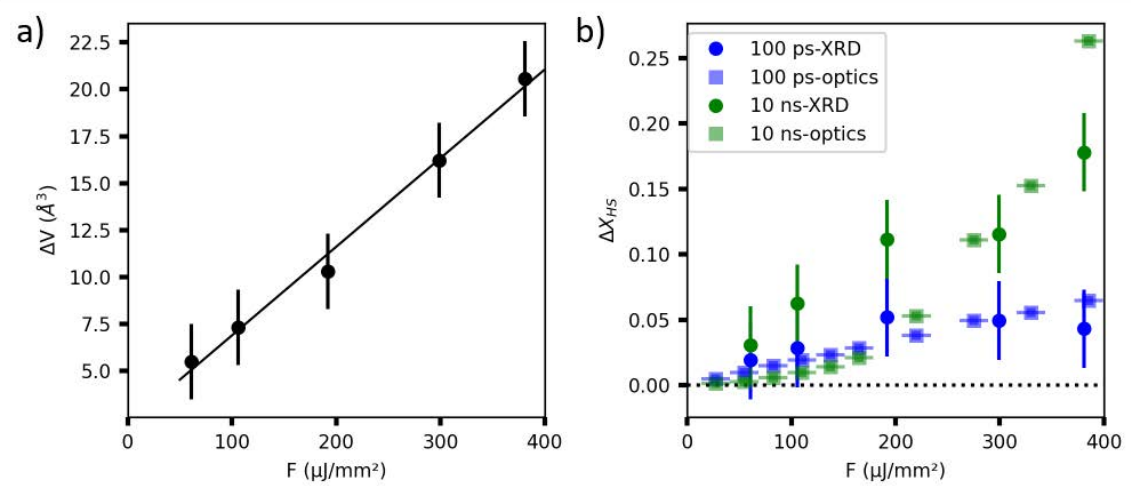


*Figure 53: a) Volume variation at 300 ps (around maximum) versus excitation density F. Black line represents a linear fit. b) HS fraction variation versus excitation density, just after photo-excitation (100 ps, blue) and at the cooperative step (10 ns, green). Lines represent linear fits of the data. X-ray diffraction data are represented with circles, while optical transmission data (adapted from [Bertoni2016]) are represented with squares.*

Considering the overall dynamics, both the build up and relaxation of volume and HS fraction do not seem to depend on the excitation density (Figure 54a,c). Actually, normalization of the signal around the maximum value (standing around 300 ps for Δ and around 100 ns for Δ $_{HS}$) for excitations densities leading to cooperative step (thus discarding the lowest one), shows no striking difference between the dynamics of the different excitation densities (Figure 54b,d). Small discrepancies can be seen in the relaxation, however they stand within the noise of the experiment. This observation is corroborated by MC simulations, which show a show very little variation of arrival time of elastic step and volume increase, regardless of the initial excitation and of the initial spring length increase (Figure 51, Figure 52b).

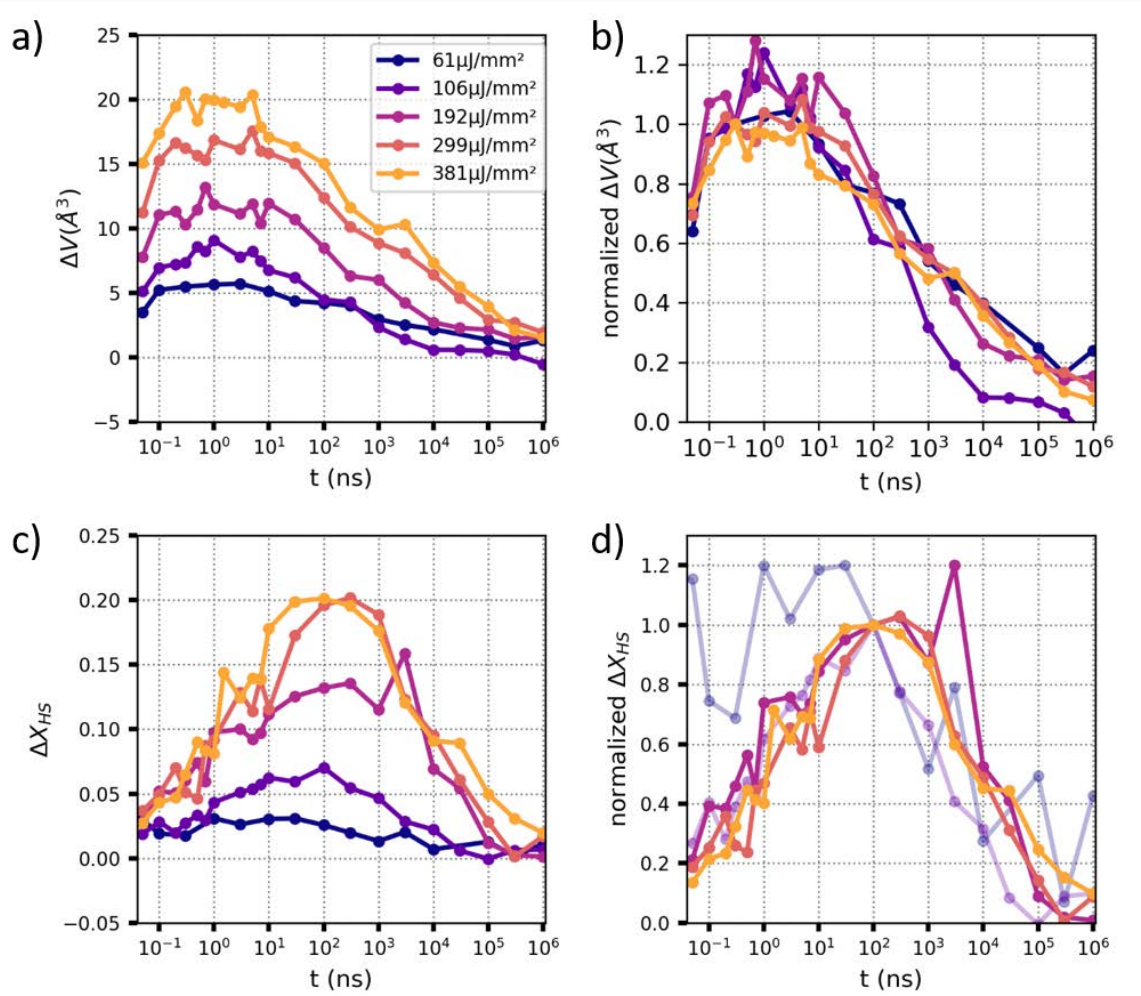


*Figure 54: Transient volume (a) and HS fraction (c) variations for several laser excitation densities. (b,d) Same signal, normalized to 300 ps value for volume (b) and 100 ns value for HS fraction (d). Increasing and decreasing dynamics seem not to depend on laser excitation density. Normalized signal corresponding to 61 and 106 µJ/mm² excitation density, which lie below cooperative threshold, are plotted in light.*

The lattice dynamics present two components occurring at similar timescale: incoherent increasing of phonon populations, mostly acoustic (lattice heating) and renormalization of the lattice potential (volume expansion). First, molecular energy coming from laser excitation is adiabatically transferred to the lattice within 20 ps, as was shown by TRIR measurements (Figure 48). This energy load triggers volume expansion of the unit cell, which completes in around 300 ps (Figure 55a). This propagation time is of the order of magnitude of the propagation of a deformation over the average crystal dimension at the speed of sound in the material: – $\sim 350\ ps$.

Then volume reaches a plateau at 5 ns (Figure 55b) and finally decreases to its equilibrium value around the µs (Figure 55c,d). Our attempts to describe the relaxation dynamics by an exponential or sigmoid curve did not provide any satisfying fit of experimental data. Better signal-to-noise ratio, along with more data points providing a better time resolution would be beneficial to better describe the relaxation dynamics. Moreover, the interplay between volume and HS fraction might be at the origin of a more complex process than simple exponential or sigmoidal decrease.

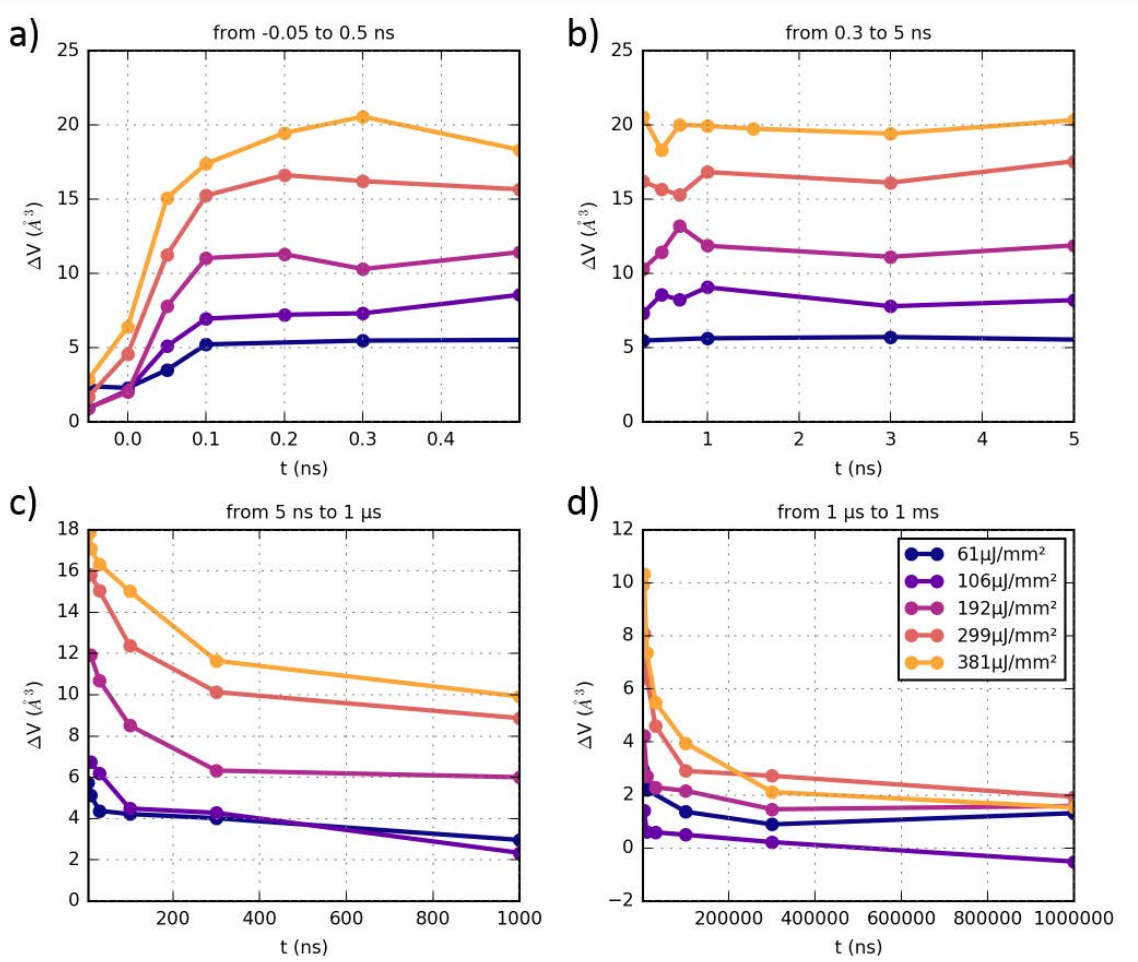


*Figure 55: Linear plot of transient volume variation over different temporal ranges. Volume expansion sets in 300 ps (a), to reach a plateau lasting until 5 ns (b), then decreases as relaxation processes (c,d).*

Considering transient HS fraction, ultrafast LIESST effect occurs within around 200 fs. However, the synchrotron x-ray pulse of about 70 ps effectively convolutes with the signal, leading to poor time resolution, compared with optical measurement. Our measurement thus shows a first increase of Δ within about 100 ps (Figure 56a). No dependence in excitation density on ultrafast dynamics was observed in previous optical measurements [Bertoni2013], which corroborates our observations by x-ray diffraction. Actually, we remind that LIESST effect is known to be linear with excitation density, with a quantum efficiency approaching one (one photon switches one molecule). Δ $_{HS}$ further increases until it reaches cooperative step around 10-30 ns (Figure 56b). The latter lasts on a plateau ranging from 10-30 ns to ≈ 300 ns (Figure 56c), then decreases towards equilibrium value (Figure 56d).

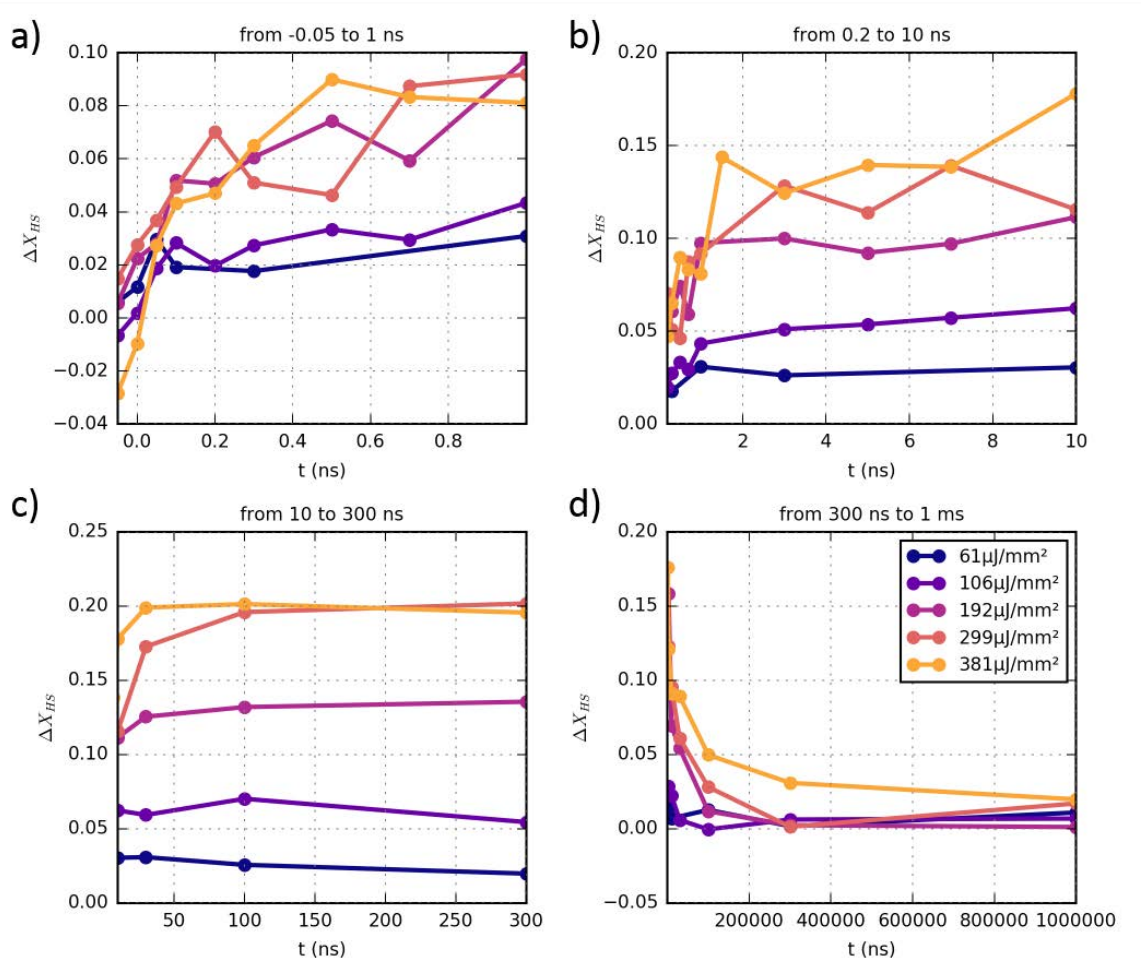


*Figure 56: Linear plot of transient HS fraction variation over different temporal ranges, for several excitation densities. A first increase is visible within 100 ps, under experimental resolution (a). Then signal continues increasing until around 10-30 ns (b), where it reaches a plateau lasting until 300 ns roughly (c). Finally, signal decreases again as relaxation processes (d).*

## III.6.f. Study of the influence of the steady state temperature

Across the thermal region of spin crossover, the fraction of HS molecules varies. To investigate the effect of the initial HS fraction on the dynamics and on the amplitude of the cooperative step, we performed time-resolved x-ray diffraction measurements at a fixed excitation density (the highest achievable before threshold damage) for different initial temperatures $_0$.

Since $_{HS}$ increases with temperature, both initial absolute volume and HS fraction values increase with increasing initial temperature (Figure 57). However, when approaching the end of the crossover region, less and less LS molecules are available for the switching to HS state, therefore transient signal amplitude decreases. The temperature parameter fitted in patterns refinement without laser (horizontal dashed lines in Figure 57a), showed a good agreement with the control temperature, with an average error of around 4%.

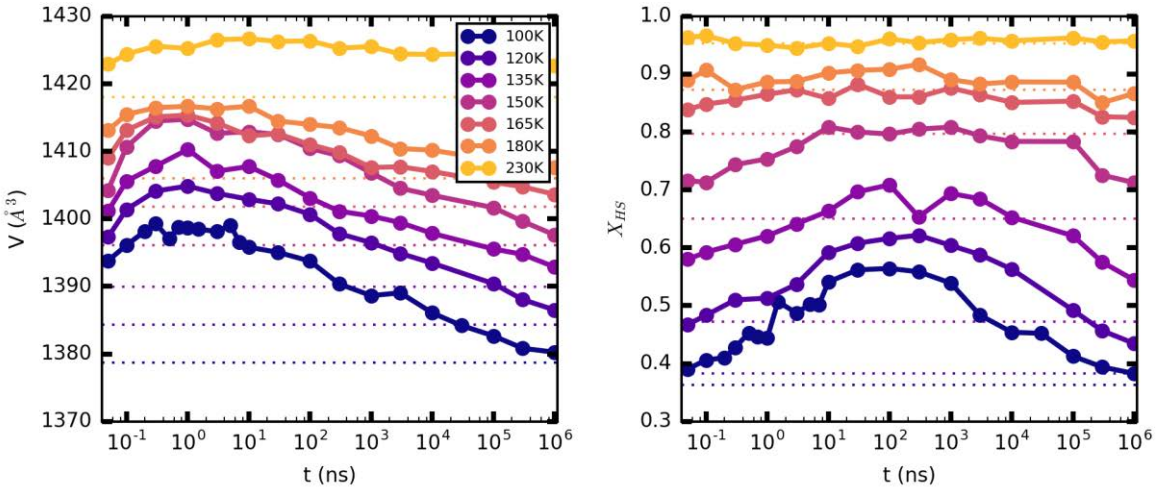


*Figure 57: Left: transient absolute volume for several initial temperatures. Dotted lines represent values at equilibrium (without laser). Right: transient absolute HS fraction for different initial temperatures. Dotted lines represent values at equilibrium. Equilibrium value increases with temperature, as expected. As the temperature approaches the end of the crossover region, curves flatten as the transient signal decreases, due to less potentially switchable LS molecules.*

Transient signal shows an increase of the cooperative step amplitude until the temperature reaches 135 K, then decreases to reach almost zero at 230 K, where the system is in majority in the HS state (Figure 58a,c). This observation of a higher probability for the elastic step close to $_{1/2}$ was already pointed out in a previous study, both experimentally and by MC simulations [Bertoni2019]. No effect of the temperature on the arrival time of the elastic step was observed, neither in our experiment nor in this previous study.

The normalization of the transient signal, at 300 ps and 100 ns for Δ and Δ $_{HS}$ respectively, shows a similar dynamics for all $_{0}$ (Figure 58b,d). Therefore, the dynamics does not seem to depend on the initial temperature. This observation might be surprising at first, since the energy barrier standing between LS and HS states should be easier to cross with increasing T. Actually, this experimental result is corroborated by MC simulations, which do not show significant difference in the arrival time of the cooperative step when changing the initial temperature $_{0}$ [Bertoni2019]. Regarding relaxation dynamics, previous experiments tend to show that relaxation rate does not vary enough to show up in this temperature range [Enachescu2006]. Therefore, temperature effect, if ever existing in this temperature range, may be too weak to be distinguished in the experiment.

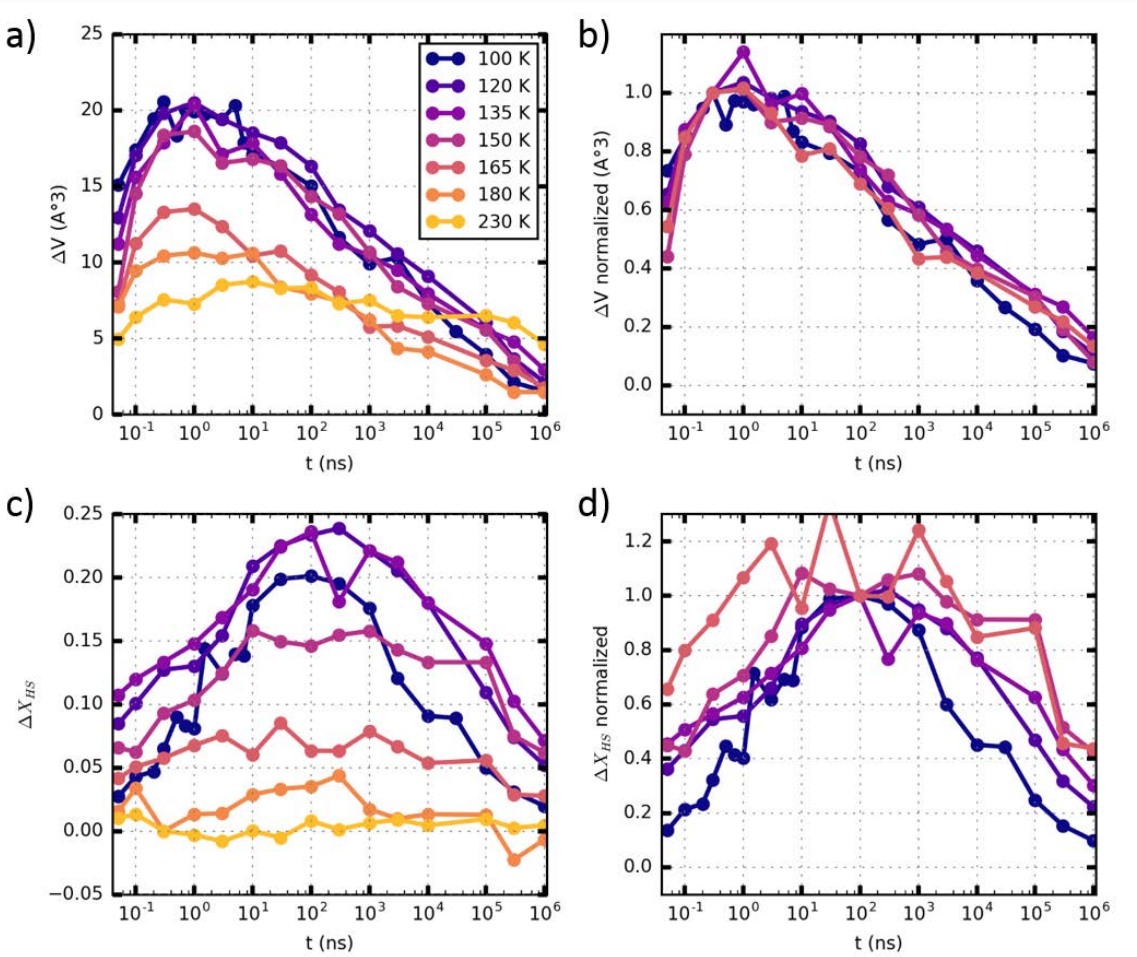


*Figure 58: Left panels: transient volume (up) and HS fraction (down) variations for several initial temperatures. Right panels: same signal, normalized to 300 ps value for volume and 100 ns value for HS fraction. Increasing and decreasing dynamics seem not to depend on initial temperature (discrepancies are in the range of experimental noise). Since transient signals at 180 and 230 K are really low, due to few remaining switchable LS molecules, normalized signals is not shown for these temperatures, being too noisy.*

The dynamics of transient volume and HS fraction shows the same behavior as previously described. The onset of volume expansion (Figure 59a) occurs within 300 ps, then reaches a plateau lasting 5 ns (Figure 59b) and decreases as relaxation proceeds (Figure 59c,d).

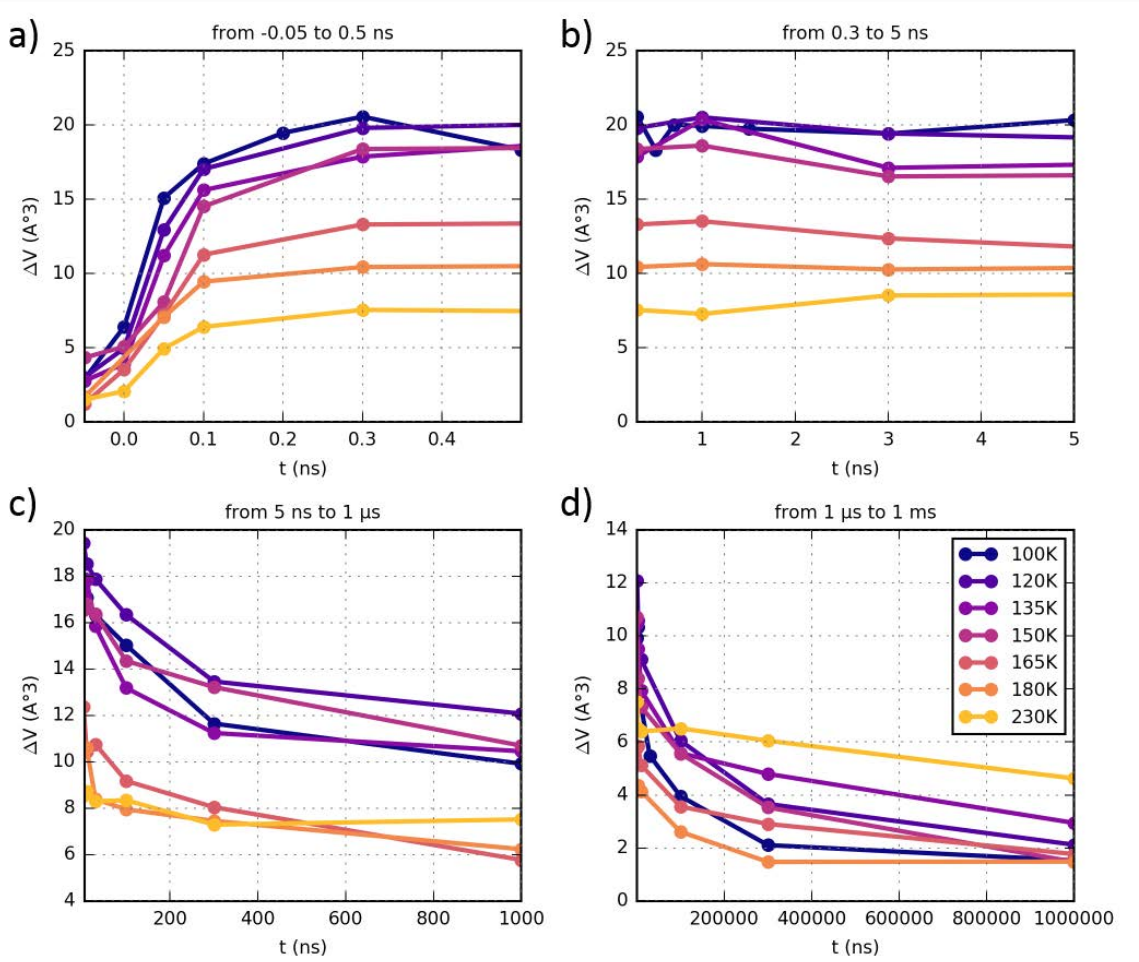


*Figure 59: Linear plot of transient volume variation over different temporal ranges. Volume expansion sets in 300 ps (a), to reach a plateau lasting until 5 ns (b), then decreases as relaxation processes (c,d).*

LIESST effect, convoluted with x-ray pulse, induces an increase of $\Delta_{HS}$ within 100 ps (Figure 60a). Signal continues increasing until 10-30 ns, as cooperative step proceeds (Figure 60b). The latter lasts on a plateau ranging up to around 300 ns (Figure 60c), then relaxes back to equilibrium value in the ms time scale (Figure 60d).

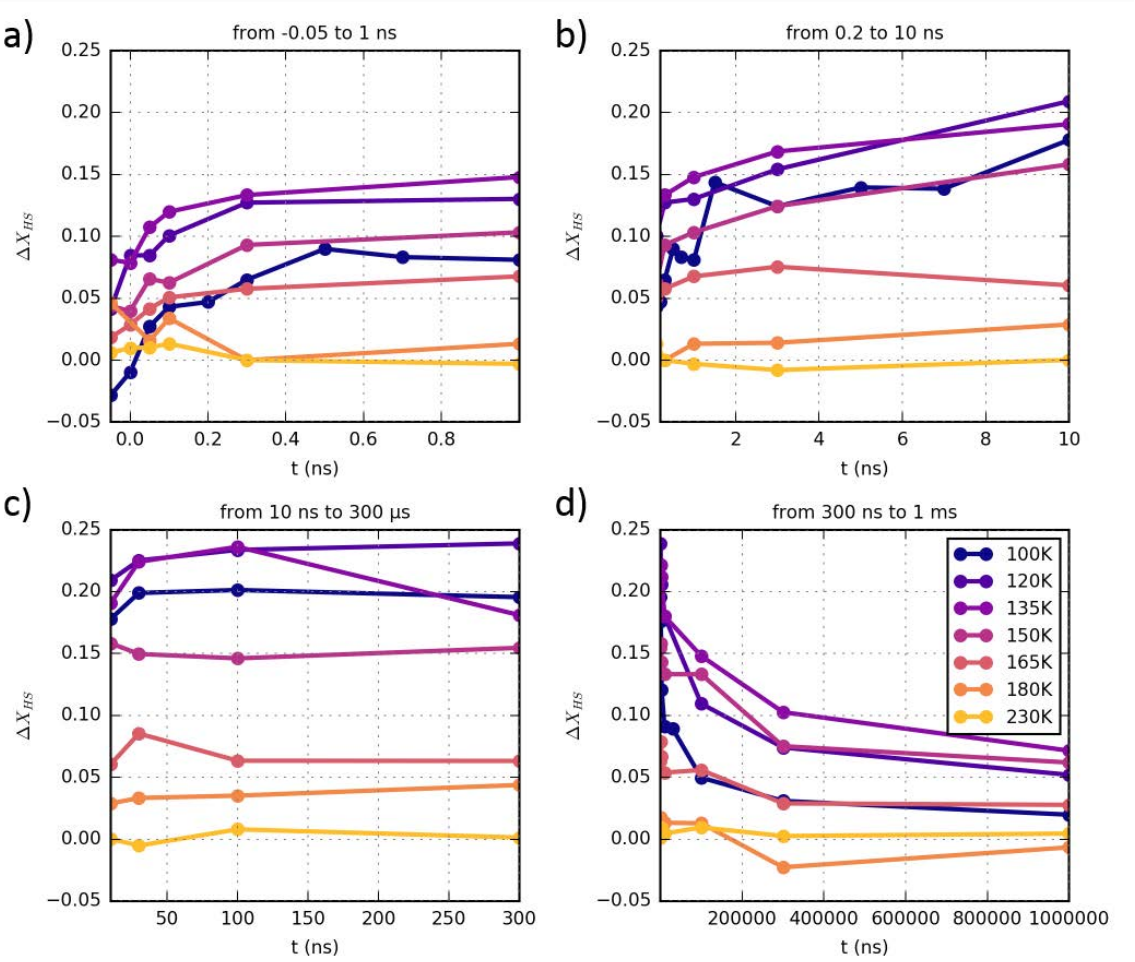


*Figure 60: Linear plot of transient HS fraction variation over different temporal ranges. A first increase is visible within 100 ps (a), under experimental resolution. Then signal continues increasing until around 10-30 ns (b), where it reaches a plateau lasting until 300 ns roughly (c). Finally, signal decreases again as relaxation processes (d).*

## III.7. Conclusion

This work represents the first time-resolved study combining information about both spin and unit cell volume dynamics under photo-excitation in a spin-crossover material in the solid state. The implication of different degrees of freedom, playing their part on different time scales, makes the description of the dynamics of spin crossover materials under transient photo-excitation challenging. The building of a complete picture requires accessing both spin state and structural information, on time scales ranging from the femtosecond, when LIESST effect occurs, to the relaxation of the system at the millisecond. By performing time-resolved x-ray diffraction measurements on the photo-excited $[Fe^{III}(3\text{-MeO-SalEen})_2]PF_6$ compound, thus bringing information about structural dynamics occurring at acoustic time scale, we made our contribution to the building of a comprehensive description of the photo-induced spin transition in molecular spin-crossover materials. Based on direct experimental evidence and Molecular Dynamics Monte Carlo simulations, we conclude that the arrival time of the second increase of switched molecules, previously evidenced by time-resolved optical transmission, seems to be limited by Arrhenius dynamics, governed by the energy barrier to cross between LS and HS state.

This finding could motivate an optimized material design, scalable with size-dependent dynamics and intrinsic energetics.

# Chapter IV: Photo-induced insulator-to-metal transition in Vanadium Sesquioxide $V_2O_3$ thin films

Vanadium sesquioxide ($V_2O_3$) is considered as the prototype system for insulator-to-metal phase transition in a correlated electron material. By lowering temperature at atmospheric pressure, this material undergoes a phase transition between metallic paramagnetic and insulating antiferromagnetic states. This change in electronic and magnetic properties is accompanied by a ferroelastic symmetry breaking and a significant change of the unit cell volume (> 1% in absolute). The presented work was realized within a CNRS French-Japanese collaboration: "Impacting materials with light and electric fields and watching real time dynamics". Thus, with two research groups from Université de Nantes (France) and Tohoku University (Japan), we studied the photo-induced phase transition of this material. My contribution to this work consisted in studying the role of the structural aspects, both ferroelastic symmetry breaking and volume change, in the phase transition dynamics. In this perspective, we performed time-resolved x-ray diffraction on $V_2O_3$ photo-excited thin films.

## IV.1. Correlated materials

Correlated materials are, as their name says, compounds in which electronic interactions play a major role in the determination of the material properties. Strongly correlated materials differ from "uncorrelated" ones by several aspects [Rozenberg2019]. A first peculiar feature of correlated materials is that they show rather complex properties and phase diagrams. In the independent electron approximation, materials are usually classified as either metals (no gap), insulators (large gap) or semiconductors (small gap). Their conduction properties are relatively easy to understand and to predict, by looking at the outer electronic shell in conventional band theory. Whereas these classic materials show rigid band structure, which only depend in atomic positions relative to each other, the nature of gap in correlated materials, on the contrary, is fully determined by electronic correlations: electronic bands change energy depending on their filling. For instance, compounds like gold, diamond or silicon remain in their stable form for a wide range of temperature without significant change of their electronic structure. Only at very high temperature (well above room temperature) may they exhibit crystalline changes. Strongly correlated systems however, exhibit strong changes in their electronic properties, at temperatures which can lie well below the room temperature. Examples can be found for instance, in the metal-insulator transition in $V_2O_3$ and in the family of nickelates $XNiO_3$ (X= La, Sm, Pr, etc.), in the magneto-resistance of manganites $La_{1-y}X_yMnO_3$ (X= Sr, Ca, etc.) and in the superconductivity in cuprates such as $La_{2-y}Sr_yCuO_4$. These changes in electronic properties are accompanied by a significant modification of spectroscopic properties, involving transfers of spectral weight which take place over energy scales of the order of 1 eV. Yet, such an energy is equivalent to a temperature of 11 000 K, whereas electronic changes occur on a much smaller temperature range, of about 100 K. With this consideration, the effect of electronic correlations becomes obviously significant.

Important members of the family of strongly correlated materials are transition metal oxides, especially the metals lying in the third row of the periodic table, filling the 3d orbital shell. Depending on this filling, a wide variety of oxide materials can be found, showing surprising insulating character.

### IV.1.a. Mott insulators

Mott insulators are correlated materials which should, according with conventional band theory, conduct electricity, but actually do not. This insulating character is due to electron-electron repulsive interactions in the material, which are not considered in the description proposed by band theory of solids.

In 1937, de Boer and Verwey [deBoer1937] pointed out a category of transition metal oxides, which should be conductors according to conventional band approach since they showed an odd number of electrons per unit cell, and behave as insulators nonetheless. Shortly following this discovery, Mott suggested this anomaly to be induced by repelling Coulomb interactions between electrons in the partially occupied band [Mott1937].

In the tight-binding approximation, underlying the band theory, electrons are viewed as occupying orbitals of their atom and "hopping" from one atomic site to another neighboring one. The physical parameter characterizing the possibility for electrons to hop is called the transfer integral . In 1949, Mott proposed a model to describe the insulating materials discovered by de Boer and Verwey [Mott1949]. In this model, the formation of an energy gap preventing conduction is explained as the result of the competition between the transfer integral of valence 3d electrons and the Coulomb intra site repulsive potential between these same electrons.

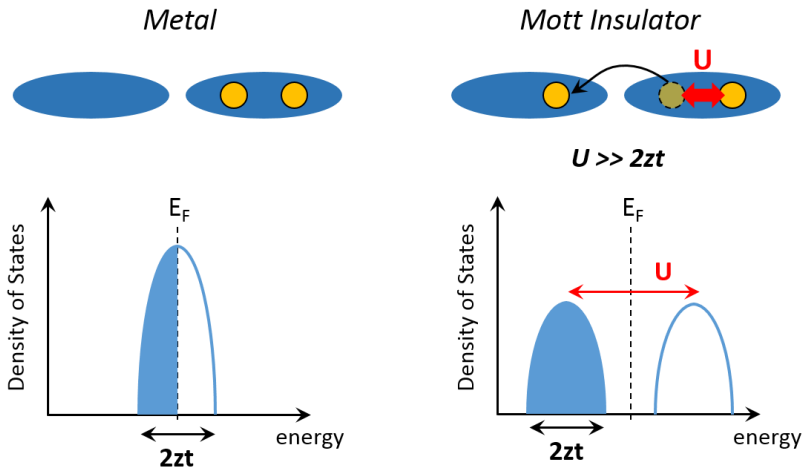


*Figure 61: Scheme of electron distribution in a metal (left) compared to a Mot insulator (right). In Mott insulators, the intra-site Coulomb repulsion U is such that an energy gap opens, with a full band below the fermi level $E_F$ and an empty band above $E_F$.*

Therefore, the gap energy writes:

$$= \quad - 2zt$$

with being the number of nearest-neighbor atoms in the crystalline lattice. The so-called "Mott insulators" are encountered when the repulsive Coulomb potential is large enough to overcome the effect of transfer integral $\gg 2zt$, thus opening an energy gap between bands (Figure 61). Both major tools used to describe Mott insulators are the Hubbard model and the dynamical mean-field theory (DMFT).

### IV.1.b. The Hubbard Model

In 1963, John Hubbard proposed a model to specifically describe the physics of Mott insulators. The Hubbard model relies on a very simple description of interacting particles in a lattice, with a two-terms Hamiltonian: a kinetic term, allowing for the tunneling of particles between sites of the

lattice and potential term, related to on-site interaction. This is a good approximation for particles in periodic potential at sufficiently low temperature, whereby long-range interactions can be ignored. Some models take into account an additional term related to long-range interactions and are referred to as “extended Hubbard models”.
The Hubbard model is based on the tight-binding approximation from solid state physics, which describes particles moving in periodic potentials, distributed in a lattice. Each site of the lattice corresponds to an ionic core, while particles represent valence electrons. In the tight-binding approximation, the Hamiltonian is written in terms of Wannier states, which consist in localized states centered on each lattice site. States of neighboring sites are coupled, such that it allows electrons on one site to “hop” to another. The strength of the coupling is defined as the transfer integral between neighboring sites. This coupling allows the hybridization of states associated to different sites. The eigenstates of such a system are represented by Bloch wave functions, with energy levels distributed into separate energy bands. The width of the band depends on the value of the hopping integral.
The Hubbard model introduces the on-site interactions between particles of opposite spins in the tight-binding model. When describing electronic systems, these interactions are repulsive. The physics of the system is determined by the competition between the strength of hopping integral and the strength of the interaction term. For strong on-site interactions, the model correctly predicts the existence of Mott insulators, conduction being prevented by the on-site repulsion. Additionally, the on-site localization of electron in the Mott insulating state leads to magnetic properties, in particular antiferromagnetic order at low temperature.

### IV.1.c. Dynamical Mean-Field Theory

Dynamical mean-field theory is a method used to determine electronic structure of strongly correlated materials, whereby the approximation of independent electrons can no longer be considered as valid. It proposes a non-perturbative treatment of local interactions between electrons, by treating a many-body lattice problem, too complicated to solve, as a many-body local problem, called an impurity model [Georges1996], usually solvable.
The only approximation made by this model is that it assumes the lattice self-energy to be momentum-independent quantity, by equating the spatial fluctuations of the latter to the impurity self-energy. This approximation becomes exact in the limit of lattices with infinite coordination, that is when the number of neighbors of each site tends to infinity. This model is thus supposed to be more accurate for high dimensionality materials [Georges1992].
However being the most advanced theory to describe correlated systems, the basis of DMFT still lacks the comprehension and description of the effects of lattice motions and volume change. Out-of-equilibrium situations and elastic phenomena for instance, stand out of the scope of DMFT in its original development. Several ongoing studies focus on extending the model beyond equilibrium description of the lattice [Aoki2014, Eckstein2020]. Photo-induced phase transitions implying volume change would therefore benefit from further model development to be properly described.

## IV.2. Vanadium sesquioxide

In solid state physics textbooks and lectures, vanadium sesquioxide ($V_2O_3$) is generally considered as the example of correlated electron material. This “canonical” Mott insulator system has been intensively studied over several decades.

## IV.2.a. Phase diagram and properties

The phase diagram of $V_2O_3$ is well-known and often discussed as a generic phase diagram in Mott physics (Figure 62). It exhibits three different phases at thermal equilibrium: Paramagnetic Metal (PM), Paramagnetic Insulator (PI) and Antiferromagnetic Insulator (AFI) [McWhan1970, McWhan1973]. It is important to realize that this generic phase diagram results from a combination of measurements as a function of temperature and pressure, in both the pristine crystalline form (undoped $V_2O_3$) and doped crystals by chemical substitution on V-site (by chromium or titanium atoms). The doping-pressure equivalence is questionable, thus doping effect cannot be described as a simple chemical pressure effect, in particular it may favor microscale phase separation [Lupi2010, Hansmann2013].

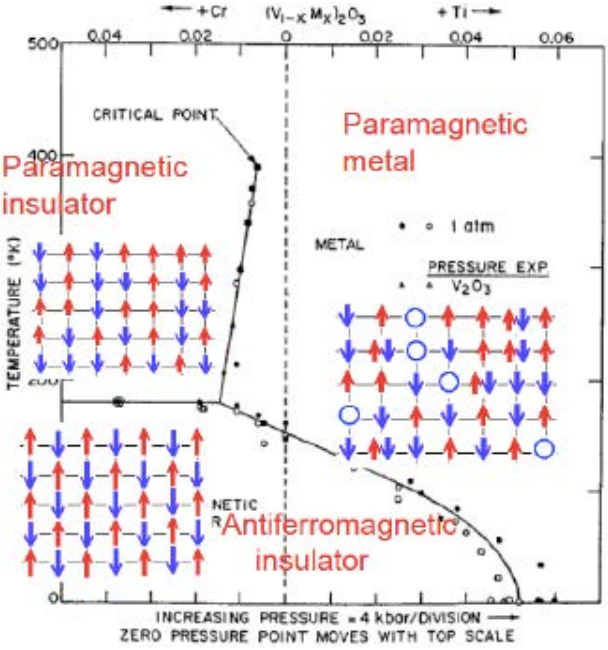


*Figure 62: Experimental phase diagram of $V_{2-x}Cr_xO_3$ from [McWhan1973]. Three different phases can be found at thermal equilibrium: an antiferromagnetic insulating monoclinic phase at low temperature, a paramagnetic metallic rhombohedral phase at high temperature and a paramagnetic insulating rhombohedral phase at low pressure-high temperature for Cr-doped material. Red and blue arrows represent spin lattices for each phase.*

$V_2O_3$ shows different phases, being in its pristine form (Figure 63a) or with Cr doping (Figure 63b). To describe this generic phase diagram requires considering not only charge and spin degrees of freedom, but also structural ones. On the one hand, the crystalline symmetry for the two paramagnetic phases, PM and PI, is identical being in the trigonal α-corundum structure, while the antiferromagnetic phase AFI, presents a lowering of this structural symmetry, with the establishment of a spontaneous ferroelastic distortion to a monoclinic crystalline system. On the other hand, volume jump are observed by crossing the different transition lines in agreement with their first-order nature. These structural features, generally less considered than electronic-magnetic ones, will be at the core of the present time-resolved structural study.

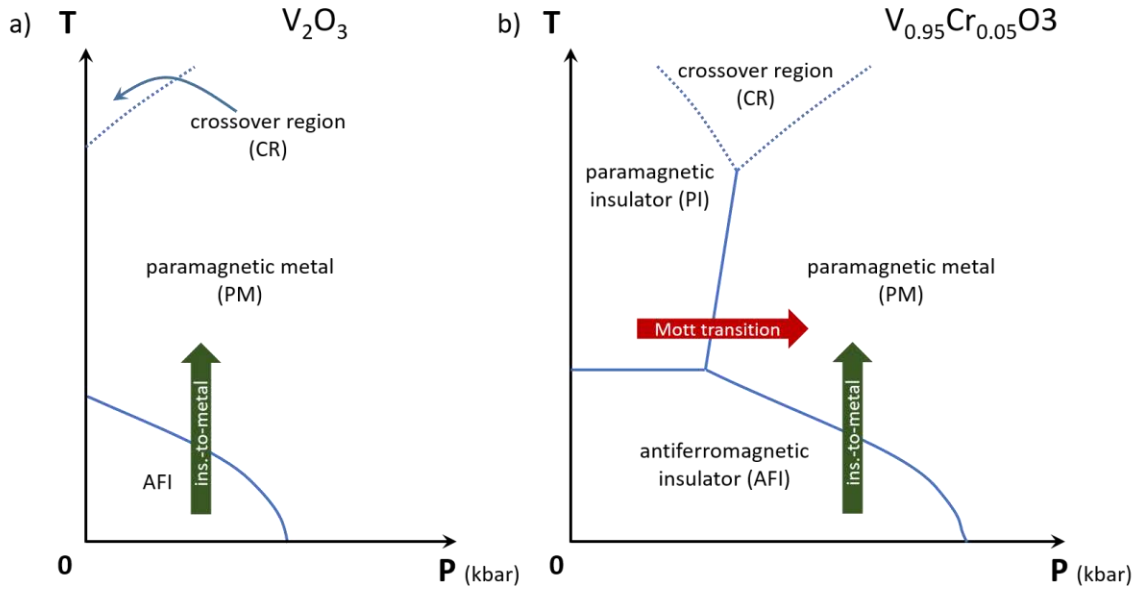


*Figure 63: Schematic phase diagram of $V_2O_3$ (a) and 5% Cr-doped $V_2O_3$ (b). At ambient pressure, pristine $V_2O_3$ undergoes an insulator-to-metal transition around 150-162 K. Above a critical temperature $T_c \approx 400$ K, the system reaches a crossover region between Mott insulator and metal. Cr doping results in negative effective pressure, unveiling a paramagnetic insulating phase at low pressure. Cr-doped $V_2O_3$ undergoes a Mott transition with increasing pressure.*

In 1946, Foëx found that pristine $V_2O_3$ showed sharp first-order transition from an insulating phase below $= 150 - 162$ to a metallic phase upon increasing temperature [Foex1946]. This transition can be observed in Figure 64, showing resistivity measured versus temperature on a $V_2O_3$ thin film. The compound shows a clear first-order phase transition, between a low-resistivity (metallic) phase at high temperature and a high-resistivity (insulating) phase at low temperature, associated with a roughly 12K-wide hysteresis. For this thermal phase transition (dotted line in Figure 62 and Figure 63a,b, green arrows), the driving force behind the transition is not only related to the Coulomb repulsion-transfer energy competition, but necessarily includes an additional magnetic and structural mechanisms. From DMFT, it is known that temperature-controlled insulator-to-metal transitions are possible in half-filled correlated systems if they exhibit a long-range (e.g. magnetic or orbital) order at low temperature.

Actually, the phase transition from the metallic to insulating state also involves a crystallographic symmetry breaking of ferroelastic nature, from trigonal (rhombohedral) to monoclinic crystalline system [McWhan1970, Janod2015]. This compound is rather unique among similar sesquioxides, with respect to its unusually high c/a ratio (around 2.8) and metallic conductivity [McWhan1970]. This type of insulator-to-metal transition strongly differs from conventional Mott transitions, the latter occurring without crystallographic symmetry breaking. It can be noticed that the ferroelastic feature is generally neglected to describe the low temperature phase, simply named AFI. AFI-to-PM first-order transition exhibits a compression, with a significant negative volume change $\Delta \ / \ \sim -1.4\%$ [McWhan1973] (Figure 69a in part IV.2.b). The positive slope of the first-order transition line $dT/dP > 0$ (Figure 62) is in agreement with $\Delta_{FI \to PM} < 0$, and an entropy jump at the transition $\Delta_{FI \to PM} > 0$.

The chemical pressure due to chromium doping of $V_2O_3$ induces a negative pressure effect, unveiling a paramagnetic insulating phase at room temperature and atmospheric pressure. Applying positive pressure on the Cr-doped system makes it switch to metallic state [McWhan1973]. This pressure-induced insulator-to-metal transition at room temperature is isostructural, without change of crystalline and magnetic symmetry between both corundum

structures and paramagnetic states. This corresponds to a conventional Mott transition (Figure 63b, red arrow), analogous to the liquid-gas transition. This is simply represented in Figure 62, where the cartoon (spin represented by red and blue arrows) shows a gas-like low-density of doubly occupied state in the insulating state and a liquid like high-density in the metallic state. The first-order transition line ends with a critical point. Above this critical point lies a crossover zone, where there is no phase transition but a gradual evolution between insulating and metallic states. In both undoped and doped $V_2O_3$, a gradual evolution of volume has been observed above the critical temperature $T_c \approx 400$ K [McWhan1973].
One of the main successes of DMFT is to describe the phase transition between a metal and a Mott insulator, when electronic interactions increase. However, the thermodynamics of this phase transition requires to consider the volume change. In particular, the positive slope of the first-order transition line from PM-to-PI, accompanied with the observed positive volume change $\Delta_{PM\to PI} > 0$, naturally implies $\Delta_{PM\to PI} > 0$. This entropy increase results, at least partially, from the spin orientation becoming free in paramagnetic insulator state.

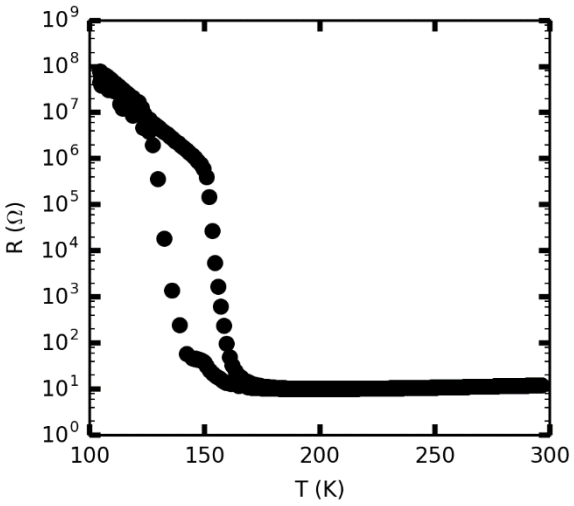


*Figure 64: Resistivity versus temperature, measured on a $V_2O_3$ 1 µm-thick film, cycling from 296 K to 105 K and back to room temperature. The drop in resistivity between low- and high-temperature phases indicates a sharp transition from insulator to metal, occurring around 150-160 K with a ≈20 K hysteresis.*

On the left side of the phase diagram (Figure 62), we can observe a quasi-horizontal transition line between the AFI and PI state. Only magnetic and ferroelastic symmetry breaking occurs, but the system stays in insulating state. The very weak slope $dT/dP$ agrees with a very small volume change from AFI-to-PI $\Delta \; / \; = (0.1 \pm 0.1)\%$ [McWhan1973], while the entropy change remains significant. This small volume increase is expected, since it is known that magnetic transition does not imply large change of volume, nor does a shear ferroelastic distortion (actually, for an infinitesimal change of angle, volume is preserved in first approximation). If we consider a small loop around the triple point, approximating $\Delta_{PI\to\ FI} \sim 0$, therefore $\Delta_{FI\to PM} \approx -\Delta_{PM\to PI} < 0$.

As already indicated, the photo-induced optical and structural studies presented in the following concern the AFI-to-PM transition in undoped $V_2O_3$ compound at atmospheric pressure. Therefore, not only magnetic and electronic but also structural degrees of freedom are involved. The pump-probe ultrafast experiments presented thereafter will give the possibility to investigate the role of coupled electronic-volume change in this phase transition at macroscopic scale.

## IV.2.b Structural changes

### *IV.2.b.i. Data from the literature*

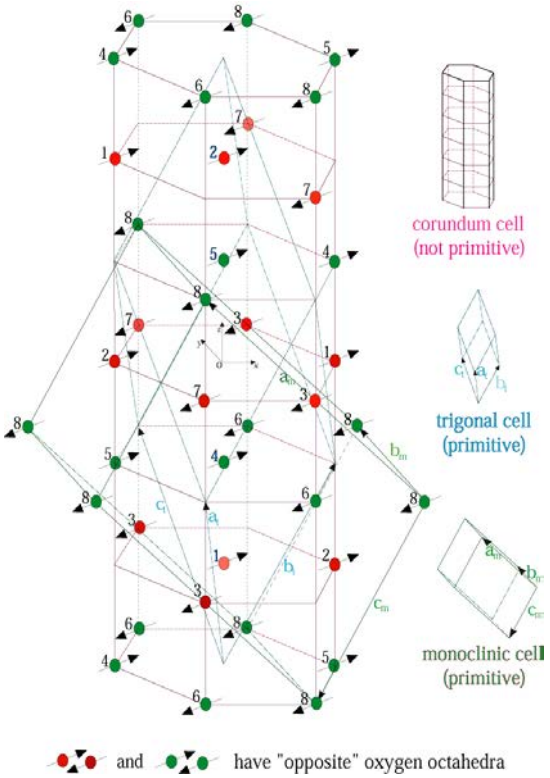


*Figure 65: from [DiMatteo2002]. Monoclinic cell (low-temperature phase) shown relatively to trigonal cell (primitive cell of high-temperature phase) and hexagonal corundum cell (conventional cell of high-temperature phase).*

At room temperature, $V_2O_3$ stands in the rhombohedral structure $\bar{3}$, with approximate hexagonal close packing of oxygen atoms and vanadium atoms occupying 2/3 of the octahedral sites, typical of the corundum structure. Vanadium atoms stand in a coordination polyhedron of oxygen ligands, forming an octahedron (Figure 66a), which is trigonally distorted along the $C^3$ axis, directed along the vertical axis [Hansmann2012] (M and H indices stand for monoclinic and hexagonal cells, respectively). Orientation of the octahedra varies from plane to plane. The conventional unit cell is hexagonal (Figure 65, Figure 66b) and includes 6 formula units, whereas the rhombohedral primitive unit cell (Figure 65) holds only 2 formula units. This primitive unit cell shows that vanadium atoms form dimers, oriented along the c axis (Figure 66c).

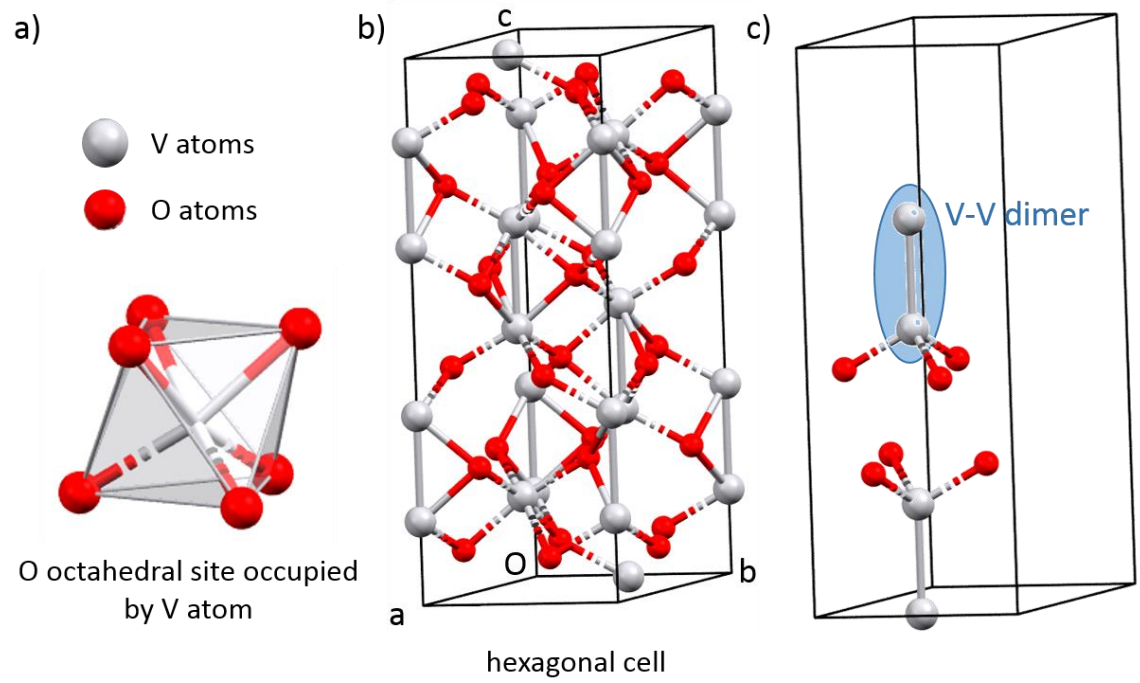


*Figure 66: a) Coordination polyhedron of V atoms, formed by an oxygen octahedron, trigonally distorted along the $C^3$ axis. b) Conventional hexagonal cell. c) Contents of the primitive rhombohedral unit cell. V atoms are arranged in dimers, oriented along $c_H$ axis. V and O atoms are represented in gray and red, respectively.*

The first order phase transition occurring around 150-160 K (Figure 64) breaks the structural symmetry towards monoclinic 2/ structure (Figure 65), with 4 formula units per unit cell, the latter being body-centered. This change from rhombohedral-to-monoclinic crystalline system is of ferroelastic nature with a spontaneous shear strain. The main feature of structural symmetry change is the disappearance of the 3-fold symmetry along , implying three equivalent ferroelastic domains [Singer2018]. Thus, three equivalent monoclinic cells can be derived from the parent hexagonal one, each with its own axis lying in the basal plane of the hexagonal cell (Figure 67a). The distortion includes a slight tilt of the axis with respect to the basal plane. Therefore, Bragg reflections along the axis split into three monoclinic reflections, arranged in a spherical equilateral triangle (Figure 67b).

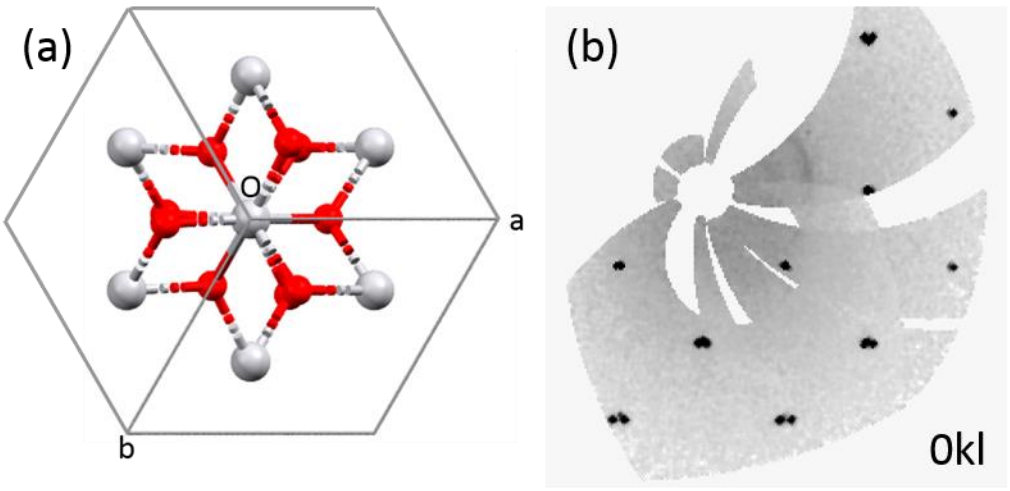


*Figure 67: a): High-temperature hexagonal cell of $V_2O_3$, viewed along the $c_H$ axis. Gray lines represent the three equivalent monoclinic cells, which can be derived from the hexagonal one, due to the $\bar{3}$ rotational symmetry. b) diffraction image in the (0kl) plane, obtained from a single crystal at 100 K, in the monoclinic phase. Peak splitting due to the twinning of monoclinic cell is clearly visible. Since the image is in the (0kl) plane, only two subpeaks are visible.*

For a given hexagonal reflection, the corresponding monoclinic indices can be determined from the three following transfer matrices:

$$\begin{pmatrix} \vec{a}_M \\ \vec{b}_M \\ \vec{c}_M \end{pmatrix} = \begin{pmatrix} \vec{a}_H \\ \vec{b}_H \\ \vec{c}_H \end{pmatrix}$$

with $= \begin{pmatrix} \frac{2}{3} & \frac{4}{3} & \frac{1}{3} \\ 1 & 0 & 0 \\ \frac{1}{3} & \frac{2}{3} & -\frac{1}{3} \end{pmatrix}; \begin{pmatrix} -\frac{4}{3} & -\frac{2}{3} & \frac{1}{3} \\ 0 & 1 & 0 \\ -\frac{2}{3} & -\frac{1}{3} & -\frac{1}{3} \end{pmatrix}; \begin{pmatrix} \frac{2}{3} & -\frac{2}{3} & \frac{1}{3} \\ -1 & -1 & 0 \\ \frac{1}{3} & -\frac{1}{3} & -\frac{1}{3} \end{pmatrix}$ [Dernier1970].

The monoclinic distortion also involves the expansion of interatomic distances between pairs of vanadium atoms. The V-V distance across the shared oxygen octahedral face increases from 2.7 to 2.745 Å, while the V-V distance across the shared octahedral edge, in the $-$ plane, goes from 2.872 to 2.987 Å. Other distances do not change significantly, except some bond length distortion in the basal honeycomb plane of V atoms, which directly influences the magnetic ordering. Therefore, a simple view of the distortion mechanism can be described as the rotation of vanadium pairs within the $-$ plane of about 1.8°, such that vanadium atoms move towards adjacent octahedral voids (Figure 68). A further distortion of the coordination octahedra occurs to accommodate this rotation. The latter is at the origin of the tilting of the axis (Figure 68) with respect to the $-$ plane. Again, pairs can rotate in three equivalent hexagonal cell directions perpendicular to the $\bar{3}$ axis, leading to the threefold degeneracy observed through the twinning of monoclinic cell (Figure 67b).

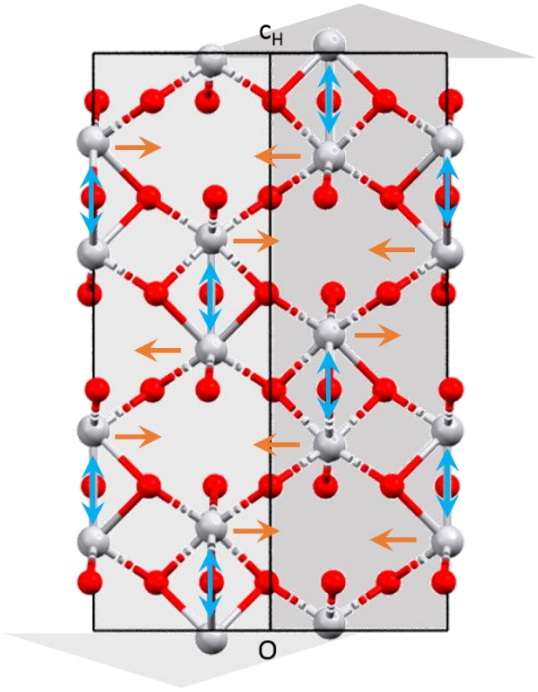


*Figure 68: View of the (110) plane of the hexagonal cell. Orange and blue arrows indicate the movement of atoms from low- to high-temperature phase. Grey arrows indicate the distortion inducing the tilting of $c_H$ axis.*

As already mentioned, these structural changes are accompanied by a macroscopic volume change, with a volume jump of about -1.4% at the transition from monoclinic to rhombohedral unit cell. On the other hand, a weak but present thermal dilation is observed in the high-temperature phase, with linear coefficients $= (20.2 \pm 0.3).10^{-6}\ ^{-1}$ and $= -(8.6 \pm 0.3).10^{-6}\ ^{-1}$ for a and c parameters, respectively [McWhan1970] (Figure 69). No thermal dilation was detected in the low-temperature phase. Surprisingly, the structural phase transition from monoclinic to rhombohedral phase is associated with simultaneous decrease of V-V dimer

length along the axis, whereas this same cell parameter increases ($\Delta / = 0.2\%$ and $\Delta / = -0.9\%$) and the overall unit cell volume decreases.

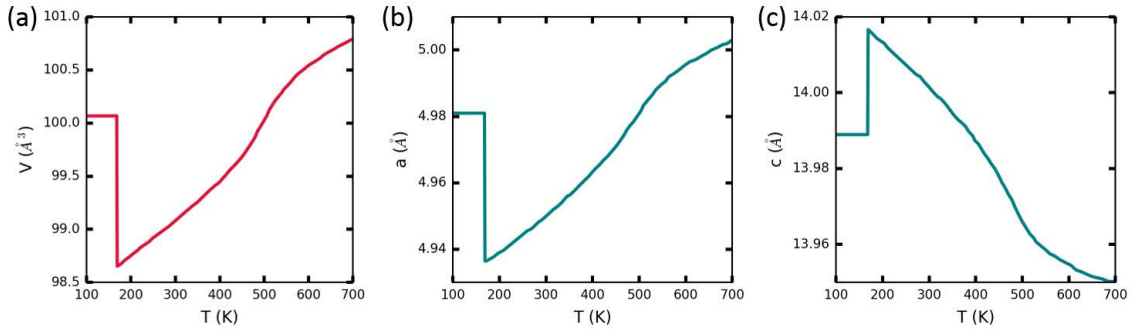


*Figure 69: adapted from [McWhan1970]. Variation versus increasing temperature of rhombohedral volume (a), a parameter (b) and c parameter (c). a and c parameters are represented in the hexagonal description.*

At very high temperature, namely above 500 K (Figure 69a), cell parameters show an anomaly [Belbeoch1978], which could be the fingerprint of crossing the Widom line, prolonging the Mott isostructural transition line beyond the critical end point in the crossover region between both insulating and metallic high-temperature states.

### *IV.2.b.ii. X-ray diffraction measurement on a single crystal*

We measured x-ray diffraction from a single crystal showing a long dimension of about 100 µm (Figure 70a) on a Mo diffractometer at λ = 0.7085 Å. Data reduction was performed with the CrysalisPro software [CrysalisPro v. 1.171.38.46, Rigaku Oxford Diffraction (2018)].

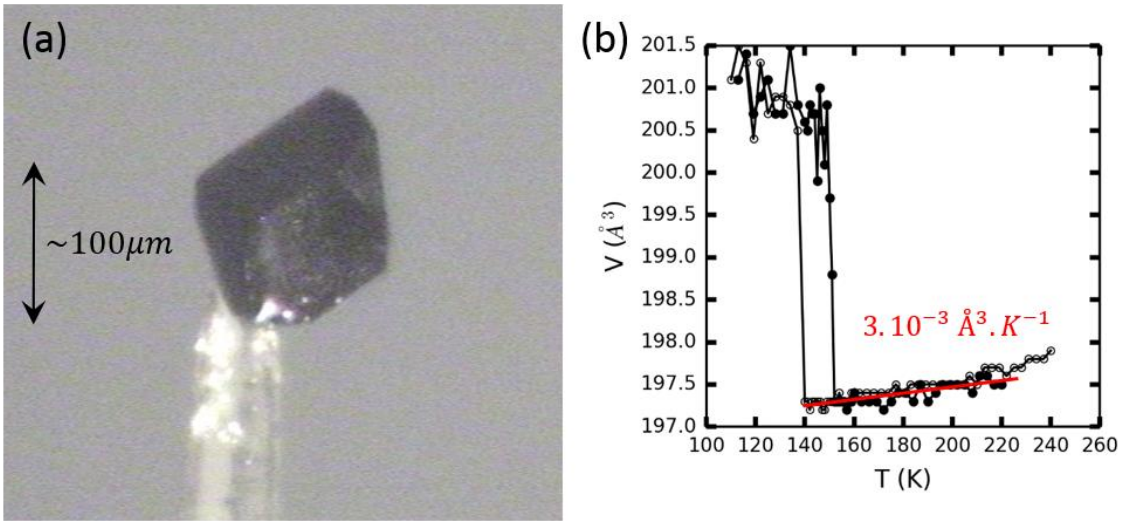


*Figure 70: a) Picture of the V2O3 single crystal, mounted for the x-ray diffraction measurement versus temperature. b) Monoclinic unit cell volume, as extracted from single crystal x-ray diffraction versus temperature with CrysalisPro software. Structural transition associated with a thermal hysteresis occurs around 138 – 150 K.*

Temperature was cycled from 240 K to 110 K, then back to 220 K, with 2 K-steps. Evolution of monoclinic unit cell volume, extracted from data reduction, shows a jump at the phase transition, around $\downarrow^{MIT} \approx 138$ upon decreasing temperature and $\uparrow^{IMT} \approx 150$ upon increasing temperature (Figure 70b). In the low-temperature phase, the splitting of peaks originating from the twinning occurring at the phase transition (Figure 71a), previously described in part 2.b.i, makes x-ray diffraction analysis difficult. This explains the noisy in the temperature range corresponding to monoclinic structure (Figure 70b). The distribution of diffracted intensity of one peak in the (0kl) plane of monoclinic unit cell shows a splitting of the peaks (Figure 71a). Upon

increasing temperature, the two peaks abruptly merge into one around $\uparrow^{IMT} \approx 150$ (Figure 71b), as the structural transition towards rhombohedral symmetry occurs. In the high-temperature phase, thermal expansion of around $3.10^{-3}$ Å$^3$.K$^{-1}$ is visible (Figure 70b), in accordance with data presented in the literature [McWhan1970].

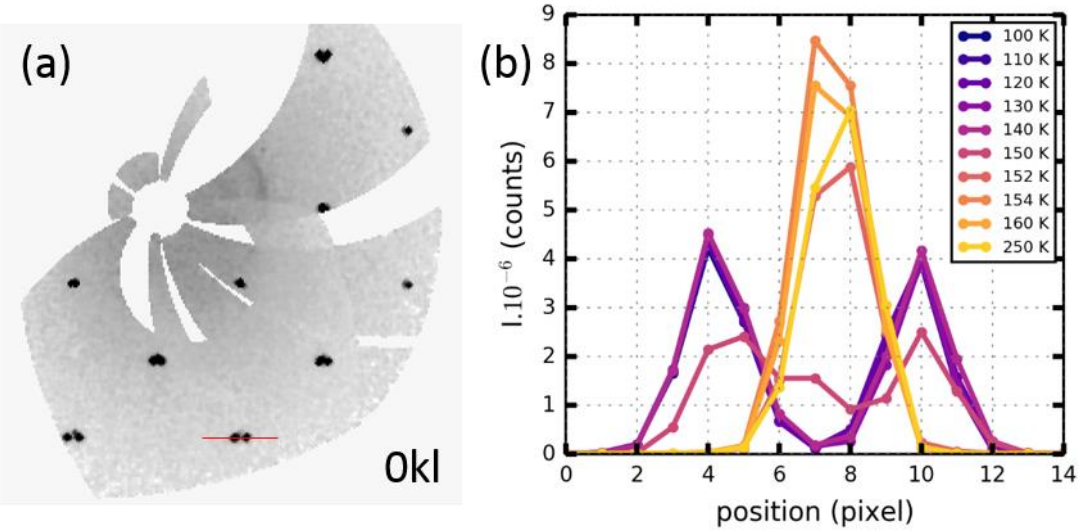


*Figure 71: a) Diffraction image in the (0kl) plane, obtained from a single crystal at 100 K, in the monoclinic phase. Peak splitting due to the twinning of monoclinic cell is clearly visible. Since the image is in the (0kl) plane, only two subpeaks are visible. b) Peak splitting under increasing temperature, observed along the red line plotted in the central image. The splitting seems to occur around 151 K, concomitant with the transition temperature reported in the literature.*

## IV.2.c. Electronic changes

Electronic properties of $V_2O_3$ are dictated by the vanadium 3d band. The octahedral crystal field lifts the degeneracy of the band, between doubly degenerate and triply degenerate $_2$, separated by about 3 eV in energy [Qazilbash2008]. The trigonal field of lower symmetry rhombohedral lattice further splits the $_2$ band into non-degenerate $_1$ and doubly degenerate bands [Stewart2012]. The strong on-site Coulomb repulsion between both 3d electrons splits each $_1$ and in two bonding and anti-bonding orbitals (Figure 72).

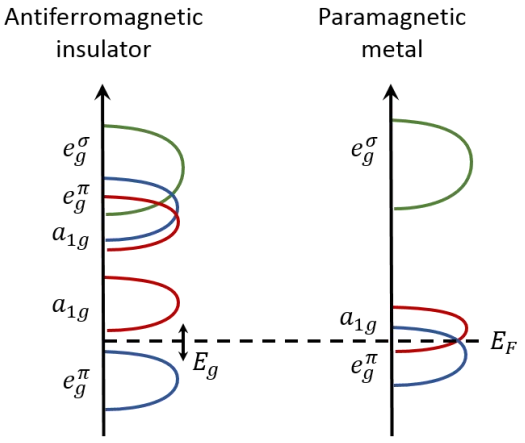


*Figure 72: adapted from [Qazilbash2008]. Energy level diagrams for the antiferromagnetic insulating (left) and paramagnetic metallic (right) phases of $V_2O_3$. The gap energy of around 0.6 eV in the low-temperature insulating phase closes in the high-temperature metallic phase.*

The Fermi level lies between $_1$ and bands, separated by a gap $\sim 0.6\ eV$ [Thomas1994] in the low-temperature insulating phase. In the high-temperature phase, $_1$ and bands overlap on the Fermi level and the system becomes metallic.
Infrared reflectivity measured at ambient pressure, on a temperature range spanning from 100 to 600 K (Figure 73), reveals striking differences below and above the temperature of transition [Baldassarre2008]. Below $^{IMT}$, the sharp feature around ω = 500 $cm^{-1}$ is attributed to the contribution of a phonon. The region of the spectrum above 500 $cm^{-1}$ is rather flat in the antiferromagnetic insulating phase. On the other hand, a Drude peak is clearly visible above the temperature of transition $^{IMT}$, witnessing metallic character. The decrease of reflectivity with increasing temperature in the metallic phase is well known as an effect of electron mobility decreasing with temperature, thus inducing a "bad metal" behavior.

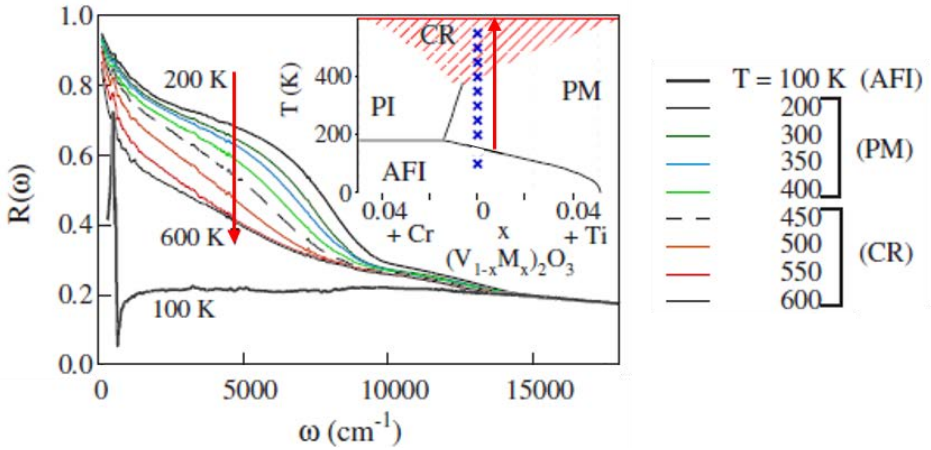


*Figure 73: from [Baldassarre2008]. Infrared reflectivity measured from 100 to 600 K at ambient pressure in $V_2O_3$ single crystal. Blue crosses on the phase diagram indicate measurement points corresponding to reflectivity curves, from antiferromagnetic insulating phase (AFI) to paramagnetic magnetic phase (PM), then crossover (CR) region.*

## IV.3. Time-resolved infrared studies on $V_2O_3$

During the last decade, several time-resolved optical studies were performed on photo-exited $V_2O_3$ systems. Again, although some of them related to photo-induced precursor phenomena in Cr-doped $V_2O_3$ around the isostructural Mott transition line [Mansart2010, Lanz2017], we will focus on the photo-induced phase transition in pure $V_2O_3$, i.e. from low temperature (LT) AFI phase to high temperature (HT) PM phase. In the next paragraphs, we first present previous works, then describe the results obtained in Sendaï within the frame of our French-Japanese collaboration.

### IV.3.a. Previous hypothesis: nucleation and growth mechanism

Liu et al. measured time-resolved infrared conductivity, performing THz time-domain spectroscopy, on a sub-100 nm $V_2O_3$ thin film grown on $Al_2O_3$ [Liu2011]. The optical pump-THz probe measurement at 120K, just under $^{IMT}$, showed an increase of the THz conductivity within around 20 ps (Figure 74). Since this duration is much longer than electron-phonon thermalization, the authors attributed the driving of the transition dynamics to a photo-thermal nucleation and growth mechanism.

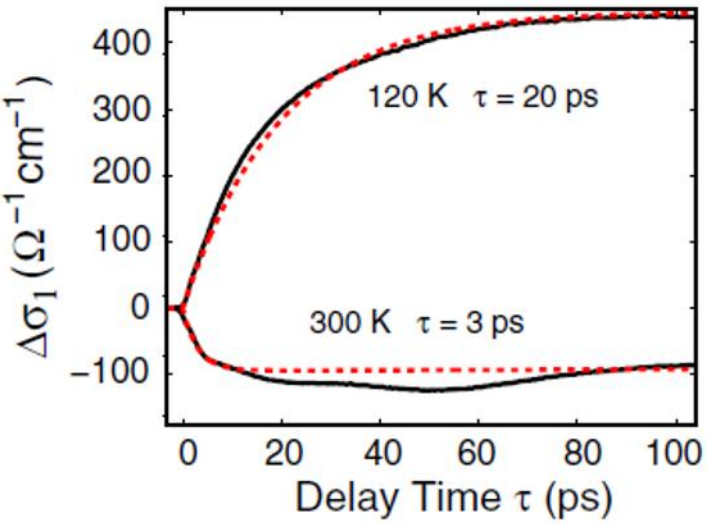


*Figure 74: from [Liu2011]. The onset of transient THz conductivity at 120 K (black line) shows a rising time of 20 ps (single exponential fit, red dashed line). The measurement at 300 K will not be discussed here.*

Several other time-resolved studies on $V_2O_3$ thin films suggest a metallic phase growth within few tens of ps following photo-excitation below $T_{tr}$ [Ronchi2019, Giorgianni2019]. Particularly, the measurement of ultrafast far-infrared conductivity through optical pump-THz probe measurement, seemed to show a dependence in laser excitation density and initial temperature on the transition dynamics [Abreu2015]. Actually, the renormalization at maximum of time-resolved conductivity data presents different rising times for different excitation and temperature (Figure 75). The authors of the study described the phenomenon with the Avrami model of nucleation and growth. They suggest temporal scaling arises from spatial scaling of the growth of photo-induced two-dimensional (cylindrical) metallic domains in the plane of the film.

First, it is important to note that, in the frame of THz probing, metallic conductivity can only be observed above the percolation threshold, i.e. the concentration of photo-induced metallic domains must reach a concentration of about 50% before current flows through the insulating matrix. Below this threshold, the system is globally insulating. Therefore, the THz conductivity cannot be crudely interpreted as a simple measure of the metallic fraction, and is not sensitive to its early increase in first ps.

Then, Abreu et al. consider a 2D cylindrical Avrami growth model, arguing that photo-excitation is roughly homogeneous throughout the film. However, this assumption does not prevent other mechanism from happening. In particular, photo-induced strain wave propagation (cf I.3.c) from the interfaces was not considered. Moreover, the volume discrepancy between growing (rhombohedral) metallic domains and (monoclinic) insulating matrix induces a significant cost in terms of elastic energy, which was not taken into account in the analysis. Actually, the authors consider a growth occurring at the speed of sound, way faster than what happens in the case of a thermal phase transition, where the system has time to adapt to the (several orders of magnitude) slower kinetics. In the case of a one-dimensional growth of metallic phase from the free surface however, the rate of growth would not be impacted by the elastic energy cost. It is also worth pointing out that this study was performed with a pump photon energy of 1.55 eV, far exceeding the gap energy of $V_2O_3$ (around 0.6 eV). This implies a significant excess energy compared to the phase transition, which can lead to additional heating of the system.

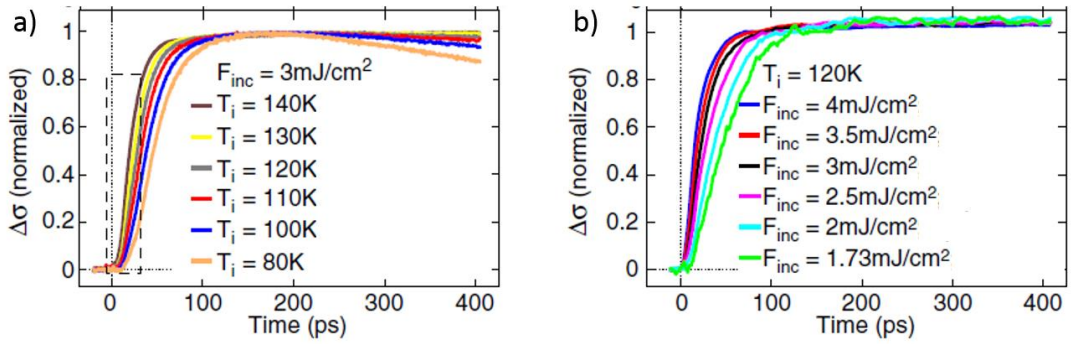


*Figure 75: adapted from [Abreu2015]. Transient far-infrared conductivity, normalized to maximum of time span. a) Comparison between different initial temperatures, under same laser excitation density. b) Comparison between different laser excitation densities, at the same temperature. In both a) and b), there seem to be a discrepancy in the rising time of transient conductivity, depending on initial conditions.*

Another study by Singer et al., performed in the coexistence region of LT and HT phases, focuses on ultrafast dynamics of structural changes [Singer2018]. Time-resolved x-ray scattering on crystalline thin film at the picosecond time scale revealed enhancement of the long-range order in the LT phase. Complementary x-ray nanoscopy suggested this early symmetry change to be the manifestation of a ferroelastic shear, propagating through the monoclinic 8 nm-domains within few ps (Figure 76). This precursor effect precedes volume change. Further unit cell volume decrease and insulator-to-metal transition occur concomitantly within 100 ps and are assumed to follow a nucleation and growth mechanism, relying on [Abreu2015]. Even though this study was performed in the coexistence region of temperature, with pre-existing HT phase, it seems to highlight the role of precursor structural deformations occurring at ultrashort (ps) time scale, to spark the phase transition.

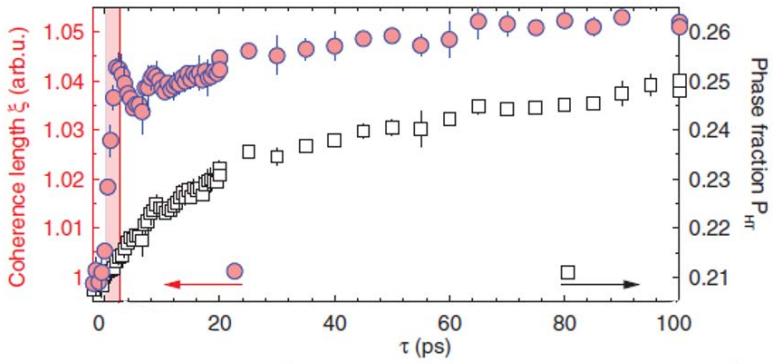


*Figure 76: from [Singer 2018]. Coherence length, corresponding to the size of oriented monoclinic domains (pink circles) shows a sharp increase within 2.5 ps, then reaches a saturation level, corresponding to the maximum value observed at equilibrium, around 70 ps. High-temperature phase fraction (white squares) shows continuous increase over 100 ps.*

## IV.3.b. Pump-probe infrared reflectivity measurements on $V_2O_3$ thin films

Recently, within the frame of our French-Japanese collaboration, time-resolved infrared reflectivity measurements were conducted at the University of Tohoku (Japan) [Amano2019]. The infrared pump-infrared probe measurements were carried out on thin films grown on $Al_2O_3$ substrate at the University of Nantes (France) [Babich2020]. 100 nm-thick film was excited at 10 K, far under the transition temperature, and at 80 K, just below the transition temperature. 1 µm-

thick film was excited at 10 K and at 120 K. Photo-induced signal coming from the substrate was measured and checked to be negligible compared with signal from the films.
The pump was an infrared short laser, with 100 fs pulse duration. The laser wavelength/energy was 1500 nm ≡ 0.8 eV, lying slightly above the $V_2O_3$ band gap. Therefore, photon energy is only enough to induce the low-temperature-to-high-temperature transition, limiting the energy excess and thus the additional heating by energy redistribution. The infrared probe pulse of 100 fs duration was generated with an Optical Parametric Amplifier (OPA), from 0.1 to 1.15 eV. Transient reflectivity of the excited samples was measured at 500 Hz.

### *IV.3.b.i. 1 µm-thick sample*

The static reflectivity spectrum of the 1 µm-thick sample shows interference features in the low-temperature phase. This oscillating structure of the spectrum originates from interferences with the reflected beam at the $V_2O_3$-$Al_2O_3$ interface, the film thickness being of the same order of magnitude than the penetration depth of infrared light in the low-temperature phase (≈ 500 nm). In the high-temperature phase, the penetration depth of infrared light in the metallic state is much shorter (≈ 50 nm) and the interferences vanish. Static reflectivity measured at 66 K and 200 K will be considered as the references for low-temperature and high-temperature phases, respectively (Figure 77a).
Time-resolved reflectivity was measured on the sample, with initial temperature of 120 K. Transient spectra show a fast onset of the relative reflectivity change $\Delta \quad / \quad$ within 1 ps, which indicates an increase of the metallic fraction (Figure 77c), taking place quasi-instantaneously just after electronic and structural precursor phenomena (few 100 fs). The transient signal increases quasi-linearly in a first step, roughly compatible with an acoustic time scale of 50 ps for a penetration depth of 500 ps and sound velocity of about $\approx \ 8000 \quad . \ ^{-1}$ (8 nm.ps$^{-1}$). It then reaches 90% of its maximum amplitude at $_{90\%} \approx 300\ ps$ (Figure 78a, with 0.25 eV probe). At this time delay and later, $\Delta \quad / \quad$ resembles the static reflectivity difference in temperature, in both shape and amplitude (Figure 77b). This suggests an almost complete transformation of the sample, from insulating state in the low-temperature phase to metallic state at time delay > 300 ps.

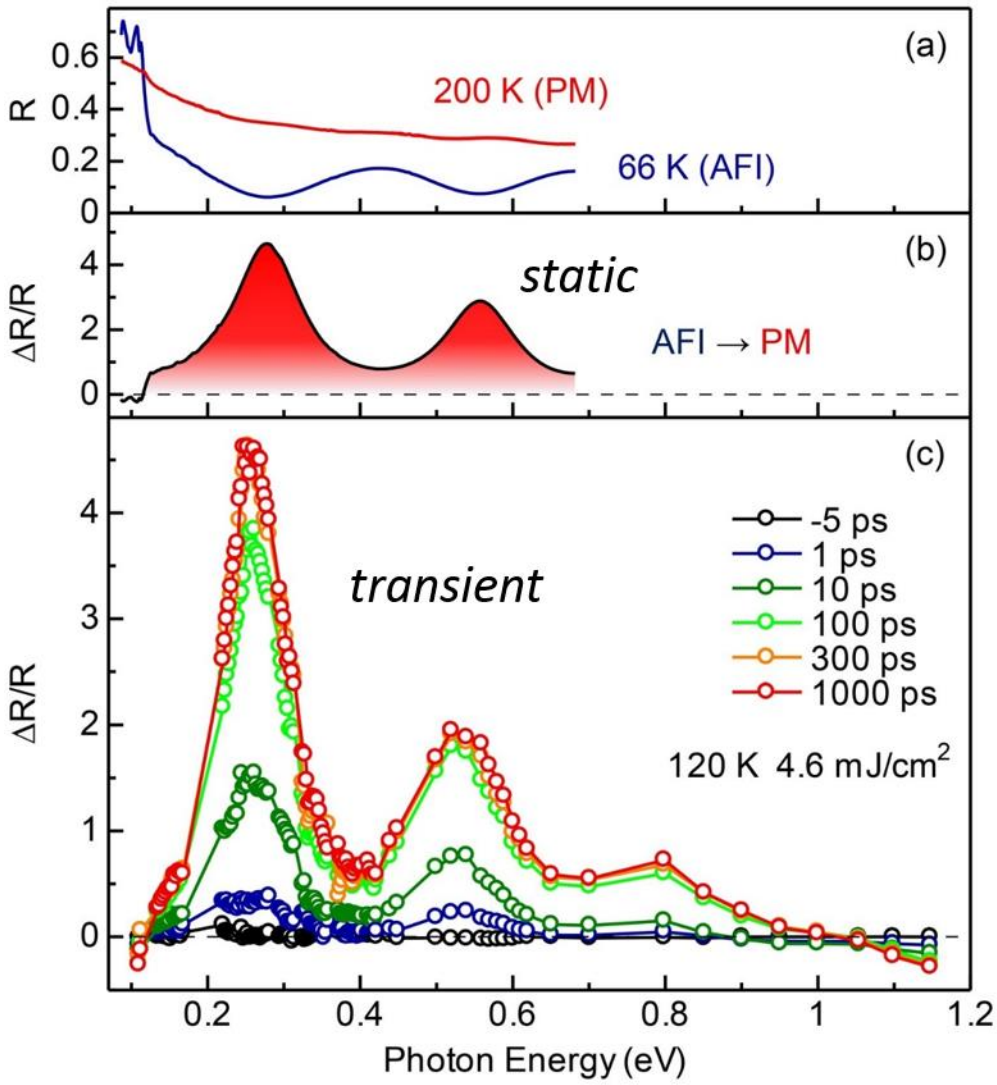


*Figure 77: adapted from [Amano2019]. a) Static reflectivity of 1 µm-thick $V_2O_3$ thin film on $Al_2O_3$ substrate, measured at 200 K (paramagnetic metallic phase, red) and 66 K (antiferromagnetic insulating phase, blue). b) Static reflectivity difference between low-temperature and high-temperature phases, calculated from a). c) Transient reflectivity spectra measured on a 1 µm-thick film at 120 K under 4.6 mJ.cm$^{-2}$ excitation density.*

Transient reflectivity measured with 0.25 eV probe and 100 fs temporal resolution demonstrates an instantaneous response of the system after photo-excitation, reaching 90% of its maximum amplitude $_{90\%} \approx 300\ ps$ (Figure 78a).

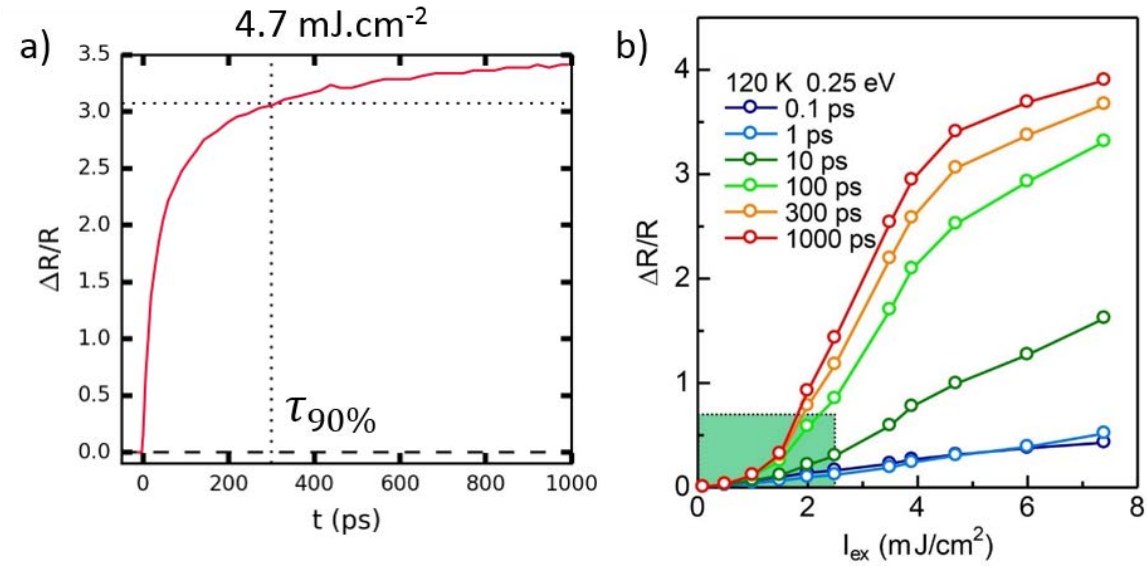


*Figure 78: adapted from [Amano2019]. a) Transient relative reflectivity Δ / measured at 120 K with 0.25 eV probe. b) Transient relative reflectivity Δ / measured at 120 K on a 1 µm-thick film, with 0.25 eV probe, versus excitation density. At time delays $\geq 100\ ps$, a nonlinear threshold appears around 1.5 mJ.cm$^{-2}$. Saturation of the signal seems to occur around 4.5 mJ.cm$^{-2}$.*

The study of transient reflectivity at 0.25 eV versus laser excitation density, shows a linear trend of the signal amplitude, for time delays until 10 ps. A nonlinear behavior of the signal amplitude is clearly visible, starting at a threshold around 1.5 mJ.cm$^{-1}$ for time delays $\geq 100\ ps$. Moreover, a weak saturation effect seems to appear for high laser excitation densities, above 4.5 mJ.cm$^{-1}$ (Figure 78b).

This nonlinear behavior raises the question of the importance of a cooperative phenomenon, as a positive feedback effect which self-amplifies the metallic transformation, as it is observed in spin-crossover molecular materials [Bertoni2016]. The transition dynamics could be interpreted as propagative at sound velocity with a first linear step (Figure 78a), corresponding to the emergence of small metallic clusters state, triggered by structural and electronic precursor phenomena and followed by the development of the metallic phase at macroscopic scale.

The same measurement was performed at 10 K and shows similar results. At this temperature, calculation of heat deposited by the laser pulse in the material leads to a maximum heating to about 145 K at highest excitation density. This value lies below the transition temperature upon increasing temperature, measured to be around 152 K in this sample, thus confirming that the photo-induced transition is probably not simply operated through heating. For an initial temperature of 120 K, the estimated maximum temperature is about 167 K. This might explain the weak saturation effect observed at high laser excitation density in these conditions.

### *IV.3.b.ii. 100 nm-thick sample*

The same study was performed on 100 nm-thick film on $Al_2O_3$ substrate. Since film thickness is significantly smaller than light penetration depth in AFI phase, static reflectivity measured on this sample does not show any interference feature at 66 K (Figure 79a).

Similar to what was observed in the 1 µm sample, transient Δ / spectra show shape and amplitude close to static reflectivity difference in temperature (Figure 79b), at 100 ps time delay (Figure 79c).

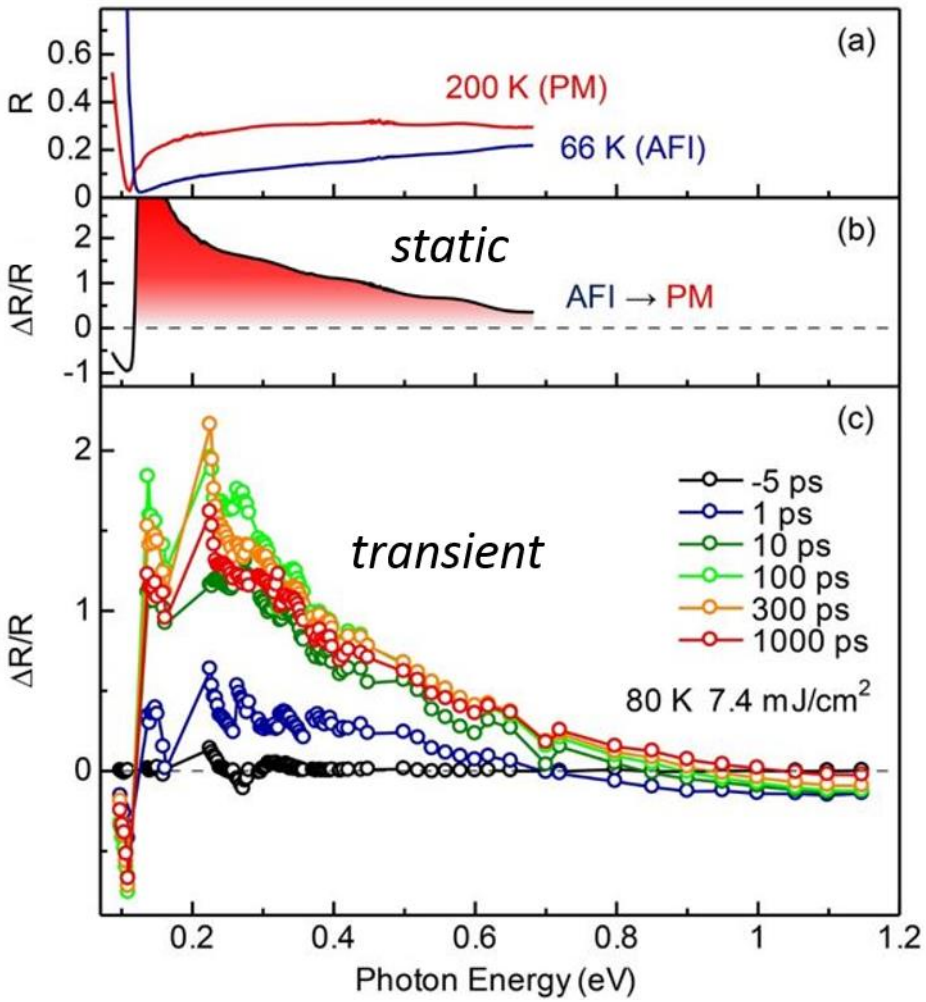


*Figure 79: adapted from [Amano2019]. a) Static reflectivity of 100 nm-thick $V_2O_3$ thin film on $Al_2O_3$ substrate, measured at 200 K (paramagnetic metallic phase, red) and 66 K (antiferromagnetic insulating phase, blue). b) Static reflectivity difference between low-temperature and high-temperature phases, calculated from a). c) Transient reflectivity spectra measured on a 100 nm-thick film at 80 K under 7.4 mJ.cm$^{-2}$ excitation density.*

Transient signal measured with 0.25 eV probe for an initial temperature of 80 K reveals fast response of the system: quasi-linear increase compatible with an acoustic time scale of 12.5 ps for the thickness of 100 nm, and reaches 90 % of maximum amplitude within $_{90\%} \approx 20\ ps$, ten times earlier than in the 1 µm-thick sample (Figure 80a).

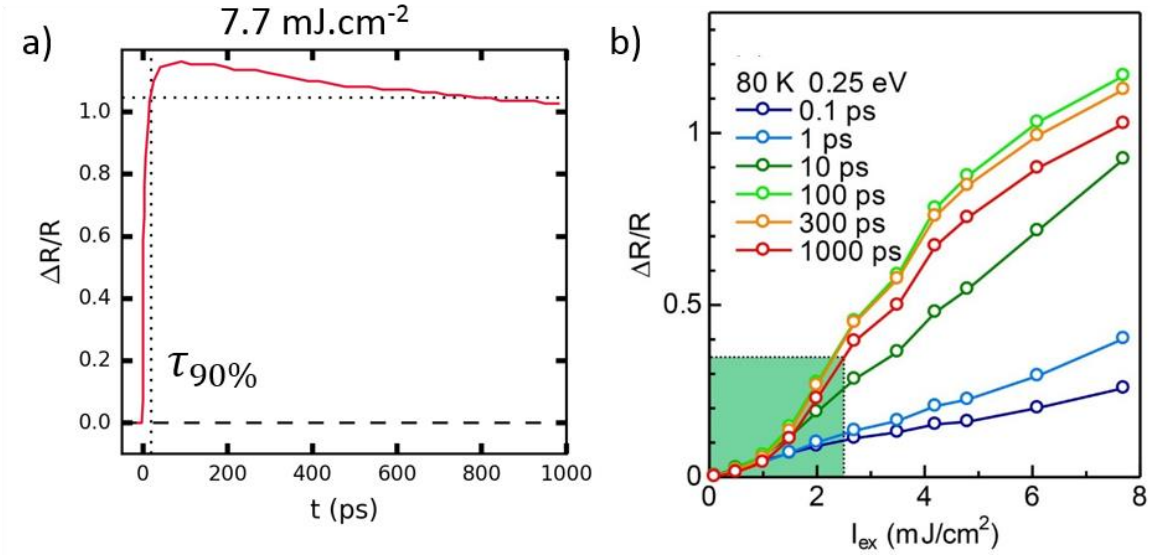


*Figure 80: adapted from [Amano2019]. a) Transient relative reflectivity Δ / measured at 80 K with 0.25 eV probe. b) Transient relative reflectivity Δ / measured at 120 K on a 1 µm-thick film, with 0.25 eV probe, versus excitation density. At time delays ≥ 100 ps, a nonlinear threshold appears around 1.5 mJ.cm$^{-2}$. No clear saturation of the signal is observed*

Nonlinear threshold in excitation density is observed around 1.5 mJ.cm$^{-1}$ at time delays $\geq 10\ ps$ and no complete saturation of the signal is visible (Figure 80b).
The same measurement was performed at 10 K and shows similar results. At this temperature, calculation of heat deposited by the laser pulse in the material leads to a maximum heating to about 148 K at highest excitation density. For an initial temperature of 80 K, the estimated maximum temperature is about 159 K. Both values lie slightly higher than the transition temperature upon increasing temperature, measured to be around 145 K in this sample. However no striking effect is distinguishable in the signal evolution versus excitation density for this film, tending to validate the non-thermal character of the photo-induced transition.

For both samples, similarities between static low-temperature-high-temperature reflectivity difference and transient reflectivity indicate the transient transformation to metallic state at macroscopic scale with a clear nonlinear increase (threshold) with excitation density. Comparing both 100 nm- and 1 µm-thick samples, the observed linear increase takes place on shorter time scale for the ultra-thin film, as does $_{90\%}$. This observation agrees with the size reduction, as expected in the hypothesis of a propagation of metallic states at sound velocity.

### IV.3.c. Reflectivity simulations with a multilayer model

This metallic phase acoustic propagation hypothesis was tested with a numerical model, calculating the resulting reflectivity of a multilayered sample.
Fresnel equations describe the reflection, refraction and absorption of light at an interface between two media. These equations, combined to a transfer-matrix method, allow calculating these values for a multilayered sample [Okamoto2004]. These calculations were implemented by S. Byrnes in the “tmm” Python software package [Byrnes2019].
In collaboration with the team from University of Nantes, we used the tmm package in an attempt to rationalize the transient reflectivity measured in pump-probe infrared experiment. We described the system with a metallic $V_2O_3$ layer, sandwiched between an air layer and an insulating

$V_2O_3$ layer deposited on $Al_2O_3$ (Figure 81). With increasing time, the thickness of the metallic layer increases, proportional to the speed of sound in $V_2O_3$ ( $\approx 8000$ . $^{-1}$).

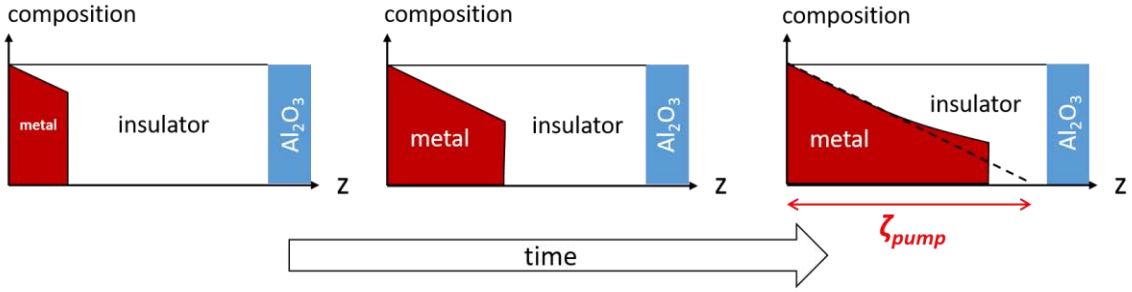


*Figure 81: Scheme of multilayer model, with metallic layer spreading at the speed of sound in the material, with a damping of a metallic fraction dictated by the pump laser penetration depth. Second layer is composed of insulating phase of $V_2O_3$, while third layer is the $Al_2O_3$ substrate. Width of the layers are not quantitative on this scheme.*

To account for the attenuation of the pump laser within the material, we considered a metallic proportion varying as a decreasing exponential in depth, with a rate equal to the penetration depth of the pump laser (Figure 81). Since the latter is approximately equal to 500 nm, the attenuation effect will be less important in the 100 nm-thick film than in the 1 µm-thick one. Using the same approach as [Okamoto2004], refractive index of the mixed metallic-insulating layer was approximated to be a sum of refractive indices of its components, weighed by their respective fraction:

$$= (1 - \quad _{al}) \quad _{ns} + \quad _{al} \quad _{al}$$

The obtained transient reflectivity spectra are compared with experimental data (Figure 82). Interference features are reproduced in the 1 µm film, whereas amplitude of both spectra is roughly the same as in the experiment. Since the speed of sound in $V_2O_3$ is about 8 nm.ps$^{-1}$, we had to limit our simulations to $ilm \quad hickn \quad / \quad \approx 12\ ps$ n the 100 nm film.

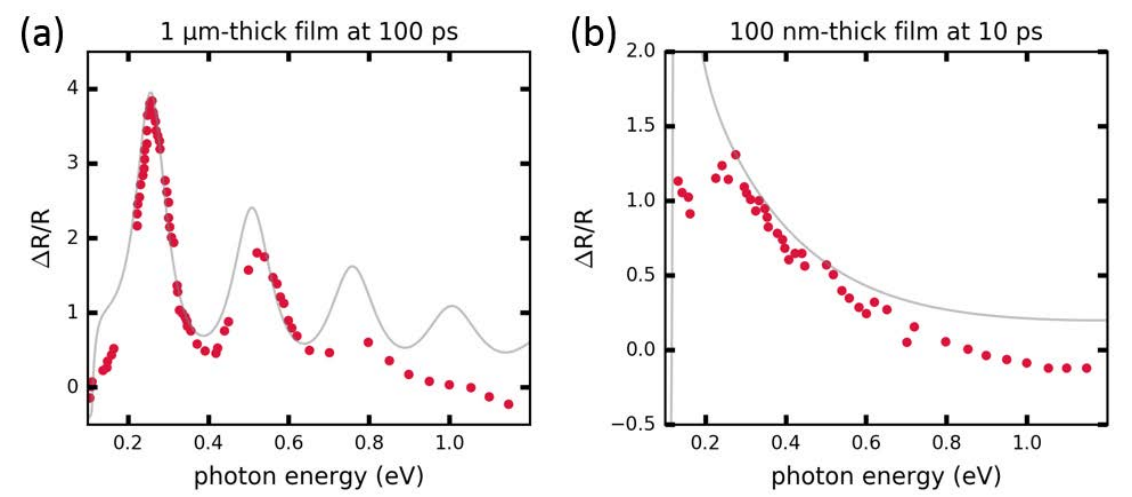


*Figure 82: a) Relative reflectivity spectrum calculated for the 1 µm film with the multilayer model, considering 50 ps propagation time (gray line). Simulations reproduce the interference features seen in the experiment (red dots). b) Relative reflectivity spectrum calculated for the 100 nm film with the multilayer model (gray line), considering 50 ps propagation time. Simulations agree quite well with the experimental measurements (red dots), quantitatively and qualitatively.*

Transient reflectivity was measured with 100 fs temporal resolution, with 0.25 eV and 0.62 eV probes at 10K. The comparison between experimental data and simulations is shown in Figure 83. Considering the 1 µm film (Figure 83a,b), the rising time of both experimental (measured at 7.4 and 7.7 mJ.cm$^{-2}$) and simulated data correspond quite well. However, interference effect, related to acoustic wave front reflection at the interfaces, is too much pronounced in simulations and the

overall amplitude reached by simulated data is also too high. For the 100 nm film (Figure 83c,d), the dynamics of the simulated data seems slightly too slow compared with experimental data (measured at 4.7 and 4.7 mJ.cm$^{-2}$). Yet, simulation at 0.62 eV probe (Figure 83d) reproduces the measurement quite well. Some discrepancies remain, which raise questions about the entire validity of the used model.

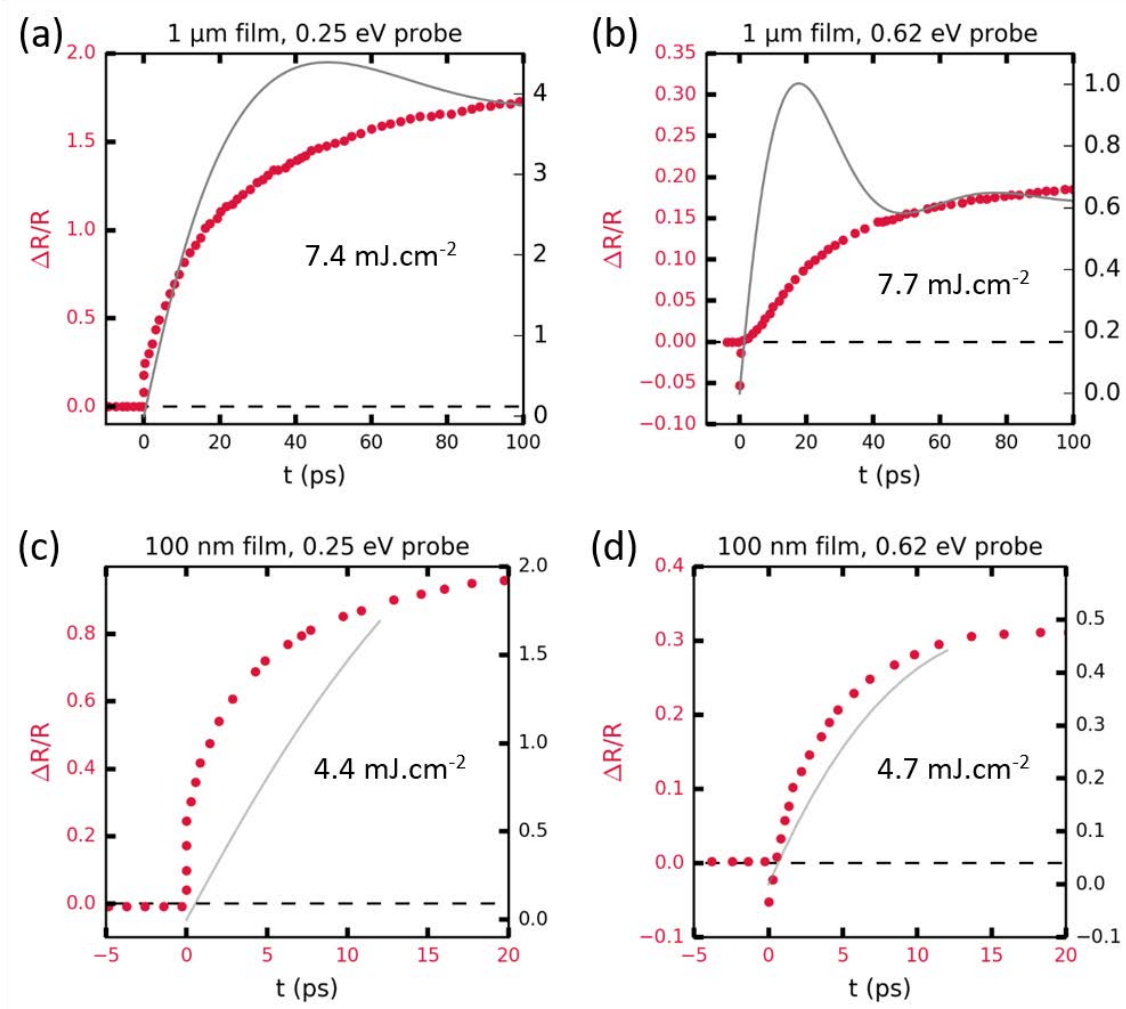


*Figure 83: Comparison of measured (red dots) and simulated (gray lines) data for 1 µm (a,b) and 100 nm (c,d) films, with 0.25 eV (a,c) and 0.62 eV (b,d) probes. For 1 µm film, even if interference effects are enhanced in the simulation, the dynamics of the build-up of the signal fits experimental data quite well. Considering the 100 nm film, the dynamics seems slightly too slow in the simulations. However, this effect is less pronounced for 0.62 eV probe. Amplitudes reached by the simulated data are slightly too high for both films.*

This multilayer model simulations allow to only roughly describe the transient reflectivity dynamics in $V_2O_3$ thin films observed by pump-probe infrared measurements, with the hypothesis of a metallic phase propagating from the surface through the film, with an exponentially attenuated profile. With a view to better describing the experimental date, we plan to perform further simulations with a mixed insulating-metallic propagating phase, the transformation being considered incomplete at z = 0, with a transformation ratio depending of the value of excitation density. We expect the reduction of optical contrast at the wave-front will also to reduce the effect of interferences in the simulation.

With this study, electronic properties of the photo-excited film were investigated. However, reflectivity does not give information about the structural dynamics of the photo-induced phase transition, which remain to be tackled.

## IV.4. Structural study by time-resolved x-ray diffraction on $V_2O_3$ thin films

Light-driven volume expansion is usually considered as a secondary phenomenon in photo-induced phase transitions. However, we know from spin-crossover materials that volume expansion of the unit cells can significantly influence the transition dynamics. Unlike previous studies, which rely on the conventional picture of nucleation and growth provided by the Avrami model, our approach focuses on feedback effects and phase front propagation at the speed of sound.

Time-resolved infrared study associated with simulations with a multilayer reflectivity model seems to demonstrate that photo-excitation of $V_2O_3$ thin film from the surface induces the transition to a metallic phase, which expands in depth at acoustic speed. Since insulator-to-metal transition in $V_2O_3$ is associated with significant volume change (-1.4%) and structural distortion, we expect this metallic phase front propagation to be concomitant with a strain wave propagation, caused by structural deformation launched by the photo-induced phase transition. We performed x-ray diffraction studies to investigate the role of structural deformations in the light-induced low-temperature-high-temperature transition in $V_2O_3$, hence pushing further the study of elastic cooperativity in photo-induced phase transitions.

### IV.4.a. Characterization of samples versus temperature

The samples considered in this experiment were $V_2O_3$ thin films grown on $Al_2O_3$ substrate by the team from University of Nantes, with the same morphology as in time-resolved infrared study. To investigate the effect of propagation within the sample after photo-excitation from the surface, three different thicknesses were considered: 500 nm, 250 nm and 100 nm.

Infrared laser transmission through the film allows characterizing the transition temperature of the samples, as laser transmission reflects their electronic properties. This measurement was performed on ID09 beamline at ESRF, prior to time-resolved x-ray diffraction.

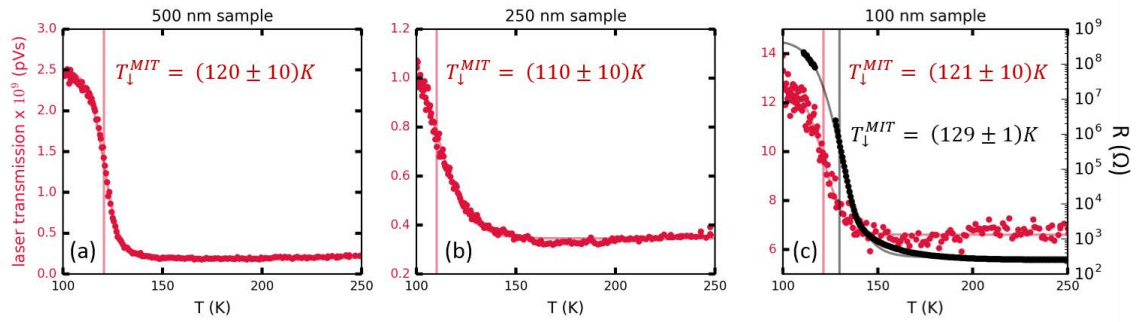


*Figure 84: 0.6 eV laser transmission (red dots) versus decreasing temperature for 500 nm- (a), 250 nm- (b) and 100 nm-thick films. Transition temperature $_{\downarrow}^{IT}$ is determined fitting the data with a step function (red line). On (c), resistivity data (black dots) are shown for comparison, also fitted with a step function (gray line). The observed shift of about 10 K in the temperature of transition stands within the calibration error of the cryostat.*

We measured the pump laser transmission throughout the samples, upon decreasing temperature (Figure 84), controlled by an Oxford Cryostream cryostat. Laser power was attenuated, such that excitation density was under the threshold for phase transition. The fit of experimental data with a step function gives $_{\downarrow}^{MIT} \approx (120, 110, 121) \pm 10$ for 500, 250 and 100 nm samples, respectively (Figure 84a,b,c).

Both resistivity and transmission are related to electronic properties of the material, and are thus expected to show the same behavior. The comparison of laser transmission with resistivity data

for the 100 nm sample (measured for this sample only) shows a discrepancy of around 10 K between both measurements in $\downarrow^{MIT}$ (Figure 84c). However, the observed shift stands within the calibration error of the cryostat, as it may exist an uncertainty of several Kelvin degrees in the absolute temperature.

### IV.4.b. Time-resolved x-ray diffraction at 95 K

The objectives of time-resolved x-ray diffraction will be to determine whether the whole sample is transformed under photo-excitation, if a fingerprint of the symmetry breaking of the transition can be defined and if the dynamics of the insulator-to-metal conversion process is compatible with a wave propagating at acoustic speed.
With these questions in mind, we performed time-resolved x-ray diffraction at the ID09 beamline (ESRF, France), which set-up was described in Chapter II.2.b. Fast rotating choppers were used to isolate x-ray single pulses (each 100 ps long) at 1 kHz repetition rate. The x-rays were partially monochromatized by using a multilayer monochromator, resulting in 1.5% bandwidth centered at 14.5 keV (λ = 0.8551 Å).
Pump laser wavelength/energy was chosen to be the same as in infrared experiment 1500 nm ≡ 0.8 eV, with an excitation of the sample from the top. Laser beam size was 1 mm².
Excitation was performed at 95 K, where the compound is in the low-temperature phase. X-ray diffraction was performed at grazing incidence, to match x-ray and laser penetration depths.

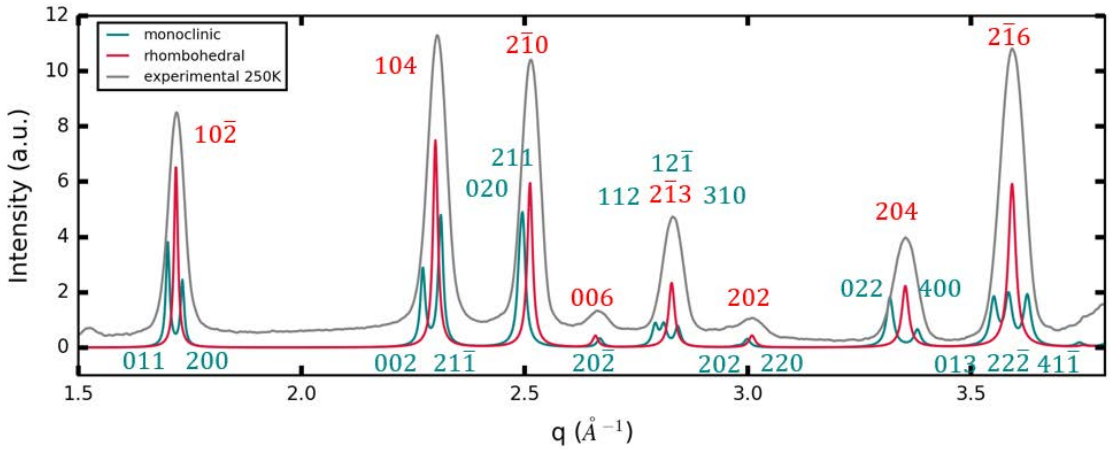


*Figure 85: Experimental diffraction pattern of 500 nm $V_2O_3$ thin film at 250 K, in the high-temperature phase (gray line). Grazing incidence geometry produces broad diffraction peaks. Expected diffraction patterns for better q resolution are shown in comparison, for low temperature (green line) and high temperature (red line) phases. Peaks indices of the low (high) temperature phase are indicated in green (red).*

One of the most striking features which can be noticed at the structural transition from low temperature to high temperature phase is the merging of groups of peaks (Figure 85): $013, 22\bar{2}$ and $41\bar{1}$ peaks in monoclinic phase become $2\bar{1}6$ in rhombohedral phase, for instance. Actually, these duo/trio of peaks become equivalent with the opening of $\beta_M$ angle at the structural transition, as the symmetry increases. Due to grazing incidence diffraction geometry, the q resolution in our experiment was not sufficient to distinguish the different peaks. However, transient x-ray diffraction showed clear narrowing of the peaks over time (Figure 86, yellow arrows), accompanied by a rise in peak intensity.
Moreover, since high-temperature phase presents slightly lower (≈ 1%) volume than low-temperature phase, a peak shift towards higher q is expected. This shift is also visible on Figure 86

(red arrows), which shows diffraction patterns plotted over time after photo-excitation on the 500 nm film.
These observations confirm photo-induced structural transition in $V_2O_3$ thin films.

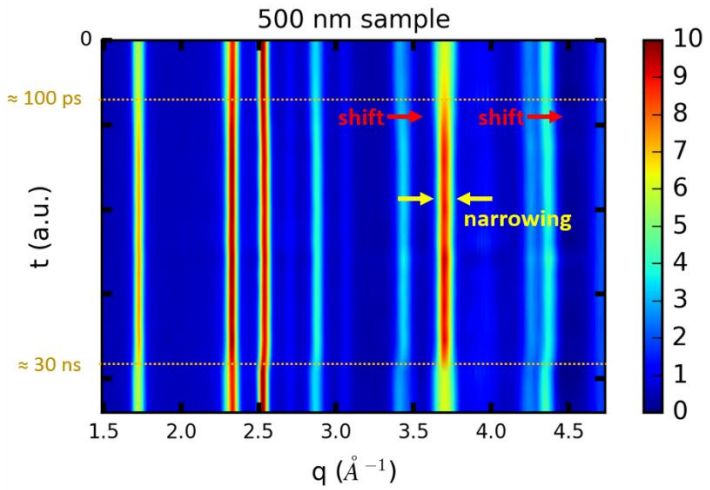


*Figure 86: X-ray diffraction patterns plotted over time (arbitrary units, logarithmic scale) for 500 nm sample, under 7 mJ.cm$^{-2}$ excitation density. A clear transient peak shift towards high q is visible (red arrows), witnessing unit cell volume contraction. Another feature to be noticed is the narrowing of the peaks (yellow arrow), associated with an increase in intensity, being the signature of symmetry change.*

## IV.4.c. Differential signal

The differential signal is calculated from the difference between a reference diffraction pattern measured at -5 ns and the diffraction pattern taken at a given time delay, as described in the Chapter II.3.a of this manuscript. It directly represents the transient diffraction signal and therefore allows to better grasp the changes in the diffraction pattern of the photo-excited system.
Differential signal measured at intermediate excitation density (≈ 4 mJ.cm$^{-2}$) is plotted in Figure 87, Figure 88 and Figure 89 for the 100, 250 and 500 nm samples, respectively.

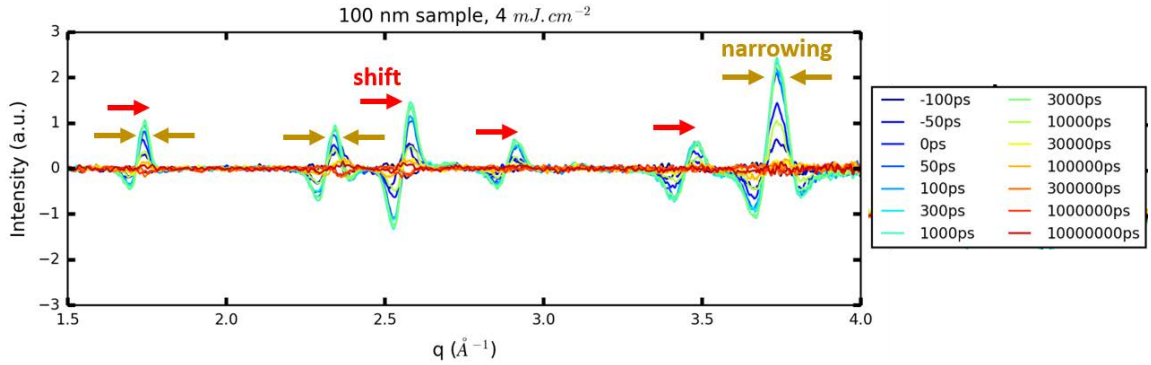


*Figure 87: Differential signal, plotted from -100 ps to 10 µs for 100 nm sample, at intermediate excitation density. Qualitative changes are characteristic of a narrowing of the peaks, coupled to a peak shift.*

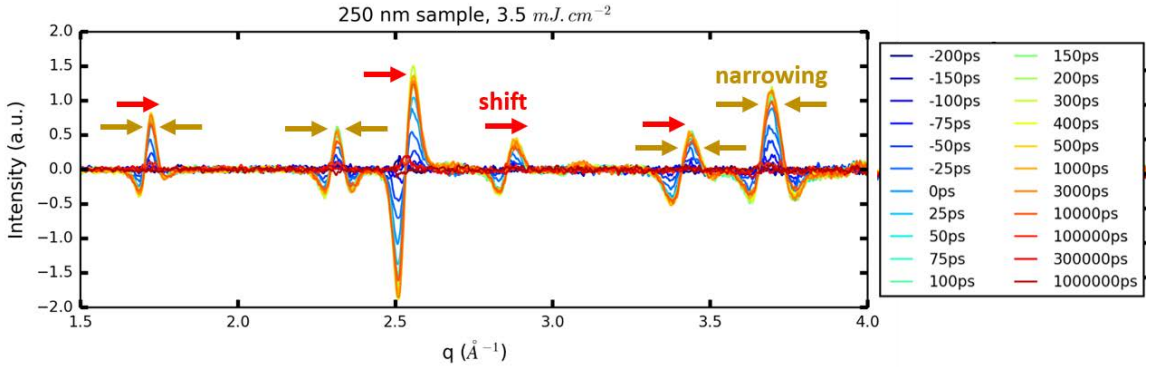


*Figure 88: Differential signal, plotted from -200 ps to 1 µs for 250 nm sample, at intermediate excitation density. Qualitative changes are characteristic of a narrowing of the peaks, coupled to a peak shift.*

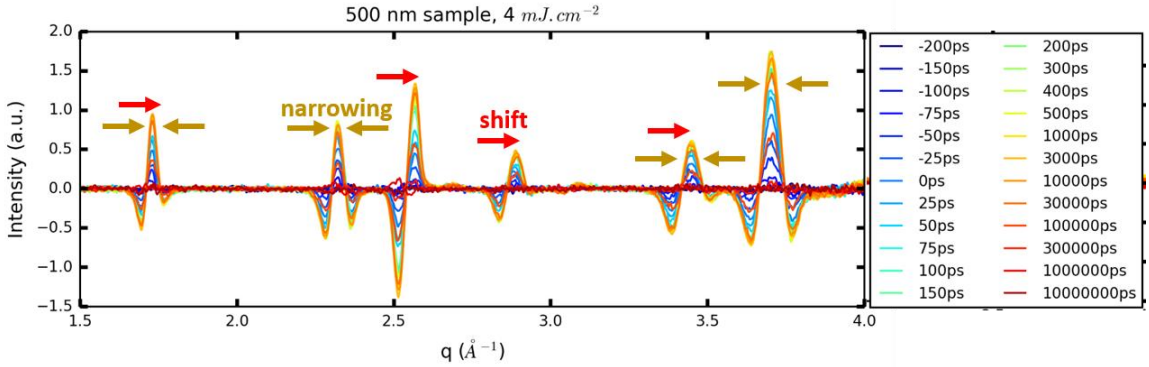


*Figure 89: Differential signal, plotted from -200 ps to 10 µs for 500 nm sample, at intermediate excitation density. Qualitative changes are characteristic of a narrowing of the peaks, coupled to a peak shift.*

For the three samples, differential signal shows bipolar signal on most of the peaks, characteristic of peak shift towards high q, witnessing a decrease of the unit cell volume. A tripolar signal is also visible (loss of intensity in the aisles of the peaks and increase of intensity in the center), characteristic of the merging of several peaks into one and thus witnessing symmetry change. The coupling of both shift and narrowing induces an asymmetric shape of the differential signal, with more intensity loss at low q value than at high q. This is induced by a peak shift towards high q value, characteristic of a decrease of unit cell volume. The peak shift is particularly visible on the peak at $\approx 2.6\ \text{Å}^{-1}$, which is almost not affected by symmetry change.

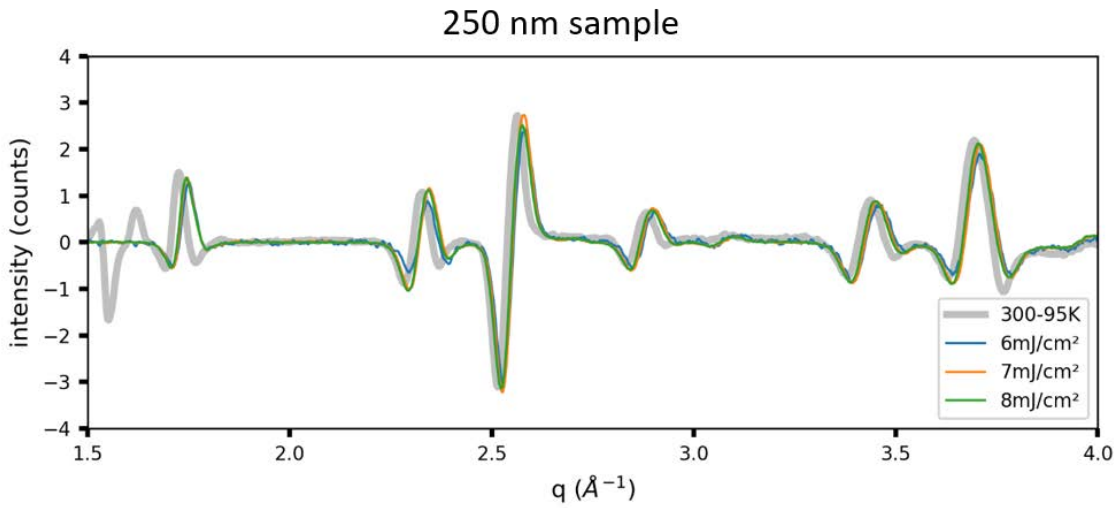


*Figure 90: Comparison of differential signal at equilibrium between 300 K and 95 K (gray line) and differential signal at 100 ps (when transient signal reaches a plateau) for high laser excitation density on 250 nm sample. Signals show strong similarities.*

The comparison between differential signal at equilibrium between 300 K and 95 K and transient differential signal at 100 ps on 250 nm sample under high excitation density shows strong similarities between both (Figure 90), confirming the hypothesis of a complete LT-to-HT phase transformation within 100 ps. 100 nm and 500 nm samples show similar signals. Hence, qualitative study of differential signal confirms what was seen in the absolute signal in Figure 86.

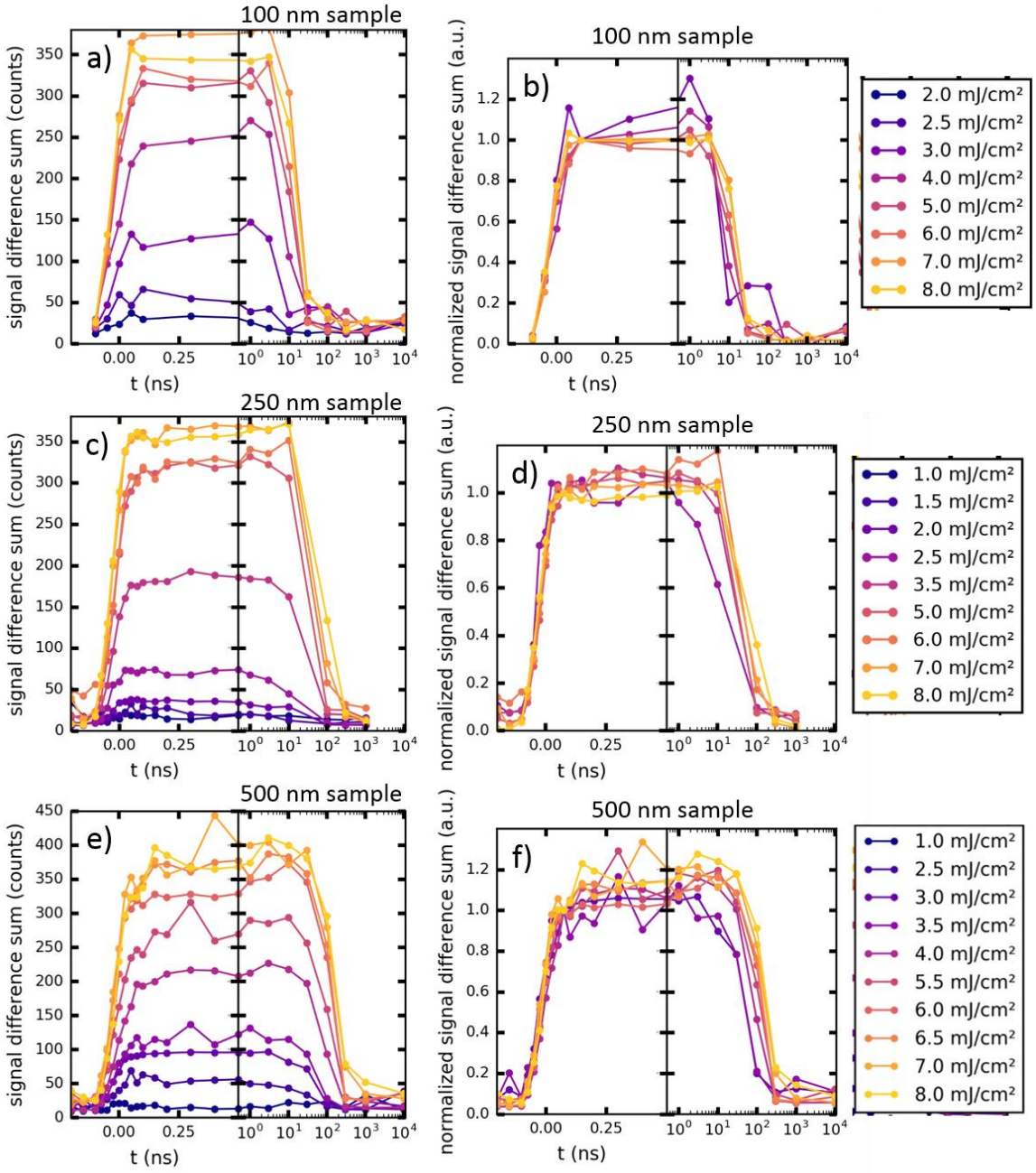


*Figure 91: Integral of the absolute differential signal, from 100 nm (a,b), 250 nm (c,d) and 500 nm (e,f) samples. (a,c,e) show signal for different excitation densities. (b,d,f) represent the same signal, normalized to 100 ps value, at the beginning of the plateau. Dynamics does not seem to vary with excitation density. Signal at very low excitation density (below 2.5 mJ.cm$^{-2}$ threshold) was not plotted, being too noisy.*

Quantitative analysis of the differential signal is performed by summing the absolute value of the signal over the six peaks visible in Figure 87, Figure 88 and Figure 89. The plot of differential sum versus time for all three samples shows a fast dynamics at short time delay, with an increase of the signal within around 100 ps (Figure 91). The signal then reaches a plateau, and suddenly decreases at long time scale, around 10-100 ns (Figure 91) and recovers initial value before next laser pulse arrives.

The plot of differential sum versus time for all three samples shows an increase in signal amplitude with increasing excitation density (Figure 91). A threshold seems to appear around $_{ex} \approx 2 - 2.5\ mJ.cm^{-2}$ (Figure 91a,c,e, Figure 92a). A weak saturation effect might also appear at $_{ex} \approx 7\ mJ.cm^{-2}$, above which signal does not increase anymore (Figure 91a,c,e). These values are close

to what was determined in time-resolved infrared reflectivity study (around 2 and 4 mJ.cm$^{-2}$, respectively). Both of these features are emphasized in Figure 92a, which shows the evolution differential signal value at 100 ps, when maximum signal is reached. This behavior seems rather similar for all three samples, as it was the case in the infrared reflectivity experiment.
Moreover, as was seen by transient infrared reflectivity, differential signal normalized at 100 ps value (Figure 91b,d,f) does not show any striking dependence versus excitation density in its dynamics. Small discrepancies, which are distinguished at long time scale, lie in the experimental uncertainty.

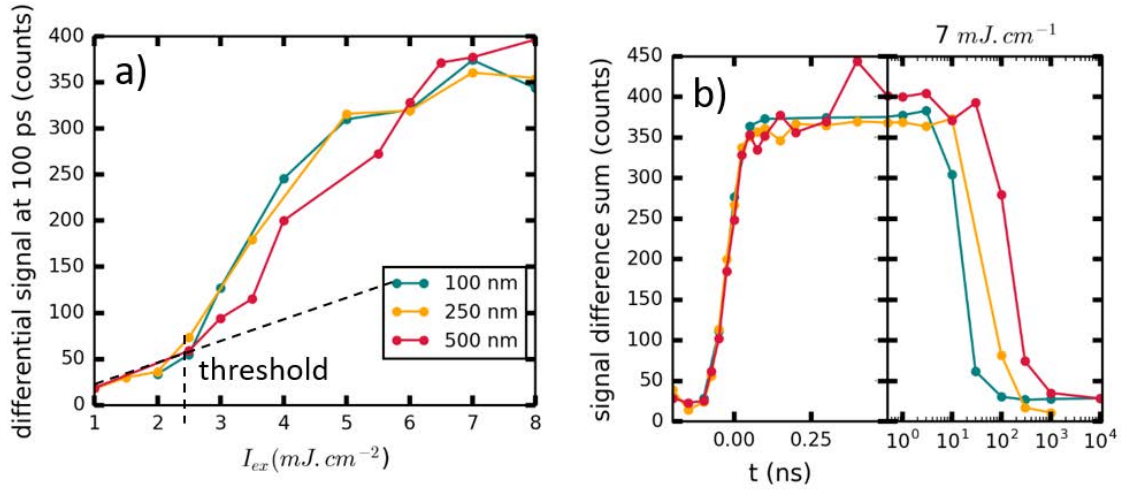


*Figure 92: a) Differential signal sum at 100 ps, when signal reaches a plateau, plotted versus excitation density for different thicknesses. A nonlinear threshold seems to appear around 2.5 mJ.cm$^{-2}$, whereas saturation effect is visible around 6 mJ.cm$^{-2}$. b) Comparison of the dynamics of differential signal sum for three different thicknesses, under 7 mJ.cm$^{-2}$ excitation density. Experimental temporal resolution is not sufficient to distinguish a dependence in thickness at short time scale. However, signal relaxation occurs around 10-100 ns and clearly depends on the film thickness.*

The comparison of the dynamics of the differential signal sum for different thicknesses (Figure 92b) does not show any variation in the onset of the signal at short time scale, depending on the sample thickness. However, the ≈ 70 ps temporal resolution of the experimental set-up does not allow to distinguish between the different thicknesses at such short delays, and unfortunately we cannot conclude on this part. At long time scale, relaxation proceeds with a dependence in the sample thickness, ranging from tens of ns for 100 nm to hundreds of ns for 500 nm. This increase of relaxation time with increasing thickness is expected, as the release of laser energy through thermal exchange with the environment becomes longer as the sample thickness increases.

### IV.4.d. Comparison with measurements at 110 and 130 K

We performed the same study for different initial conditions, with slightly higher temperature. Thus, 100 nm and 500 nm samples were photo-excited at 110 K and 250 nm measurement was performed at 130 K.

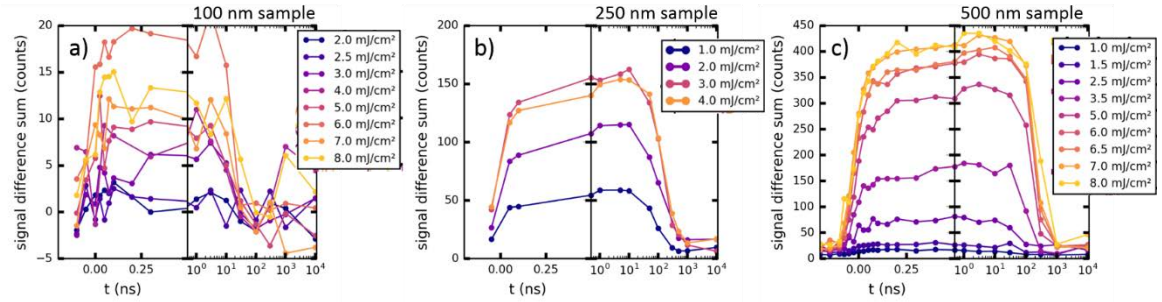


*Figure 93: Integral of the absolute differential signal, from 100 nm sample at 110 K (a), 250 nm sample at 130 K (b), 500 nm sample at 110 K (c). Signal shows similar shape and amplitude as in the 95 K case.*

The sum of differential signal resulting from transient x-ray diffraction at these temperatures and measured for several excitation densities (Figure 93) shows similar behavior as in the 95 K case, both in shape and in amplitude. Therefore, no thermal effect can be distinguished for this temperature range.

What can be noticed, which was less marked yet present at 95 K, is the slow rise in amplitude of the signal on the plateau, occurring before relaxation of the signal takes place. This feature will be further investigated by individual peak fitting.

## IV.4.e. Peak fitting

In the case of photo-excited $V_2O_3$ thin films, the differential signal sum originates from two contributions, as we saw in part 4.c. of this chapter: narrowing of the peaks and peak shift both induce a change in the transient diffraction pattern. To disentangle the effects of these two contributions, we performed peak fitting: each peak was fitted by a Gaussian profile $= \frac{2\sqrt{ln(2)}}{\pi\sigma}\ xp\ (-4ln(2)\ (\frac{-}{}_0)^2)$, using the TOPAS software, allowing to extract both peak position $_0$ and width versus time.

### *IV.4.e.i. Peak width*

The $(\bar{2}16)_H$ peak is strongly affected by symmetry change (Figure 85), with three peaks in the low-temperature phase merging into one in the high-temperature phase, thus leading to significant peak narrowing under photo-excitation. On the other hand, the peak shift effect is quite low on this peak. We thus select this peak to monitor peak narrowing, as a signature of symmetry change.

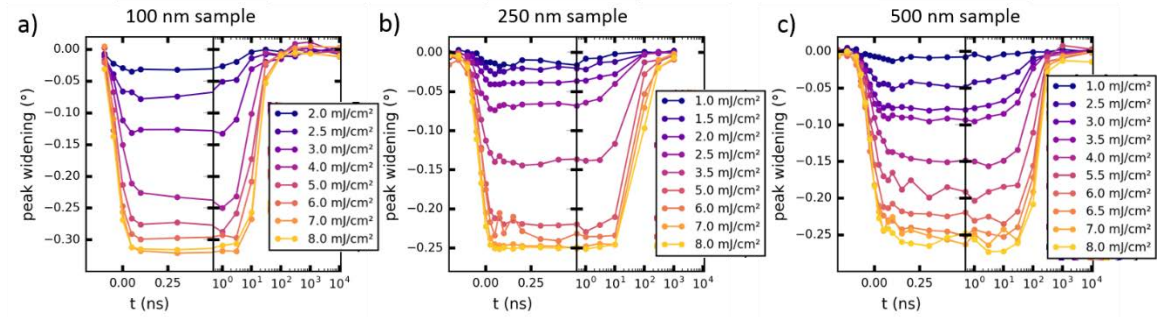


*Figure 94: Transient peak widening, as extracted from Gaussian fit of the $(\bar{2}16)_H$ peak, for 100 nm (a), 250 nm (b) and 500 nm (c) samples. Negative widening actually corresponds to narrowing of the peak, witnessing symmetry change from low-temperature to high-temperature phase.*

The observed change in peak width (Figure 94) is negative, corresponding to the narrowing of the peak. The dynamics of the amplitude of the signal is similar to what was observed for differential signal sum (Figure 91): a fast rise within 100 ps, followed by a plateau ranging up to 10-100 ns, depending on the sample thickness, then a decrease of signal amplitude. However, the slow increase of amplitude across the plateau, observed for the differential signal sum is less prominent in peak narrowing, especially for 100 nm and 250 nm samples (Figure 94a,b). This would suggest that symmetry stays the same on the 100 ps – 10 ns range. Considering the 500 nm sample (Figure 94c), which seems to show a slight peak across the 100 ps – 10 ns plateau, the mean symmetry might continue to evolve in this sample due to larger thickness.

### *IV.4.e.ii. Peak shift*

We saw in section 4.b. of this chapter that $(\bar{2}10)_H$ peak is little affected by symmetry change, with almost no change in width. However, since its components are along $a_H$ and $b_H$ axes, which decrease at the phase transition, the $(\bar{2}10)_H$ peak shows strong positive peak shift. Therefore, we chose this peak to monitor the peak shift (Figure 95), associated with unit cell volume change.

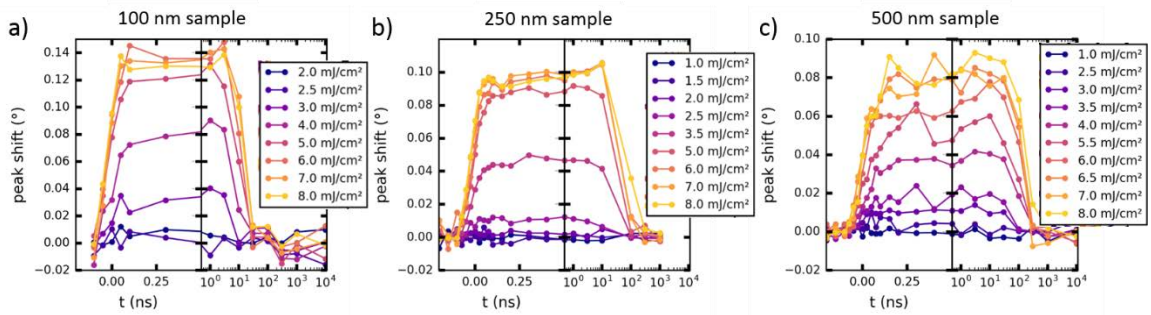


*Figure 95: Transient peak shift, as extracted from Gaussian fit of the $(\bar{2}10)_H$ peak, for 100 nm (a), 250 nm (b) and 500 nm (c) samples. Positive peak shift corresponds to decrease of unit cell parameters.*

As was the case for peak width, peak shift dynamics is similar to signal differential sum behavior (Figure 91). Yet, a slow increase of the signal across the plateau is visible, for all three samples (Figure 95). This witnesses a further decrease of unit cell volume on the 100 ps - 10 ns range.

Hence, for 100 nm and 250 nm samples, slow transient signal increase on the 100 ps – 10 ns plateau seems to be mainly due to a decrease of unit cell volume, rather than in further symmetry change. Actually, the comparison of signal difference between off and 100 ps, corresponding to phase transition, and between 100 ps and 10 ns, corresponding to the evolution on the plateau, shows strong differences in terms of shape (Figure 96): differential signal over the plateau shows rather bipolar signal on all peaks, corresponding to a global peak shift towards large q values, witnessing volume decrease, whereas the reduction of tripolar signal associated with symmetry breaking suggests no symmetry change over the plateau, as was extracted from peak fitting.

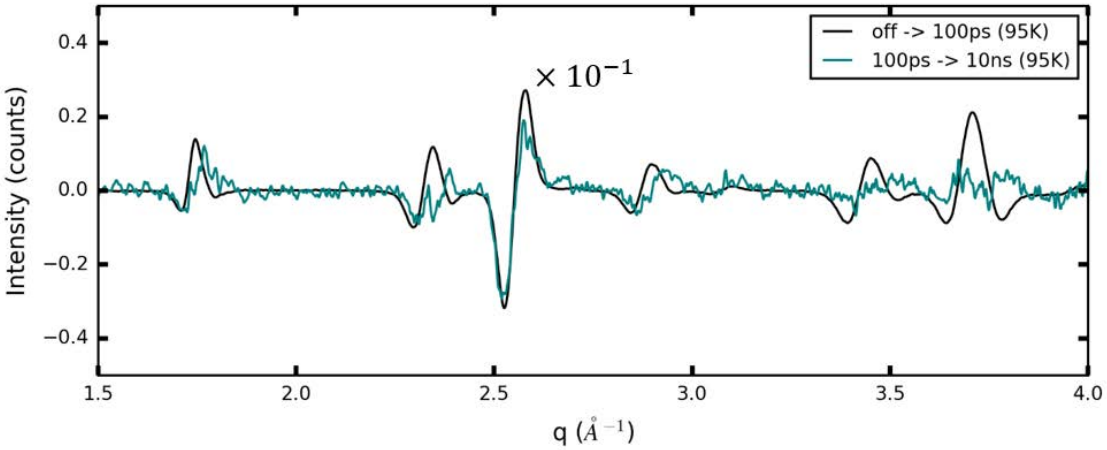


*Figure 96: Difference between photo-excited pattern at 100 ps and off pattern (black), measured at 95 K under 7 mJ.cm$^{-2}$ excitation density on 250 nm sample, compared with difference between photo-excited pattern at 10 ns and 100 ps (green). Black signal is divided by 10 for clarity. Signals show significantly different shapes, especially for peaks witnessing symmetry change between off and 100 ps, which do not show the same feature over the plateau.*

On the other hand, data from the literature (Figure 97), supported by our single crystal x-ray diffraction measurement (Figure 70b), show that $V_2O_3$ presents thermal expansion in the high-temperature phase, which means that "cold" high-temperature phase volume is smaller than "hot" one. Therefore, these observations on photo-excited 100 nm and 250 nm films could be explained by a three-steps scenario (Figure 97):

1. first, transformation proceeds from low-temperature phase to an excited "high-volume high-temperature" phase within 100 ps (signal rise),
2. then this "high-volume high-temperature" phase relaxes towards "low-volume high-temperature" phase within around 10 ns (plateau),
3. finally the system relaxes back to low-temperature phase after 10-100 ns (signal decrease).

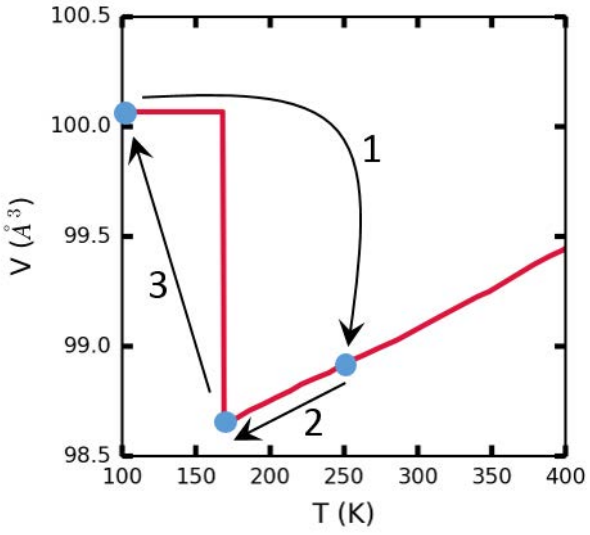


*Figure 97: Suggestion for a multistep excitation. 1: transformation from low-temperature phase to an excited "high-volume high-temperature phase within 100 ps, 2: high-volume high-temperature phase relaxes towards low-volume high-temperature phase within around 10 ns, 3: system relaxes back to low-temperature phase after 10-100 ns. Data from [McWhan1970]*

### IV.4.f. Measurement in the high-temperature phase (160 K): heating signature

To investigate further this hypothesis of cooling effect across the 100 ps – 10 ns plateau, we studied the photo-excitation of 250 nm sample at 160 K, in the high-temperature phase. In this configuration, the premise is that laser excitation effect will result in heating of the high-temperature phase, therefore in the increase of its unit cell volume.

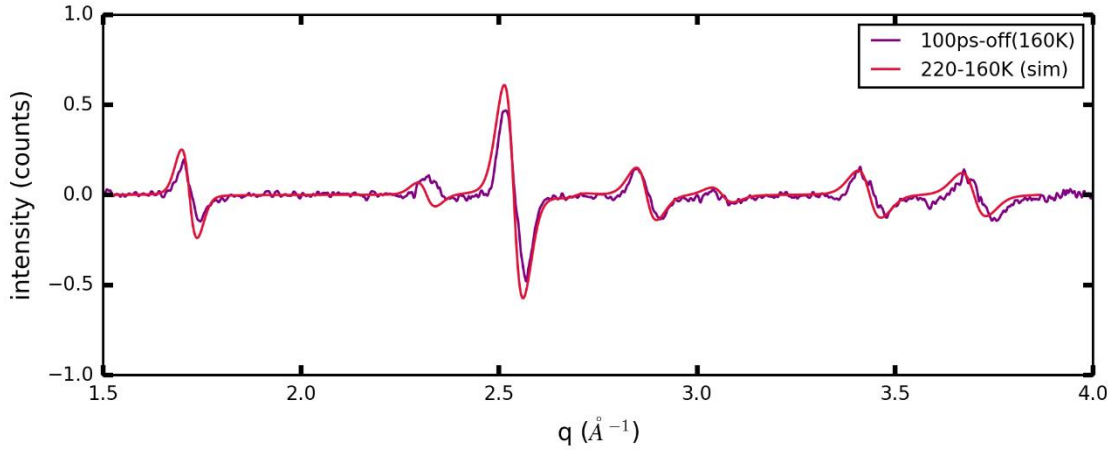


*Figure 98: Difference between photo-excited pattern at 100 ps and off pattern (purple), measured at 160 K under 4 mJ.cm$^{-2}$ excitation density measured on 250 nm sample, compared with difference between simulated patterns of high-temperature phase at 220 K and 160 K (red), using thermal expansion coefficients from the literature [McWhan1970]. Both signals are really similar.*

Photo-excited signal at 100 ps, measured at 160 K, where the sample is in the high-temperature phase, is compared with the difference of static 220 K and 160 K patterns (Figure 98). 220 K pattern is obtained from TOPAS simulation, using thermal expansion coefficients from the literature [McWhan1970]. Both signals are really similar, confirming that photo-excitation of high-temperature phase amounts to heat the sample by several tens of degrees, thus increasing its unit cell volume (Figure 97).

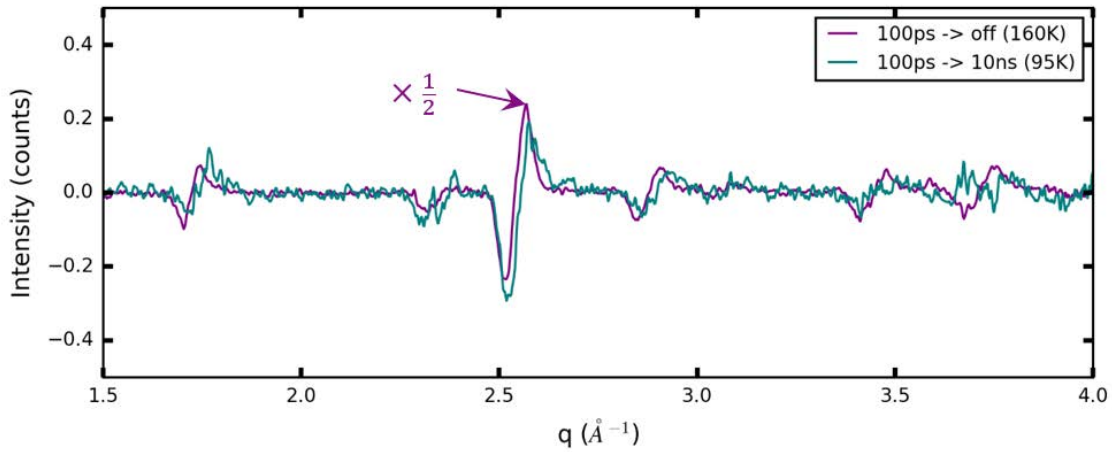


*Figure 99: Difference between photo-excited patterns at 10 ns and 100 ps (green), measured at 95 K under 7 mJ.cm$^{-2}$ excitation density on 250 nm sample, compared with difference between off pattern and photo-excited pattern at 100 ps (purple), measured at 160 K under 4 mJ.cm$^{-2}$ excitation density, and corresponding to cooling down of high-temperature phase. Both signals share similar features. Purple signal was divided by 2 for clarity.*

Therefore, taking the opposite of photo-excited signal at 100 ps, measured at 160 K, we get the signature of a cooling down of the high-temperature phase (Figure 99, purple line). Considering

the measurement at 95 K, the evolution of differential signal across the plateau is obtained by subtracting the 100 ps pattern (beginning of the plateau) to the 10 ns pattern (end of the plateau) (Figure 99, green line). Comparing both (Figure 99) shows that these signals share similar features. This corroborates the hypothesis of volume decrease due to effective cooling down of photo-excited high-temperature phase across the 100 ps – 10 ns plateau. This theory deserves deeper investigation and should be completed by time-resolved x-ray diffraction measurements with better q resolution. Such a study, which could be achieved using smaller x-ray beam as it can be found in XFELs for instance, would allow for Pawley or Rietveld refinement and thus for the precise determination of unit cell parameters dynamics.

## IV.5. Short time scale: light-induced elastic wave model as a tool to rationalize the phase propagation in $V_2O_3$ photo-induced transition

Pump-probe infrared reflectivity measurements, presented in part 3.b of this chapter, showed that the onset of transient signal from photo-excited $V_2O_3$ thin films builds up within 20 – 200 ps for samples of 100 nm – 1 µm thickness. We used a multilayer model to test the hypothesis of a metallic phase propagating at acoustic speed, from the film surface throughout the sample (part 3.c).
Despite lower time resolution than infrared experiment, pump-probe x-ray diffraction demonstrates fast structural change, occurring within 100 ps. Therefore, both electronic and structural transformations seem to appear simultaneously. Similar to what was performed with multilayer reflectivity model and infrared measurement, we used a light-induced elastic wave propagation model to investigate the hypothesis of the propagation of a lower volume-high-temperature phase, and its impact on volume deformation, i.e. strain.

### IV.5.a. Light-induced elastic wave propagation model

In their 1986 paper, Thomsen et al. suggest a model to describe the dynamics of the strain generated by an ultrashort light pulse impinging on a film sample of thickness , with penetration depth [Thomsen1986].
As was introduced in chapter I, part 3.c of this manuscript, Thomsen et al. restrict their model in the case of semi-infinite films, with ≫ . To describe ps lattice dynamics of photo-excited thin films studied by ultrafast x-ray diffraction, Schick et al. developed a unifying model, adapted to both cases where the photo-induced stress profile decays on a length longer or shorter than the film thickness [Schick2014].
In chapter I.3.c, we presented the different origins of photo-induced stress. Yet, structural phase transition represents another driving force, where the establishment of mechanical equilibrium generates a deformation. To describe the propagation of a photo-induced low-volume phase, we used equations developed by Thomsen et al. and Schick et al., however considering a stress predominantly of electronic origin rather than thermo-elastic origin. In either case, the excitation density and therefore the initial stress will follow the exponential laser penetration depth profile ∝ $^{-\delta x}$, with = / the normalized spatial coordinate and = / the shape factor.

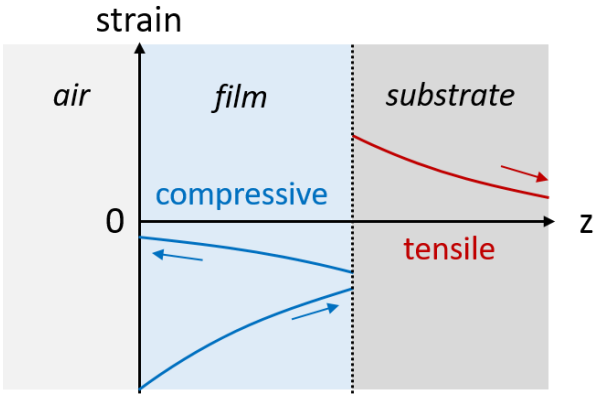


*Figure 100: Scheme of propagating strain waves as described by the elastic model. Here, compressive strain waves (in blue) counter-propagate in the film from both interfaces with air and substrate. A tensile strain wave (in red) propagates within the substrate.*

In the case of our experiment, the 0.8 eV-pump laser penetration depth in $V_2O_3$ in low-temperature phase is around 500 nm, which is ≥ . The film can thus not be considered as a semi-infinite medium, and the situation requires using the model improved by Schick et al. The film and its substrate are considered to fulfill acoustic impedance matching. This is the case of $V_2O_3$ on $Al_2O_3$, with both materials showing an acoustic impedance of about 40 $kg.s^{-1}.m^{-2}$.

Since our goal is to describe the effect of the propagation of a phase of lower volume than the unperturbed sample, we used the elastic wave propagation model described in chapter I.3.c, to simulate a compressive strain propagating from the surface throughout the film. For = / ≪ 1, photo-excited stress is spatially homogeneous in the film. In our case, = [0.2, 0.5, 1] and the strain profile decays slightly across the film thickness (Figure 101a). The lattice dynamics starts at the surface and interface of the film, which are the regions of highly imbalanced stress. At the interface with the substrate, a compressive strain front travels into the film (Figure 100), compensated by a tensile strain front propagating into the substrate (Figure 100). At the film surface, tensile strain front can of course not propagate in air and is therefore reflected in the film as a contraction (Figure 100).

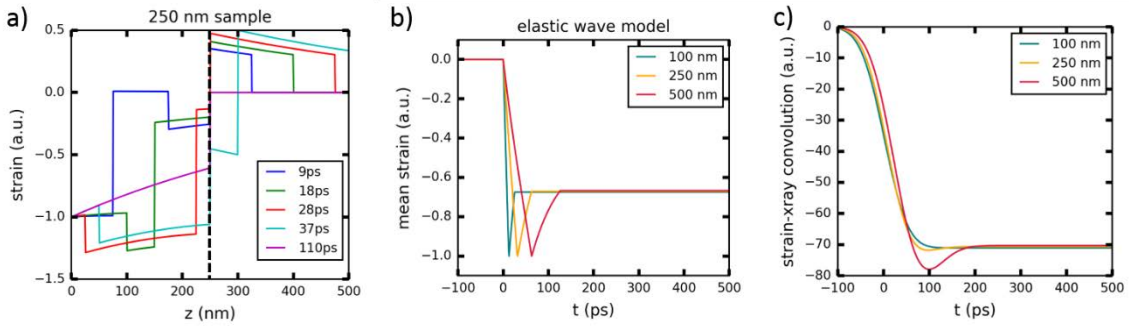


*Figure 101: a) Strain profile simulated for 250 nm film with elastic wave model, for several delays. The dashed black line delimits the film-substrate interface. Strain effect in the film is opposite to its effect in the substrate. b) Strain simulated with elastic wave model, plotted versus time for different film thicknesses. Dynamics get faster as the film thickness decreases. c) Signal from (b) convoluted with a Gaussian x-ray pulse of 100 ps duration (FWHM). The time scale of signal onset becomes similar for all three thicknesses.*

We performed elastic wave model simulations, considering the three different film thicknesses 100, 250 and 500 nm. Mean strain is calculated by integrating the strain over the film thickness. As expected, the evolution of mean strain versus time shows faster dynamics as the film thickness decreases (Figure 101b). However, when convoluted with a 100 ps-duration x-ray pulse, as it was the case in our pump-probe experiment, the time scale of signal onset becomes similar for all

three thicknesses (Figure 101c). This corroborates what we observed at short time scale for time-resolved x-ray diffraction (Figure 92).

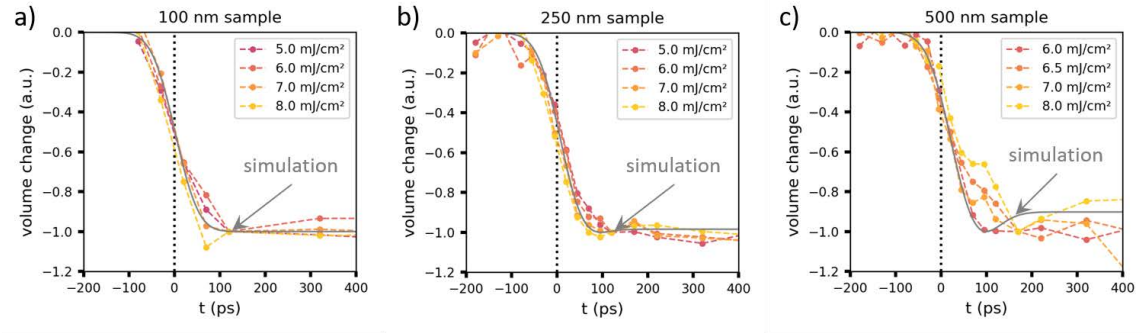


*Figure 102: Comparison between mean strain, calculated from elastic wave model and convoluted with 100 ps x-ray pulse (gray lines), and volume change (qualitatively estimated from peak shift) observed by transient x-ray diffraction, for 100 nm (a), 250 nm (b) and 500 nm (c) samples. Volume change was normalized at 100 ps value for 100 nm and 250 nm samples and at 150 ps value for 500 nm sample. Experimental time was shifted by +20 ps to better fit the simulation. Both simulation and experiment show similar dynamics.*

Experimental volume change dynamics is estimated from the peak shift, with opposite sign (positive peak shift in reciprocal space is associated with volume contraction in real space). The obtained volume change is normalized at 100 ps value for 100 nm and 250 nm samples (Figure 102a,b) and at 150 ps value for 500 nm sample (Figure 102c), when the onset of the signal is completed. Following the same approach as in [Mariette2020], we compare mean strain, calculated from elastic wave model and convoluted with 100 ps x-ray pulse (gray lines on Figure 102), and volume change observed by transient x-ray diffraction. Simulated signal was shifted by -20 ps to fit experimental data better. This shift stands within the calibration error of the experimental set-up.

However being approximations, simulations show qualitative agreement with experimental data, considering the lack of temporal resolution of our experiment. Therefore, we do not exclude the possibility to describe structural dynamics at short time scale (< 500 ps) with acoustic propagation of a strain wave.

### IV.5.b. Conclusion about the strain wave propagation hypothesis

Our approach gathers an infrared reflectivity study, coupled with simulations from a multilayer model considering the propagation of a photo-excited metallic phase at the speed of sound, and a structural study, associated with an elastic wave model, simulating the propagation of a lower-volume phase. The hypothesis of the one-dimensional acoustic propagation of a photo-excited phase, showing the characteristics of the high-temperature phase in terms of both electronic and structural properties, as an elastic wave launched from the sample surface and propagating within the film, seems corroborated by both of these studies. First and foremost, the linear behavior of reflectivity in terms of amplitude and time, covering the range of optical wavelengths mostly prone to insulator-to-metal transition (Drude-type response), strongly suggests a propagation with speed of sound of metal-like transformation, at least partly. Secondly, the appearance of threshold excitation, when reflectivity change becomes nonlinear with excitation density, is a strong indication of the role of cooperative interactions during the transformation, leading to higher and higher metallic fraction. The time-resolved structural study established that photo-induced phase generated after 100 ps shows a diffraction pattern corresponding to contracted unit cell volume and monoclinic-to-rhombohedral symmetry change (Figure 90 in part 4.c), as expected by a transformation to metallic state.

This picture questions the so far prevailing description of macroscopic transition, as being predominantly caused by nucleation and slow thermal kinetics. As such, also the origin of the transition can be sought elsewhere than in simple thermal effects as previously considered.

A recent study, of which experimental and analysis methods were described in chapter II, part 2.b and 4.c.iv, evidenced precursor structural changes in $Ti_3O_5$, another type of correlated metal oxide [Mariette2020]. As was observed by Singer et al. in $V_2O_3$ thin films, this study evidenced ultrafast shear at the picosecond time scale, propagating through small monoclinic domains in the λ phase of $Ti_3O_5$. Precursor structural deformations occurred before long-range cell deformations were observed, whereas unit cell volume and photo-induced high-temperature phase fraction seemed to change simultaneously, in the same way as presented in [Singer2018].
In the frame of our French-Japanese collaboration, time-resolved infrared reflectivity measurement in $V_2O_3$ thin films, performed with 10 fs resolution, actually witnessed early structural deformations, evidenced by the detection of coherent phonons [Amano2019]. Vibration modes associated with these phonons could act as precursor effects of the LT-to-HT phase transition in $V_2O_3$, as they imply similar atomic motions (oxygen octahedral deformation and shortening of the V-V dimer length, Figure 103).

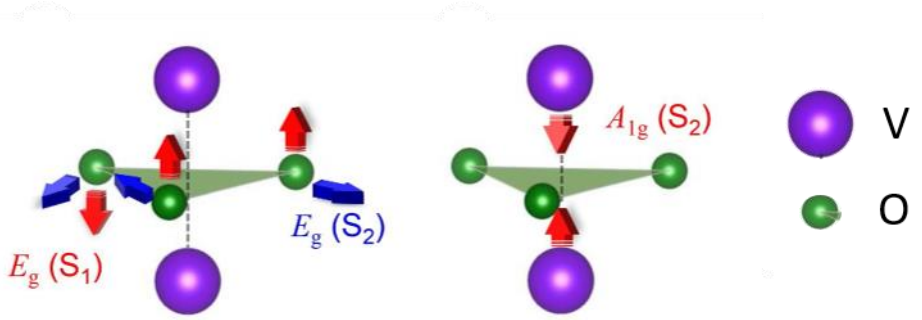


*Figure 103: from [Amano2019]. Phonon modes observed at ps time scale by time-resolved infrared reflectivity in $V_2O_3$ thin films. Purple and green spheres represent vanadium and oxygen atoms, respectively, while arrows indicate the atomic motions associated with phonons.*

The ultimate confirmation, that structural deformations actually drive and stabilize the photo-induced high-temperature phase in $V_2O_3$, would come from ultrafast x-ray diffraction with picosecond temporal resolution, allowing to fully describe structural dynamics at ultrashort time scale.

# Conclusion

The goal of the work presented before in this manuscript was to explore through ultrafast x-ray diffraction some aspects of the coupled strain-transformation dynamics, in the frame of phase transitions induced by a laser pulse in volume-changing materials. This may shine new light on two unifying concepts in condensed matter:

- the emergence of new and often unexpected collective behavior, resulting from the interactions between a large number of constituting elements of diverse nature (electrons, spins, atoms, …);
- the question of the universality in the physical behavior around phase transitions far away from equilibrium, while it is observed to be the "same" at thermal equilibrium for situations of different nature (electronic, magnetic, structural, …).

For the last 20 years, large progresses were made in the field of photo-induced phase transformations. However, the key role of volume effects and long-range elastic interactions during the photo-induced dynamics of these ultrafast phase transitions, and in the stabilization at macroscopic scale of the new formed phase, was largely neglected up to now.

It has been important to underline how physics becomes different when switching from the well-known situation of phase transitions at thermal equilibrium to ultrafast phase transitions induced by a laser pulse, where a global view remains lacking and the key role of volume in the process is still to be highlighted (Chapter I). In the same way, it was essential to establish a method of analysis to exploit data provided by time-resolved powder x-ray diffraction, the most adapted experimental tool to investigate the strain wave pathway for a photo-induced phase transition (Chapter II).

The first results reported in this manuscript concern the photo-induced phase transformation in spin-crossover molecular materials, which complement by structural studies the previous results obtained by optical spectroscopy on elastic effects (Chapter III). These transformations represent a prototype of isostructural phase transition in the solid state. The switching of molecules from low to high spin state induces a swelling of the molecular "volume", which yields a local deformation of the lattice at microscopic scale. This deformation is at the origin of long-range elastic interactions (positive feedback) and represents an uncommon mechanism for the generation of strain waves. The essential point of our investigation lies in the fact that switching dynamics is slow in contrast with small atomic displacements generally observed in many compound. Hence, our study reveals a decoupling in time between volume change on the acoustic time scale with size reduction and slower molecular spin state dynamics. Actually, we demonstrated that the time scale of this cooperative process remains intrinsically limited by Arrhenius dynamics, governed by the local energy barrier to cross between low and high spin molecular states.

Secondly, the investigation of metal oxides, such as $Ti_3O_5$ and $V_2O_3$, has allowed to generalize our strain wave approach to a completely different kind of materials and thus to explore the universality of ultrafast cooperative elastic coherent pathway, in contrast with the common nucleation-growth picture inspired from thermal kinetics. In this type of materials, the dynamics is faster than in spin-crossover molecular crystals, being not limited by any energy barrier between considered states.

In $Ti_3O_5$ pellets, we evidenced this strain wave pathway by using the SwissFEL source [Mariette2020, Annex]. My main contribution related to structural dynamics of $V_2O_3$ thin films (Chapter IV). In the latter study, the situation was similar to the $Ti_3O_5$ one. However, measurements were performed at low temperature, out of the coexistence region, which simplified the situation. This project, focused on a textbook example of insulator-to-metal transition, was performed in the frame of an international collaboration with Tohoku University (Japan). Time-resolved optical measurements, performed at Sendai, showed that it is possible to photo-induce a complete phase transition, even at very low temperature and for a photon excitation energy close to the optical gap. This pumping configuration limits heating of the lattice, by reducing excess energy to the minimum and therefore excludes the possibility of thermal conversion. Moreover, no dependence in laser excitation density of the propagation rate of the photo-induced phase transition was observed, suggesting an ultrafast coherent process. Reflectivity simulations, performed to rationalize these optical results, tend to corroborate the hypothesis of a photo-induced metallic phase propagating at the speed of sound from the surface in the sample. X-ray diffraction measurements, fitted with thermo-elastic wave model, are in agreement with the acoustic propagation of structural deformation and low-volume rhombohedral phase propagating at speed of sound in the film. However, this study still lacks better temporal resolution, of the order of 1 ps, to carefully check this hypothesis of co-propagating elastic (volume change) and phase (electronic state) fronts. Such a measurement might be performed at large scale facilities providing ultra-short x-ray pulses, for instance free electron lasers.

Another perspective for this study would be to perform time-resolved x-ray diffraction with in-depth resolution, by changing the x-ray incidence angle to probe the sample at different depths [Johnson2008], building a two-dimensional (depth, time) picture of the phase transition propagation. This could not be envisioned on $Ti_3O_5$ pellets, since the rugosity at the sample surface was too high to allow for exploitable x-ray diffraction results. Such an experiment performed in $V_2O_3$ thin films or single crystal would allow checking the validity of the hypothesis of in-depth acoustic propagation of low-volume rhombohedral phase. Moreover, the use of ultrafast x-ray source would give the possibility to investigate precursor dynamics, such as coherent optical phonons.

Bistable volume-changing materials are diverse and we are still rather far from a universal picture describing photo-induced transitions in this class of materials. However, with this manuscript, we dare to believe that we brought a new brick in the wall in the building of the comprehension of elastic processes, playing their part in photo-induced phase transitions in volume-changing materials. This work paves the way to further studies, to continue refining our comprehension of these mechanisms.

“To play our role well, we must know the entire piece and in the same time, the conception of the ensemble should never be lost in individuality.” [Kakuzo O., *The Book of Tea*, 1906].

# References


[Abrahams1971] Abrahams, Materials Research Bulletin 6, 881 (1971)
[Abreu2015] Abreu et al., Physical Review B 92, 085130 (2015)
[Abreu2017] Abreu et al., Physical Review B 96, 094309 (2017)
[Agarwal1981] Agarwal et al., Physical Review A 23, 5 (1981)
[Aizu1969] Aizu, Journal of Physical Society of Japan 27, 387 (1969)
[Amano2019] Amano T., Master Thesis, Tohoku University (2019)
[Aoki2014] Aoki et al., Review of modern Physics 86, 779 (2014)
[Asahara2014] Asahara et al., Physical Review B 90, 014303 (2014)
[Ashiotis2015] Ashiotis et al., Journal of Applied Crystallography 48, 510 (2015)
[Azzolina2019] Azzolina et al., European Journal of Inorganic Chemistry 3142 (2019)
[Babich2020] Babich D., PhD, *to be defended in December 2020*
[Baldassarre2008] Baldassarre et al., Physical Review B 77, 113107 (2008)
[Baruchel1993] Baruchel et al., "Neutron and Synchrotron Radiation for Condensed Matter Studies", Vol. 1, EDP Sciences – Springer-Verlag (1993)
[Belbeoch1978] Belbeoch et al., Solid State Communications 25, 1043 (1978)
[Bertoni2013] Bertoni R., *Ultrafast photo-switching of spin-crossover crystals: coherence and cooperativity,* PhD (2013)
[Bertoni2015a] Bertoni et al., Accounts of Chemical Research 48, 774 (2015)
[Bertoni2015b] Bertoni et al., Coordination Chemistry Review, 282-283, 66 (2015)
[Bertoni2016] Bertoni et al., Nature Materials 15, 6, 606 (2016)
[Birks1946] Birks et al., Journal of Applied Physics 17, 687 (1946)
[Borroni2020] Borroni et al., Physical Review B 101, 054303 (2020)
[Bostedt2016] Bostedt et al., Review of Modern Physics 88 (2016)
[Boukheddaden2000] Boukheddaden et al., The European Physical Journal B – Condensed Matter and Complex Systems 15, 317 (2000)
[Bousseksou2004] Bousseksou et al., *Spin Crossover in Transition Metal Compounds III*, vol. 235 in Topics in Current Chemistry, Springer Verlag (2004)
[Bousseksou2011] Bousseksou et al., Chemical Society Review 40, 3313 (2011)
[Byrnes2019] Byrnes, arXiv:1603.02720v4 (2019)
[Cailleau2010] Cailleau et al., Acta Crystallography A 66, 189 (2010)
[Cambi1934] Cambi et al., Berichte der Deutschen Chemischen Gesellschaft 64, 2591 (1934)
[Cammarata2009] Cammarata et al., Review of Scientific Instruments 80, 0125101 (2009)
[Chastanet2018] Chastanet et al., Compte-Rendu Chimie 21, 1075 (2018)
[Chernyshov2004] Chernyshov et al., Physical Review B 70, 094116 (2004)
[Coelho2018] Coelho, Journal of Applied Crystallography 51, 210 (2018)
[Collet2012] Collet et al., Physical Review Letters 109, 257206 (2012)
[Crisp2011] Crisp et al., European Journal of Pharmaceutical Sciences 42, 5 (2011)
[Deacon1977] Deacon et al., Physical Review Letters 39, 892 (1977)
[deBoer1937] deBoer et al., Proceedings of the Physical Society 49 (1937)
[Decurtins1984] Decurtins et al., Chemical Physics Letters 105, 1 (1984)
[Desaix1998] Desaix et al., European Physics Journal B 6, 2, 183 (1998)
[DiMatteo2002] Di Matteo et al., Physical Review B 65, 054413 (2002)
[Diu1989] Diu et al., *Elements de physique statistique*, Hermann (1989)

[Diu2007] Diu et al., *Thermodynamique*, Hermann (2007)
[Dlott1990] Dlott, Journal of Luminescence 45, 1 (1990)
[Dong2017] Dong X., *Ultrafast infrared spectroscopy applied to spin-crossover materials*, PhD (2017)
[Eckstein2020] Eckstein M., *Non-equilibrium Dynamical Mean-Field Theory*, Springer (2020)
[Elder1947] Elder et al., Physical Review 71, 829 (1947)
[Enachescu2017] Enachescu et al., Physical Review B 95, 224107 (2017)
[Enachescu2018] Enachescu et al., CRC 21, 12 (2018)
[Feidenhans1989] Feidenhans, Surface Science Reports 10, 3 (1989)
[Feynman1972] Feynman, *Statistical Mechanics: A Set of Lectures, CRC Press* (1972)
[Fleming2008] Fleming et al., Physics Today 61, 7, 28 (2008)
[Foex1946] Foëx, Comptes Rendus 223, 1126 (1946)
[Fraser1986] Fraser et al., Nuclear Instruments Methods Physical Ressources, Sect A 250, 71 (1986)
[Galle2013] Galle et al., Applied Physics Letters 102, 063302 (2013)
[Galloway2009] Galloway et al., Applied Spectroscopy 63, 12 (2009)
[Garcia2004] Garcia et al., *Thermal Spin Crossover in Mn(II), Mn(III), Cr(II) and Co(III) Coordination Compounds, in: Spin Crossover in Transition Metal Compounds II*, vol. 234, in Topics in Current Chemistry, Springer Verlag (2004)
[Gati2016] Gati et al., Science Advances 2, 12 (2016)
[Georges1992] Georges et al., Physical Review B 45, 6479 (1992)
[Georges1996] Georges et al., Reviews of Modern Physics 68, 13 (1996)
[Giorgianni2019] Giorgianni et al., Nature Communications 10, 1159 (2019)
[Grieger2015] Grieger et al. Physical Review B 92, 075121 (2015)
[Guionneau2004] Guionneau et al., Topics in Current Chemistry, vol.234, Springer-Verlag (2004)
[Gütlich2004] Gütlich et al., *Spin Crossover in Transition Metal Compounds I, II and III*, vol. 233, 234, 235 in Topics in Current Chemistry, Springer Verlag (2004)
[Gütlich2005] Gütlich et al., Coordination Chemistry Review 249, 23 (2005)
[Guzman2019] Guzman-Verri et al., Nature 576, 429 (2019)
[Haddad1981] Haddad et al., Inorganic Chemistry 20, 123 (1981)
[Hansmann2013] Hansmann P., Physica Status Solidi B 250, 1251 (2013)
[Harris2001] Harris et al., Angewandte Chemie 40, 9 (2001)
[Hase1996] Hase et al., Applied Physics Letters 69, 2474 (1996)
[Hase2003] Hase et al., Applied Physics Letters 83, 24 (2003)
[Hauser1986] Hauser et al., Inorg. Chem. 25, 4245 (1986)
[Hauser1991] Hauser et al., Journal of Chemical Physics 94, 2741 (1991)
[Hauser2004] Hauser, *Light-Induced Spin Crossover and the High-Spin→Low-Spin Relaxation*, Spin Crossover in Transition Metal Compounds II. Topics in Current Chemistry, vol. 234, Springer (2004)
[Hauser2006] Hauser et al., Coordination Chemistry Review 250, 1642 (2006)
[Hayami2001] Hayami et al., Journal of American Chemistry Society 123, 11644 (2001)
[Hazen1988] Hazen et al., Physical Review Letters 60, 1174 (1988)
[Janod2015] Janod et al., Advanced Functional Materials 25, 40 (2015)
[Jiang1999] Jiang et al., Journal of Material Research 14, 2 (1999)
[Johnson2008] Johnson et al., Physical Review Letters 100, 155501 (2008)
[Kagawa2004] Kagawa et al., Physical Review B 69, 064511 (2004)
[Karlak1966] Karlak et al., Analytical Chemistry 38, 12 (1966)
[Kim2012] Kim et al., Talanta 94 (2012)
[Konishi2008] Konishi et al., Physical Review Letters 100, 067206 (2008)

[Landau1937] Landau**,** Zhurnal Eksperimentalnoi Teoreticheskoi Fiziki 7, 19 (1937)
[Lanz2017] Lanz et al., Nature Communications 8, 13917 (2017)
[Lawthers1984] Lawthers et al., Journal of American Chemistry Society 106, 15, 4280 (1984)
[Lemke2017] Lemke et al., Nature Communications 8, 15342 (2017)
[Letard1997] Letard et al., Journal of American Chemistry Society 119, 10861 (1997)
[Levanyuk2020] Levanyuk et al., arXiv:2008.06269v1 (2020)
[Lindenberg2000] Lindenberg et al., Physical Review Letters 84, 1 (2000)
[Liu2011] Liu et al., Physical review Letters 107, 066403 (2011)
[Lorenc2009] Lorenc et al., Physical Review Letters 103, 028301 (2009)
[Luo2014] Luo et al., Physical Review Letters 112, 135701 (2014)
[Lupi2010] Lupi et al., Nature Communications 1, 105 (2010)
[Madey1971] Madey et al., Journal of Applied Physics 42, 1906 (1971)
[Mansart2010] Mansart et al., Europhysics Letters 92, 37007 (2010)
[Mariette2020] Mariette et al., arXiv:2002.08152v2 (2020)
[Matsuda2015] Matsuda et al., Ultrasonics 56, 3 (2015)
[McCusker1993] McCusker et al., Journal of American Society 115, 298 (1993)
[McWhan1970] McWhan et al., Physical Review B 2, 9 (1970)
[McWhan1973] McWhan et al., Physical Review B 7, 5 (1973)
[Mikolasek2014] Mikolasek et al., New Journal of Chemistry 38, 1834 (2014)
[Mott1937] Mott et al., Proceedings of the Physical Society 49, 4S (1937)
[Mott1949] Mott, Proceedings of the Physical Society, series A, 62, 7 (1949)
[Moussa2007a] Moussa et al., Physical Review Letters 94, 10 (2007)
[Moussa2007b] Moussa et al., Physical Review B 75, 5 (2007)
[Mozzanica2018] Mozzanica et al., Synchrotron Radiation News, 31, 16 (2018)
[Nasu2004] Nasu, *Photo-Induced Phase Transitions*, World Scientific Publishing (2004)
[Nishino2011] Nishino et al., Scientific Reports 1, 162 (2011)
[Ohkoshi2010] Ohkoshi et al., Nature Chemistry 2, 539 (2010)
[Okamoto2004] Okamoto et al., Physical Review B 70, 165202 (2004)
[Onoda1998] Onoda et al., Journal of Solid State Chemistry 136, 67 (1998)
[Panjikar2005] Panjikar et al., Acta Crystallographica D 61, 449 (2005)
[Parpiiev2017] Parpiiev et al., Applied Physics Letter 111, 151901 (2017)
[Pawley1981] Pawley, Journal of Applied Crystallography 14, 357 (1981)
[Prevey1986] Prevey, *Metals Handbook*, American Society for Metals, 380 (1986)
[Qazilbash2008] Qazilbash et al., Physical Review B 77, 115121 (2008)
[Reid2018] Reid et al., Nature Communications 9, 388 (2018)
[Renault2003] Renault et al., Applied Physics Letters 83, 473 (2003)
[Rene2017] Rene et al., Structural Dynamics 4, 4 (2017)
[Ridier2017] Ridier et al., Physical Review B 96, 134106 (2017)
[Rietveld1969] Rietveld, Journal of Applied Crystallography 2, 65 (1969)
[Ronchi2019] Ronchi et al., Physical Review B 100, 075111 (2019)
[Rowles2017] Rowles et al., Journal of Applied Crystallography 50, 240 (2017)
[Rozenberg2019] Rozenberg, E. Pavarini, E. Koch, and S. Zhang (eds.) Many-Body Methods for Real Materials,Modeling and Simulation Vol. 9, Forschungszentrum Jülich, 2019
[Ruello2009] Ruello et al., Physical Review B 79, 094303 (2009)
[Ruello2015] Rueello et al., Ultrasonics 56, 21 (2015)
[Schick2014] Schick et al., Structural Dynamics 1, 064501 (2014)
[Shepherd2013] Shepherd et al., Nature Communications 4, 2607 (2013)
[Singer2018] Singer et al., Physical Review Letters 120, 207601 (2018

[Spiering1982] Spiering et al., Chemical Physics 68, 65 (1982)
[Spiering2004] Spiering et al., Physical Review B 70, 184106 (2004)
[Sollogoub2008] Sollogoub et al., European Journal of Chemical Biology 9, 1201 (2008)
[Stanley1971] Stanley H., *Introduction to phase transitions and critical phenomena*, Oxford University Press (1971)
[Stewart2012] Stewart et al., Physical Review B 85, 205113 (2012)
[Strogatz2014] Strogatz S., *Nonlinear Dynamics and Chaos: With Applications to Physics, Biology, Chemistry and Engineering*, Westview Press (2014)
[Strukov1998] Strukov et al., *Ferroelectric Phenomena in Crystals*, Physical Foundations, Springer (1998)
[Tanasa2014] Tanasa et al., Applied Physics Letters 104, 031909 (2014)
[Thomas1994] Thomas et al., Physical Review Letters 73, 11 (1994)
[Thomsen1986] Thomsen et al. Physical Review B 34, 6 (1986)
[Tissot2011] Tissot et al., Journal of Materials Chemistry 21, 18347 (2011)
[Tissot2012] Tissot et al., Journal of Materials Chemistry 22, 3411 (2012)
[Tokoro2015] Tokoro et al., Nature Communications 6, 7037 (2015)
[vanKoningsbruggen2004] van Koningsbruggen et al., *Spin Crossover in Transition Metal Compounds I*, vol. 233, in Topics in Current Chemistry, Springer Verlag (2004)
[VonReppert2018] Von Reppert et al., Applied Physics Letters 113, 123101 (2018)
[Wadhawan1984] Wadhawan, Bulletin of Material Science 6, 4, 733 (1984)
[Wajnflasz1970] Wajnflasz, physica status solidi 40, 537 (1970)
[Wajnflasz1971] Wajnflasz et al., Journal de Physique Colloques, 32, C1 (1971)
[Wang2002] Wang et al., Science 296, 5565 (2002)
[Weiss1907] Weiss, Journal de Physique Théorique et Appliquée 6, 1 (1907)
[Wright1994] Wright, Physical review B 49, 9985 (1994)
[Wright2001] Wright et al., Physical Review B 64, 081202 (2001)
[Wulff2002] Wulff et al., Proceedings of the Faraday Discussion 122, 13 (2002)
[Yonemitsu2008] Yonemitsu et al., Physics Reports 465, 1 (2008)
[Yu2003] Yu et al., Physical Review B 68, 064109 (2003)
[Zewail1994] Zewail, *Femtochemistry: ultrafast dynamics of chemical bond., vol. I, II & III in World Scientific series in 20$^{th}$ century chemistry*. World Scientific (1994)

# Annex

# Strain Wave Pathway to Semiconductor-to-Metal Transition Revealed by Time Resolved X-ray Powder Diffraction

C. Mariette[1*], M. Lorenc[1*], H. Cailleau[1], E. Collet[1], L. Guérin[1], A. Volte[1], E. Trzop[1], R. Bertoni[1], X. Dong[1], B. Lépine[1], O Hernandez[2], E. Janod[3], L. Cario[3], V. Ta Phuoc[4], S. Ohkoshi[5], H. Tokoro[5,6], L. Patthey[7], A. Babic[7], I. Usov[7], D. Ozerov[7], L. Sala[7], S. Ebner[7], P. Böhler[7], A. Keller[7], A. Oggenfuss[7], T. Zmofing[7], S. Redford[7], S. Vetter[7], R. Follath[7], P. Juranic[7], A. Schreiber[7], P. Beaud[7], V. Esposito[7,a)], Y. Deng[7], G. Ingold[7], M. Chergui[8], G. F. Mancini[7,8], R. Mankowsky[7], C. Svetina[7], S. Zerdane[7], A. Mozzanica[7], A. Bosak[9], M. Wulff[9], M. Levantino[9], H. Lemke[7], M. Cammarata[1,b)*]

1 Univ Rennes, CNRS, IPR (Institut de Physique de Rennes) - UMR 6251, F-35000 Rennes, France

2 Univ Rennes, CNRS, ISCR (Institut des Sciences Chimiques de Rennes) - UMR 6226, F-35000 Rennes, France

3 Institut des Matériaux Jean Rouxel (IMN), Université de Nantes, CNRS, 2 rue de la Houssinière, F-44322 Nantes, France

4 GREMAN – UMR 7347 CNRS, Université de Tours, Parc de Grandmont, F-37000 Tours, France.

5 Department of Chemistry, School of Science, The University of Tokyo, 7-3-1 Hongo, Bunkyo-ku, Tokyo, Japan

6 Department of Materials Science, Faculty of Pure and Applied Sciences, University of Tsukuba, 1-1-1 Tennodai, Tsukuba, Ibaraki, Japan

7 SwissFEL, Paul Scherrer Institut, 5232 Villigen PSI, Switzerland

8 Laboratory of Ultrafast Spectroscopy, Lausanne Center for Ultrafast Science (LACUS), École Polytechnique Fédérale de Lausanne,14 CH-1015 Lausanne, Switzerland

9 European Synchrotron Radiation Facility, 71, avenue desMartyrs, F-38000 Grenoble, France.

*to whom correspondence should be addressed: celine.mariette@univ-rennes1.fr, maciej.lorenc@univ-rennes1.fr, marco.cammarata@univ-rennes1.fr

a) current address: Stanford Institute for Materials and Energy Science , Stanford University and SLAC National Accelerator Laboratory , Menlo Park, California 94025, USA

b) current address: European Synchrotron Radiation Facility, 71, avenue desMartyrs, F-38000 Grenoble, France.

## Abstract

Thanks to the remarkable developments of ultrafast science, one of today's challenges is to modify material state by controlling with a light pulse the coherent motions that connect two different phases. Here we show how strain waves, launched by electronic and structural precursor phenomena, determine a macroscopic transformation pathway for the semiconducting-to-metal transition with large volume change in bistable $Ti_3O_5$ nanocrystals. Femtosecond powder X-ray diffraction allowed us to quantify the structural deformations associated with the photoinduced phase transition on relevant time scales. We monitored the early intra-cell distortions around absorbing metal dimers, but also long range crystalline deformations dynamically governed by acoustic waves launched at the laser-exposed $Ti_3O_5$ surface. We rationalize these observations with a simplified elastic model, demonstrating that a macroscopic transformation occurs concomitantly with the propagating acoustic wavefront on the picosecond timescale, several decades earlier than the subsequent thermal processes governed by heat diffusion.

## Introduction

Unprecedented opportunities have emerged for transforming a material with a femtosecond (fs) laser pulse [***Fleming2008***, ***Nasu2004, Yonemitsu2008, Zhang2014, Basov2017***]. New breakthroughs are anticipated, such as attaining a macroscopic transformation by driving the material on a deterministic pathway from one phase to another, ideally in a fast and highly efficient fashion. During these transformations different degrees of freedom couple sequentially and give rise to multiscale dynamics in space and time. Some of these degrees of freedom result in structural reorganisations that are crucial for stabilizing a photoexcited electronic state. Many studies have focused so far on optical coherent phonon oscillations around new atomic positions [***Johnson2017***, **Beaud2014**]. However, this process drives intracell atomic displacements that preserve the crystal shape and volume. Stabilization of the new macroscopic structural order requires the establishment of long range crystal deformations that involve propagating acoustic waves. In a recent study on spin-crossover (SCO) molecular crystals we showed that cooperative interactions of elastic origin help attain a macroscopically robust switched state [***Bertoni2016***]. In another study of photo-induced insulator to metal transition, it was proposed that the local expansion of the lattice drives the propagation of the metallic region [***Okimoto2009***]. Suspecting key role of the lattice strain in photo-induced phase transition [***Wang2019a***], we investigate the semiconducting-to-metal phase transition in $Ti_3O_5$ nanocrystals which exhibit even greater volume change on transition than the above examples, and high resilience to laser flux. Importantly, in the aforementioned studies [***Bertoni2016, Okimoto2009***], transient optical spectroscopy was used to follow the photo-induced changes. Unfortunately optical observables are hard to relate to actual structural changes, in particular lattice deformations. In this contribution we use X-ray pulses from an X-ray Free Electron Laser (XFEL) and Synchrotrons to perform time-resolved powder diffraction, allowing a quantitative refinement of the evolving structures on fs to microsecond time scales. The ultrafast strain dynamics have been further rationalized by adopting a well-known phenomenological elastic model [***Thomsen1986a, Schick2014***] and accounting for phase transformation. The highly sensitive X-ray probe revealed significant and physically sound structural changes acting as precursor stress for the macroscopic phase switching, found to move with a strain wave at the speed of sound, and hereafter referred to as acoustic front.

## Semiconductor-to-metal phase transition in $Ti_3O_5$

The trititanium pentoxide ($Ti_3O_5$, Fig. 1) undergoes a thermal phase transition between a semiconducting (so-called $\beta$) and a metallic (so-called $\lambda$) phase around $T_{SM}$ = 460 K (upon heating) [**Onoda1998**, ***Okhoshi2010***]. This semiconducting to Metal (S-M) phase transition is isostructural [***Zacharias2015***] (i.e. same monoclinic space group *C2/m* for both phases, Fig. 1a), strongly first order and characterized by significant changes in volume (+ 6.4 %) and latent heat (230 $kJ.L^{-1}$) [***Tokoro2015***]. This increase in volume is mainly caused by expansion of the lattice along the ***c*** crystalline axis. As shown in Fig. 1 the S-M phase transition is related to large intra-cell structural reorganization and the dissociation of the $Ti_3$-$Ti_3$ dimers sharing electrons on a band just below the Fermi level in the $\beta$-phase (Fig. 1a and b). From the electronic standpoint, the S-M phase transition is therefore characterized by a vanishing electronic gap related to the dissociation of such $Ti_3$-$Ti_3$ dimers [***Okhoshi2010, Kobayashi2017***]. A striking feature of this transition is that reducing the crystallite size has a spectacular influence on the metastability region of the $\lambda$-phase. For nano-sized crystallites, the $\lambda$-phase is stable down to room temperature (RT) and below, effectively making the system bistable in a broad temperature range [***Ohkoshi2010***]. Stabilisation of $\lambda$-phase was reported to be also possible by doping [***Wang2019b, Shen2017, Takahama2020***]. In the present study, we focus on a $Ti_3O_5$ pellet of nanocrystals containing 72.5 % $\beta$ phase and 27.5 % residual metastable $\lambda$ phase at room temperature (weight percentages, see Methods). The $Ti_3O_5$ nanocrystals have a typical size of about 100 nm and a morphology similar to the "*neat-flakes form*" described in [***Ohkoshi2010***]. The crystal size was estimated from static synchrotron powder diffraction measurements performed at ESRF, ID28 beamline, and described in Figure S10. X-Ray diffraction patterns were

recorded for this pellet from 300K to 700 K. Figs. 1 g and h show the temperature dependence of the ***c***-axis parameter and monoclinic angle $\phi$ of the different phases. As expected, the $\lambda$ and $\beta$ phases coexist from room temperature to $T_{SM}$ . At higher temperature ($T_c$ = 500 K) a second order phase transition occurs towards a high symmetry metallic phase (so-called $\alpha$, of orthorhombic space group *Cmcm*) [***Onoda1998***]. This phase transition is of ferroelastic nature: symmetry lowering from orthorhombic to monoclinic crystal system is characterized by a spontaneous shear strain. Thus the monoclinic angle $\phi$ of $\lambda$-phase locks to 90° at $T_c$. In contrast to the S-M transition, it is continuous and does not exhibit any volume discontinuity (see orange curve in Fig. 1h). The metastable $\lambda$-phase can be switched to $\beta$ - phase by applying external pressure ($P_{MS}$= 0.5 GPa here, but generally strongly dependent on the morphology [***Tokoro2015***, ***Ohkoshi2019***]). Also a photo-reversible persistent phase transition between $\beta$ and $\lambda$ phases was reported under intense ns irradiation [***Ohkoshi2010***, ***Asahara2014***, ***Ould2014***]. Such a photoresponsive phase change material with robust RT bistability is not only of fundamental interest but also holds promise for different technological applications, such as efficient optical or heat storage [***Tokoro2015***, ***Okoshi2019***]. The photoinduced $\beta$-to-$\lambda$ transition was also investigated in the transient regime, i.e. below the excitation threshold for permanent switching [***Asahara2014***, ***Tasca2017***]. Full scale dynamics, from fs to µs, was probed by ultrafast diffuse reflection spectroscopy on a nanogranular pellet of $Ti_3O_5$; those measurements have been interpreted in terms of nucleation and growth process of $\lambda$ regions [***Asahara2014***]. Unfortunately the previous studies have lacked either the time resolution [**Tasca2017**] or the structural sensitivity [***Asahara2014***] to confirm such a hypothesis and to investigate the role of strain wave propagation and volume change in stabilising the photoinduced phase.

## Time-resolved XRD

Here we use ultrafast X-ray diffraction (XRD) at SwissFEL beamline Bernina [***Ingold2019***] to investigate the mechanism of the photoinduced semiconductor ($\beta$ - phase) to metal ($\lambda$ - or $\alpha$ - phase) transition on a pellet of $Ti_3O_5$ nanocrystals. The experimental geometry is sketched in Fig. 2a. The X-ray photon energy was set to 6.6 keV and the grazing angle to 0.5°. Considering both X-ray absorption and pellet roughness, the estimated effective probed depth for this geometry was $z_p$ = 400 nm (Figs. S2 and S3). The 1.55 eV, 500 fs long pump laser impinged the sample at 10° incident angle. At this energy, the pump penetration depth calculated from the refractive index reported in [**Hakoe2017**] was $\xi_L$ = 65 nm. The measured time resolution was about 600 fs FWHM [***Ingold2019***]. These studies are complemented by experiments at the ID09 beamline at ESRF, probing longer time scale with time resolution around 100 ps (Fig. S4). Unless stated otherwise, we will refer to the SwissFEL experiment. Fig. 2b compares powder diffraction differential patterns taken at various time delays. The low noise, featureless transient at -4.5 ps, highlights the high quality of the differential data and data reduction procedures. The differential patterns in Fig. 2b emphasize that major changes occur already at very early delays indicating rapid structural deformations within 500 fs. At picosecond time scale the difference signal increases in amplitude; the signal around some Bragg peaks, for instance (110) and (020), changes towards a characteristic “bi-polar shape”, i.e. positive change towards low angles and negative change towards higher angles indicating an increase of unit-cell parameters. Broadening of some Bragg peaks is also observed (“butterfly shape”), indicating inhomogeneous lattice distortions. Such behaviour is clearly observed for the isolated Bragg peak (204) from $\beta$ phase. Besides, significant changes in the absolute diffracted intensity suggest inter-atomic re-organisations. The high amplitude of the differential patterns (from 10 % to 30 % depending on the q region) indicates large photo-induced deformations/transformations taking place in the sample. Despite the complexity of structural changes, the high-fidelity data allow a complete Rietveld analysis of the patterns for each time delay. Figs. 2c-d show the results of the Rietveld refinement of the diffraction patterns for a reference pattern (pump laser off) and for a pump / probe delay of 7.5 ps (see also Fig. S5). The full q range measured and used in the refinement is displayed, namely 1.09 to 3.45 $Å^{-1}$. In both cases the Rietveld analysis with unconstrained cell

and atomic position parameters for the $\lambda$ - and $\beta$ -phases yielded similar reliability factors ($R_p$= 3% and $R_{wp}$= 7-8%) and difference profile curves compared to the refinement of the pattern recorded under equilibrium condition. This attests to the quality of the Rietveld analysis at positive time delays and enables the discussion of the time evolution of the structure at the sub-ps time-scale, which we discuss hereafter. All details about the sample, experiment, data reduction and analysis are given in the Methods section).

## Sub-ps dynamics: structural changes induced by direct optical pumping

We first describe the ultra-fast structural changes occurring within the first 500 fs where significant intra-cell distortions are already observed. The evolution of selected distances and angles are displayed in Fig. 3 for delays up to 7 ps, typical changes being in the order of $10^{-2} \pm 2 \times 10^{-3}$ Å and 0.5-1 ± 0.02 °. Comparison with calculated electronic structure (Fig. 1a to f) helps to rationalize the observed photoinduced changes. The calculated optical conductivity is particularly insightful for describing the possible electronic transitions induced by the 1.55 eV pump photons (Fig. 1e and f).

**For the majority $\beta$ -phase**, the two bands closest to and below the Fermi level centered at 1.1 eV and 0.3 eV have a strong $Ti_2$ and $Ti_3$ character, respectively. Although both $Ti_2$-$Ti_2$ and $Ti_3$-$Ti_3$ dimers are excitable above the gap by 1.55 eV photons, the calculated optical conductivity is mainly contributed in this range by excitation from $Ti_3$-$Ti_3$ dimers to the conduction band. Electron depletion of the bonding $Ti_3$-$Ti_3$ states thus leads to the observed fast increase of the associated $D_{33}$ distance (Fig. 3b); $D_{ij}$ stands for distance between $Ti_i$ and $Ti_j$ atoms. These dimers also undergo rotation quantified by the decrease of $\Theta_{332}$ angle and the increase of $\Theta_{322}$ angle (Fig. 3a and 3g); $\Theta_{ijk}$ stands for angle formed between $Ti_i$, $Ti_j$ and $Ti_k$ atoms. These motions of small amplitude are precursor structural signatures of the isostructural phase transition from the $\beta$ - towards the $\lambda$ - phase. However, the incomplete rotation (compared to transition at thermal equilibrium) results in a significant decrease of the $D_{23}$ distance, whereas in the $\lambda$ - phase this bond would be longer. On the same time scale, the bond length of the second dimer $D_{22}$ remains unchanged (Fig. 3b), and indeed expected to undergo a much smaller change on phase transition to the $\lambda$ - phase.

**For the minority $\lambda$ -crystallite**, the photoexcitation promotes the $Ti_2$ and $Ti_3$ electrons above the Fermi level. The contributions to the calculated optical conductivity from both $Ti_2$ and $Ti_3$ electrons around 1.55 eV are comparable (see Fig. 1h), albeit they lead to different structural effects. We observe a significant increase of $D_{22}$ on a sub-ps time scale (Fig. 3e): depletion of the $Ti_2$-$Ti_2$ bonding orbital weakens the $Ti_2$-$Ti_2$ dimer, consequently, $D_{22}$ and non-dimerized $D_{33}$ become less distinguishable. In the high symmetry $\alpha$ phase, $Ti_2$ and $Ti_3$ are equivalent through a mirror plane (Fig. 3h). The relative evolution of $D_{22}$ and $D_{33}$ (Fig. 3e), as well as $\Theta_{322}$ and $\Theta_{332}$ (Fig. 3d), directly probe the ultrafast evolution of the degree of symmetry breaking in the low symmetry monoclinic metallic phase. This points to a distortion towards $\alpha$ atomic structure.

These precursor structural changes occur before long-range cell deformations are observed (Fig. 3 c and f). The volume of the $\lambda$ - phase has a linear increase with no discontinuity around time zero. This notwithstanding, the unit cell of this $\lambda$ - phase undergoes ultrafast shear. The decrease of the monoclinic angle ($\phi$) plotted in Fig. 3f indicates partial symmetry change within 4 ps, slower than sub-picosecond structural changes yet faster than unit cell volume.

## Dynamics of long-range structural changes

The dynamics of the aforementioned long-range cell deformations is discussed in this paragraph, first by describing the results of the Rietveld refinement and then by applying a phenomenological model to explain the results.

**The evolution of the $\lambda$ - phase unit cell volume** takes place on the few ps time scale ($\Delta V_\lambda$, Fig. 4a). The increase is almost linear up to ≈ 16 ps; simultaneously the maximum of Bragg peak broadening is observed. It results from the strain distribution, quantified here by a microstrain parameter ($\varepsilon_\lambda$) conventionally used in powder diffraction analysis. The evolution of the $\lambda$ - macroscopic phase fraction ($\Delta X_\lambda$, Fig. 4c), signals that part of the $\beta$ - crystallites undergoes the phase transition. At around 20 ps, $X_\lambda$ has increased from 27.5 % to 33.0 ± 0.8 % on average within the X-ray probed depth (400 nm). Importantly its evolution is also quasi linear up to ≈ 16 ps, thereby the dynamics of the $\lambda$ - phase unit cell volume and $\lambda$ - phase fraction develop at the same time.

**The behaviour of the $\beta$ -phase unit cell volume** is less straightforward. Its evolution ($\Delta V_\beta$, Fig. 4c) reveals a small decrease to a minimum around t ≈ 16 ps. Subsequently, the volume starts to increase to a level similar to the equilibrium value and well above. The latter changes remain small, the volume of this $\beta$ - phase increases from 349.3 to 350.7 Å$^3$ (+0.4%), while it increases from 371.7 to 381.3 ± 0.1 Å$^3$ (+2.5%) for the metallic phase.

## Strain-wave model

The connection between ultrafast photo-excitation and strain dynamics leading to the overall volume change has been described by Thomsen [***Thomsen1986a***] and later extensively used to describe strain propagation [***Schick2014***, ***Ruello2015***]. We performed numerical calculations for $\lambda$ - and $\beta$ - crystallites separately, in order to rationalize our observations (see SI "Model calculations of Strain, Volume change and Microstrain"). In the case of a metal, the original model assumes that stress is set up by lattice heating. In the case of semiconductors, the creation of electron-hole results in a more complex contribution, separated by Thomsen as electronic (proportional to deformation potential [***Matsuda2015***]) and phononic (thermal phonon, proportional to excess energy $E_{ph}$-$E_g$, respectively photon and gap- energy). In the present case however, stress arises primarily from the precursor photoinduced electronic changes and structural distortions described in the previous paragraphs, which we argue will lead to phase transition. We consider the same semi-infinite medium as in the seminal work by Thomsen [***Thomsen1986***]. We also assume that significant contributions to the stress have exponential profile of the laser absorption. To establish the mechanical equilibrium between crystallites and their environment, acoustic wave packets propagate from the surface inwards, leaving behind a static deformation. Note that electronic diffusion, and how it affects the strain wave, was deliberately neglected in the model. Although this process probably occurs, it is not required to take into consideration for reproducing the experimental data satisfactorily. The solution of strain always takes on the following form [***Thomsen1986***]:

$$(z,\ t)\ =\ S \times f(z,\ t)$$

where $f(z,\ t)\ =\ \left[e^{-z/\xi}\ \left(1 - \frac{1}{2}e^{-v_s t/\xi}\right) - \frac{1}{2}e^{-|z-v_s t|/\xi} \times sign(z - v_s t)\right]$,

S is the strain at z = 0, where the stabilised deformation is maximal. It determines the amplitude (and the sign) of the volume change induced by the initial stress. Time dependent *f(z,t)* determines the profile of the acoustic pulse, travelling at the speed of sound $v_s$, as well as the static deformation left behind. The speed of 6.5 × 10$^3$ m.s-1 was determined independently with picosecond interferometry [***Thomsen1986b***], sensitive to propagating acoustic wavepackets [***Asahara2014***] (Fig. S8). In the following, the time t and position z are related through $v_s$.

Based on this approach we performed numerical calculations, taking into account different possible responses of the two phases. These calculations qualitatively reproduce the experimentally observed changes in lattice volumes, microstrain and phase fractions as shown in figure 4.

**For the $\beta$ crystallite, (75 % of sample before excitation)** We first consider the case where no phase transition occurs (56 % of the sample). Then, maximum volume expansion is expected to have an amplitude expressed by $S_{\beta,T} \propto V_\beta(T_c) - V_\beta$ (T = 300 K) = 1.5 Å$^3$. Its time evolution is strictly that proposed by Thomsen (fig. 5b to d, upper left panel). The occurrence of a phase transition (19% of the sample) raises the complexity of description, and we account for two consequences. Firstly, the dilated region is assumed to transition to the $\lambda$ phase, and as such no longer counts in the strain of $\beta$ phase (figure 5b to d, right panels). The related stress will lead to an increase of volume expressed by $S_{\beta,PT} \propto V_\lambda$ (T = 300K) - $V_\beta$ (T = 300K) = 20 Å$^3$ (see figure S7). The incurred distortion launches a significant compressive wave (fig 5b and c), hence the second consequence: volume shrinkage of the $\beta$ phase in the vicinity of the phase front, as observed experimentally (figure 4 d)). The transformation stops at (t = $\tau_{PF}$, z = $z_s$), yet the strain wave generated at *t = 0* continues travelling into the region z > $z_s$ of the $\beta$ phase and induce a positive strain therein.

Even though we cannot distinguish experimentally between transitioning and non-transitioning $\beta$ crystallites, the respective contributions $S_{\beta,PT}$ and $S_{\beta,T}$, determine the sign and amplitude of the average negative change of volume observed at $\tau_{PF}$. The amplitude of $S_{\beta,PT}$ approximately 13 times greater than that of $S_{\beta,T}$ as justified above, gives a very good agreement with the observation (Figure 4c and d). However, any ratio in the range [10-20] would still give reasonable agreement.

**For the $\lambda$ crystallites**, we first consider the lattice heating induced by the photo-excitation of the lambda crystallite (25 % of sample before excitation). For the calculation of the average strain in this phase, we also have to factor in the new $\lambda$ crystallites transitioned from $\beta$. The two contributions $S_{\lambda,PT}$ and $S_{\lambda,T}$ are both of phononic origin and scale with energy deposited into the lattice. For the new $\lambda$ phase, the energy transferred to the phonon bath is at best equal to $E_{ph} - E_g - Q = 0.55\ eV$ ($E_g$ = 0.7 eV, latent heat Q = 230 kJ.L-1 [***Tokoro2015***], corresponding to 0.25 eV/dimers($Ti_3$-$Ti_3$)). In the excited $\lambda$ phase, the whole photon energy (1.55 eV) is assumed to be transferred to the phonon bath. The calculations presented in figure 4 and 5 are performed with the amplitude of $S_{\lambda,PT}$ approximately third of $S_{\lambda,T}$, however, the variation of these relative contributions in the range [0 - 0.5] would still give a reasonable agreement.

Details of the calculations of the parameters shown in figure 4b and d are given in SI. The strain gradient, arising from the initial stress distribution, can be quantified by the standard deviation of the calculated strain (Fig. 4b). It can then be compared with the observed Bragg peak broadening, quantified in the Rietveld refinement by the microstrain parameter $\varepsilon_\lambda$ (Fig. 4a).

## Discussion

The simple model described above is a first attempt to generalize the Thomsen model to include phase transformation. This is essential for systems where the volume change associated with the transition is comparable (or higher) that the laser induced thermal expansion included in the original model. For the $\beta$-phase, we accounted for a partial transformation of the crystallites, and the associated unit cell volume changes. The initially excited $\beta$-crystallites are assumed to be promptly transformed to $\lambda$- phase simultaneously with the moving acoustic front, and no additional strain upon feedback from the phase transition was included in the calculations. This model has clear limits, most notably the feedback mechanism between volume change and transition was not rigorously solved by the model equations. Despite that, the physical picture of a phase front moving with the acoustic front seems to well reproduce the experimental data. The phase front is assumed to stop at $z_s$ = 100 nm, matching the average crystallite size as observed by X-ray diffraction. The acoustic front takes $\tau_{PF}$ ~ 16 ps to travel this distance (see black line in Fig. 4 a - d). This is exactly when the $\beta$-phase volume shows a well defined minimum, a direct consequence of the compression exerted by the relatively high volume of the layer transformed to the $\lambda$-phase (Fig. 5). The latter also influences the calculated mean strain for $\lambda$ (Fig. 4 b). The calculated $\lambda$-phase fraction is plotted in Fig. 4 d and it reproduces very accurately the behavior in Fig. 4 c . As a consequence, the increase of the latter by 5% on average within the estimated

X-ray probed depth $z_p$ = 400 nm, amounts to approximately 26% within $z_s$ =100 nm below the surface, where the phase front stops (see Fig. S9). Because the laser penetration, the average crystallite size, and phase-front breakdown limit all fall near 100 nm, we refrain from speculating on the exact nature of the transition limit. Only a quarter of crystallites undergo transition by the strainwave, which we tentatively assign to residual static stresses pre-existing in the sample ($\lambda / \beta$ coexistence) and/or to the random orientation of crystallites. The latter would be related to the predominant role of dilation along c-axis to stabilise the new phase. Lastly, the exact origin of the phase transition requires further structural insights into the $\lambda$-$\beta$ interface. Our study probes the bulk average within the penetration of X-rays, so it would be premature to claim that transition within that interface is uniquely strain driven. Yet, the strain and phase propagate at the same velocity thereby establishing that the strain wave determines the pathway of a truly macroscopic semiconductor to metal transition in this class of nano material exhibiting volume change during phase transition. Relying on the same physical picture, the 4 ps shear dynamics described above, would correspond to propagation on 10 nm with a transverse acoustic velocity of $3 \times 10^3$ m.s$^{-1}$ [***Tokoro2015***]. High resolution single crystal studies of the same compound performed at ID28 (ESRF), seem to suggest the presence of relatively dense stacking faults along the c axis (Figure S6). Ferroelastic domains of similar size were also recently reported for an archetypal oxyde [***Singer2018***].

On longer time-scales ($t > \tau_{PF}$), temperature and strain distributions [**Thomsen1986a, Schick2014**] persist until heat diffusion equilibrates the temperature over the probed area. This process was investigated by XRD with 100 ps time resolution at the ID09 synchrotron beamline of ESRF [**Cammarata2009**] (Fig. 6). The slow process can be clearly distinguished because it develops until 100 ns. The fraction of transformed $\beta$ - crystallites reaches 30 % in the probed volume (see fig S9). The 100 ns value is consistent with expected time for heat diffusion over D ≈ 200 nm (in a bulk material with thermal diffusivity of 230 nm$^2$.ns$^{-1}$) [***Tokoro2015***]. The complete recovery of thermal equilibrium with the environment is observed on a 10 µs time scale, in agreement with ***Tasca2017***.

## Conclusion

In summary, this work offers a new perspective for the ultrafast control of materials with evidence of a strain wave pathway for achieving a phase transition in nanocrystallites excited by a light pulse. Key role of the long-range lattice deformation dynamics in the transformation process is highlighted, and so are the benefits of direct structural probes for visualising thereof. In particular, we show that state of the art XFEL sources permit measurements of the real-time interatomic motions and lattice distortions, even in a bi-phasic polycrystalline powder. Our experiment, corroborated with a phenomenological elastic model, unambiguously reveals a phase front starting from the sample surface and moving with sonic speed into the bulk. Notably, the strain waves are launched directly in the material by internal precursor stresses that store mechanical energy. This coherent process, restoring mechanical equilibrium, takes place on an ultrafast timescale and clearly precedes the much slower thermal homogenization. We claim a coherently propagating macroscopic order, as opposed to random growth induced by incoherent thermal kinetics. It is a step forward for self-contained transformation, compared to previously reported phase front propagation which required a hetero-structure for launching the strain waves at the inferface of a strongly absorbing transducer film into the phase change film [***Först2015***, ***Först2017***]. We reveal a pathway that is non-destructive, and opens fascinating prospects for an advanced degree of strain control through electronic and structural precursors. All in all, the mechanism revealed herein is fundamentally different from the nucleation and growth, rooted in phase transitions at thermal equilibrium and so far proposed in a similar context [***Asahara2014***, ***Singer2018***]. We also believe that the strain wave pathway is likely to be valid in a variety of volume changing materials.

# Acknowledgements

The authors want to thank Gemma Newby and Martin Pedersen from ESRF for support during earlier phases of this project, Guénolé Huitric (IPR) for his contribution to the optical spectroscopy measurements performed at IPR and discussed in SI. MC wants to thank PSI for accepting his proposal to study $Ti_3O_5$ nanoparticles as the first experiment for the entire facility and for providing excellent support. MLo gratefully acknowledges Agence Nationale de la Recherche for financial support under grant ANR-16-CE30-0018 ("Elastica"). BL would like to thank Bruno Bêche (IPR) for help with AFM measurement. MC and MLe acknowledge the support of European Union Horizon 2020 under the Marie Sklodowska-Curie Project "X-Probe" Grant No. 637295. SO and HT acknowledge support from JSPS Grant-in-Aid for specially promoted Research Grant Number 15H05697, and JSPS KAKENHI Grant Number 16H06521 Coordination Asymmetry. MCh and GFM acknowledge funding from the European Research Council (ERC) H2020 DYNAMOX (grant No 695197 and from the swiss NSF via the NCCR:MUST). Parts of this research were carried out in the frame of the IM-LED LIA (CNRS).

# Author contributions

CM, MLo, HC and MC coordinated the project. HC and MLo proposed the study of the photoinduced phase transition of $Ti_3O_5$. MC coordinated the X-ray studies. CM developed the thermo-elastic model with the help of MLo. Nanocrystals of $Ti_3O_5$ have been characterized and synthesized by SO and HT. CM and LC performed Rietveld refinement with help from OH. OH performed the static powder XRD measurements. AB carried out diffuse scattering measurements and high resolution powder diffraction measurement. MC and MLe developed the setup at ESRF with help of MW, SZ, ET, EC, XD, CM, MLo. MC and HL developed the setup at SwissFEL with help from LG, AV, CM, MLe, LP, PB, VE, YF, GI, GM, RM, CS, SZ. MC developed the data reduction procedure. AM developed the Jungfrau detector used for the experiment. VT performed DFT calculations with help from EJ. CM, MLo, HC and MC wrote the manuscript with significant contributions from EC, EJ, LC, MLe, PB, critical reading from MCh and help from all authors.

# Methods

## Static powder laboratory X-ray diffraction - temperature measurements

The static powder XRD as a function of temperature was measured in Debye-Scherrer geometry on a Bruker AXS D8 Advance (Mo-$K_\alpha$ radiation selected with a focusing Göbel mirror) equipped with a MRI high temperature capillary furnace and a high-energy LynxEye detector. The flake form $Ti_3O_5$ powder sample [***Ohkoshi2010***] was sealed in a quartz capillary of 0.3 mm in diameter.

## DFT/optical properties calculations

All calculations have been carried out by using the Quantum ESPRESSO package within the framework of DFT+U, with the Perdew-Burke-Ernzerhoff (PBE) generalized gradient approximation (GGA) to describe the exchange-correlation functional. Both Projector Augmented Wave basis (PAW) and norm-conserving pseudo-potentials. The Monkhorst-Pack grid of 8x8x4 in the reciprocal space was used for the Brillouin zone sampling for both $\lambda$ - phase and $\beta$ - phase. The total energy of the system converged to less than 1.0 x $10^{-6}$ Ry. Electronic wave functions were represented in a plane wave basis up to an energy cut-off of at 90 Ry. Crystallographic structures were taken from [***Okhoshi2010***]. Ferromagnetic and antiferromagnetic (AFM) orders were considered. AFM order was found to be the ground-state for both $\lambda$ - and $\beta$ -phases. The optical properties were computed using epsilon.x post-processing tool of the Quantum Espresso package, at the independent-particle approximation level. Both intraband and interband contributions were considered. Calculated optical density shown in Fig. 1 is the average of the 3 diagonal elements (Fig. S1).

## Samples preparation

Flakes-form $\lambda$-phase samples were obtained following the synthesis method described in [***Ohkoshi2010***]. Pellets were made from flakes powder using a uniaxial press at 3 GPa. The resulting pellets have a density of 3.2 g.cm$^{-3}$ (a ratio of 0.8 compared to single crystal, measured by X-ray absorption). They contain a mixture of pressure-induced $\beta$-phase crystallites and $\lambda$-phase crystallites due to residual stress. The absolute $\lambda$-phase fraction is determined by Rietveld refinement around 25-30% (depending on the pellet), in good agreement with the ratio usually observed with this method [***Ohkoshi2010***]. Whether $\beta$ - and $\lambda$ - could coexist within a single grain remains an open question and cannot be answered with our XRD measurements.

## Experimental details - time resolved experiment

Experiments were performed at ESRF Synchrotron (Grenoble, France) using the ID09 time resolved beamtime (**exp1**) and at SwissFEL (PSI, Villigen, Switzerland) at the Bernina beamline (**exp2**). The latter was part of the very first commissioning experiment of the entire facility .

### EXP1: ESRF experiment detail

The ID09 setup has been discussed in detail previously [***Cammarata09***]. Briefly, fast rotating choppers were used to isolate X-ray single pulses (each 100 ps long) at 1 kHz repetition rate. A fast shutter was used to lower the frequency to 10 Hz. The X-rays were partially monochromatized by using a Ru/$B_4C$ multilayer monochromator resulting in 1.5% bandwidth centered at 11.5 keV and focused by a toroidal mirror to a size of 0.1 x 0.06 mm$^2$. In order to reduce the X-ray beam footprint on the sample, the last slits (~0.6 m from the sample) were closed vertically to a 0.03 mm gap. A synchronized laser (800 nm) at 10 Hz was used to excite the sample using a perpendicular geometry configuration, with the laser hitting the sample from the top. Laser Beam size was 10x0.23 mm$^2$ or 4.6x0.21 mm$^2$ depending on power densities (respectively below and above 1 mJ.mm$^{-2}$). Diffracted X-rays were integrated on a Rayonix

MX170-HS CCD detector and azimuthally integrated using pyFAI [***Ashiotis2015***].

## EXP2: SwissFEL experiment

The experimental setup is shown in Fig. 2a. The SwissFEL and the Bernina beamline layout are described elsewhere [***Ingold2019***]. Since the experiment was performed as part of the commissioning for the facility, the X-ray photon energy was limited to 2.2 keV. The third harmonic (6.6 keV) was used to probe the structural changes after photoexcitation. The energy per pulse was ~0.2mJ and the third harmonic content of about 1%. The fundamental was suppressed using absorbers. We estimate about $10^9$ 3rd harmonic photons per pulse at the sample position. The X-rays were focused by a Kirkpatrick-Baez mirror system. The spot was set to ~ 200 x 7.5 $\mu m^2$ (FWHM h x v). Because of the small grazing incidence angle of 0.5° the small vertical spot was essential to minimize the footprint on sample which with a length of 0.86 mm footprint is still one of the major contributions to the peak broadening. The pump laser pulses, generated by a Coherent CPA amplifier (Legend) were purposely stretched to 0.5 ps to limit the peak intensity on the sample increasing the overall time resolution to ~600 fs. Note that no jitter correction [***Harmand2013***] was used for the experiment. The measured instrumental time resolution of 350 fs FWHM [***Ingold2019***] increased due to the pump pulse stretching to about 600 fs. The laser beamsize at the sample position was 300 um (FWHM). With an incident angle of 10° the resulting footprint was 300 x 730 $\mu m^2$. The repetition rate of the laser was set to 5 Hz minimizing residual heating effect.

### Data reduction/correction

Diffracted X-rays were measured (for every single pulse) by the Jungfrau pixel detector [***Mozzanica2018***]. The detector was calibrated to convert ADU directly in equivalent keV photon energy. Most pixels (> 70%) had zero counts, the others detected either one elastic photon (~6.6 keV reading, about 3% of the pixels), a Ti fluorescent photon (centered around 4.4 keV, 11% of the pixels) or a combination of the two (1 elastic +1 fluorescence photon). By eliminating the fluorescence photons from each image a lower background image was obtained. Each "fluorescence corrected" image has been azimuthally integrated to obtain 1D curve [***Ashiotis2015***]. Each data point was collected by acquiring 500 images (250 with pump laser and 250 without pump laser). The two sets were averaged (after "fluorescence correction" and azimuthal integration) to provide two curves (laser off and on). To correct for drifts in photon energy each "off image" was used to extract the average photon energy during collection of a given time delay. The corresponding "laser on" image was treated using the optimized X-ray photon energy. To further verify the stability of the data collection and correction strategy, every 10 delays a reference time delay was acquired to be sure that no drifts or permanent sample change had happened. Each powder pattern was normalized to the intensity of the air scattering contribution dominating at low scattering vectors (between 0.7 and 0.9 $Å^{-1}$). All raw data and data reduction scripts will be made available.

### Data analysis (Rietveld refinement)

Rietveld whole powder pattern profile refinements were performed following a fundamental parameter approach using the TOPAS software [***Coelho2018***]. Pawley refinements were also used and both methods gave consistent evolutions of the unit cell parameters and scales factors. In both cases, refinement was performed using the q range from 1.09 to 3.45 $Å^{-1}$, corresponding in this case to diffraction angles from 19° to 63°. The profiles were described using a beam energy of 6.5 keV ( $\lambda$ = 1.899 Å) and a gaussian emission profile with 1.3% FWHM. The peak width and sample displacement were described using the expressions from [***Rowles2017***], vertical width and incident angle of the beam being fixed as measured (4 µm and 0.5° respectively). The sample detector-distance was fixed to 61 mm, as refined in the azimuthal integration step. The absorption coefficient at 6.5 keV was calculated as 800 $cm^{-1}$ (for a packing density of 0.8, measured from x-ray transmission measurement). These parameters were fixed for the refinements against time resolved patterns. The refinements included two phases ($\beta$ -

and $\lambda$ -). For each phase, the free parameters were the cell parameters (a, b, c, $\phi$), the atomic position in the (***a***, ***c***) plane for the five independent atoms (position along ***b*** being symmetry-restricted) and the scale factor. An additional microstrain-type gaussian convolution (FWHM = $\varepsilon$ x tan($\theta$)) accounted for the strain distribution observed during the propagation (Fig. 5). The initial Bragg peak profile was well defined by the experimental resolution function defined as described above. Thus no extra size contribution was considered in the refinement of the reference patterns. The transformation being reversible and isostructural, no evolution of the crystallite size was expected and thus considered either. In any case, the choice was made to retain the simplest convolution functions to ensure the robustness of the refinement. Hence no lorentzian contribution, asymmetry or anisotropy was taken into account. The background was described as a 3$^{rd}$ order polynomial. The texture of the majority phase was described using Spherical Harmonics corrections, whose coefficients were refined on reference patterns and then kept constant for all delays. The $R_{wp}$ agreement factors were around 7.5%; $R_{Bragg}$ were calculated around 2% for the majority $\beta$ - phase and around 7% for the $\lambda$ - phase. For the SwissFEL data refinement, errors were estimated from the distribution (standard deviation *SD*) of the refined values obtained on reference pattern (interleaves data with no laser), and thus have to be understood as relative errors; the errors given in the text and in the figures corresponds to *2*x*SD*. Note that for the ESRF data, the quality of the extracted patterns did not allow to refine the atomic positions. In both cases, reference structures were taken from [***Ohkoshi2010***, ***Onoda1998***]. The atomic displacement parameters could never be refined accurately due to the limited q region measured and large beam footprint resulting in poor q-resolution. These values were fixed with those reported in the litterature.

# Figures

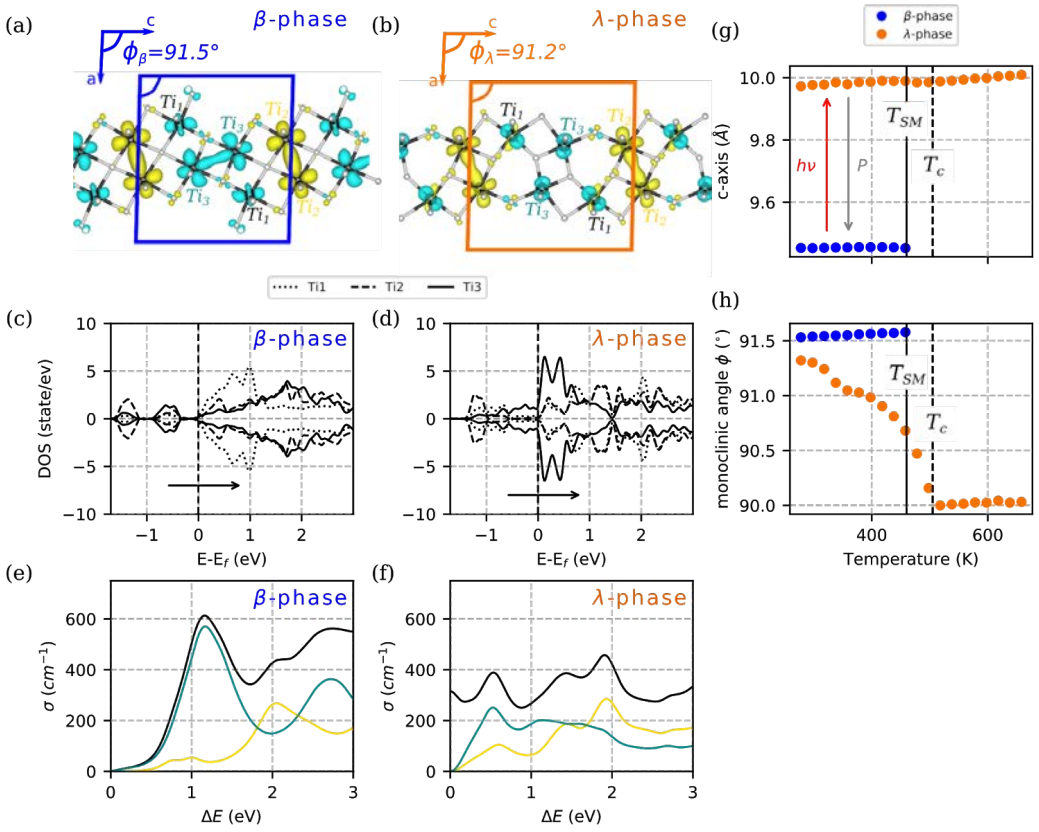


***Figure 1 : Structural and optical changes upon phase transition in $Ti_3O_5$ nanocrystals at thermal equilibrium*** **a**) and **b**) atomic structure of $\beta$ - and $\lambda$ - phases, respectively, with calculated charge density for the two bands centered at 1.1 (yellow) and 0.3 eV (cyan) below the Fermi level, strongly localized around $Ti_2$-$Ti_2$ and $Ti_3$-$Ti_3$ dimers; **c**) and **d**) Calculated density of state projected on $Ti_1$ (dotted lines), $Ti_2$ (dashed lines) and $Ti_3$ (solid lines) for $\beta$ - and $\lambda$ - phases, respectively. The black arrow stands for the energy transfer corresponding to the 1.55 eV pump photons.; **e**) and **f**) Mean calculated Optical conductivity for $\beta$ - and $\lambda$ - phases, respectively (black line). Yellow (blue) curve represents the contribution arising from the band at -1.1 eV (-0.3 eV). Diagonal contributions are shown in Fig. S1; **g**) and **h**) X-ray powder diffraction study on $Ti_3O_5$ nanocrystals: **g**) change in c-parameter of the monoclinic unit cell revealing with a jump which underlines the strongly first order phase transition at $T_{SM}$ = 460 K between $\beta$ - and $\lambda$ -phases ; **h**) Evolution with temperature of the monoclinic angle $\phi$ exhibiting a jump upon the first order phase transition at $T_{SM}$ = 460 K (between $\beta$ - and $\lambda$ -phases which co-exist in these nanocrystals below $T_{SM}$), and a continuous locking at 90 ° characterizing the symmetry change towards *Cmcm* high temperature $\alpha$-phase. The critical temperature $T_c$ = 500 K for this second order phase transition is pointed out with a dotted vertical line.

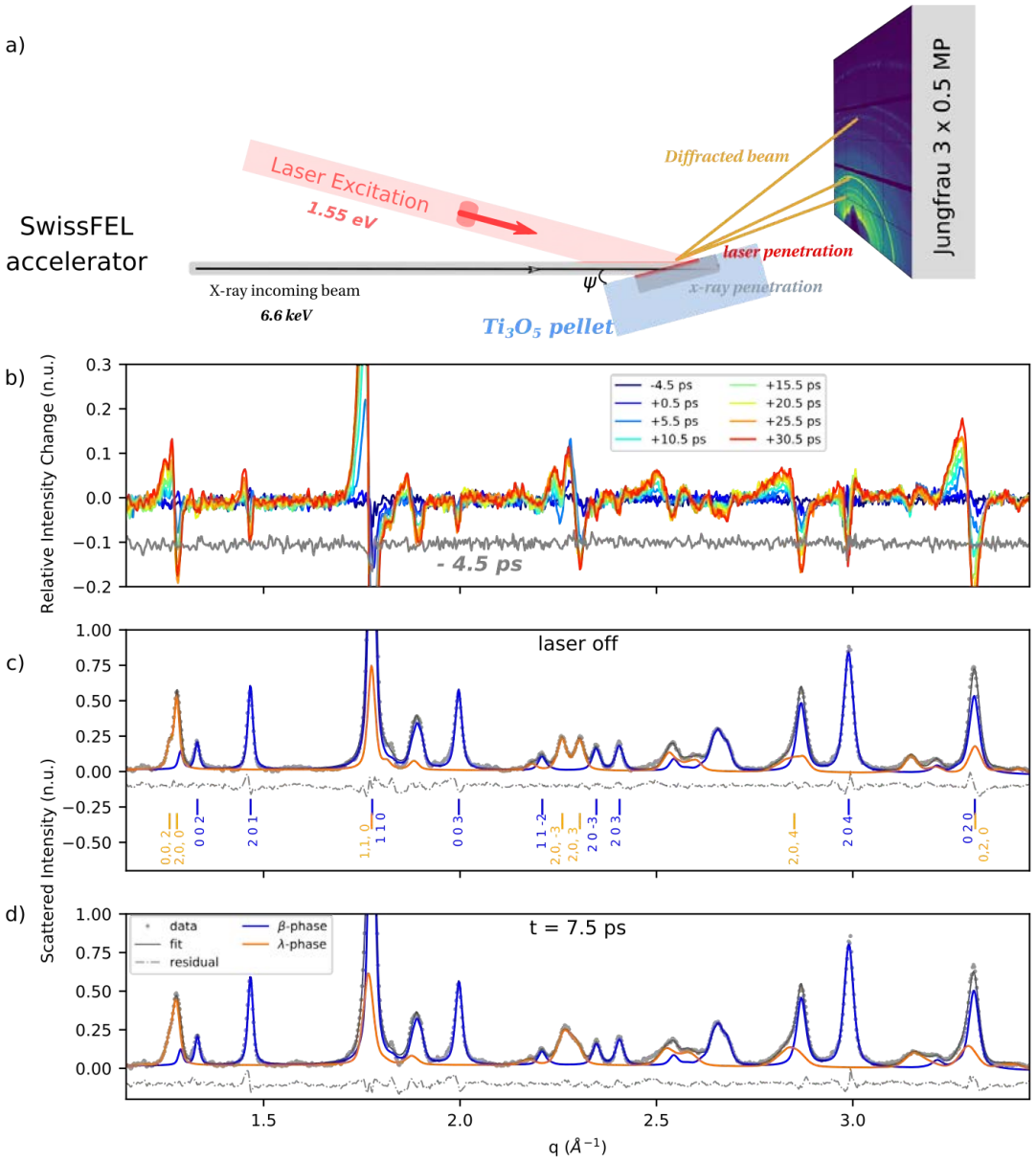


***Figure 2: Experimental setup, raw data and structural refinement.*** **a**) Experimental setup for time resolved powder X-ray diffraction in quasi grazing angle geometry. The Debye-Scherrer rings are collected on a 2D Jungfrau fast readout detector with single photon sensitivity [***Mozzanica2018***]. **b**) Differential patterns *($laser_{on}$-$laser_{off}$)* showing up to 30% variations of the signal (pump fluence 0,85 mJ.mm$^2$) on ps time scales ( < 35 ps ). Grey curve shows negative -4.5 ps delay for reference (shifted by -0.1 along y for clarity). **c**) and **d**) Rietveld refinement of reference spectrum (spectrum with laser off, and spectrum at t = 7.5 ps respectively). Measured powder patterns are plotted in light grey circles and result of Rietveld refinement in black, solid line. Orange and blue patterns are contributions to the refinement of the $\lambda$ - and $\beta$ - phases respectively; the residual curve is shown in grey, dashed lines.

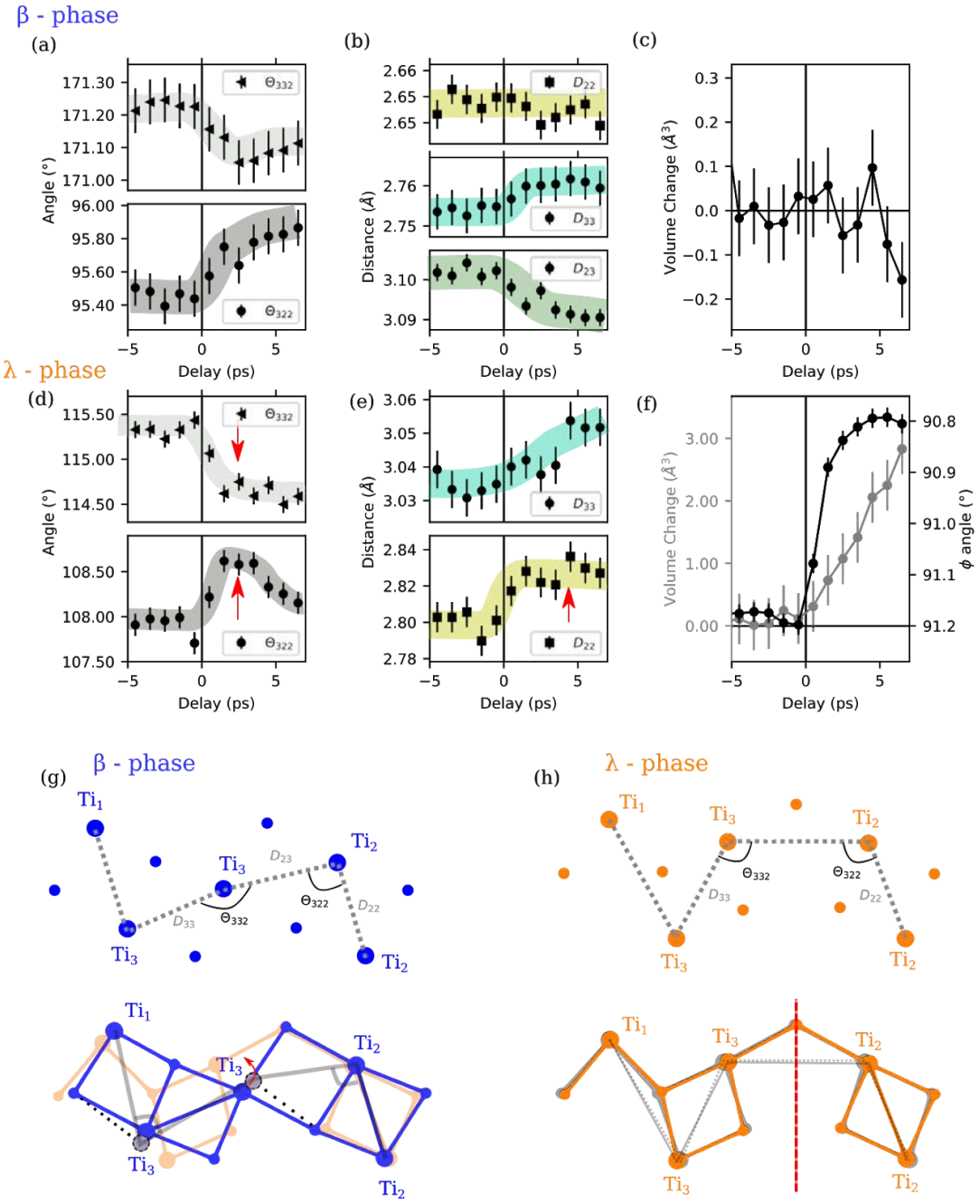


***Figure 3: Ultrafast structural changes extracted from X-ray diffraction data.*** **a-f**: Evolution of relevant inter-atomic angles, distances and unit cell volume change for the $\beta$ - (**a-c**) and $\lambda$ - (**d-f**) phases ($\theta_{ijk}$ = $Ti_i$-$Ti_j$-$Ti_k$ angles and $D_{ij}$ = $Ti_i$-$Ti_j$ distances). The evolution of the monoclinic $\phi$ angle is also reported for the $\lambda$ - phase (**f**). Thick transparent solid colored lines are guides for the eye. **g-h**: schematic representation of the observed local distortions (exaggerated for clarity) for the $\beta$ - (**g**) and $\lambda$ - (**h**). in (**g**), the $\lambda$ - structure is represented in light orange for reference and in (**h**), the red line is the *m* mirror planes lost at $T_c$. A topo of structural distortion shown in grey contour lines : dotted -before, solid -after excitation.

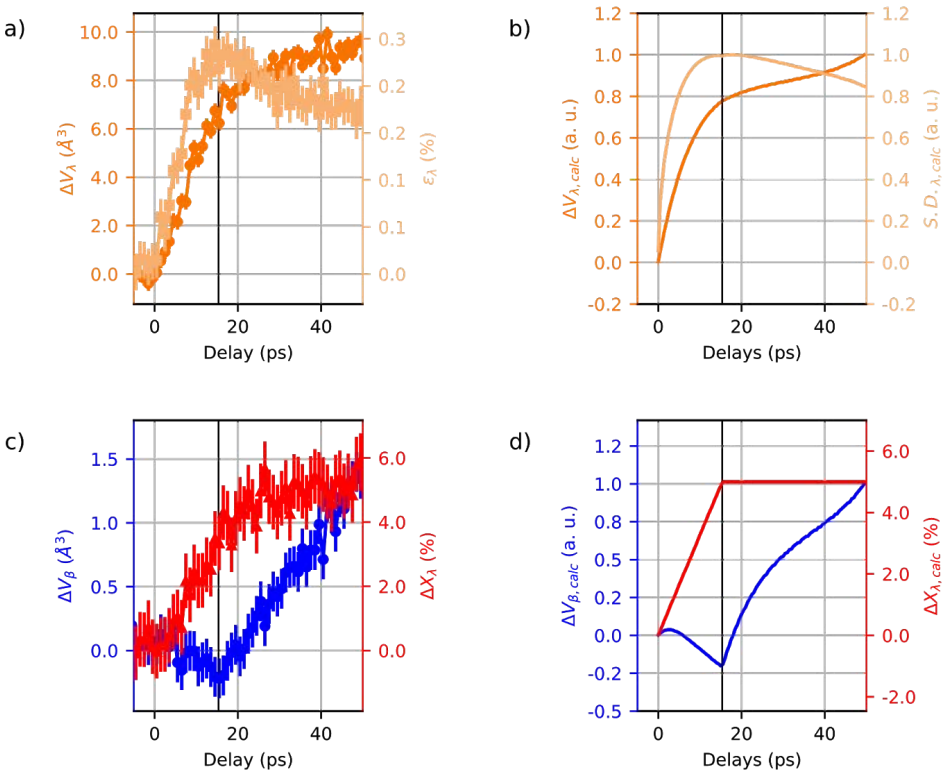


***Figure 4 : Evolution of long range order and phase change on the acoustic time scales:*** **a**) and **c**) Parameters extracted from Rietveld refinement of time resolved XRD data. **a**) Temporal evolution of $\lambda$ - phase unit cell volume ($\Delta V_{\lambda}$ , dark orange, filled circles) and microstrain parameter $\varepsilon_{\lambda}$ (light orange, filled squares). **c**) Temporal evolution of $\beta$ - phase unit cell volume ($\Delta V_{\beta}$ ,blue) and $\lambda$ - phase fraction ($\Delta X_{\lambda}$ , red). Relative changes normalized to the change at 50 ps and errors estimated as described in the Methods section. **b**) and **d**) Simulation with Thomsen model [***Thomsen1986a***] of parameters shown in **a**) and **c**) . All details are given in the SI. **b**) $\lambda$ - crystallites. Calculation of expected evolution of the volume change ($\Delta V_{\lambda,\,calc}$ , dark orange) and microstrain (S. $D._{\lambda,\,calc}$ , light orange) following ultrafast excitation. Parameters of the model are taken as follows: laser penetration depth of $\xi_L$ = 65 nm, sound velocity of $V_s$ = 6.5e3 $m.s^{-1}$; curves normalized to the value at t = 50 ps. **d**) $\beta$ -crystallites. Calculation of expected evolution of the volume change ($\Delta V_{\beta,calc}$ blue) and $\lambda$ - phase fraction ($\Delta X_{\lambda,calc,}$ red) following ultrafast excitation. The corresponding acoustic front propagation time corresponding to $z_S$= 100 nm, $\tau_{PF} = z_S / v_s$) is shown with solid black lines in **a**), **b**),**c**) and **d**).

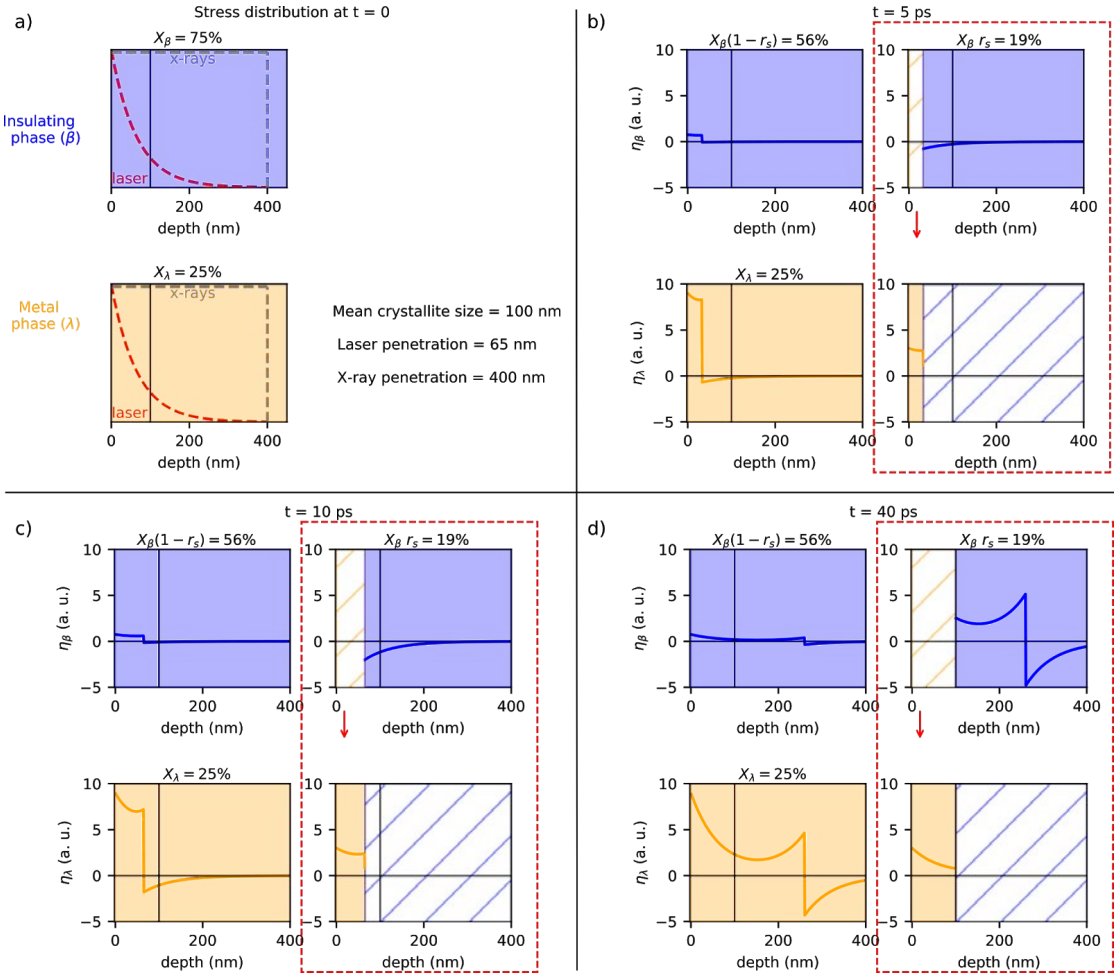


Figure 5 : **Strain wave model with phase transition:** The spatial dependence of the elastic strain at different times (tagged top of each panel), for $\beta$-phase crystalites (in blue) remaining in the initial phase (56%, left side on each panel) and transitioning to $\lambda$ (19%, right side on each panel), $\lambda$-phase crystallites (in orange) remaining in the initial phase (25%, left side on each panel) and the newly formed from $\beta$ (19%, right side on each panel). To further distinguish the strained-transitioning crystalites from those strained-non transitioning, the former situation is contoured on each panel with a red dashed line and red arrow points to the transition direction. The solid vertical line at *z = 100* nm on all panels delimits the phase-transition zone. Semi-infinite 1D medium approximates the real sample and the experimental conditions. a) Initial photo-induced stress following the laser absorption profile (in red). X-ray probe depth is indicated in grey (details given in Fig. S9). The inset recalls the most important values characterizing the experiment. (b) to (d) strain profile $\eta$(z,t) as calculated according to the model described in the main text. For transitioning crystallites (contoured dashed red) the strain due to transition is calculated separately for the $\lambda$- and $\beta$-phase.

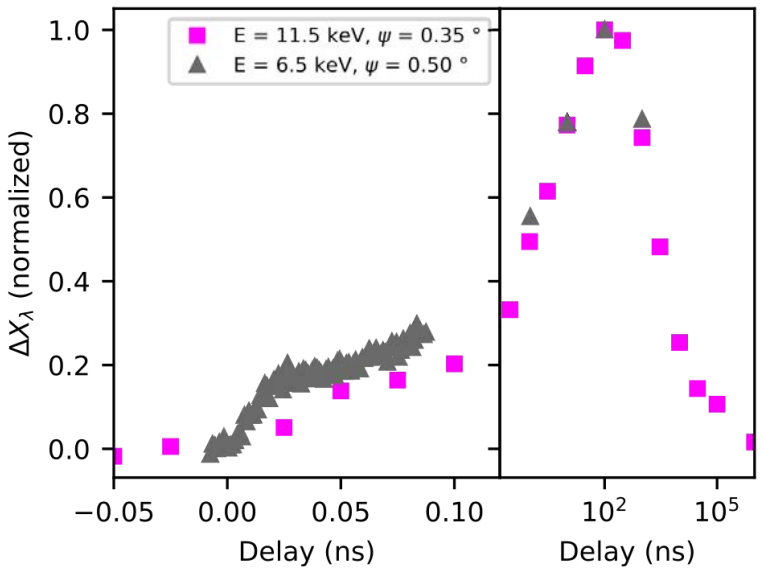


***Figure 6: Thermal propagation in the bulk pellet.*** Multiscale evolution (from ps to ms) of the normalized $\lambda$ fraction ($\Delta X_\lambda$) as extracted from time resolved XRD measurements at the ESRF beamline ID09 (magenta squares). The fraction change is normalized to the maximum value for allowing a direct comparison with the evolution observed at SwissFEL Bernina (grey triangles). Long time delays are presented on a logarithmic time scale.

# References


**Ashara2014** A. Asahara, H. Watanabe, H. Tokoro, S.I. Ohkoshi, T. Suemoto *Ultrafast dynamics of photoinduced semiconductor-to-metal transition in the optical switching nano-oxide Ti3O5*, Phys. Rev. B 90, 014303 (2014) doi 10.1103/PhysRevB.90.014303

**Ashiotis2015** G. Ashiotis, A. Deschildre, Z. Nawaz, J. P. Wright, D. Karkoulis, F. E. Picca and J. Kieffer, *The fast azimuthal integration Python library: pyFAI*, Journal of Applied Crystallography 48, 510 (2015) doi 10.1107/S1600576715004306

**Baldini2019** E. Baldini, A. Dominguez, T. Palmieri, O. Cannelli, A. Rubio, P. Ruello, M. Chergui *Exciton control in a room temperature bulk semiconductor with coherent strain pulses*, Sci. Adv. 5, eeax2937 (2019) doi 10.1126/sciadv.aax2937

**Basov2017** D.N. Basov, R.D. Averitt, D. Hsieh *Towards properties on demand in quantum materials*, Nature Mater. 16, 1077-1088 (2017) doi 10.1038/nmat5017

**Beaud2014** P. Beaud, A. Caviezel, S.O. Mariager, L. Rettig, G. Ingold, C. Dornes, S-W. Huang, J. A. Johnson,M. Radovic, T. Huber, T. Kubacka, A. Ferrer, H.T. Lemke, M. Chollet, D. Zhu, J. M. Glownia, M. Sikorski, A. Robert, H. Wadati, M. Nakamura, M. Kawasaki, Y. Tokura, S.L. Johnson, U. Staub, *A time-dependent order parameter for ultrafast photoinduced phase transitions*, Nature Materials volume 13, 923 (2014) doi 10.1038/nmat4046

**Bertoni2012** R. Bertoni, M. Lorenc, A. Tissot, M. Servol, M.-L. Boillot, and E. Collet, *Femtosecond Spin-State Photoswitching of Molecular Nanocrystals Evidenced by Optical Spectroscopy.* Angew. Chem. Int. Ed., 51: 7485-7489 (2012) doi 10.1002/anie.201202215

**Bertoni2016**, R. Bertoni , M. Lorenc, H. Cailleau , A. Tissot, J. Laisney, M.L. Boillot, L Stoleriu, A. Stancu, C. Enachescu C, E. Collet, *Elastically driven cooperative response of a molecular material impacted by a laser pulse*, Nature Materials 15, 606 (2016) doi 10.1038/nmat4606

**Cammarata2009**, M. Cammarata, F. Ewald, L. Eybert, W. Reichenbach, M. Wulff, P. Anfinrud, F. Schotte, Q. Kong, B. Lindenau, J. Rabiger, S. Polachowski, *Chopper system for single pulse experiments with synchrotron radiation*, Review of Scientific Instruments, 80 015101 (2009) doi 10.1063/1.3036983

**Coelho2018**, A.A. Coelho, *TOPAS and TOPAS-Academic: an optimization program integrating computer algebra and crystallographic objects written in C++*. J. Appl. Cryst., 51, 210 (2018) doi 10.1107/S1600576718000183

**Henke1993** B.L. Henke, E.M. Gullikson, and J.C. Davis. *X-ray interactions: photoabsorption, scattering, transmission, and reflection at E=50-30000 eV, Z=1-92*, Atomic Data and Nuclear Data Tables Vol. 54, 181 (1993) doi 10.1006/adnd.1993.1013

**Fleming2008** G. Fleming and M. Ratner, *Grand challenges in basic energy sciences*, Physics Today 61, 28 (2008); doi 10.1063/1.2963009

**Först2015** M. Först, A.D. Caviglia, R. Scherwitzl, R. Mankowski, P. Zubko, V. Khanna, H. Bromberger, S.B. Wilkins, Y.-D. Chuang, W.S.Lee, W.F. Schlotter, J.J. Turner, G.L. Dakoski, M.P. Minitti, J. Robinson, S.R. Clark, D. Jaksch, J.-M. Triscone, J.P. Hill, S.S. Dhesi, A. Cavalleri, *Spatially resolved ultrafast magnetic dynamics initiated at a complex oxide heterointerface*, Nature Materials 14, 883-889 (2015) doi 10.1038/nmat4341

**Först2017** M. Först, K.R. Beyerlein, R. Mankowski, W. Hu, G. Mattoni, S. Catalano, M. Gibert, O. Yefanov, J.N. Clark, A. Frano, J.M. Glownia, M. Chollet, H. Lemke, B. Moser, S.P. Collins, S.S. Dhesi, A.D. Caviglia, J.-M. Triscone, A. Cavalleri, *Multiple supersonic phase fronts launched at a complex-oxide heterointerface*, Phys. Rev. Lett. 118, 027401 (2017) doi 10.1103/PhysRevLett.118.027401

**Hakoe2017** F. Hakoe, H. Tokoro, S.I. Ohkoshi, *Dielectric and optical constants of λ-$Ti_3O_5$ film measured by spectroscopic ellipsometry*, Materials Letters 188, 8 (2017) doi 10.1016/j.matlet.2016.09.084

**Harmand2013** M. Harmand, R. Coffee, M. R. Bionta, M. Chollet, D. French, D. Zhu, D. M. Fritz, H. T. Lemke, N. Medvedev, B. Ziaja, S. Toleikis, M. Cammarata, *Achieving few-femtosecond time-sorting at hard X-ray free-electron lasers*, Nature Photonics 7, 215 (2013) doi 10.1038/nphoton.2013.11

**Ingold2019** G. Ingold, R. Abela, C. Arrell, Paul Beaud, Pirmin Böhler, Marco Cammarata, Yunpei Deng, Christian Erny, Vincent Esposito, Uwe Flechsig, Rolf Follath, Christoph Hauri, Steven Johnson, Pavle Juranic, Giulia Fulvia Mancini, Roman Mankowsky, Aldo Mozzanica, Roland Alex Oggenfuss, Bruce D. Patterson, Luc Patthey, Bill Pedrini, Jochen Rittmann, Leonardo Sala, Matteo Savoini,c Cristian Svetina, Thierry Zamofing, Serhane Zerdanea and Henrik Till Lemke, *Experimental station Bernina at SwissFEL: condensed matter physics on femtosecond time scales investigated by X-ray diffraction and spectroscopic methods*, Journal of Synchrotron Radiation 26, 874 (2019) doi 10.1107/S160057751900331X

**Iwai2006** S. Iwai, Y. Ishige, S. Tanaka, Y. Okimoto, Y. Tokura, and H. Okamoto, Coherent Control of Charge and Lattice Dynamics in a Photoinduced Neutral-to-Ionic Transition of a Charge-Transfer Compound,Phys. Rev. Lett. 96, 057403 (2006) doi 10.1103/PhysRevLett.96.057403

***Johnson2017*** S. L. Johnson, M. Savoini, P. Beaud, G. Ingold, U. Staub, F. Carbone, L. Castiglioni, M. Hengsberger, and J. Osterwalder , *Watching ultrafast responses of structure and magnetism in condensed matter with momentum-resolved probes*, Structural Dynamics 4, 061506 (2017); doi 10.1063/1.4996176

**Kobayashi2017** K. Kobayashi, M. Taguchi, M. Kobata, K.Tanaka, H. Tokoro, H. Daimon, T. Okane, H.Yamagami, E. Ikenaga, and S.I. Ohkoshi, *Electronic structure and correlation in β-$Ti_3O_5$ and λ-$Ti_3O_5$ studied by hard x-ray photoelectron spectroscopy*, Phys. Rev. B 95, 085133 (2017) doi 10.1103/PhysRevB.95.085133

**Matsuda2015** Osamu Matsuda and Maria Cristina Larciprete and Roberto Li Voti and Oliver B. Wright, Fundamentals of picosecond laser ultrasonics, Ultrasonics 56, 3 - 20 (2015) doi 10.1016/j.ultras.2014.06.005

**Mozzanica2018** A. Mozzanica, M. Andrä, R. Barten, A. Bergamaschi, S. Chiriotti, M. Brückner, R. Dinapoli, E. Fröjdh, D. Greiffenberg, F. Leonarski, C. Lopez-Cuenca, D. Mezza, S. Redford, C. Ruder, B. Schmitt, X. Shi, D. Thattil, G. Tinti, S. Vetter, J. Zhang, *The JUNGFRAU Detector for Applications at Synchrotron Light Sources and XFELs*, Synchrotron Radiation News, 31, 16 (2018) doi 10.1080/08940886.2018.1528429

**Nasu2004** K. Nasu, (ed.) *Photoinduced Phase Transitions* (World Scientific, 2004). doi 10.1142/5476

**Ohkoshi2010** S.I. Ohkoshi, Y. Tsunobuchi, T. Matsuda, K. Hashimoto, A. Namai, F. Hakoe, H. Tokoro *Synthesis of a metal oxide with a room-temperature photoreversible phase transition*, Nature Chemistry 2, 539 (2010) doi 10.1038/nchem.670

**Ohkoshi2019**, S.I. Ohkoshi, H. Tokoro, K. Nakagawa, M. Yoshikiyo, F. Jia, A. Namai, *Low-pressure-responsive heat-storage ceramics for automobiles*, Scientific Reports 9, 13203 (2019) doi 10.1038/s41598-019-49690-0.

***Okimoto2009***, Y. Okimoto, X. Peng, M. Tamura, T. Morita, K. Onda, T. Ishikawa, S. Koshihara, N. Todoroki, T. Kyomen, and M. Itoh, *Ultrasonic Propagation of a Metallic Domain in Pr0.5Ca0.5CoO3 Undergoing a Photoinduced Insulator-Metal Transition*, Phys. Rev. Lett. 103, 027402 (2009), doi 10.1103/PhysRevLett.103.027402

**Onoda1998** M. Onoda, *Phase Transitions of $Ti_3O_5$*, Journal of Solid State Chemistry 136, 67 doi 10.1006/jssc.1997.7657

**Ould2014** A.Ould-Hamouda, H.Tokoro, S.I. Ohkoshi, E.Freysz, *Single-shot time resolved study of the photo-reversible phase transition induced in flakes of $Ti_3O_5$ nanoparticles at room temperature* Chemical Physics Letters 608, 106 (2014) doi 10.1016/j.cplett.2014.05.073

**Rowles2017** M.R. Rowles, C.E. Buckley, *Aberration corrections for non-Bragg–Brentano diffraction geometries*, J. Appl. Cryst. 50, 240 (2017) doi 10.1107/S1600576717000085

**Ruello2015** P. Ruello, V.E. Gusev, Physical mechanisms of coherent acoustic phonons generation by ultrafast laser action, Ultrasonics 56, 21-35 (2015) doi 10.1016/j.ultras.2014.06.004

**Schick2014** D Schick, M. Herzog, A. Bojahr, W. Leitenberger, A. Hertwig, R. Shayduk, M. Bargheer, *Ultrafast lattice response of photoexcited thin films studied by X-ray diffraction*, Structural Dynamics 1, 064501 (2014) doi 10.1063/1.4901228

**Shen2017** Z. Shen, Q. Shi, W. Huang, B. Huang, M. Wang, J. Gao, Y. Shi, T. Lu, *Stabilization of microcrystal λ-Ti3O5 at room temperature by aluminum-ion doping*, Appl. Phys. Lett. **111**, 191902 (2017) doi 10.1063/1.5010684

**Singer2018** Andrej Singer, Juan Gabriel Ramirez, Ilya Valmianski, Devin Cela, Nelson Hua, Roopali Kukreja, James Wingert, Olesya Kovalchuk, James M. Glownia, Marcin Sikorski, Matthieu Chollet, Martin Holt, Ivan K. Schuller, and Oleg G. Shpyrko, *Nonequilibrium Phase Precursors during a Photoexcited Insulator-to-Metal Transition in $V_2O_3$*, Phys. Rev. Lett. 120, 207601 (2018) doi 10.1103/PhysRevLett.120.207601

**Sokolowski2003** K. Sokolowski-Tinten, C. Blome, J. Blums, A. Cavalleri, C. Dietrich, A. Tarasevitch, I. Uschmann, E. Förster, M. Kammler, M. Horn-von-Hoegen, D. von der Linde, *Femtosecond X-ray measurement of coherent lattice vibrations near the Lindemann stability limit*, Nature 422, 287-289 (2003) doi 10.1038/nature01490

**Takahama2020** R. Takahama, T. Ishii, D. Indo, M. Arizono, C. Terakura, Y. Tokura, N. Takeshita, M. Noda, H. Kuwahara, T. Saiki, T. Katsufuji, R. Kajimoto, T. Okuda, *Structural, magnetic, transport, and thermoelectric properties of the pseudobrookite $AlTi_2O_5$–$Ti_3O_5$ system*, Phys. Rev. Materials 4, 074401 (2020) doi 10.1103/PhysRevMaterials.4.074401

**Tasca2017** K.R. Tasca, V. Esposito, G. Lantz, P. Beaud, M. Kubli, M. Savoini, C. Giles, S.L. Johnson *Time-Resolved X-Ray Powder Diffraction Study of Photoinduced Phase Transitions in $Ti_3O_5$* Nanoparticles, Chem Phys Chem. 18, 1385 (2017) doi 10.1002/cphc.201601337

**Tokoro2015** H. Tokoro, M. Yoshikiyo, K. Imoto, A. Namai, T. Nasu, K. Nakagawa, N. Ozaki, F. Hakoe, K. Tanaka, K. Chiba, R. Makiura, K. Prassides, S.I. Ohkoshi, *External stimulation-controllable heat-storage ceramics*, Nature Communications 6, 7037 (2015) doi 10.1038/ncomms8037

**Thomsen1986a**, C. Thomsen, H. T. Grahn, H. J. Maris, and J. Tauc, *Surface generation and detection of phonons by picosecond light pulses*, Phys. Rev. B 34, 4129-4138 (1986) doi 10.1103/PhysRevB.34.4129

**Thomsen1986b**, C. Thomsen, H.T. Grahn, H.J. Maris, J. Tauc, *Picosecond interferometric technique for study of phonons in the Brillouin frequency range*, Optics Communications 60, 55 (1986) doi 10.1016/0030-4018(86)90116-1

**Yonemitsu2008** K. Yonemitsu, K. Nasub, *Theory of photoinduced phase transitions in itinerant electron systems*, Physics Reports 465, 1 (2008) doi 10.1016/j.physrep.2008.04.008

**Wang2019a** X. Wang, A. Jarnac, J. C. Ekström, A. U. J. Bengtsson, F. Dorchies, H. Enquist, A. Jurgilaitis, M. N. Pedersen, C.-M. Tu, M. Wulff, and J. Larsson, *Generation of a large compressive*

*strain wave in graphite by ultrashort-pulse laser irradiation*, Structural Dynamics 6, 024501 (2019) doi 10.1063/1.5089291

**Wang2019b** M. Wang, W. Huang, Z. Shen, J. Gao, Y.iShi, T. Lu, Q. Shi, *Phase evolution and formation of $\lambda$ phase in Ti3O5 induced by magnesium doping*, Journal of Alloys and Compounds **774**, 1189 (2019) doi 10.1016/j.jallcom.2018.09.350

**Zacharias2015** M. Zacharias, A. Rosch, and M. Gars, Critical elasticity at zero and finite temperature, Eur. Phys. J. Special Topics 224, 1021–1040 (2015) doi 10.1140/epjst/e2015-02444-5

**Zeiger1992** H.J. Zeiger, J. Vidal, T.K. Cheng, E.P. Ippen, G. Dresselhaus, M.S. Dresselhaus, *Theory of displacive excitation of coherent phonons*, Phys. Rev. B 45, 768-778 (1992) doi 10.1103/PhysRevB.45.768

**Zhang2014** J Zhang and R.D. Averitt, *Dynamics and Control in Complex Transition Metal Oxides*, Annual Review of Materials Research 44, 19 (2014) doi 10.1146/annurev-matsci-070813-113258

**Zhong2001** Zhenyang Zhong, V. Holý, J. H. Li, J. Kulik, J. Bai, T. D. Golding, S. C. Moss, *X-ray study of antiphase boundaries in the quadruple-period ordered $GaAs_{0.87}Sb_{0.13}$ alloy*, Journal of Applied Physics **90**, 644 (2001) doi 10.1063/1.1379056

# Supplementary Figures

## Optical conductivity calculations

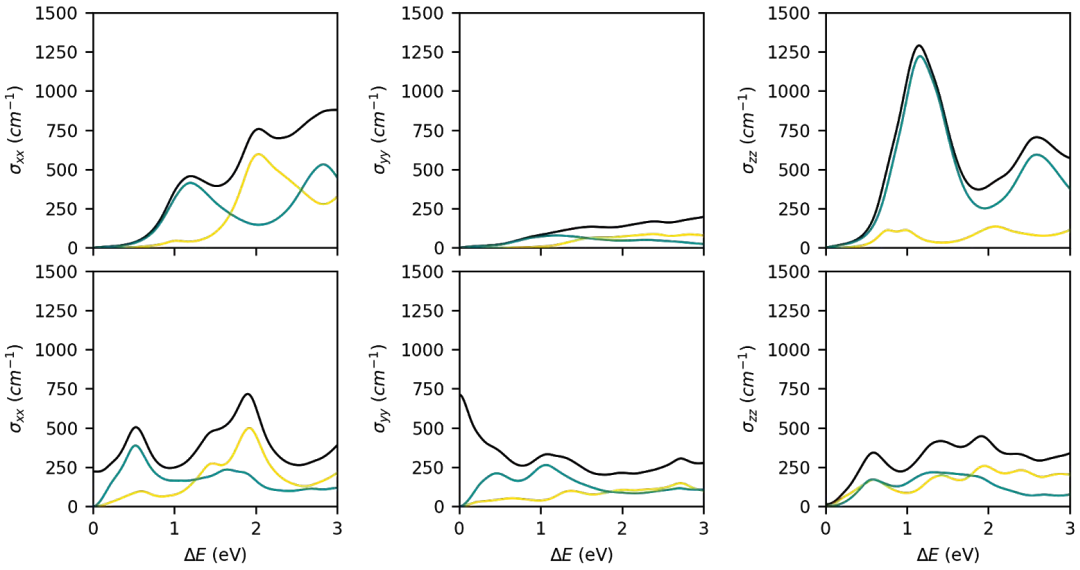


**Figure S1**: Diagonal contributions of the optical conductivity tensor for the □- (top) and λ- (bottom) phases of $Ti_3O_5$, calculated along the x, y, z direction of the primitive unit cell. Total calculated conductivity in black; Yellow (blue) curve represents the contribution arising from the band at 1.1 eV (0.3 eV) below Fermi level.

## Surface Morphology

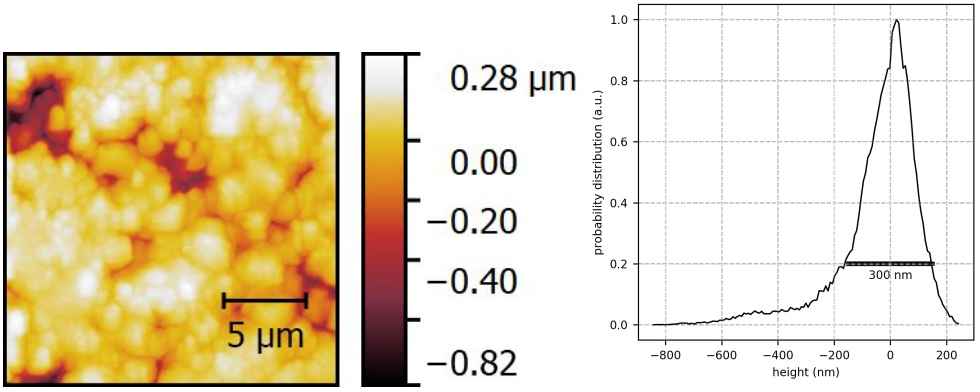


**Figure S2** : 20 x 20 $um^2$ AFM height image of $Ti_3O_5$ pellet surface revealing the surface roughness with typical peak to valley amplitude around 1 µm. Such roughness limits the surface sensitivity of the X-ray experiments as discussed in the Methods. Measurement on the very same pellet that was used for the SwissFEL experiment.

## Angle dependent penetration depth for a perfect surface

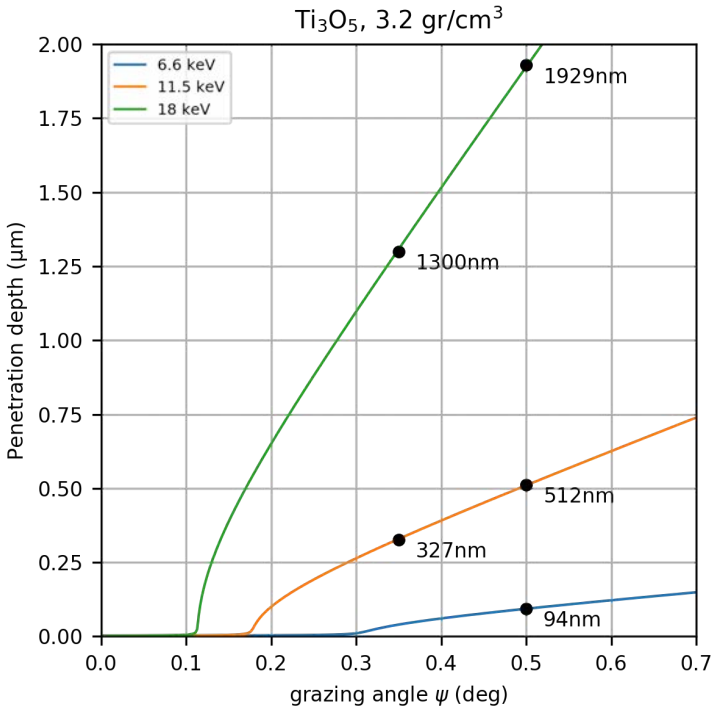


**Figure S3**: Dependence of the X-ray penetration depth as a function of photon energy and grazing angle, calculated using the [**Henke1993**]; The density for the $Ti_3O_5$ was set to the one measured by X-ray absorption on the pellets (3.2 g/cm$^3$). Black circles show the conditions reported in Fig. S4 (right panel).

## Long time scale dynamics

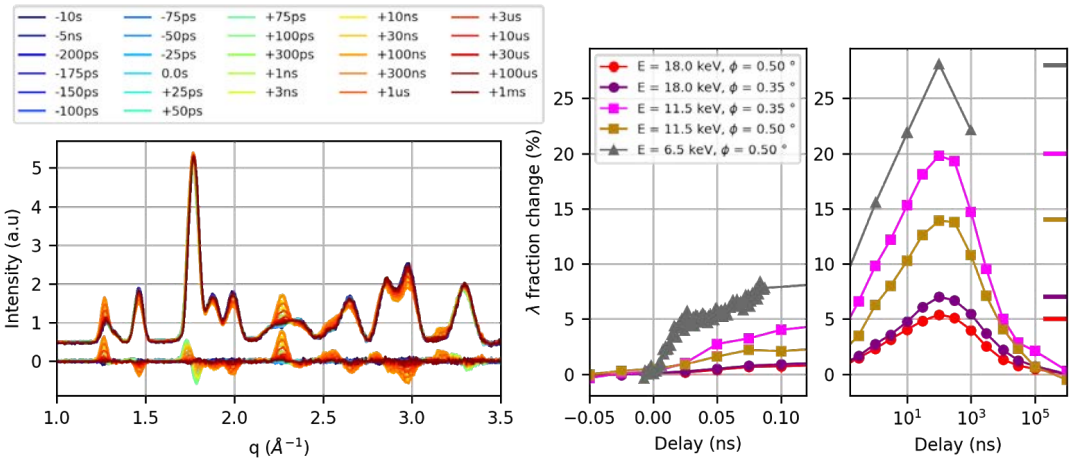


**Figure S4**: Evolution of the $\lambda$ - phase fraction from ps to ms time-scales as extracted from TR-XRD data measured on beamline ID09 at ESRF. Right panel) Effect of x-ray probe energy and incidence angle at fixed pump power density (1.84 mJ/mm$^2$). Data emphasise decreased X-ray penetration into pellets at smaller incidence angles or x-ray photon energy; the reduction of probed depth results into higher $\lambda$ - phase fraction as described in S9. The Swissfel data are also shown for comparison (grey triangles). The short horizontal lines on the right axis represent the expected fraction of photoinduced $\lambda$ phase, calculated according to the procedure described in the SI paragraph "Probed Penetration Depth for $Ti_3O_5$ pellet and switching efficiency"; colours are matched with data. Left panel) Typical time-resolved absolute and differential patterns measured at ID09 (x-ray energy = 11.5 keV, power density = 1.84 mJ/mm$^2$) The larger beamsize results in longer footprint and reduced q-resolution preventing a full Rietveld refinement of the ESRF data.

## Rietveld refinement

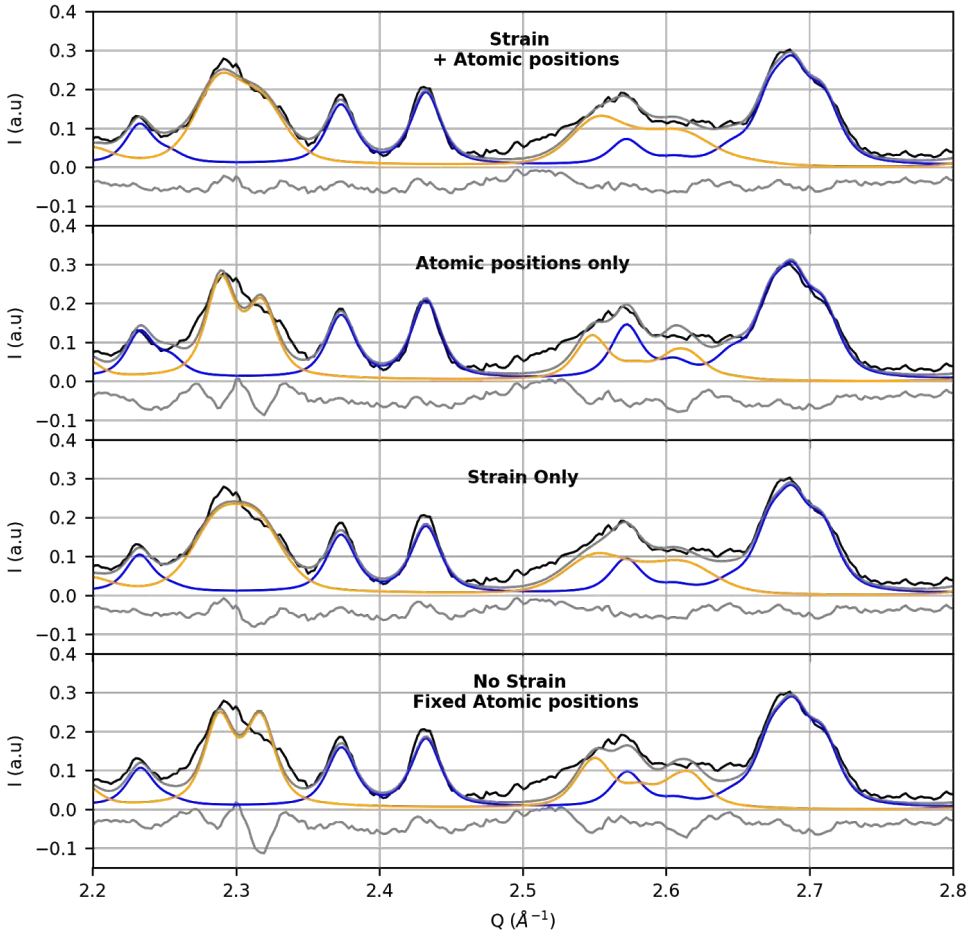


**Figure S5**: Comparison between different sets of refined parameters, for a diffraction pattern at t = 7.5 ps. In all sets, unit cell parameters a, b, c, $\phi$ are refined. Experimental patterns are shown in black, refined patterns in grey, contributions of $\beta$- and $\lambda$ - phase in blue and orange respectively, residual values in grey. From bottom to top: atomic positions fixed and microstrain not considered, microstrain refined, only atomic positions refined, atomic positions and microstrain refined.

## Diffuse scattering measured of single crystals

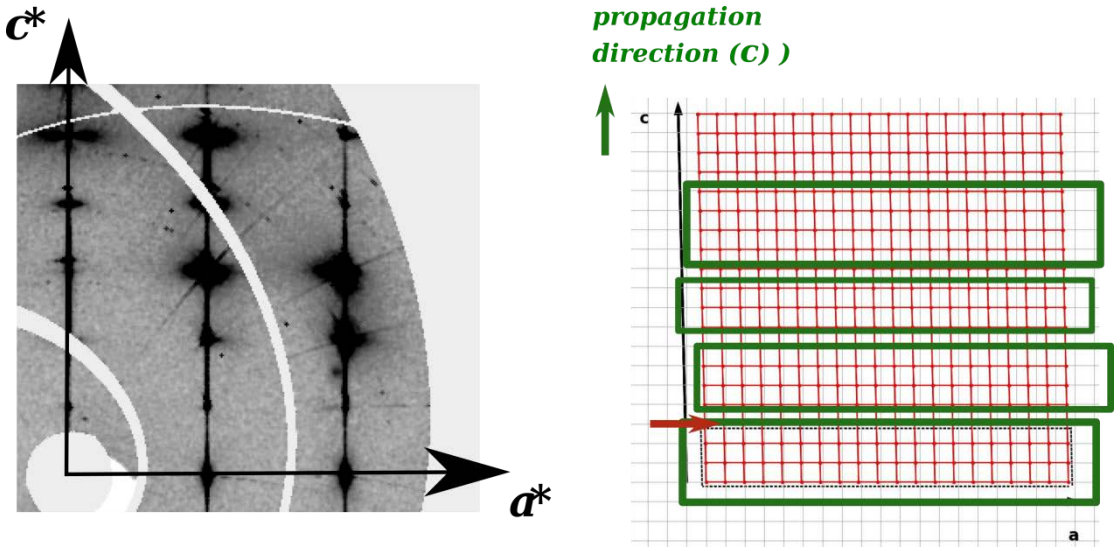


**Figure S6**: left : (***a****, ***c****) reciprocal plane reconstructed from X-ray diffraction measurements at room temperature on $Ti_3O_5$ single crystals (360° rotation, 0.1° per images, shutterless mode). Measurement was performed on ID28 beamline at ESRF on a 4-circle diffractometer equipped with pilatus 2M detector. X-ray photon energy was 26 keV. Contrast is enhanced to highlight strong diffuse scattering lines lying along the ***c**** axis, at integer position along ***a****. These lines indicate stacking faults propagating along ***c***, which might arise from the ferroelastic distortion as shown schematically on the right. The exact coherence length could not be quantified precisely, but the intensity suggests only a few unit cells (green rectangle on the right scheme), compared with analogous observations for inorganic crystals [**Zhong2001**].

## Temperature dependance of Unit cell volumes

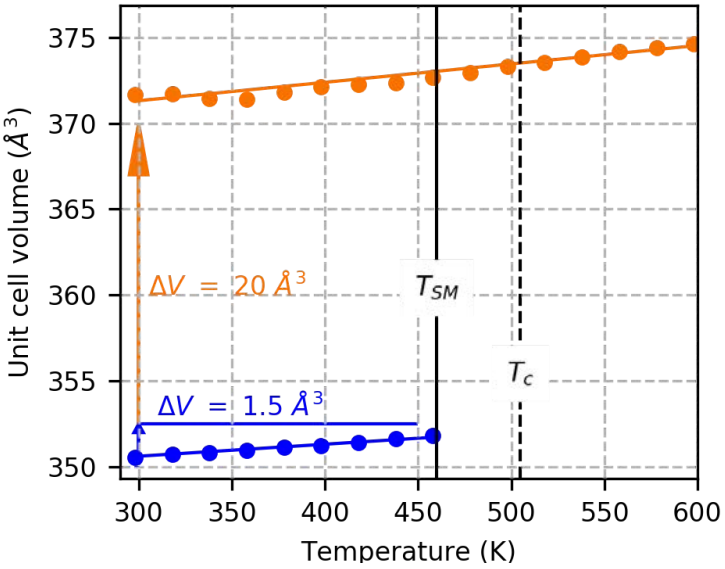


**Figure S7**: X-ray powder diffraction study on $Ti_3O_5$ nanocrystals: change in unit cell volume of the $\beta$ - and $\lambda$ - phase (respectively in blue and orange) revealing the volume jump of 20 $Å^3$ between the two phase and thermal dilation (1,5 $Å^3$ between T = 300 K and transition temperature $T_{SM}$ = 460 K for $\beta$ - phase).

## Model calculations of Strain, Volume change and Microstrain

In the model proposed by Thomsen and further developed by other authors [Matsuda, Ruello] the mechanical stress has the form:

$$\sigma(z,\ t) = 3\ \frac{1-\nu}{1+\nu}\ B\eta(z,t)\ + \sigma_{t=0}(z)\ (eq.\ 1)$$

In the above expression $\sigma$ represents the stress, $\nu$ the Poisson ratio, B the bulk modulus, $\eta$ the strain, z the distance from the surface. The initial stress $\sigma_{t=0}(z)$ depends on the electron-photon interaction and might include different contributions.

In the case of a metal, the original model assumes that stress is set up by lattice heating and takes the form:

$\sigma_T(z) = -\ Bb_l\Delta T(z)$ for a "thermal " distribution

where $b_l$ is the linear expansion coefficient.

In the case of semiconductors, the creation of electron-hole results in a more complex contribution, separated by Thomsen as electronic (depending on deformation potential [ref Matsuda]) and phononic (Thermal phonon, depending on excess energy $E_{h\nu}$-$E_g$). :

$\sigma^e_{ij}(z) = -B\frac{dE_g}{dP}\delta_{ij}\delta n_e(z)$ electron-hole contribution

$\sigma^p_{ij}(z) = -B\frac{3b_l}{C}(E-E_g)\delta_{ij}\delta n_e(z)$ phononic contribution due to "thermal" electron-phonon relaxation within conduction band; notations taken from [***Thomsen1986***].

In our case we assume that the electron-phonon coupling favours dimers rotation that seeds the phase transition, referred to in the text as local precursors. The density of local precursors is however expected to depend on the excitation density ($\delta n_e(z)$). In either case the excitation density (here $\delta n_e(z),$ or $\Delta T(z)$) , and thus the initial stress, will follow the exponential profile of the laser penetration:

$Ae^{-z/\xi}$, where $\xi$ is the laser penetration depth and A is a constant that depends on the origin of the stress.

With these hypothesis, the strain can be written as:

$\eta_{ph,\,i}(z,\ t) = S_{ph,\,i} \times f(T)$ , $ph = \beta,\ \lambda$

Where $f(T) = \left[e^{-z/\xi}\left(1-\frac{1}{2}e^{-v_s t/\xi}\right)-\frac{1}{2}e^{-|z-v_s t|/\xi}\times sign(z-v_s t)\right]$

The strain and standard deviation are then integrated between $z = 0$ (surface) and $z_p$ =400 nm (estimated penetration depth of the X-rays) (see Fig. 4 b and d in the main text). The following contribution are calculated:

$$\Delta V_{\beta,calc}\ (t) = \frac{1}{X_\beta(1-r_s)z_p + X_\beta r_s(z_p - z_m(t))}\left[X_\beta(1-r_s)\int_{z=0}^{z_P} S_{\beta,T}f(t,z)dz\ + X_\beta r_s\int_{z_m(t)}^{z_P} S_{\beta,PT}f(t,z)dz\right]$$

$$\Delta V_{\lambda,calc}\ (t) = \frac{1}{X_\lambda z_p + X_\beta r_s\ z_m(t)}\left[X_\lambda\int_{z=0}^{z_P} S_{\lambda,T}f(t,z)dz\ +\ X_\beta r_s\int_{z=0}^{z_m(t)} S_{\lambda,PT}f(t,z)dz\right]$$

$$S.D.^{\lambda}(t) = \sqrt{\frac{1}{z_p + (z_p - z_m(t))}\left[ X_{\lambda} \int_{z=0}^{z_p} \left( S_{\lambda,T} f(t,z) - \overline{S_{\lambda,T} f(t,z)} \right) dz + X_{\beta} r_s \int_{z_m(t)}^{z_p} \left( S_{\lambda,PT} f(t,z) - \overline{S_{\lambda,PT} f(t,z)} \right) dz \right]}$$

$$\Delta X_{\lambda,\,calc}(t) = X_{\beta} r_s \times z_m(t) / z_p$$

$z_m(t) = v_L t$ if t < $\tau_{PF}$

$z_m(t) = v_L \tau_{PF}$ if t> $\tau_{PF}$

$v_L \tau_{PF}$ = 100 nm

$Z_p$ = 400 nm the penetration of x-ray

$X_{\beta} r_s$ = 19 % transformed beta to lambda percentage at $\tau_{PF}$ (see Fig S9), $X_{\beta}(1 - r_s)$= 56% untransformed beta percentage, $X_{\lambda}$ = 25 % initial lambda percentage

## Picosecond Interferometry measurement

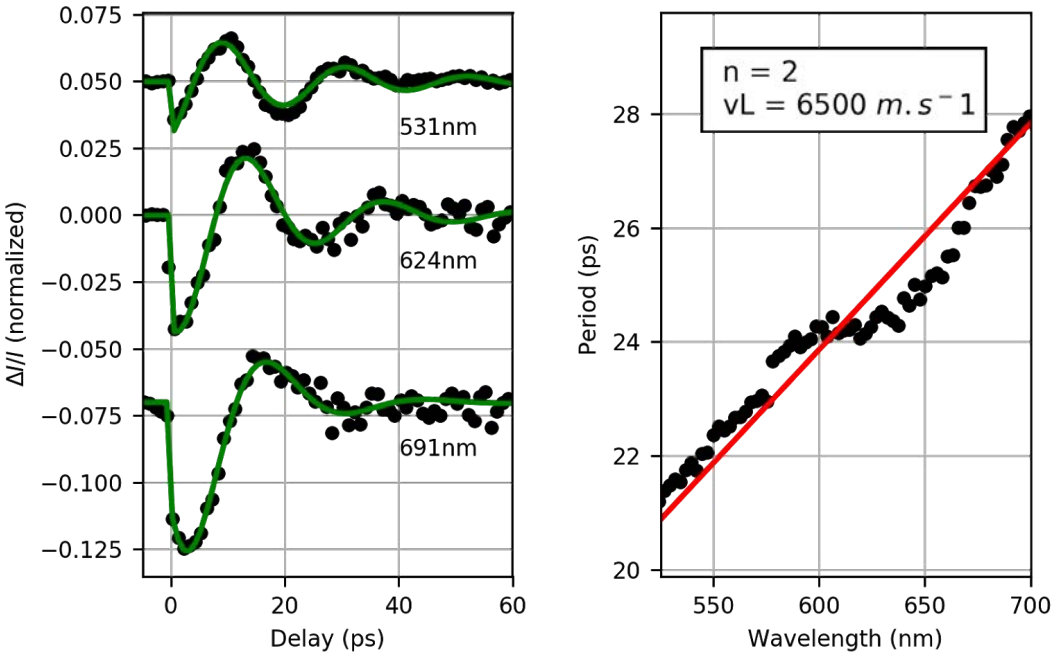


**Figure S8**: Time resolved reflectivity measured on $Ti_3O_5$ single crystal with visible pump / white light probe setup at IPR , pump set to 1.55 eV. Left: oscillatory part of the time dependent reflectivity for selected wavelengths of white light probe illustrating oscillation period dependence on wavelength. Right: oscillation period extracted from data refinement. The linear dependence of period was refined following the model proposed in [**Thomsen1986b**]. Extracted periods are in agreement with those previously reported for a pellet sample [**Asahara2014**], and with real part of optical index from [**Hakoe2017**], they yield sound velocity of 6.5e3 $m.s^{-1}$.

## Probed Penetration Depth for $Ti_3O_5$ pellet and switching efficiency

This section aims at obtaining the switching efficiency from the experimentally determined one. The latter one is influenced by the X-ray penetration depth. For ideal surfaces, the X-ray penetration depth can be calculated using tabulated values [**Henke1993**] as implemented using the CXRO website http://henke.lbl.gov/optical_constants/atten2.html. The results for few X-ray photon energies and angles are given in Fig. S3. For sufficiently low angles total external reflection results in an extremely small penetration depth (few nm). The calculated values for the X-ray photon energies and grazing angles shown in Fig. S4 are given in Fig. S3. They range from 92 nm (SwissFEL experiment, 6.6 keV, $\psi$ = 0.5°) to 1.93 µm (ESRF experiment, 18 keV, $\psi$ = 0.5°). The pellet granularity also determines the effective probed depth. The pellets have a typically roughness of 300 nm (Fig. S2). The combined effect of the roughness and ideal penetration depth results in what we call "effective penetration depth" ($z_p$ in the equations below). Since the layer converted by the strain wave ($z_s$ = 100 nm) is smaller than the effective penetration depth ($z_p$ > 300 nm) a smaller apparent phototransformed fraction will be observed.

By using a simplified model shown in Fig. S9 we can calculate the apparent fractions as a function of relevant physical parameters. In particular we assume that strain wave propagation and heat diffusion processes transform a finite fraction of the $\beta$ phase, and the respective efficiencies are denoted $r_s$ and $r_h$.

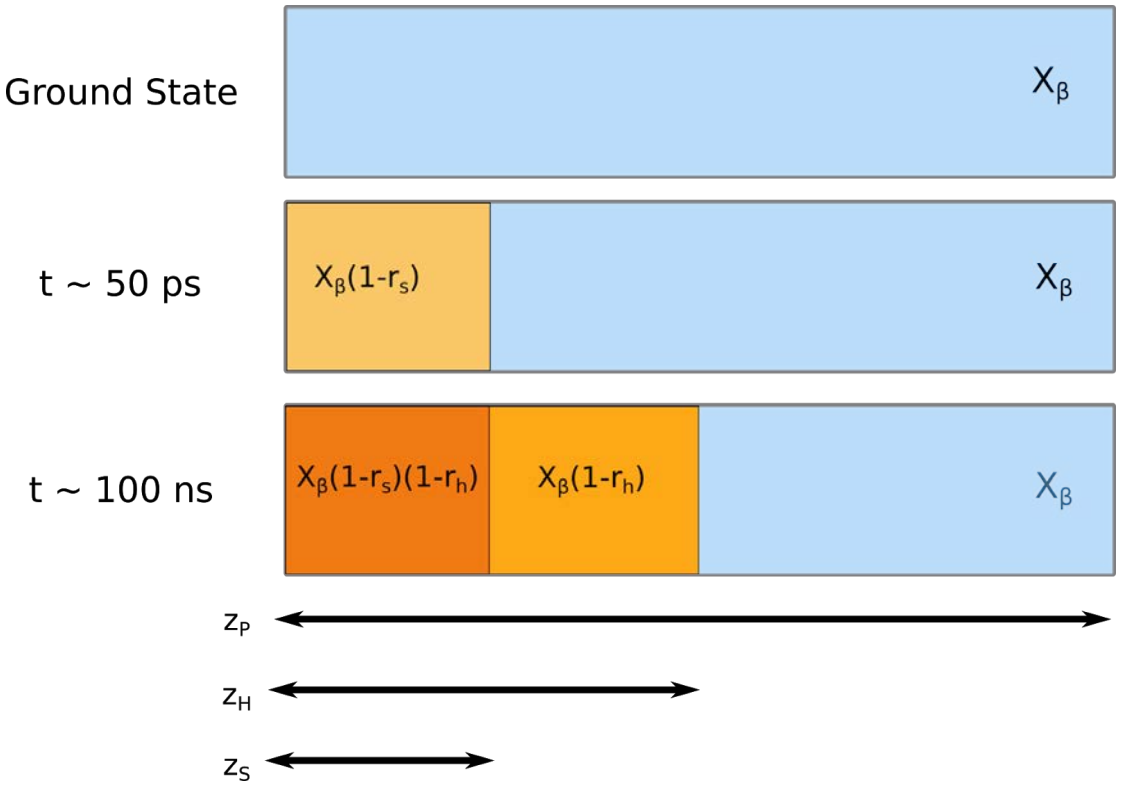


**Figure S9**: Model used to calculate the switching efficiencies. The horizontal axis represents the sample thickness. Without photoexcitation the sample is in a mixture of $\lambda$ and $\beta$ phases indicated respectively as $X_\lambda$ (~0.25) and $X_\beta$ (~0.75). After the strain wave propagation a fraction of the $\beta$ phase will be converted to $\lambda$ with a certain efficiency ($r_s$). At longer time extra switching is observed due to thermal transition. In each region the increase of the $\lambda$ phase is assumed to be equal to the remaining $\beta$ fraction in that region times the efficiency of "heating

switching" ($r_h$). Summing the $\beta$ and $\lambda$ phase fraction at each step and in each region allows us to calculate the expected measured values.

These models results in simple expressions that link the physical parameters to the observed change of fraction at t ≈50 ps and t≈100 ns:

$$\Delta X_\lambda(50\ ps) = X_\beta r_s \frac{z_S}{z_P}$$

$$\Delta X_\lambda(100\ ns) = X_\beta r_s \frac{z_S}{z_P} + X_\beta(1-r_s) r_h \frac{z_S}{z_P} + X_\beta r_h \frac{z_h - z_s}{z_P}$$

With $z_s$,$z_h$,$z_p$ are the strain wave propagation (100 nm), heat diffusion (200 nm) and probed depth respectively. Assuming $r_s$ and $r_h$ to be 0.26 and 0.7, respectively, results in values reported in the table below. The calculated values are obtained from the above expression, the experimental ones from Fig. S4.

| | E (keV) | $\psi$ (°) | $z_P$ (nm) | $\Delta X_\lambda(50\ ps)$ (calc) | $\Delta X_\lambda(50\ ps)$ (exp) | $\Delta X_\lambda(100\ ns)$ (calc) | $\Delta X_\lambda(100\ ns)$ (exp) |
|---|---|---|---|---|---|---|---|
| SwissFEL | 6.6 | 0.5 | 394 | 0.048 | 0.05 | 0.27 | 0.28 |
| ESRF | 11.5 | 0.35 | 627 | 0.030 | 0.03 | 0.17 | 0.20 |
| | 11.5 | 0.50 | 812 | 0.023 | 0.025 | 0.13 | 0.14 |
| | 18.0 | 0.35 | 1600 | 0.011 | 0.01 | 0.07 | 0.07 |
| | 18.0 | 0.50 | 2229 | 0.008 | 0.01 | 0.05 | 0.05 |

## Size determination

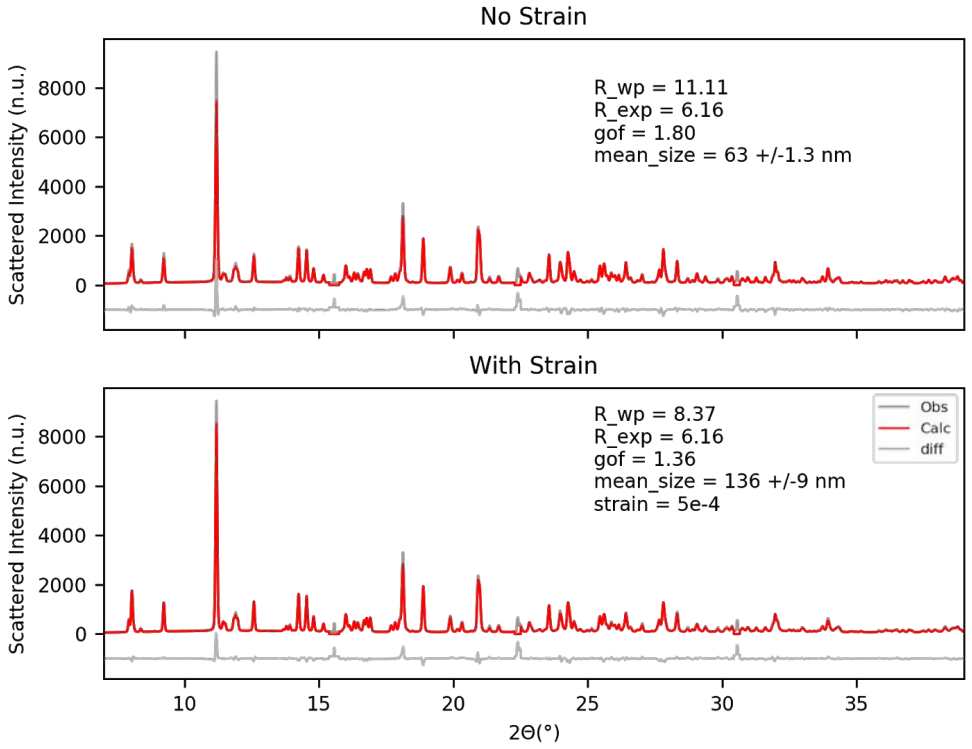


**Figure S10**: Static powder diffraction patterns used for determination of crystallite size of $Ti_3O_5$ powder discussed in the main text. Measurements were performed at ESRF, ID28 beamline, using a 2D pilatus 2M detector. The measurements were performed in transmission geometry with a 10 µm diameter capillary. 45 images were recorded in shutterless mode, with 1° rotation step per image. The X-ray energy was 18 keV, and sample - detector distance set to 250 mm. Rietvelt refinements were performed using Topas software [***Coelho2018***]. Instrumental broadening was determined based on measurement of Lanthanum hexaboride standart [NIST - SRM660a]. Size and strain broadening were refined using the approach defined in ***Balzar2000*** and ***Bazar2004*** and implemented in Topas [***Coelho2018***]. They were constrained to same value for - and $\lambda$ - phase. As described in this article, the size is strongly affected by the consideration of an extra strain broadening. So both cases were considered to estimate the mean size and uncertainty (see upper and lower panels). The mean size is estimated as the average of these two results, namely 100 nm +/- 40 nm.

**Balzar2004** D. Balzar, N. Audebrand, M. R. Daymond, A. Fitch, A. Hewat, J. I.Langford, A. Le Bail, D. Loue, O. Masson, C. N. McCowan, N. C. Popa, P. W. Stephens and B. H. Toby, Size–strain line-broadening analysis of the ceria round-robin sample, J. Appl. Cryst. 37, 911–924 (2000) doi 10.1107/S0021889804022551

**Balzar2000** D. Balzar, Voigt function model in diffraction-line broadening analysis, in Defect and Microstructure Analysis by Diffraction, ed. by Robert L. Snyder, Jaroslav Fiala, and Hans J. Bunge, Published: 16 March 2000, A International Union of Crystallography Publication, International Union of Crystallography Monographs on Crystallography, ISBN: 9780198501893

# Résumé en français

Dans le manuscrit qui précède, nous présentons tout d'abord l'état de l'art concernant le rôle du volume en tant que paramètre agissant sur la dynamique des transitions de phase (chapitre I). Les méthodes expérimentales utilisées pour accéder à l'information structurale en temps réel sont décrites dans le chapitre II. Enfin, les chapitres III et IV sont dédiés à la présentation de l'étude de transitions de phase photo-induites au sein de deux systèmes bistables subissant un changement de volume : un matériau à transition de spin (chapitre III) et un isolant de Mott (chapitre IV).
Le résumé ci-après présente brièvement la démarche et les résultats principaux de la thèse de doctorat rédigée en anglais dans les pages précédentes.

Dans notre contexte, la transformation photo-induite d'un matériau désigne l'excitation, à l'aide d'une impulsion laser ultra-courte, de ce matériau. Cette impulsion laser de durée femtoseconde excite les électrons du système. Ce changement d'état électronique génère ensuite des mouvements atomiques. Ces déformations structurales induites au niveau local par l'excitation primitive des électrons sont définies comme des effets précurseurs. Selon la nature du système, les effets précurseurs peuvent eux-mêmes se présenter sous différentes formes :

- Par exemple, l'excitation laser peut amener à la population d'orbitales électroniques. Dans le cas de matériaux moléculaires, il est possible de faire commuter l'état de spin de l'atome métallique central de la molécule, d'un état bas-spin (BS) liant vers un état haut spin (HS) anti-liant. Ainsi, le changement d'état de spin est associé au gonflement de la molécule, à travers l'augmentation de la longueur des liaisons entre l'atome métallique et les ligands environnants. Considérant le cas du matériau $[Fe^{III}(3\text{-MeO-SalEen})_2]PF_6$ étudié dans le cadre de cette thèse, la longueur moyenne des liaisons <Fe – ligand> augmente d'environ 7% (Figure 1).

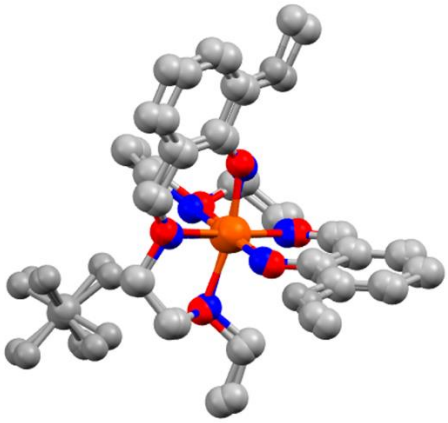

*Figure 1: Unité moléculaire constitutive du $[Fe^{III}(3\text{-MeO-SalEen})_2]PF_6$. L'atome de Fe est représenté en orange. Les atomes des ligands reliés au Fe sont représentés en rouge pour le HS et en bleu pour le BS : les longueurs de liaison sont plus grandes dans le cas du HS. Les ligands et le contre-ion $PF_6^-$ sont représentés en gris.*

- D'autre part, dans le cas d'oxydes de métaux corrélés, la population de bandes électroniques par transfert direct d'électrons peut être associée à un changement de la longueur du dimère métallique. C'est le cas dans le sesquioxide de vanadium $V_2O_3$, où la distance entre les atomes de vanadium constitutifs du dimère diminue lorsque les bandes d'énergie supérieures sont peuplées (Figure 2).

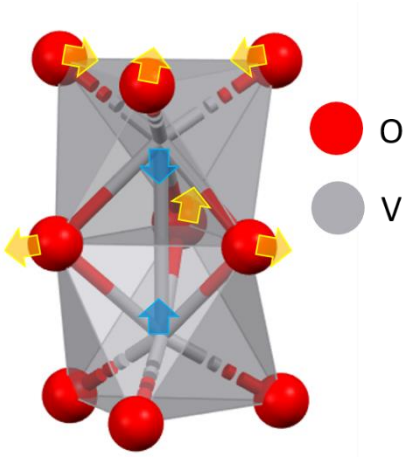


*Figure 2: Unité constitutive de $V_2O_3$. Les flèches en jaune et en bleu représentent les mouvements des atomes d'oxygène et de vanadium respectivement, à la transition isolant-métal.*

Lorsque l'on considère l'ordre à longue distance, les distorsions structurales d'une phase à l'autre se traduisent par la déformation du réseau cristallin. Dans le cas du composé à transition de spin $[Fe^{III}(3\text{-MeO-SalEen})_2]PF_6$, le volume de la maille augmente et les angles changent, induisant une distorsion du réseau, bien que la transition préserve la symétrie cristalline. Ces effets sont clairement visibles lorsque l'on compare le réseau BS et le réseau HS (Figure 3a). Dans le sesquioxide de vanadium, le volume de la maille diminue à la transition de la phase basse température vers la phase haute température. De plus, la transition fait également intervenir une brisure de symétrie. Lors du passage de la phase haute-symétrie-haute-température vers la phase basse-symétrie-basse-température, les déplacements atomiques au sein de la maille sont accompagnés d'une distorsion autour de l'axe cristallin c, ce qui complète la transition depuis la symétrie rhomboédrale vers une symétrie monoclinique (Figure 3b).

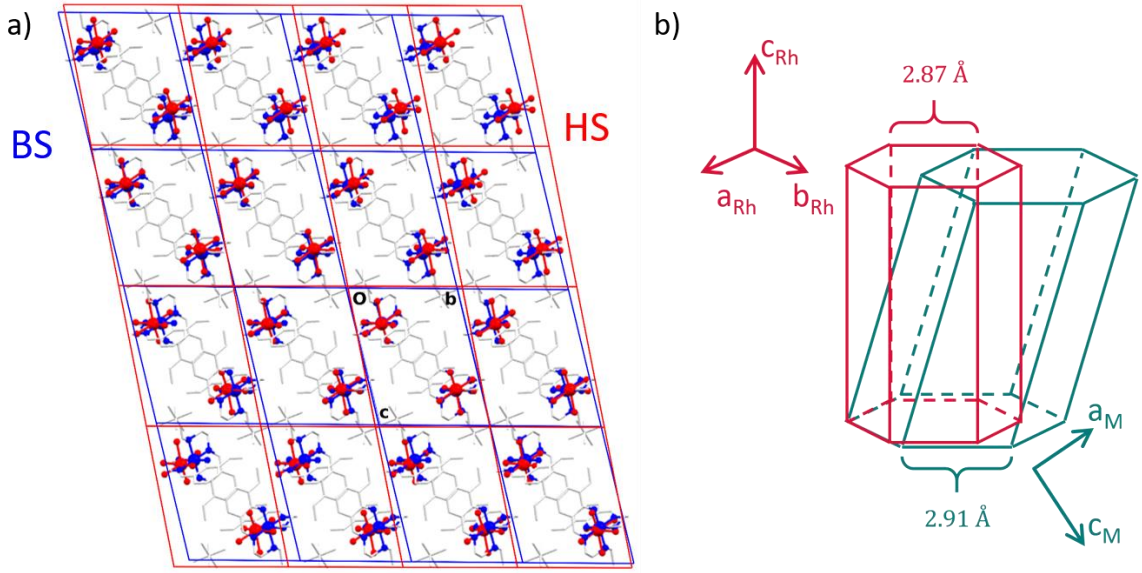


*Figure 3: a) Réseaux BS en bleu et HS en rouge dans $[Fe^{III}(3\text{-MeO-SalEen})_2]PF_6$. La distorsion et le changement de volume associés à la commutation de spin sont clairement visibles. b) Représentation de la distorsion ferroélastique entre la maille haute température de $V_2O_3$ en rouge et la maille basse température en vert.*

La transformation d'un composé à un niveau macroscopique est appelée transition de phase, laquelle correspond à la transformation coopérative d'une phase à une autre. A l'état solide, certaines transitions de phase ne sont associées à aucun changement de symétrie. Ces transitions sont appelées « isostructurales » et se caractérisent par un saut abrupt d'entropie ou de volume

au passage de la ligne de transition dans le diagramme pression-température (P, T). Ce type de transitions peut être décrit en faisant appel à une analogie avec la transition liquide-gaz, au moyen d'un nouveau système de coordonnées (A', H'), fonctions de P et T. Dans cette configuration, on peut définir un paramètre d'ordre généralisé η, lequel caractérise l'évolution à la transition d'une variable interne pertinente et totalement symétrique.

Dans le cas des matériaux à changement de volume, le nouvel état excité doit être stabilisé dans un volume différent de celui de la phase de départ. Cette étape, dans le cadre des transitions de phase photo-induites, est plus lente que les effets précurseurs, étant donné qu'elle implique des mouvements atomiques à longue distance, lesquels se produisent à l'échelle des temps acoustiques. Le changement de volume affecte l'énergie du système et, en sus d'une contribution élastique $\frac{1}{2}$ $^2$, apparaît un terme de couplage $\alpha\varepsilon\eta$ entre phase et volume :

$$( , ) = _0 - ' + \frac{1}{2} ' ^2 + \frac{1}{4} ^4 + \alpha\varepsilon\eta + \frac{1}{2} ^2$$

On démontre aisément que la somme de ces deux contributions est négative, ce qui amène à un gain d'énergie. Ainsi, le changement de volume contribue à la stabilisation de la phase nouvellement formée.

Les deux matériaux présentés plus haut se caractérisent par des changements simultanés de phase et de volume à l'équilibre thermique. Cet effet est clairement visible dans le cas du matériau à transition de spin, lorsque l'on compare la susceptibilité magnétique (reliée à l'état de spin) et le volume de la maille cristalline (Figure 4b). Tous deux montrent un saut brusque accompagné d'une hystérèse autour de la température de transition. Dans le cas de $V_2O_3$, le changement de résistivité témoigne d'une transition d'un état isolant à métallique, caractérisée par une diminution abrupte associée à une hystérèse (Figure 4b). Ce comportement est reproduit par le volume de maille. La présence d'une hystérèse est caractéristique de la bistabilité de ces systèmes, lesquels présentent une région de coexistence de deux phases.

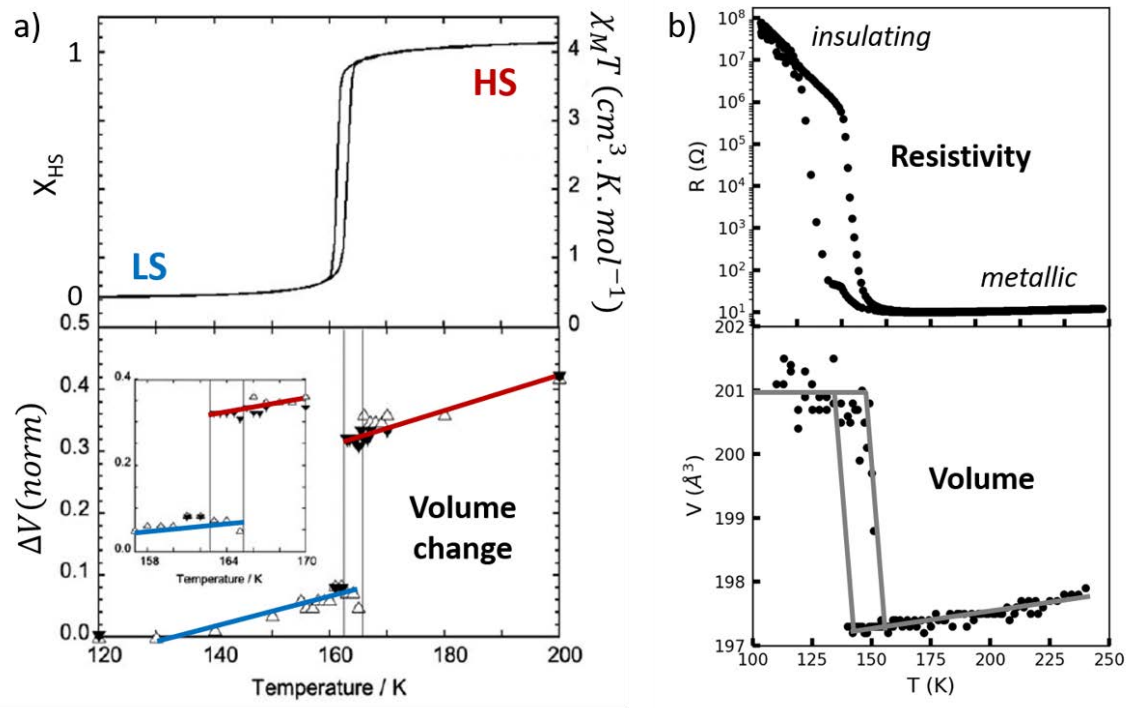


*Figure 4: a) Evolution thermique de la susceptibilité magnétique, reliée à la fraction de HS (en haut), comparée à l'évolution du volume de maille (en bas) dans [$Fe^{III}$(3-MeO-SalEen)$_2$]$PF_6$. Les deux grandeurs montrent un changement simultané et une hystérèse. b) Evolution thermique de la résistivité dans $V_2O_3$ (en haut), comparée à l'évolution du volume de maille. Les deux grandeurs présentent une évolution similaire.*

Le caractère simultané des changements de phase et de volume, ainsi que la possibilité d'un couplage phase-volume, soulèvent la question du rôle du volume dans les transitions de phase photo-induites. Dans le cas extrême, le changement de volume pourrait-il à lui seul induire la transition ? Ou tout du moins, pourrait-il permettre de prolonger le temps de vie de l'état excité ? Les études résolues en temps présentent l'avantage de permettre une certaine sélectivité. Dans notre cas, l'objectif est d'agir temporellement sur le volume en tant que degré de liberté du système, et ainsi d'influencer le paramètre d'ordre à travers le couplage phase-volume.

Afin d'accéder aux dynamiques structurales, nous avons utilisé la diffraction de rayons X résolue en temps. Lorsque l'on évoque des changements structuraux, plusieurs types de déformations peuvent être envisagés : changement de volume de maille local, global ou graduel le long d'une dimension cristalline, ou encore modification des positions atomiques au sein de la maille… Ces modifications, qui se produisent dans l'espace réel, se traduisent par différentes réponses dans l'espace réciproque : déplacement de pics, changements d'intensité relative, changement de largeur des pics… La diffraction de rayons X, en sondant cet espace réciproque, permet d'accéder à l'information quant à ces déformations structurales.

Une transition de phase photo-induite consiste intrinsèquement en un processus multi-échelle : l'échelle de taille sur laquelle on se focalise détermine l'échelle temporelle à interroger. Les effets précurseurs, liés à des mouvements atomiques locaux, se tiennent dans la gamme de la picoseconde, tandis que les déformations macroscopiques, qui impliquent une propagation acoustique, arrivent entre la pico- et la nanoseconde. Ces échelles de temps constituent donc notre gamme temporelle d'intérêt. La dynamique des changements photo-induits est suivie grâce à des mesures pompe-sonde résolues en temps. En effet, l'effet photo-induit étant transitoire, le temps devient une coordonnée, le long de laquelle évoluent les propriétés du système. Le principe des mesures pompe-sonde réside en une excitation du système à l'aide d'une impulsion de pompe, puis par l'interrogation, après un certain délai, de ce système excité par une impulsion de sonde. Cette mesure est ensuite répétée de manière stroboscopique pour différents délais entre pompe et sonde, ce qui permet de reconstruire la dynamique de la propriété du système sondée. Un des avantages majeurs de cette méthode consiste en sa résolution temporelle, laquelle est uniquement dictée par la durée des impulsions de pompe et de sonde et par leur synchronisation. La comparaison du signal transitoire mesuré, avec un signal de référence, apporte des informations au sujet des changements transitoires se produisant dans le système.

La diffraction de rayons X résolue en temps nécessite l'utilisation d'une impulsion X ultra-courte, afin d'accéder changements structuraux photo-induits. De telles impulsions peuvent être fournies par de grands instruments de recherche, comme les sychrotrons et les lasers à électrons libres. Les deux études présentées dans ce manuscrit reposent sur des mesures réalisées au European Synchrotron Radiation Facility (ESRF) à Grenoble. Dans cette infrastructure, les électrons circulant le long d'un rayon de presque 1 km de circonférence génèrent des impulsions X de 70 ps, à un taux de répétition allant de 10 à 900 Hz. Plus spécifiquement, la ligne de lumière ID09, où nous avons mené nos expériences, tire profit de la nature impulsionnelle des rayons X dans le synchrotron et offre un montage pompe-laser sonde-rayons X, avec des impulsions laser et X synchronisées.

Notre hypothèse réside dans le fait que, dans le cadre des transitions de phase photo-induites, le changement de volume peut stabiliser la nouvelle phase. Ainsi, le nouveau volume doit s'établir avant que l'état excité ne relaxe. Ceci nécessite que le système soit suffisamment peu étendu pour que la déformation se propage avant que la relaxation n'ait lieu. Dans notre cas, cette exigence amène à une taille de système entre le nm et le µm. Les échantillons que j'ai étudiés au cours de ma thèse étaient, d'une part des micro-cristaux d'un composé moléculaire à transition de spin ($[Fe^{III}(3\text{-MeO-SalEen})_2]PF_6$), polydispersés dans un film de polymère et déposés sur substrat

vitreux. Ces cristaux ont la forme de plaquettes, dont la dimension longue atteint quelques microns, tandis que la dimension courte se tient dans la gamme des centaines de nm. L'autre types d'échantillons étudiés étaient des films fins de $V_2O_3$ cristallin, dont l'épaisseur allait de 100 à 500 nm, développés sur un substrat de saphir.

Les cristallites constituant un échantillon polycristallin étant orientées de façon aléatoire, la condition de diffraction est toujours vérifiée, quel que soit l'angle azimutal ϕ. La diffraction de rayons X sur ces matériaux génère donc des anneaux de diffraction (Figure 5), que nous avons mesurés à l'aide d'un détecteur à deux dimensions, pour les deux matériaux étudiés. Une fois dépliées et intégrées selon l'angle azimutal, ces images de diffraction en deux dimensions génèrent des schémas de diffraction à une dimension. Bien que constituant une gageure concernant la géométrie expérimentale ainsi que la description des anneaux de diffraction, ce type de diffraction de rayons X présente l'avantage d'accéder à toute l'information à travers une image unique, et donc d'effectuer une analyse quantitative.

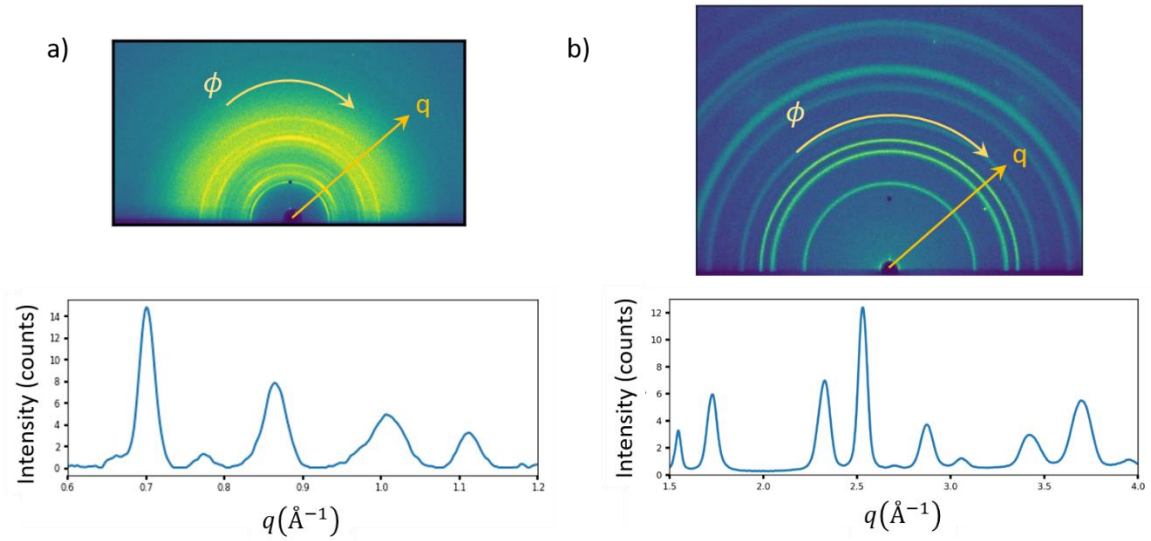


*Figure 5: a) Image de diffraction obtenue à partir de l'échantillon de [$Fe^{III}$(3-MeO-SalEen)$_2$]$PF_6$ (en haut). q représente le vecteur réciproque et φ l'angle azimutal. Le schéma de diffraction 1D est montré en bas, après dépliement de l'image et intégration. b) Image de diffraction obtenue à partir du film de $V_2O_3$ (en haut) et schéma de diffraction calculé à partir de l'image (en bas).*

Lorsque l'on effectue de la diffraction de rayons X résolue en temps sur des échantillons polycristallins, plusieurs types de caractéristiques transitoires sont attendus. La soustraction d'un schéma de référence, à partir d'un schéma de diffraction mesuré à un certain délai, génère un signal appelé « signal différentiel » :

$$ignal\ \ iff\ renti\ \ =\ \ ignal(\ )-\ \ ignal$$

Cette différentielle prend différentes formes, en fonction de la nature des changements structuraux transitoires. Les signatures typiques peuvent être :

- un déplacement de pic, induit par un changement de volume, vers les faibles q pour une augmentation de volume et vers les q élevés pour une diminution de volume. Dans la différentielle, ce changement se traduit par un signal bipolaire (Figure 6a) ;
- un changement des positions atomiques au sein de la maille cristalline, qui conduit à la modification des intensités relatives des pics, induisant un signal unipolaire dans la différentielle (Figure 6b) ;
- un changement de symétrie, lequel peut induire une division ou une fusion de pics, dans le cas d'une distorsion ferroélastique par exemple, conduisant à un signal tripolaire (Figure 6c, d), tandis que le doublement ou la division de maille peut faire disparaître ou apparaître des pics et génère donc un signal unipolaire (Figure 6e, f).

Toutes ces caractéristiques – signaux unipolaires, bipolaires, tripolaires – doivent être recherchées lors de l'analyse du signal différentiel.

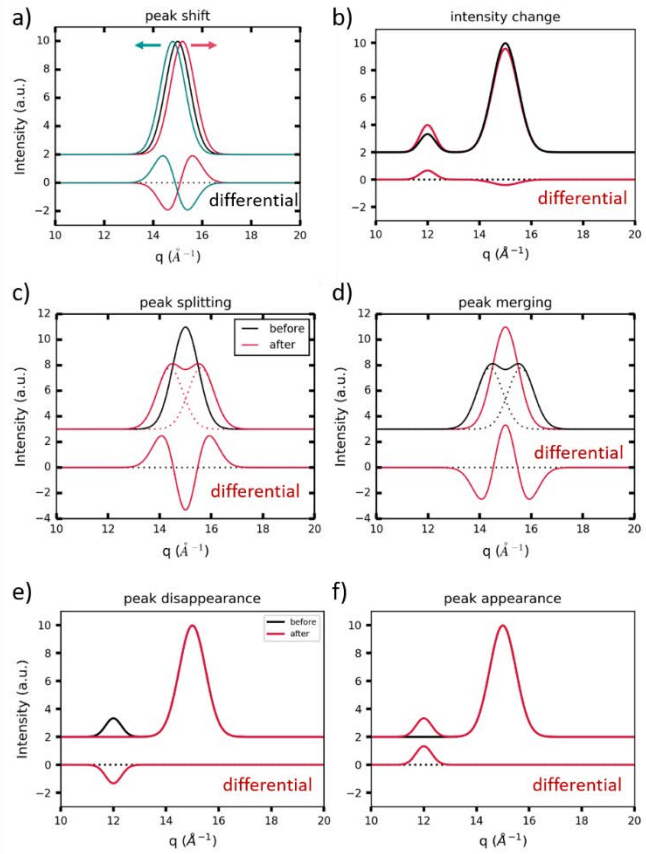


*Figure 6: Le schéma de diffraction initial est tracée en noir pour toutes les sous-figures. a) Simulation d'un décalage de pic et signal différentiel associé, b) simulation d'un changement relatif d'intensité des pics, c) et d) simulation d'une division et d'une fusion de pic, e) et f) simulation de la disparition et de l'apparition d'un pic.*

Ce travail de thèse n'est pas pionnier dans le fait de réaliser de la diffraction X résolue en temps, ni de la diffraction X résolue en temps sur systèmes polycristallins, ou même de la diffraction X sur des matériaux moléculaires à transition de spin ou des systèmes $V_2O_3$. Néanmoins, notre approche combine ces différents aspects, dans l'espoir de porter un nouveau regard sur les transitions de phase photo-induites impliquant un changement de volume dans ce type de systèmes.

La première partie expérimentale de cette thèse consiste en une étude structurale de la commutation de spin photo-induite dans des matériaux moléculaires polycristallins de taille micrométrique.

Des mesures de transmission optique résolues en temps ont été effectuées dans mon groupe sur des cristaux moléculaires à transition de spin, avant le début de ma thèse. La fraction HS en fonction du temps montre une première augmentation (Figure 7a), laquelle correspond au processus bien connu de photo-commutation à l'échelle sub-picoseconde. Ce processus est linéaire en fonction de la densité d'excitation, un photon commutant une molécule. A l'échelle nanoseconde cependant, cette étude a révélé une augmentation non-linéaire de la fraction HS excitée, pour les hautes densités d'excitation. Ce comportement suggère des effets coopératifs d'origine élastique au sein du matériau photo-excité. Ce processus coopératif semble montrer une dépendance en taille, arrivant plus tôt pour des cristaux plus petits (Figure 7b). Ces observations ont soulevé la question de l'influence du volume dans la dynamique de la commutation de spin

photo-induite et motivé des mesures de diffraction X résolue en temps, pour accéder à l'information structurale.

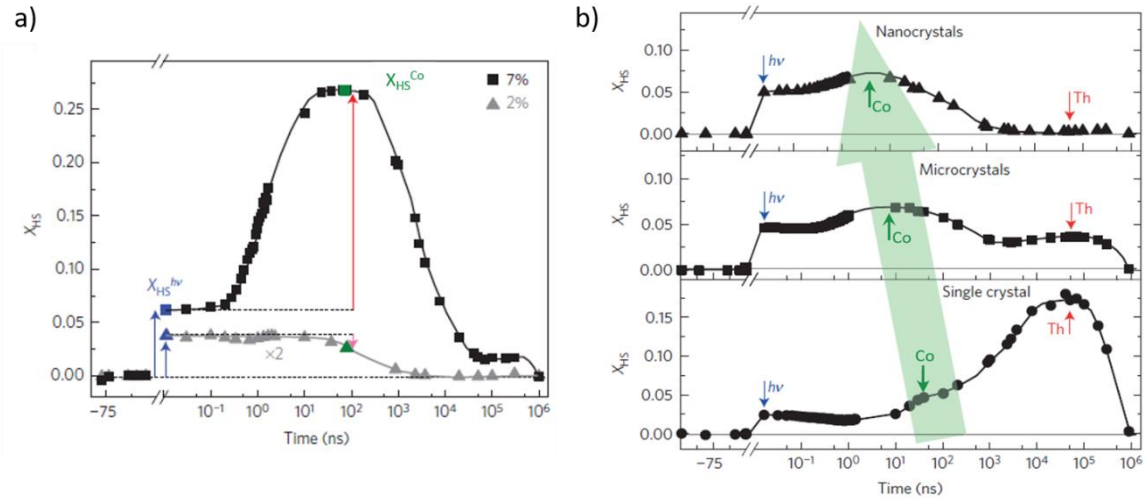


*Figure 7: a) Fraction HS en fonction du temps, à faible (gris) et haute (noir) densité d'excitation. b) Comparaison du temps d'arrivée de l'étape coopérative pour des cristaux de différente taille, avec la même densité d'excitation.*

Ma contribution à cette étude a été, premièrement de paramétrer l'analyse structurale, en effectuant des mesures de diffraction X en fonction de la température sur un mono-cristal (Figure 8a), à l'Institut de Physique de Rennes. Après réduction des données, cette mesure montre que, en sus du saut de volume associé à la commutation de spin à 165 K, le comportement thermique du composé présente une forte expansion du volume dans les deux phases, avec un coefficient d'environ 0.17 $Å^3.K^{-1}$ dans l'état BS et 0.26 $Å^3.K^{-1}$ dans l'état HS (Figure 8b).

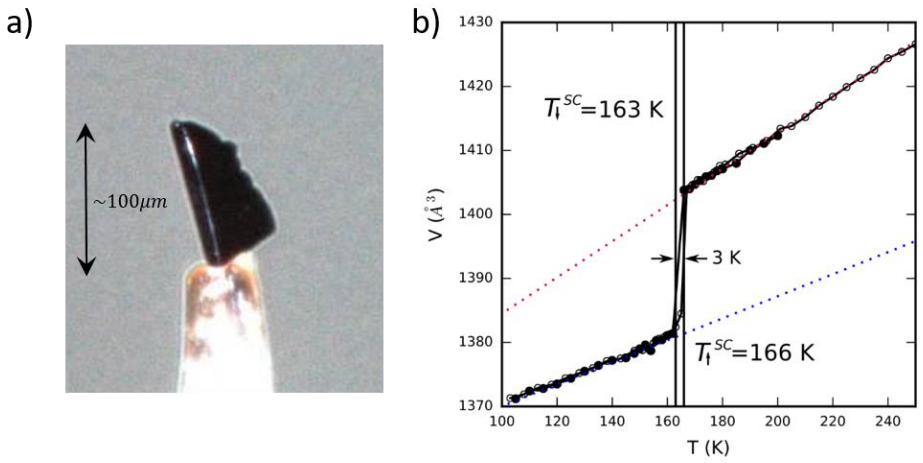


*Figure 8: a)Mono-cristal de $[Fe^{III}(3\text{-MeO-SalEen})_2]PF_6$ sur lequel a été réalisée la diffraction X en température. b) Evolution du volume de maille en fonction de la température en descendant (cercles pleins) et en remontant (cercles vides). Les lignes pointillées matérialisent l'expansion de la phase BS (en bleu) et HS (en rouge).*

Nous avons également extrait l'évolution de chaque paramètre de maille, avec une approximation linéaire, dans les deux phases BS et HS.

Les mesures suivantes ont été réalisées sur les micro-cristaux décrits plus haut, à l'ESRF sur la ligne ID09. Nous avons d'abord effectué de la diffraction X en fonction de la température, entre 293 et 99 K. L'analyse de données à partir des schémas de diffraction obtenus a été élaborée comme suit :

- les paramètres de maille ont été contraints par la température, en utilisant les coefficients extraits de l'étude sur mono-cristal,

- les intensités relatives des pics ont été extraites en utilisant la méthode d'affinement Pawley, à 293 K pour l'état HS et à 99 K pour l'état BS,
- les schémas mesurés aux températures intermédiaires ont été considérés comme une somme de ces intensités relatives, pondérées par leurs fractions respectives.

Cette méthode a permis d'extraire l'évolution en température de la fraction HS et du volume (Figure 9).

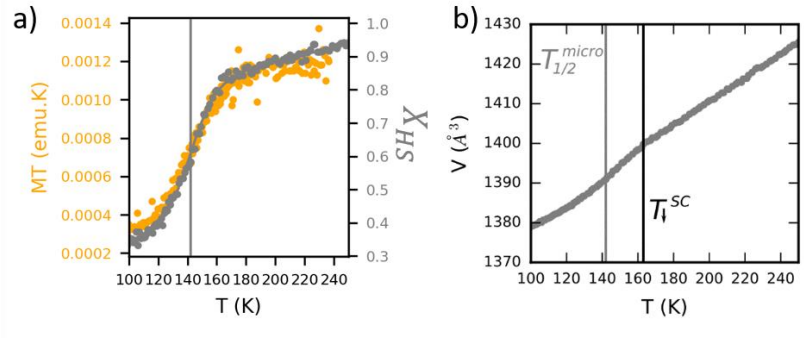


*Figure 9: a) Comparaison de la fraction HS obtenue à partir de l'analyse des données de diffraction X en température sur micro-cristaux (en gris) et des mesures magnétiques (en orange). b) Evolution thermique du volume de maille, extrait de l'analyse des données de diffraction X.*

La comparaison de la fraction HS obtenue avec des mesures magnétiques effectuées sur l'échantillon montre un bon accord entre les deux jeux de données (Figure 9a), ce qui valide notre méthode d'analyse pour la diffraction X sur cet échantillon polycristallin. Des commentaires peuvent être ajoutés au sujet de la température de transition, décalée de -10 K par rapport au mono-cristal. Ceci a déjà été constaté dans des études précédentes et est certainement dû à des effets de réduction de taille. De plus, un gradient de pression effectif dans le polymère étale la transition, comme on le voit sur l'évolution du volume (Figure 9b).

Nous avons ensuite réalisé la diffraction X résolue en temps sur ces micro-cristaux. Les différentielles mesurées à différents délais après photo-excitation montrent toutes un signal bipolaire, correspondant à un décalage vers les faibles q et donc à une augmentation de volume (Figure 10). Cette signature ressemble fortement à celle d'une transition vers l'état HS.

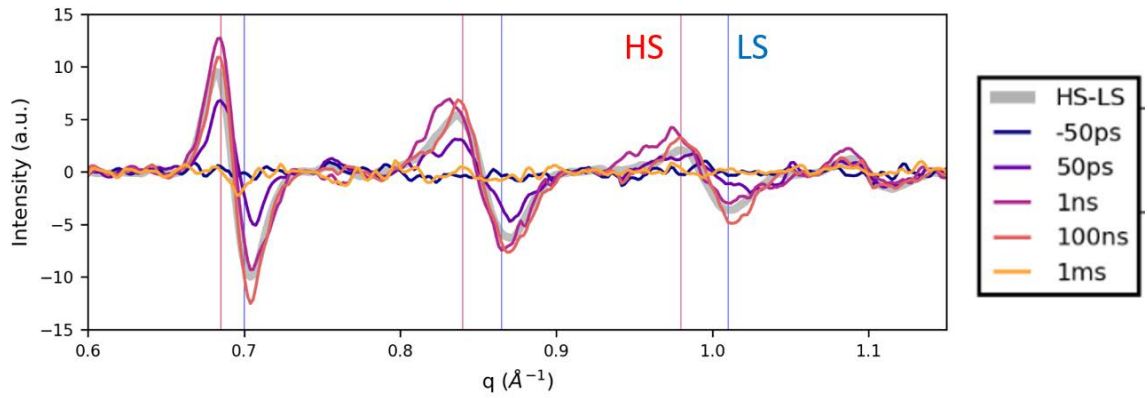


*Figure 10: Signal différentiel mesuré à différents délais après photo-excitation. La diféfrence statique entre schémas de diffraction BS et HS et représentée en gris pour comparaison. Les lignes verticales matérialisent les positions des pics BS (en bleu) et HS (en rouge).*

Afin d'extraire l'information concernant le volume de maille et la fraction HS à partir des schémas résolus en temps, j'ai utilisé la même méthode d'analyse que pour l'étude en température : les intensités relatives des pics ont été fixées et les paramètres de maille ont été supposés suivre l'évolution thermique déterminée auparavant. La température et la fraction HS ont ensuite été

affinées, dans le cas de densités d'excitation faible et forte. Le volume augmente en 300 ps environ (Figure 11a), ce qui est en accord avec l'hypothèse d'une propagation acoustique de la déformation le long de la dimension moyenne du cristal $/ \sim 1.4\,\mu m/4000 \quad . \ ^{-1} \sim 350\,ps$. La fraction HS transitoire obtenue à partir de la diffraction X (Figure 11b) est corroborée par les précédentes mesures de réflectivité, effectuées à des densités d'excitation similaires (Figure 11c), ce qui renforce la validité de notre méthode d'analyse. Enfin, la caractéristique frappante mise en avant par ces résultats est que l'augmentation de volume se produit environ 2 décades temporelles avant la commutation coopérative de l'état de spin.

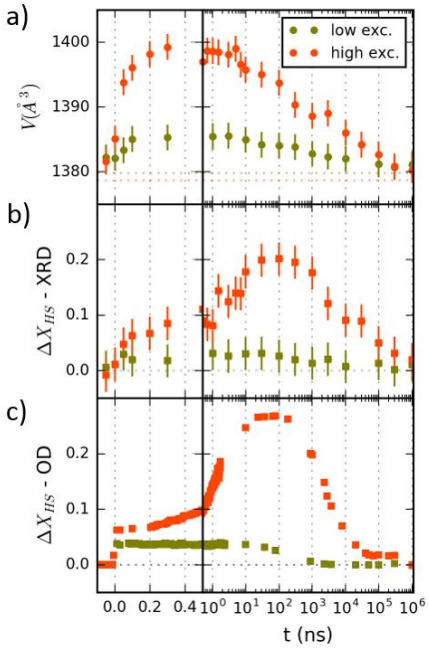


*Figure 11: a) Evolution temporelle du volume de maille moyen à faible (vert) et haute (orange) densités d'excitation, extraite de l'analyse des données de diffraction X résolue en temps. b) Evolution temporelle de la fraction HS extraite de cette même analyse. c) Evolution de la fraction HS précédemment obtenue par transmission optique résolue en temps.*

Une façon habituelle de décrire la commutation coopérative de l'état de spin dans des matériaux moléculaires à changement de volume est le modèle Monte-Carlo appelé « boule et ressort ». Le système est représenté comme un réseau à deux dimensions, composé de boules de différents rayons, représentant des molécules de différents états de spin, connectées par des ressorts, lesquels miment les interactions élastiques au travers du réseau. Le changement d'état de spin d'une molécule induit un déplacement des boules adjacentes, qui en retour exercent des forces de traction ou de poussée sur leurs voisines, favorisant l'état HS ou BS, respectivement (Figure 12).

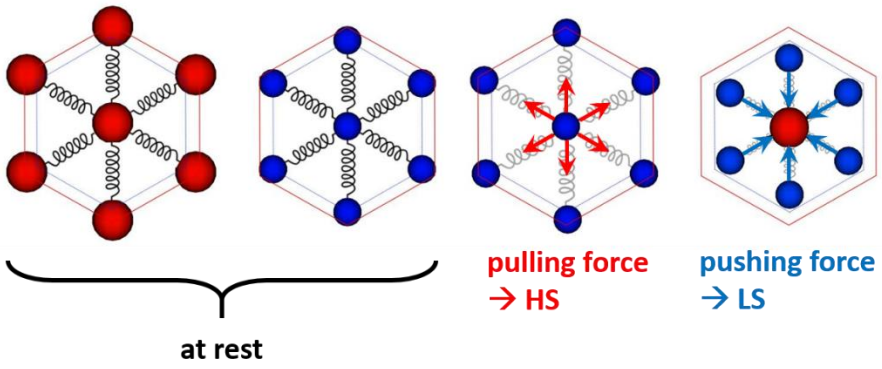


*Figure 12: Schéma du modèle de boules et ressorts. Les molécules BS et HS sont représentées en bleu et rouge, respectivement. Une force de traction (flèches rouges) favorise l'état HS, tandis qu'une compression (flèches bleues) favorise l'état BS.*

Le modèle consiste à résoudre alternativement les équations du mouvement pour chaque boule, la force élastique représentant à la fois les interactions à courte et longue portée, et les probabilités de commutation de spin, définies par la dynamique Arrhenius, considérant deux puits de potentiel harmoniques séparés par une barrière d'énergie $E_a$ :

$$\frac{^2}{^2} = xi - \overline{dt}$$

$$\{\frac{^2}{^2} = yi - \overline{dt}\}$$

$$_{HS\to LS} = \frac{1}{} \; xp\,(\frac{-\quad lng}{2}) \;\; xp\,(-\frac{-}{\quad\quad})$$

$$_{LS\to HS} = \frac{1}{} \; xp\,(-\frac{-\quad Tln}{2}) \;\; xp\,(-\frac{+}{\quad\quad})$$

Ce modèle a été utilisé dans le cadre d'une collaboration avec l'Université de Iasi en Roumanie, pour expliquer les précédents résultats optiques. Cependant, s'il a réussi à décrire l'augmentation non-linéaire de fraction HS après photo-excitation initiale, ce modèle prédisait une augmentation simultanée du volume de maille moyen. Afin de tenir compte de la forte expansion thermique du composé, nous avons interagi avec nos collaborateurs de l'Université de Iasi pour proposer une modification de ce modèle. En effet, des mesures de réflectivité infrarouge résolue en temps, réalisées par nos collaborateurs de l'Université de Poznan, ont montré que le transfert d'énergie depuis les molécules vers le réseau opère en moins de 20 ps après photo-excitation. Nous avons donc adapté le modèle Monte-Carlo, en ajoutant une augmentation initiale de la longueur des ressorts, en raison de ce transfert d'énergie aux échelles de temps courtes. Cette longueur « thermo-élastique » a été choisie pour être du même ordre de grandeur que celle induite par la commutation d'état de spin, ce qui correspond aux observations expérimentales. Cette modification du modèle résulte en un décalage de l'expansion de volume vers les courtes échelles de temps, en comparaison avec le précédent modèle. Ceci reproduit le délai de 2 décades temporelles entre les augmentations de volume et de fraction HS, observé expérimentalement par diffraction X résolue en temps (Figure 13).

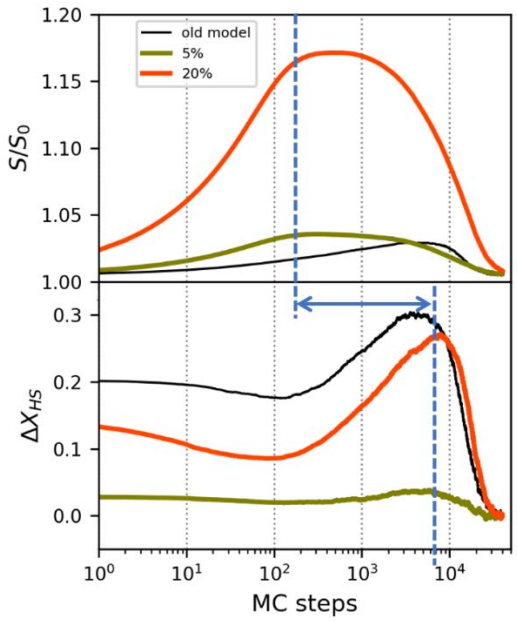


*Figure 13: Résultats des simulations Monte-Carlo à partir du modèle modifié, à faible (vert) et haute (orange) densités d'excitation. L'évolution du volume (en haut) montre bien une expansion, antérieure de 2 décades temporelles environ à l'augmentation de fraction HS (en bas).*

Cette étude révèle un facteur limitant dans le temps d'arrivée de la commutation non-linéaire d'état de spin. Celui-ci semble limité par l'énergie d'activation, avec un temps incompressible nécessaire pour passer la barrière énergétique. Ainsi, la précédente hypothèse commune d'un temps d'arrivée de l'étape coopérative uniquement définie par la taille du cristal ne semble pas être valide. Même si la taille du cristal peut être limitante dans le cas où elle est trop grande, nous avons démontré que la dynamique Arrhenius définit une limite basse absolue pour ce temps d'arrivée. En conclusion, l'augmentation thermo-élastique du volume est inévitable, étant donné qu'une haute énergie de photon est nécessaire pour effectuer la commutation d'état de spin, bien plus haute que la différence d'énergie entre états BS et HS. Une perspective pourrait être de contourner l'excitation électronique et de tester si le seul changement de volume peut induire la commutation de spin. L'idée serait d'apporter de l'énergie uniquement thermo-élastique au cristal, en l'excitant avec une énergie de photon basse, dans l'infrarouge. Ce procédé permettrait de manipuler uniquement des états fondamentaux, sans passer par des états hautement excités. Concernant le design futur des matériaux moléculaires à transition de spin, une perspective envisageable serait, plutôt que de jouer sur la taille des cristaux, de modifier les ligands ou l'atome métallique pour ajuster la barrière énergétique.

La seconde partie expérimentale de cette thèse concerne l'étude structurale d'une transition isolant-métal photo-induite dans un film fin de sesquioxide de vanadium.
$V_2O_3$ est un exemple type d'isolant de Mott. Ce composé peut exister sous trois phases connues, en fonction des conditions extérieures et du dopage chimique (Figure 14). La transition de phase que nous étudions ici s'opère à pression ambiante dans du $V_2O_3$ pur, entre une phase basse température en-dessous de 150 K environ et une phase haute température au-dessus. La phase basse température présente un comportement antiferromagnétique et isolant, tandis que la phase haute température est paramagnétique et métallique. De plus, une distorsion ferroélastique est associée à la transition, la symétrie cristalline passant de rhomboédrale à haute température à monoclinique à basse température. Enfin, le volume de maille diminue d'environ

1.4 % à la transition isolant-métal. Dans ce travail de thèse, nous nous concentrerons sur les aspects électroniques et structuraux, laissant de côté les caractéristiques magnétiques.

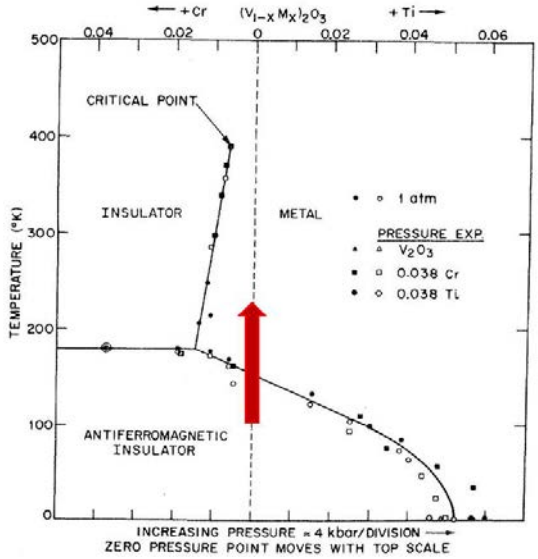


*Figure 14: Diagramme de phase de $V_2O_3$. La transition étudiée dans cette thèse est matérialisée par une flèche rouge.*

Plusieurs études se sont penchées sur la transition de phase photo-induite dans des films de $V_2O_3$. Le point de vue habituel est de décrire le mécanisme de la transition à l'aide du modèle de nucléation-croissance : l'excitation laser génère des effets précurseurs, qui se comportent comme des germes locaux de la transition, puis nucléent et croissent pour atteindre l'échelle macroscopique. Ainsi, Singer et al. ont démontré une pré-orientation des domaines monocliniques à l'échelle picoseconde, sondée par diffusion X résolue en temps. La dynamique ultérieure a été explorée par des mesures de conductivité optique résolue en temps, par Abreu et al., qui suggèrent un modèle de nucléation-croissance pour expliquer leurs observations. Cependant, ce modèle de nucléation-croissance a été développé à l'origine pour décrire des dynamiques plus lentes de transitions de phase thermiques, et n'est donc pas approprié dans le cas d'une croissance de domaines à la vitesse du son, où le système n'a pas le temps de s'adapter à la différence de volume. De plus, la propagation d'onde élastique photo-induite n'est pas considérée dans ces études, tandis que nous pensons qu'elle joue un rôle dans la dynamique de la transition.

Nous avons photo-excité des films polycristallins de V2O3 à l'aide de lumière dans le proche infrarouge, d'énergie de photon 0.8 eV, environ égal au gap optique du matériau. Cette approche limite les effets de chauffage additionnel par redistribution d'énergie dans le réseau, et favorise de purs effets électroniques précurseurs. Des mesures de réflectivité infrarouge résolue en temps ont été conduites par nos collaborateurs de l'Université de Tohoku, au Japon. Les spectres transitoires obtenus, mesurés à différents délais après photo-excitation à 80 K, ressemblent fortement à la différence statique entre spectres à basse et haute températures (Figure 15a). Cette observation représente un indice important de transition isolant-métal photo-induite. La réflectivité transitoire, mesurée à 0.25 eV (dans une région où le spectre est particulièrement affecté par les changements d'état électronique), ne semble montrer aucune variation du taux de conversion en fonction de la densité d'excitation (Figure 15b), ce qui représente un autre argument en faveur d'un mécanisme différent de la nucléation-croissance. Le signal transitoire atteint son maximum autour de quelques dizaines de ps, ce qui est du même ordre de grandeur que la propagation acoustique au travers de l'épaisseur du film $/ \sim 100\, nm/8\, nm.ps^{-1} \sim 12.5\, ps$. Ces mesures ont motivé une étude en diffraction X, pour accéder à la dynamique structurale.

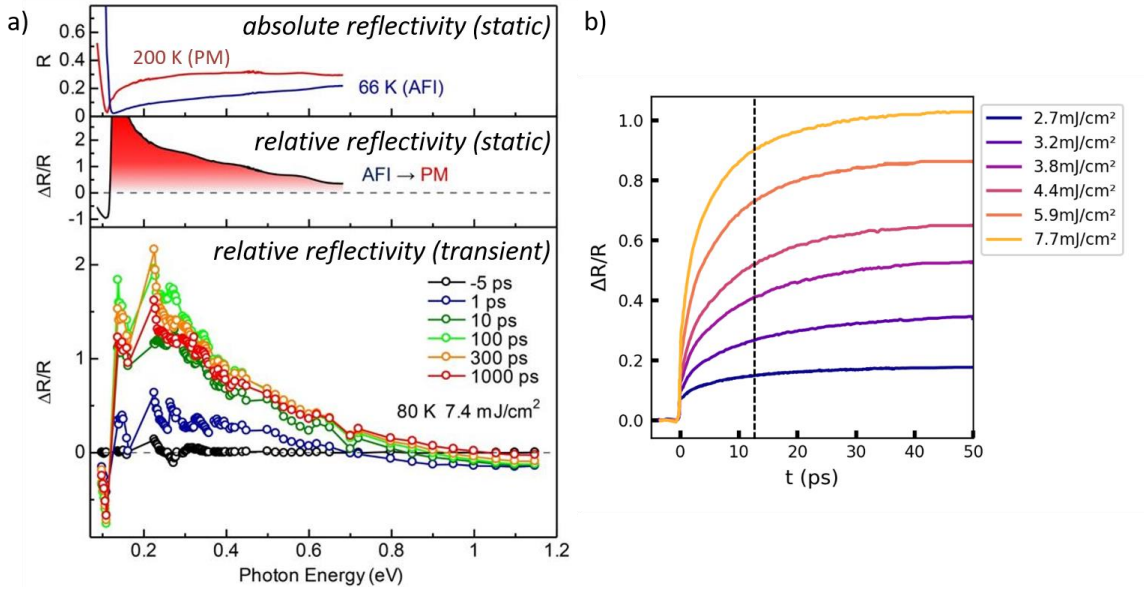


*Figure 15: a) Mesures de réflectivité infrarouge résolue en temps. Les spectres transitoires ressemblent fortement à la différence statique entre phases haute et basse température. b) Réflectivité transitoire mesurée à 0.25 eV. Le taux de transformation ne semble pas dépendre de la densité d'excitation. La ligne verticale noire représente le temps acoustique, nécessaire à la déformation pour se propager au travers de l'épaisseur du film.*

En ce qui concerne les changements structuraux, les schémas de diffraction simulés à partir des structures cristallines connues, montrent que l'on s'attend à un décalage des pics vers les grands q et à une fusion de groupes de pics, au passage de la phase basse à la phase haute température (Figure 16). Ces caractéristiques découlent de la diminution de volume de maille et de la distorsion associées à la transition.

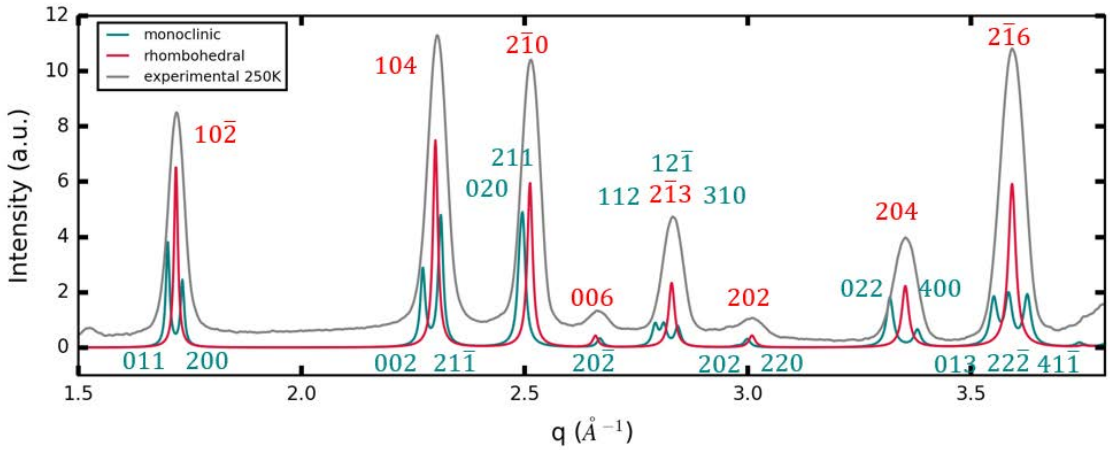


*Figure 16: Schémas de diffraction simulés à partir des structures connues de la phase basse temperature (en vert) et haute temperature (en rouge). Les labels respectifs des pics sont indiqués. Un schéma de diffraction expérimental, mesuré à haute température, est montré en gris pour comparaison : la géométrie expérimentale utilisée induit un élargissement significatif des pics.*

Nous avons effectué des mesures de diffraction X résolue en temps sur la ligne de lumière ID09 à l'ESRF, sur trois films de $V_2O_3$ de différente épaisseur (100 nm, 250 nm, 500 nm), à 95 K. Les résultats étant qualitativement similaires pour les différents films, les données présentées dans ce résumé concernent seulement le film de 250 nm d'épaisseur. Le signal différentiel mesuré à différents délais après photo-excitation reproduit la signature d'une transition de phase de la phase basse vers haute température, avec un signal bipolaire correspondant à un décalage de pics vers les hauts q et un signal tripolaire caractéristique d'une fusion de pics (Figure 17). De plus, la

comparaison de la différence statique entre schémas de diffraction à haute et basse température, avec la différentielle mesurée à 100 ps pour de hautes densités d'excitation montre des ressemblances frappantes (Figure 17). Ces observations sont clairement en faveur d'une transition de phase photo-induite quasi-complète.

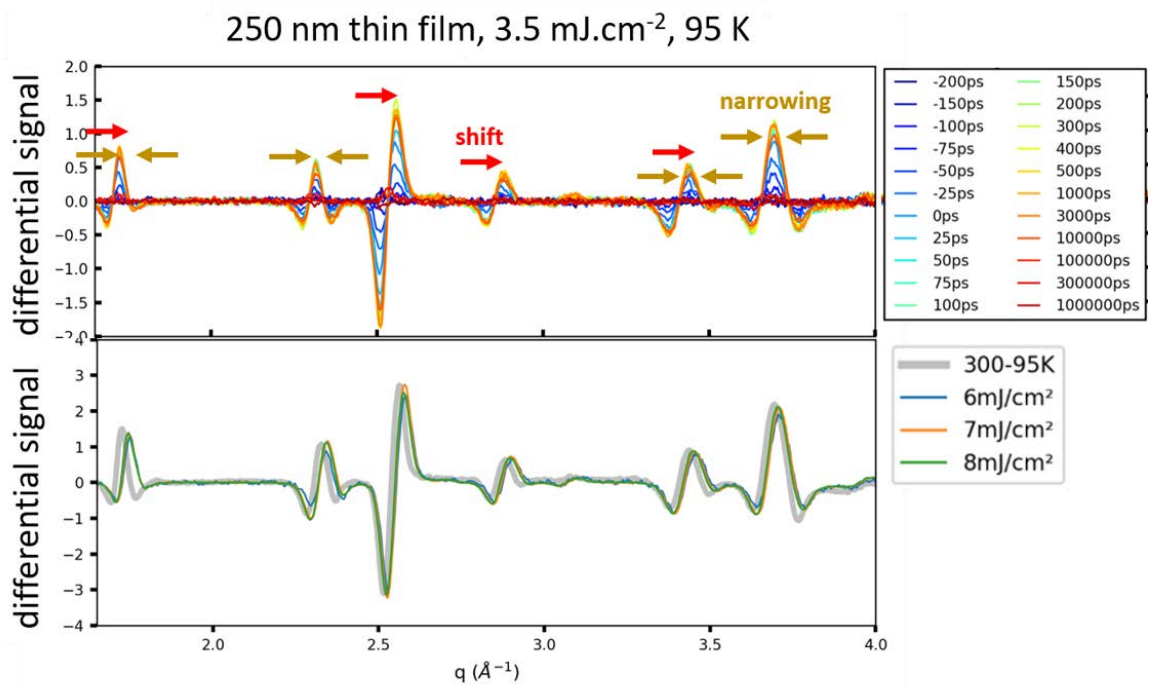


*Figure 17: Signal différentiel mesuré à different délais après photo-excitation (en haut) : le décalage et l'étrécissement des pics sont clairement visibles. La comparaison de la différentielle à 100 ps à hautes densités d'excitation (en bas) avec la différence statique entre phases haute et basse température montre une forte ressemblance.*

Afin d'extraire l'information structurale de ces schémas de diffraction, j'ai réalisé un fit individuel des pics. Ces derniers ont été modélisés par une fonction gaussienne, ce qui a permis d'extraire leur largeur ainsi que leur position. Je me suis concentrée sur deux pics, l'un d'eux étant particulièrement affecté par le décalage dû au changement de volume (pic $\bar{2}10$ dans la phase haute température), l'autre (pic $\bar{2}16$ dans la phase haute température) étant plus sensible au changement de symétrie, avec un étrécissement significatif à la transition.
Quelle que soit la densité d'excitation, les dynamiques de la position et de la largeur des pics sont similaires (Figure 18) : en premier lieu, le volume décroit et la symétrie change, en moins de 100 ps. Puis, le signal atteint un plateau, le long duquel le volume continue légèrement de décroître, tandis que la symétrie ne change plus. Enfin, le volume et la symétrie retrouvent leur état initial.

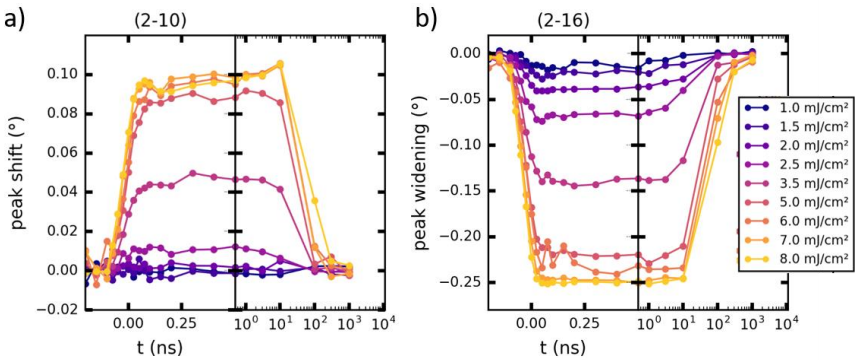


*Figure 18: a) Evolution temporelle du décalage du pic ($\bar{2}10$) pour différentes densités d'excitation. b) Evolution temporelle de la largeur du pic ($\bar{2}16$) pour différentes densités d'excitation.*

Pour interpréter cette dynamique, nous suggérons un scénario en trois étapes : tout d'abord, une phase haute température « chaude » est créée, présentant un volume légèrement plus grand que la phase haute température « froide ». En effet, la différentielle à 100 ps ressemble fortement à celle entre les schémas de diffraction à 95 et 300 K (Figure 19a). Ensuite, cette phase haute température excitée se refroidit, ce qui induit une réduction additionnelle du volume. Cette hypothèse est corroborée par la différentielle entre le début et la fin du plateau, qui ressemble fortement à la signature d'un refroidissement de la phase haute température (Figure 19b). Finalement, le système relaxe vers la phase basse température.

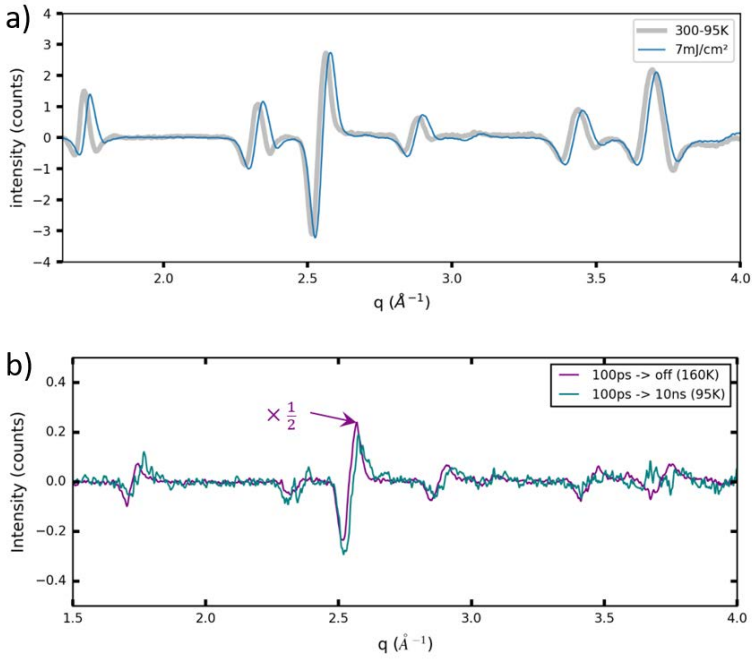


*Figure 19: a) Comparaison de la différentielle à 100 ps à haute densité d'excitation avec la différence statique entre phases haute et basse température. b) Comparaison de la différence entre début et fin de plateau (en bleu) avec la signature d'un refroidissement de la phase haute température (en violet).*

Afin d'expliquer la dynamique aux temps courts, nous avons utilisé un modèle décrit par Bargheer et al., qui simule la propagation à une dimension d'une onde de contrainte dans un échantillon sous forme de film. Notre but ici était d'expliquer les résultats obtenus aux temps courts, où le changement de volume extrapolé à partir du décalage des pics montre un creux au début du plateau (Figure 20).

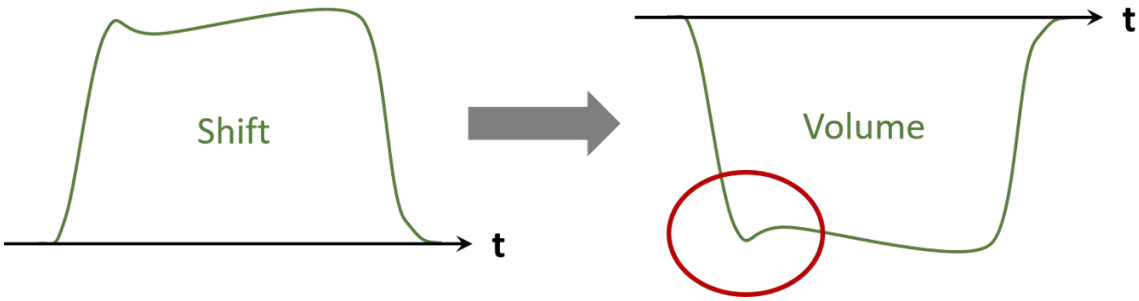


*Figure 20: Schéma de la variation temporelle de volume, extrapolée à partir du décalage de pic. Un creux est visible en début de plateau.*

Bargheer et al. présentent deux cas extrêmes, en fonction du ratio entre l'épaisseur du film et la longueur de pénétration du laser de pompe, pour décrire la propagation d'une onde de tension générée à travers un effet thermo-élastique photo-induit. Nous proposons de décrire la

dynamique observée dans nos expériences, en simulant une onde de compression, générée par une phase photo-induite de volume plus bas se propageant depuis la surface du film. Dans notre cas, le ratio de l'épaisseur du film sur la profondeur de pénétration du laser de pompe est plus petit que 1, ce qui implique une contrainte presque homogène dans le film. La phase se propageant étant de volume plus bas que le matériau initial, l'effet de contrainte est donc compressif (Figure 21a). J'ai ensuite calculé la valeur moyenne de la contrainte dans le film ( ), par intégration de la contrainte ( , ) le long de l'épaisseur du film. Cette contrainte moyenne a ensuite été convoluée avec une gaussienne de 70 ps FWHM, correspondant à l'impulsion de rayons X de sonde (Figure 21b). Cette convolution est ensuite comparée au changement de volume extrapolé du décalage de pics. En effet, étant donné l'absence de contrainte transverse due à la nature polycristalline du film, le changement de volume est libre de se propager le long de la direction du laser de pompe, normal à la surface. Ainsi, la comparaison de Δ / avec la contrainte = Δ / demeure valide. Malgré la faible résolution temporelle des données expérimentales, la contrainte simulée et le changement de volume montrent un bon accord qualitatif (Figure 21c).

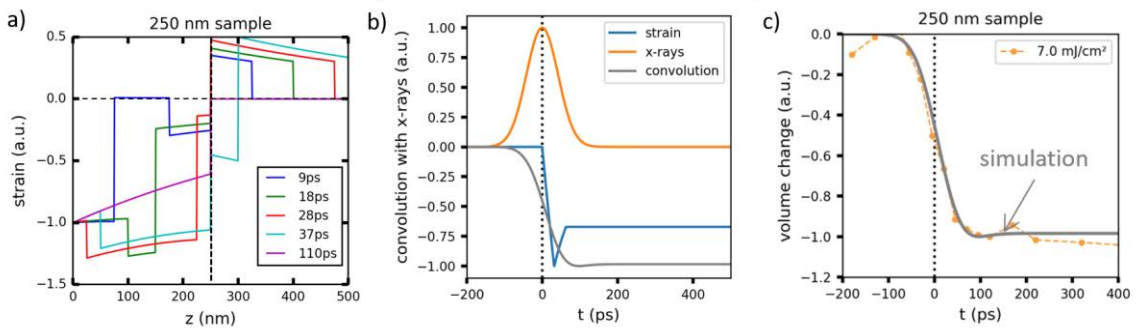


*Figure 21: a) Contrainte spatiale dans le film, modélisée à différent délais après photo-excitation. La ligne pointillée verticale représente la face interne du film. b) Convolution (en gris) de la contrainte temporelle moyenne dans le film (en bleu) avec l'impulsion de rayons X (en orange). c) Comparaison de la contrainte moyenne convoluée (en gris) avec le changement de volume extrapolé à partir du décalage de pic, à haute densité d'excitation.*

En conclusion, cette étude a montré la possibilité de photo-induire une transition de phase dans V2O3, même à faible température et pour une énergie de photon proche du gap du composé. L'absence de dépendance du taux de transformation envers la densité d'excitation suggère un processus cohérent et ultra-rapide.
Des mesures de diffraction X résolue en temps avec une meilleure résolution temporelle seraient bénéfiques pour explorer la dynamique structurale à la picoseconde, ainsi que des mesures résolues en angle afin de sonder la propagation en profondeur de la phase excitée et de conclure définitivement à propos du mécanisme de propagation.

Le but de cette thèse était d'explorer les dynamiques couplées de contrainte et transformation, au travers de mesures de diffraction X, dans le cadre de transitions de phase photo-induites dans des matériaux à changement de volume. En effet, la physique devient complètement différente, lorsque l'on passe des transitions de phase à l'équilibre au domaine des transitions de phase ultra-rapides : une vue d'ensemble reste à définir et le rôle clé du volume est encore à mettre en lumière. Nous avons développé une nouvelle méthode d'analyse pour l'exploitation des données de diffraction X résolue en temps sur des échantillons polycristallins, et l'avons appliquée à deux systèmes significativement différents.
Dans le matériau à transition de spin, nous avons montré un découplage temporel entre le changement de volume au temps acoustique et la dynamique plus lente de l'état de spin moléculaire. Contrairement à l'hypothèse précédente basée uniquement sur la taille des cristaux,

nous avons démontré que l'échelle de temps du processus coopératif reste intrinsèquement limitée par la dynamique Arrhenius.

Dans le cas des films de $V_2O_3$, la physique est complètement différente : aucune barrière énergétique ne sépare les deux états. Nous avons questionné la validité du précédent modèle de nucléation-croissance pour décrire la transition de phase photo-induite. Nos mesures de diffraction X, associées à un modèle de propagation d'onde de contrainte, sont en accord avec l'hypothèse d'une propagation acoustique d'une phase rhomboédrale de faible volume dans le film.

L'évidence du rôle joué par le volume dans ces deux systèmes, très différents l'un de l'autre, tend à montrer l'universalité du concept.

Les perspectives pour une exploration future du rôle du volume dans les transitions de phase photo-induites dans ce type de matériaux pourraient être :

- dans le cas des composés à transition de spin, tester si le changement de volume peut à lui seul induire la commutation de spin. L'objectif serait d'apporter uniquement de l'énergie thermo-élastique au cristal. De plus, la commutation de spin pourrait être adressée par le couplage avec les phonons, en utilisant la phononique non-linéaire. Ce thème sera le sujet d'une prochaine thèse, qui débute dans notre groupe.
- concernant $V_2O_3$, une piste intéressante serait de réaliser une étude similaire sur des films de $VO_2$. En effet, ce composé présente un comportement opposé à $V_2O_3$, dans le sens où le changement de volume à la transition isolant-métal est pratiquement nul, tandis qu'une forte distorsion ferroélastique se produit. Il serait intéressant de comparer les deux systèmes, dans le but d'explorer les rôles respectifs de la distorsion et du changement de volume dans la dynamique de la transition de phase photo-induite.

Enfin, un objectif important serait d'explorer la dynamique d'un nano-objet unique, par exemple en utilisant la diffraction électronique, afin de déterminer si plusieurs phases peuvent coexister au sein d'une seule et même cristallite, et ainsi affiner notre compréhension du mécanisme de propagation.